

FROM ELECTRONIC STRUCTURE OF POINT DEFECTS TO PHYSICAL PROPERTIES  
OF COMPLEX MATERIALS USING ATOMIC-LEVEL SIMULATIONS

By

HAIKUAN XU

A DISSERTATION PRESENTED TO THE GRADUATE SCHOOL  
OF THE UNIVERSITY OF FLORIDA IN PARTIAL FULFILLMENT  
OF THE REQUIREMENTS FOR THE DEGREE OF  
DOCTOR OF PHILOSOPHY

UNIVERSITY OF FLORIDA

2010

© 2010 Haixuan Xu

To my family with love and gratitude

## ACKNOWLEDGMENTS

First, I would like to express my deepest gratitude and respect to my advisor Prof. Simon R. Phillpot, not only for his invaluable guidance throughout my Ph.D study, but also his enthusiasm towards science and patience with students with a great sense of humor, which has made my time at UF extremely special. I admire him as a great researcher, mentor and motivator. I feel extremely fortunate to have him as my advisor. I would like to expand my appreciation to my committee members Prof. Susan B. Sinnott, Prof. Fereshteh Ebrahimi, Prof. Eric D. Wachsman, Prof. Jacob Jones and Prof. Aravind Asthagiri for their continuous support and advice.

I would like to thank Dr. Roger E. Stoller, with whom I had the fortune to work as a student intern at Oak Ridge National Laboratory. His kindness and insights into the subject have made my time there enjoyable and unforgettable. I would also like to convey my thanks to my experimental collaborator Prof. Venkatraman Gopalan at PSU and Prof. Volkmar Dierolf at Lehigh University. I would like to express my appreciation to all the members of Computational Materials Science Focus Group (CMSFG), especially Dr. Rakesh Behera, Dr. Jun He, Dr. Tao Liang, Prof Man Yao (Dalian University of Technology), Dr. Alex Chernatinsky, and Dr. Wen-Dung Hsu. The CMSFG had a positive impact on my research and life outside the school.

Finally, I would like to express my gratitude to my wife, Luyi Yin, for her unconditional love and invaluable support. She has been the constant inspiration to me. My heartfelt appreciation goes out to my parents, to whom I owe the most. Their love and belief has shape me to who I am today. This dissertation is dedicated to them.

## TABLE OF CONTENTS

	<u>page</u>
ACKNOWLEDGMENTS.....	4
LIST OF TABLES.....	8
LIST OF FIGURES .....	10
ABSTRACT .....	14
CHAPTER	
1 INTRODUCTION.....	16
1.1 Point Defects in Crystalline Materials .....	16
1.1.1 Energetics and Diffusion of Point Defects.....	17
1.1.2 Electronic Structure of Point Defect.....	20
1.1.3 The Effects of Point Defects on Properties of Materials.....	23
1.2 Defect Stability in Lithium Niobate.....	27
1.3 Mechanical Properties of Ceria-based Materials .....	29
1.4 Radiation Damage in Titanium .....	31
1.5 Overview of This Dissertation.....	32
2 SIMULATION METHODS .....	34
2.1 Density Functional Theory .....	35
2.1.1 Schrodinger Equation.....	35
2.1.2 Born-Oppenheimer Approximation.....	35
2.1.3 Hohenberg-Kohn Theorem .....	36
2.1.4 Kohn-Sham Equation .....	37
2.1.5 Exchange-Correlation Functionals .....	38
2.1.6 Pseudopotential Approximation .....	39
2.1.7 Limitations .....	40
2.1.8 DFT+U .....	41
2.2 Molecular Dynamics (MD) Simulation .....	41
2.2.1 Interatomic Interactions.....	42
2.2.2 Integration Scheme .....	44
2.2.3 Thermostat.....	46
2.2.4 Barostat .....	47
2.2.5 Ensembles.....	48
3 INTRINSIC DEFECTS IN LITHIUM NIOBATE .....	50
3.1 Background of Intrinsic Defects.....	50
3.2 Structure of LiNbO <sub>3</sub> and Constitute Binary Oxides.....	52
3.3 Computational Details .....	54

3.4	Thermodynamic Framework .....	58
3.5	Defect Formation Energy .....	64
3.5.1	Formalism.....	66
3.5.2	Point Defects .....	67
3.5.3	Defect Clusters .....	70
3.5.4	Defect Stability Range.....	73
3.6	Association Effects and Defect Configurations .....	74
3.7	Diffusion Mechanisms .....	82
3.8	Discussion .....	86
4	EXTRINSIC DEFECTS IN LITHIUM NIOBATE.....	91
4.1	Background of Extrinsic Defects .....	91
4.2	Structure of Reference Binary Oxides .....	92
4.2.1	Crystal Structure of MgO and FeO.....	93
4.2.2	Crystal Structure of Er <sub>2</sub> O <sub>3</sub> , Nb <sub>2</sub> O <sub>3</sub> , and Fe <sub>2</sub> O <sub>3</sub> .....	94
4.3	Computational Details .....	96
4.4	Formation Energies and Site Preference.....	101
4.4.1	Single Defects .....	102
4.4.2	Defect Clusters .....	106
4.5	Charge Transfer Levels.....	114
4.6	Discussions .....	117
4.6.1	Er Doped LiNbO <sub>3</sub> .....	117
4.6.2	Fe Doped LiNbO <sub>3</sub> .....	121
5	POINT DEFECTS IN CERIA-BASED ELECTROLYTES .....	124
5.1	Solid Oxide Fuel Cell Electrolytes.....	124
5.2	Structure of Ceria-Based Materials.....	125
5.3	Computational Details .....	128
5.4	Interatomic Potentials Evaluation .....	130
5.4.1	Lattice Constant and Thermal Expansion .....	130
5.4.2	Chemical Expansion .....	132
5.4.3	Dielectric Properties and Oxygen Migration Energy .....	134
5.4.4	Elastic Constants.....	135
5.4.5	Potential Summary.....	137
5.5	Mechanical Softening Effects.....	138
5.6	Oxygen Diffusion.....	143
5.7	Summary .....	146
6	CASCADE SIMULATIONS IN TITANIUM .....	148
6.1	Background.....	148
6.2	Structure of Titanium.....	150
6.3	Computational Details .....	152
6.3.1	MEAM Potential.....	154
6.3.2	ZBL Potential.....	159

6.4	Defect Analysis Method .....	160
6.4.1	Common Neighbor Analysis.....	161
6.4.2	Lattice Matching Analysis .....	162
6.5	Single Crystal Results and Discussions .....	163
6.6	Effects of Grain Boundaries .....	172
7	SUMMARY AND FUTURE WORK .....	175
7.1	Lithium Niobate .....	175
7.2	Ceria-based Materials .....	178
7.3	Titanium.....	179
	LIST OF REFERENCES .....	180
	BIOGRAPHICAL SKETCH .....	194

## LIST OF TABLES

<u>Table</u>	<u>page</u>
3-1	The comparison of bond lengths and coordination numbers between $\text{Li}_2\text{O}$ , $\text{Nb}_2\text{O}_5$ , and $\text{LiNbO}_3$ ..... 53
3-2	Lattice parameters calculated by PAW-LDA and PAW-GGA, compared with previous results..... 54
3-3	Difference in DFE, and relative energy difference, between $2 \times 2 \times 1$ system and $2 \times 2 \times 2$ system for various defects. .... 58
3-4	The heats of formation of $\text{Li}_2\text{O}$ , $\text{Nb}_2\text{O}_5$ , and $\text{LiNbO}_3$ calculated from the GGA calculations, compared with experimental results..... 62
3-5	The energy of lithium metal, niobium metal, oxygen gas, $\text{Li}_2\text{O}$ , $\text{Nb}_2\text{O}_5$ , and $\text{LiNbO}_3$ as calculated by GGA. .... 63
3-6	Change in oxygen chemical potential with respect to 0 K value from experiment <sup>130</sup> . .... 64
3-7	Defect formation energies for various defects, compared with previous electronic-structure and atomistic simulations..... 72
3-8	Association energy of $\text{Li}_2\text{O}$ -Pseudo Schottky, $\text{Nb}_2\text{O}_5$ Pseudo-Schottky, $5 \text{Nb}_{\text{Li}}^{\text{''''}} + 4 \text{V}_{\text{Nb}}^{\text{''''}}$ , and $\text{Nb}_{\text{Li}}^{\text{''''}} + 4 \text{V}_{\text{Li}}^{\text{'}}$ ..... 75
3-9	Defect formation energies and polarization of various A3 configurations.. .... 79
3-10	Defect formation energies and polarization of various A4 configurations..... 81
3-11	Activation Energy ( $E_a$ ) obtained from first principles calculations, compared with the experimental results. .... 85
4-1	Wyckoff position and fraction coordinates of $\text{Er}_2\text{O}_3$ ..... 95
4-2	Wyckoff position and fraction coordinates of $\text{Nd}_2\text{O}_3$ ..... 94
4-3	Fundamental properties comparison between GGA, GGA+U and experiments for $\text{FeO}$ ..... 98
4-4	Fundamental properties comparison between GGA, GGA+U and experiments for $\text{Fe}_2\text{O}_3$ . .... 98
4-5	Fundamental properties comparison between GGA, GGA+U and experiments for $\text{Nd}_2\text{O}_3$ . .... 99

4-6	Defect formation energies for defect reactions under different reference states. The chemical potential of Er is assumed to be the same as the value in Er <sub>2</sub> O <sub>3</sub> . .....	107
4-6	Charge transfer level of impurities calculated by GGA with comparison of experiments. ....	116
5-1	Potential Fluorite structure data from International Tables of Crystallography, Volume A: space-Group Symmetry, Fourth Edition. ....	127
5-2	Atomic position of ceria from neutron diffraction .....	127
5-3	Parameters of the five Buckingham potentials for ceria-based systems. ....	131
5-4	Parameters of the Inaba <sup>220</sup> Born-Huggins-Mayer potential for CeO <sub>2</sub> . No shell model is available for this potential. ....	131
5-5	Properties of CeO <sub>2</sub> from experiment and from various interatomic potentials. ....	134
5-6	Comparison of elastic properties of CeO <sub>2</sub> from experiment, DFT calculations and as predicted by empirical potentials. ....	136
5-7	Anisotropy in the Young's modulus of CeO <sub>2</sub> using different methods. Numbers in brackets indicate fractional value relative to that in the <001> direction. ....	137
5-8	Ionic Radii for relevant ions from Shannon. ....	141
6-1	The system size and number of simulations performed for each PKA energy. The neutron energy that is equivalent to average PKA energy is also listed. ....	154
6-2	The parameters of spline function for MEAM_II <sup>83</sup> . ....	158
6-3	The fundamental properties calculated using MEAM_I and MEAM_II, compared with EAM, FS, DFT and experimental data. ....	159
6-4	The fundamental properties calculated using MEAM_I and MEAM_II, compared with EAM, FS, DFT and experimental data. ....	159
6-5	The predefined parameters of the ZBL potential <sup>246</sup> . ....	160
6-6	Coordination number distributions provided by CNA with distinguishing HPC and FCC stacking sequence. ....	162

## LIST OF FIGURES

<u>Figure</u>	<u>page</u>
1-1 The Gibbs free energy as functional of defect concentration.....	18
1-2 Dieke's Diagram. ....	22
1-3 Sugano -Tanabe diagram. ....	23
1-4 Illustration of defect polarization interacting with bulk polarization. $P_s$ is the polarization of the bulk system, and $P_d$ is the polarization of defects. ....	25
1-5 Brouwer diagram of fluorite structure mixed ionic-electronic conductor. ....	27
2-1 Illustration of the concept of pseudopotential. ....	40
2-2 Cubic spline function of MEAM_II, which are fitted for hcp titanium metal. ....	44
3-1 Schematic of possible defect arrangement involving one niobium antisite and four lithium vacancies.....	52
3-2 The density of state (DOS) and partial DOS (PDOS) using GGA for $\text{LiNbO}_3$ . ....	56
3-3 Difference in defect formation energy (relative to the 1 x 1 x 1 system) as a function of system size. ....	57
3-4 Stability range of chemical potentials (in eV) of the elements in $\text{LiNbO}_3$ .....	65
3-5 Defect formation energies of various point defects as a function of Fermi energy. ....	68
3-6 Thermodynamic transition levels of O-related and Nb-related defects. The values under the line are with respect the valence band maximum (VBM). ....	69
3-7 Formation energies of neutral defects and defect clusters under $\text{Nb}_2\text{O}_5$ rich conditions (blue) and $\text{Li}_2\text{O}$ rich conditions (red). ....	71
3-8 Defect stability range: in the region AEFD, the Li-Frenkel is the dominant defect reaction; whereas in EBCF, the niobium antisite compensated by lithium vacancies is dominant.. ....	73
3-9 Defect formation energies dependence on the number of lithium vacancies in the first nearest neighbor positions of niobium antisite.....	77
3-10 Local structure of niobium antisite. ....	78
3-11 Schematics of possible diffusion paths in the $\text{LiNbO}_3$ .....	83

3-12	NEB calculations of diffusion barriers for lithium vacancy for several diffusion paths..	84
3-13	The DFEs of model III, Li-Frenkel and model I as a function of niobium chemical potential..	88
4-1	Crystal structure of MgO and FeO.....	93
4-2	Crystal structure of Er <sub>2</sub> O <sub>3</sub> .....	94
4-3	Crystal structure of Nd <sub>2</sub> O <sub>3</sub> .....	95
4-4	Crystal structure of $\alpha$ -Fe <sub>2</sub> O <sub>3</sub> .....	96
4-5	Electronic density of States of Er <sub>2</sub> O <sub>3</sub> calculated using GGA and GGA+U. The parameters U – J = 4 eV, U - J = 7.85 eV, and U - J=10.3 eV are considered.....	100
4-6	Defect formation energies of the lowest energy charge state of Er <sub>Li</sub> and Er <sub>Nb</sub> as a function of Fermi energy .....	104
4-7	Partial density of state (PDOS) for Er <sub>Li</sub> and Er <sub>Nb</sub> .....	105
4-8	Formation energies of Er-related defect clusters under Li <sub>2</sub> O rich conditions (blue) and Nb <sub>2</sub> O <sub>5</sub> rich conditions (red).....	108
4-9	Possible lithium vacancy positions in the first nearest neighbor (FNN) around Er sitting on lithium site. The oxygen sub-lattice is not shown. ....	109
4-10	Defect formation energy for Er <sub>Li</sub> + 2V <sub>Li</sub> shows the effects of association of the lithium vacancies around Er <sub>Li</sub> site. ....	110
4-11	Defect formation energies of various possible defect reactions for impurities under Nb <sub>2</sub> O <sub>5</sub> reference state.....	112
4-12	Defect formation energies of various possible defect reactions for impurities under Li <sub>2</sub> O reference state.....	113
4-13	Schematics of calculations of charge transfer levels. ....	115
4-14	The relative position of Fe <sup>2+</sup> /Fe <sup>3+</sup> charge transfer level with regard to the band gap.....	123
5-1	Electrical conductivity of various electrolytes as a functional of temperature. ....	125
5-2	Schematics of fluorite structure for CeO <sub>2</sub> .....	126
5-3	Kagome net formed by Ce from <1 1 1> view. Only the Ce-sublattice is shown. ....	127

5-4	Temperature dependence of the lattice parameter of CeO <sub>2</sub> obtained from MD simulation using different potentials, compared with experiment data. ....	132
5-5	The effect of composition on the lattice constants of CeO <sub>2-x</sub> obtained from MD simulations at 1073K. The values are compared with experimental results. ....	133
5-6	Composition dependence on the room temperature Young's modulus of CeO <sub>2-x</sub> obtained from MD simulation and from experiment. ....	139
5-7	The effects of temperature on the normalized bulk modulus (B), shear modulus (G), Young's modulus (Y), and anisotropic factor (Z) for CeO <sub>2</sub> .....	140
5-8	The effect of dopant ion size on the lattice parameter of Ce <sub>0.8</sub> M <sub>0.2</sub> O <sub>1.9</sub> (where M = In <sup>3+</sup> , Y <sup>3+</sup> , Gd <sup>3+</sup> , Ce <sup>3+</sup> , La <sup>3+</sup> ) obtained from MD simulation, compared with the experimental results. ....	141
5-9	Dopant size dependence on the Young's modulus of Ce <sub>0.8</sub> M <sub>0.2</sub> O <sub>1.9</sub> (where M = In <sup>3+</sup> , Y <sup>3+</sup> , Gd <sup>3+</sup> , Ce <sup>3+</sup> , La <sup>3+</sup> ) obtained using Grimes Potential.....	143
5-10	Diffusivity dependence on temperature for various doped-ceria systems.....	144
5-11	Activation energies of oxygen diffusion of various ceria-based electrolytes. The results are compared with experimental values and DFT results.....	145
5-12	Migration barrier along [001], [110], and [111] directions obtained from NEB calculations. ....	146
6-1	Phase diagram of titanium . ....	150
6-2	Structure of α and β phase of titanium.....	151
6-3	Structure of ω phase of titanium. ....	152
6-4	The evolution of number of Frenkel defect with time in cascade simulations at 100K with PKA = 1 keV using different time steps. ....	153
6-5	The schematics of lattice matching analysis (LMA). Both interstitials and vacancies are shown. ....	163
6-6	Threshold energies at various crystallographic orientations using MEAM_I, compared with previous results using FS potential. ....	164
6-7	Snapshot of cascade simulation in single crystal system at different simulation time. Only the atoms with coordination rather than 12 are shown.....	166
6-8	The number of survival Frenkel defects as a function of simulation time with various directions, positions, and energies of primary knock-off atom.....	167
6-9	The effect of PKA directions on survival Frenkel defects. ....	168

6-10	The comparison of number of survival Frenkel defects as a function of PKA energies between MEAM_I, MEAM_II, and FS potentials.....	169
6-11	The potential energy as a functional of nearest neighbor distance using FS, MEAM_2006 and MEAM_2008 potentials. ....	171
6-12	Polycrystalline structure of titanium in the cascade simulations. Courtesy of D. H. Kim.....	172
6-13	Snapshot of cascade simulation of polycrystalline system when PKA = 10 keV at 100K. Only the atoms with coordination rather than 12 are shown. ....	174

Abstract of Dissertation Presented to the Graduate School  
of the University of Florida in Partial Fulfillment of the  
Requirements for the Degree of Doctor of Philosophy

FROM ELECTRONIC STRUCTURE OF POINT DEFECTS TO PHYSICAL PROPERTIES  
OF COMPLEX MATERIALS USING ATOMIC-LEVEL SIMULATIONS

By

Haixuan Xu

May 2010

Chair: Simon R. Phillpot  
Major: Materials Science and Engineering

Point defects play a significant role in determining the physical and chemical properties of materials. Atomic-level simulation is a powerful tool to investigate and characterize the effect of these point defects. In this study, various aspects of the structure and stability of complex materials have been determined and predicted for lithium niobate, ceria-based systems, and titanium. The production, evolution, and dynamic behavior of defects have been explored. The focus has been on establishing the relationship between point defects and fundamental properties of bulk materials.

Lithium niobate is an important ferroelectric and non-linear optical material. For lithium niobate, the dominant defects with the lowest formation energies and their equilibrium structures are predicted under various experimentally relevant environments. The site preferences with corresponding charge compensation mechanisms are compared with experimental observations. The diffusion mechanism and energy barrier are determined to elucidate the dynamic behavior of defect and defect clusters. The effects of point defects on the polarization of the system are also discussed.

Ceria-based systems are considered as potential electrolytes of solid oxide fuel cells. In ceria-based systems, the effects of sub-stoichiometry, temperature and ionic radii on the mechanical properties are evaluated using molecular dynamics simulation. It is observed that sub-stoichiometry lead to a significant softening of the elastic constants. Similar results are predicted for doped ceria systems. These softening effects arise from the significantly reduced strength of ionic interactions.

Titanium is a candidate material for cladding of fast nuclear reactor system due to its high corrosion resistance and excellent mechanical properties. In this study, cascade simulations are carried out to investigate its radiation resistance. The effect of a high-energy atom (primary knock-on atom) is simulated with various energies, positions and orientations. A high disordered region with a large number of point defects is observed during the initial phases of simulations (ballistic phase), followed by recombination of interstitials and vacancies (relaxation phase). The effects of primary knock-on atom energies on remnant defects are established. The orientation effects of primary knock-on atom and the effects of grain boundaries are also evaluated.

## CHAPTER 1 INTRODUCTION

### 1.1 Point Defects in Crystalline Materials

The long-range order of atoms is the defining feature of crystalline materials. However, most crystalline materials are not perfect: the atomic arrangement can be interrupted and altered by various types of defects. According to their geometry and shape, the defects can be classified into point, line and planar defects<sup>1,2</sup>. For instance, point defects can be a regular lattice point not occupied by the proper ion. Linear defects, such as dislocations, are defects that some of the atoms in the crystalline materials are misaligned. Planar defects are surface imperfection in polycrystalline materials, such as grain boundaries or surfaces. It has been shown that properties of materials are strongly affected by the presence of these defects<sup>1</sup>. Therefore, it is of great importance to establish the relationship between these defects and the physical properties of materials. This study will focus on point defects.

There are many types of point defects<sup>1</sup>.

*Vacancy:* Site usually occupied by atom or ion is not occupied.

*Interstitial:* Atom is at a location in the crystal lattice that is usually empty.

*Antisite:* Site usually occupied by a specific type of atoms or ions (A) is occupied by a different type of atoms or ions (B).

*Substitutional impurity:* An atom, which is of the different type than any of the bulk atoms of the materials, replaces one of the bulk atoms in the crystal lattice.

Vacancies, interstitials, and antisites are considered to be intrinsic point defects, while substitutional impurities are considered to be extrinsic defects. Combination of these point defects forms defect complexes, such as Schottky defects and Frenkel pairs.

A Schottky defect is a combination of different types of vacancies that are on different sublattice<sup>1</sup>. For Schottky defects, the numbers of vacancies formed on each sublattice needs to satisfy the requirement of charge balance. For example, in a ABO<sub>3</sub> oxide with A +1 charged and B +5 charged, the Schottky defects can be expressed as

$$Null = V'_A + V''''_B + 3V''_O \quad [1-1]$$

By contrast, a Frenkel pair is a combination of a vacancy and interstitial of the same species<sup>1</sup>, which can be formed when an atom moves from its original crystal lattice site to a nearby interstitial site, creating a vacancy behind. The Frenkel pairs can occur on both cation and anion sublattice. The Frenkel pairs on anion sublattice are usually represented as anti-Frenkel defects. In the ABO<sub>3</sub> oxide mentioned above, the Frenkel defects can be:

$$Null = A_i^\bullet + V'_A \quad [1-2]$$

In addition, other types of defect complexes could form in materials. For example, in a ABO<sub>3</sub> oxide, an antisite can be formed when a B ion occupy a A site (B<sub>A</sub><sup>''''</sup>). This antisite needs to be compensated by defects with opposite charges to maintain the overall charge neutrality, either locally or globally, such as by vacancies of B cations. The possible defect reaction is:

$$Null = 5B_A^{''''} + 4V''_B \quad [1-3]$$

In specific materials, all the above defect complexes are possible. However, only one will prevail, depending on the energetics of these defect reactions.

### 1.1.1 Energetics and Diffusion of Point Defects

**Energetics:** The competition between the energy of creating a point defect (enthalpy change  $\Delta H$ ) and the entropy increases leads to a total Gibbs free energy decrease in the materials. In the dilute limit, the Gibbs free energy change ( $\Delta G$ ) as a functional of defect number can be expressed by<sup>1</sup>:

$$\Delta G = n_d h_d + kT n_d \zeta \ln \frac{\nu'}{\nu} + kT \left( N \ln \frac{N}{N+n_d} + n_d \ln \frac{n_d}{n_d+N} \right) \quad [1-4]$$

where  $n$  is the number of defects,  $N$  is the number of the atoms involved,  $k$  is the Boltzmann constant,  $T$  is the temperature,  $\zeta$  is the coordination number of defect,  $h_d$  is the enthalpy of formation,  $\nu$  is vibration frequency when atoms are at equilibrium structure, and  $\nu'$  is the vibration frequency when the defects are present in the nearest neighbor positions. As the equation shows, the Gibbs free energy change is a function of both temperature and  $n_d$ . If  $T$  is kept constant, the dependence of Gibbs free energy on  $n_d$  is shown in Figure 1-1.

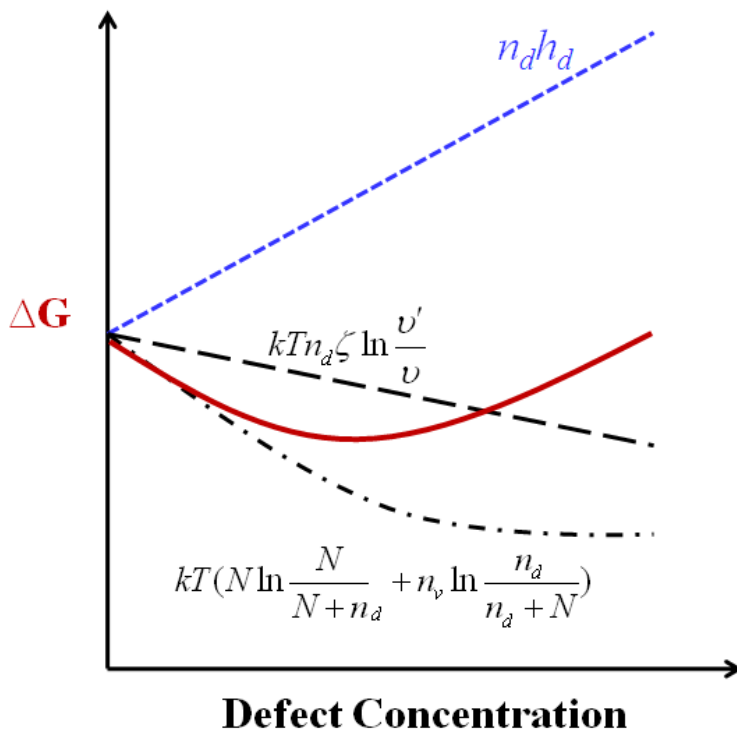


Figure 1-1. The Gibbs free energy as functional of defect concentration <sup>1</sup>.

The defect concentration, at which Gibbs free energy is minimum, is the equilibrium defect concentration ( $n_{eq}$ ).  $n_{eq}$  can be obtained using the following standard formula <sup>1</sup>:

$$\frac{n_{eq}}{N} \approx \exp\left(-\frac{h_d - T\Delta S}{kT}\right) \quad [1-5]$$

As mentioned previously, the equilibrium concentration of defects is also a functional of temperature. Increasing the temperature leads to an exponential increase in the number of the defects in the system.

**Diffusion:** The motion of these defects could happen when the energy of an atom is large enough to overcome the energy barrier of diffusion.

The diffusivity of vacancy can be calculated by <sup>1</sup>:

$$D_{vac} = \lambda^2 \nu_o \exp\left(-\frac{\Delta H_m}{k_B T}\right) \quad [1-6]$$

where  $\alpha$  is a geometric constant depending on crystal structure,  $\lambda$  is the jump distance,  $\nu_o$  is the vibration frequency of the atoms,  $\Delta H$  is the migration energy,  $k_B$  is the Boltzmann constant, and  $T$  is the temperature. Since the multiplication of  $\alpha$  and  $\zeta$  is unity, the vacancy diffusivity solely depends on the jump frequency and the distance of the jump. In the vacancy mechanism, the atom and vacancy swap lattice site, which leads to:

$$D_{ion} c_{ion} = D_{vac} c_{vac} \quad [1-7]$$

where  $D_{ion}$  is the diffusivity of ions,  $c_{ion}$  is the ion concentration,  $D_{vac}$  is the diffusivity of vacancy, and  $c_{vac}$  is the concentration of vacancies. In general,  $c_{vac}$  is very small, and  $c_{ion}$  can be approximated as unity. The equation can be simplified as

$$D_{ion} = D_{vac} c_{vac} \quad [1-8]$$

This indicates that the diffusivity of ions is much smaller than vacancy diffusivity. The vacancies move often, however, they are not numerous. By contrast, atoms move less frequently,

but there are a lot of them.  $D_{ion}$  is the self-diffusivity, which can be calculated from mean square displacement (MSD) of the ions:

$$D_{ion} = \frac{1}{6t} \langle |r_i - r_o|^2 \rangle \quad [1-9]$$

where  $r_i$  is the position of ion  $i$  at time  $t$  and  $r_o$  is the original position of ions.

The interstitial mechanism involves defect jumps from one interstitial site to another interstitial site. The interstitial diffusivity can be calculated by <sup>1</sup>:

$$D_{int} = \alpha_{int} \lambda^2 \nu_o \exp\left(-\frac{\Delta H_m}{k_B T}\right) \quad [1-10]$$

From comparison between Equation 1-6 and 1-10, it can be seen that there is little difference between the formulas for vacancy and interstitial diffusivity, except the successful jump frequency and jump distance. In addition, interstitial diffusivity is affected by a geometry factor, which depends on the structure of the materials. However, it is noted that the migration energy of interstitial is generally different from that of vacancies.

### 1.1.2 Electronic Structure of Point Defect

The electronic structure and properties of a material are modified by the presence of point defects. The interaction between point defects and bulk materials sometimes give unique feature of the material, such as the F-center defects (color center) in alkali-halides <sup>3</sup>. This is because point defects can introduce new energy levels into the band gap of the host crystal, which leads to transitions involving these levels, thereby producing electronic features not present in the perfect materials.

Many practical applications are based on the deliberate incorporation of impurities in the system, such as introducing rare earth elements and transition metals. Rare earth elements have unfilled  $4f$  electrons screened by fully filled  $5s$  and  $5p$  shells. Transition metals have unfilled  $3d$

outer shells. The electronic configurations of rare earth elements and transition metals give them different features from bulk and lead to various applications, such as solid-state laser, amplifiers, and superconductors <sup>4</sup>.

The rare earth elements, sometimes called lanthanide ions, have an electron configuration of  $5s^2 5p^6 4f^n$ , where n varies from 1 (Ce) to 13 (Yb). The valence electrons of these elements are from  $4f$  orbitals. However, they are shielded by  $5s$  and  $5p$  outer electrons, which usually make them weakly affected by the host ions. Therefore, the Stark energy levels of rare earth elements in crystal are very similar to those of free ions <sup>4</sup>, which also leads to the energy levels similar from one material to another. In fact, the energy level of rare earth elements provided by Dieke <sup>5</sup> based on particular host (lanthanum chloride) can be used for a wide range of materials. This energy level diagram, the so-called Dieke diagram <sup>5</sup>, is shown in Figure 1-2. The diagram shows the energy of  $^{2S+1} L_J$  states for rare earth elements in  $\text{LaCl}_3$ , in which S is the total spin, L is the orbital angular momentum, and J is the sum of L and S. The width of each state indicates the magnitude of the crystal field splitting, which the center of each multiplet gives the approximate location of its corresponding free ions energy level <sup>4</sup>.

Transition metal ions, on the other hand, have an unshielded  $3d$  outer shells. Therefore, there is a strong interaction between the ions and host lattice. Due to this strong interaction, the energy levels of transition metal ions in one material may be very different from another <sup>4</sup>, depending on the crystal field. Sugano and Tanabe have calculated the energy of the states for  $3d^n$  ions (n=2 to n=8) as a function of crystal field strength, generating the so-called Sugano-Tanabe diagram <sup>6,7</sup>, which is quite useful in understanding these ions in a variety of materials (Figure 1-3). The x-axis of the diagram is expressed in terms of ligand field splitting parameter,  $\Delta$ , divided by the Racah parameter B. The y axis is expressed in terms of energy (E) divided by

B. Sugano-Tanabe diagram shows how the  $^{2S+1}L_J$  levels split up as the ratio between the crystal field strength and the interelectronic interaction ( $Dq/B$ ) increases, which allows deducing useful information about the nature of the optical bands of transition metal ions <sup>4</sup>.

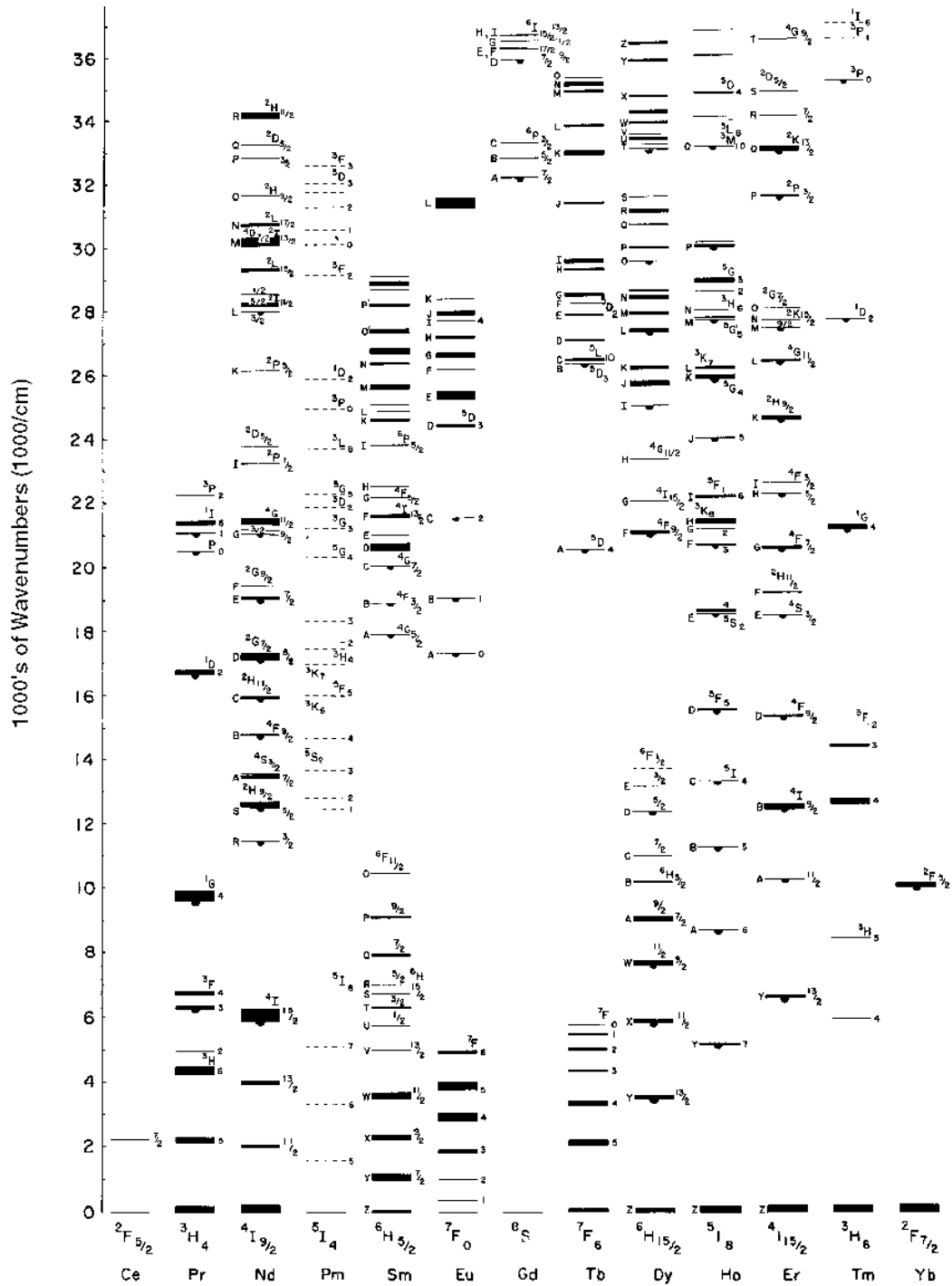


Figure 1-2. Dieke's Diagram <sup>5</sup>.

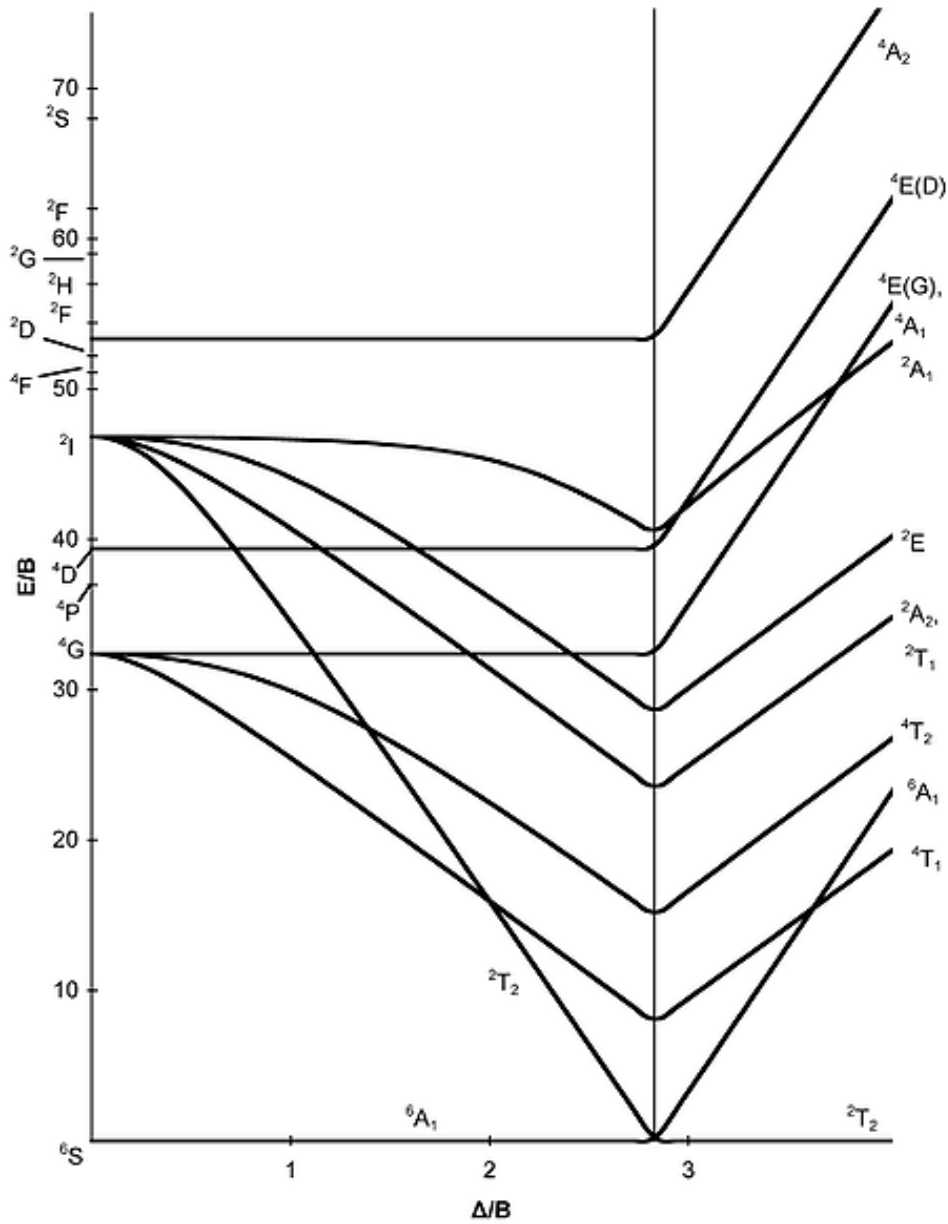


Figure 1-3. Sugano -Tanabe diagram <sup>6,7</sup>.

### 1.1.3 The Effects of Point Defects on Properties of Materials

When defects are introduced into the system, the local elastic and electrostatic environments change. The elastic interaction comes from the mismatch in size between defects and host ions, while the electrostatic interaction is from the charge difference. Due to this change of elastic and electrostatic interactions, many properties of the system can be affected by the

presence of point defects, including mechanical properties, thermal properties, electrical and magnetic properties, ferroelectricity, and optical properties.

**Mechanical properties:** The mechanical behaviors consist of elastic and plastic parts. Both plastic and elastic properties could be significantly affected by point defects. This is because that elastic modulus is a measure of the interatomic force or bond strength. The elastic modulus in a simple model can be expressed as the first derivative of the interatomic force. The presence of point defects can modify the interatomic forces, and hence the elastic modulus. In some cases, the influence of the point defects on elastic modulus could be significant. For instance, it has been shown experimentally that elastic modulus of  $\text{TiN}_x$  decreases substantially as the function of the concentration of nitrogen vacancies increase<sup>8,9</sup>.

The fracture toughness, which is the function of both Young's modulus and surface energy, will also be affected by the point defects through the effect in the Young's modulus. For example, it has been found that the fracture strength and fracture toughness of doped ceria appear to decrease with increasing the dopant concentration when the dopant level is less than 20 mol %. Further studies on the fracture properties of rare earth doped ceria showed that the fracture toughness was influenced by the dopant concentration rather than the dopant species. Since the oxygen vacancy concentration is directly associated with dopant concentration in doped ceria system, the results indicate the critical role of oxygen vacancy on the fracture properties. In summary, point defects play an important role in determining the mechanical properties of the materials

**Ferroelectricity:** A ferroelectric material possesses a spontaneous polarization, which can be reversed by an external electric field. In ceramic materials, several polarization mechanisms exist, such as electronic polarization, ionic displacement polarization, and space charge

polarization. The electronic polarization is caused by the displacement of the electron cloud relative to its nucleus. For the ionic polarization, the effective cation center is separated from the effective anion center by a certain distance<sup>1</sup>. Ferroelectric materials can form polarization domains, resulting in a domain wall between two domains with opposite polarization directions. However, the presence of point defects may significantly change the local polarization, domain wall structure, and domain wall motion.

The arrangement of the point defects may not preserve the long-range symmetry of the material, therefore, forming a local polarization itself. An illustration of how the defect polarization may interact with bulk polarization is given in Figure 1-4. The direction of local polarization does not necessarily have to be the same as bulk polarization, in most cases, it is different<sup>10</sup>. Therefore, the interaction between polarization due to point defects and bulk polarization could change the macroscopic properties of the materials, such as coercive field for domain reversal.

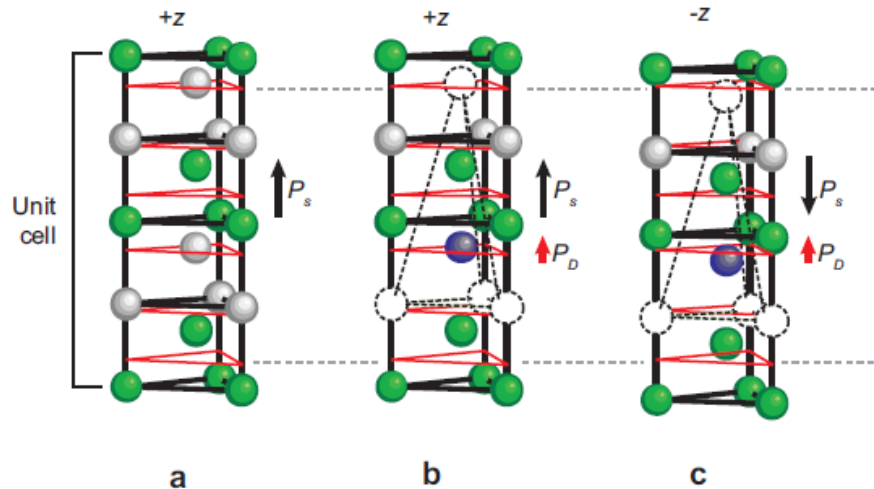


Figure 1-4. Illustration of defect polarization interacting with bulk polarization<sup>10</sup>.  $P_s$  is the polarization of the bulk system, and  $P_d$  is the polarization of defects.

When point defects are located at domain walls, the local structure of domain wall will be changed as point defects can introduce strain and electrostatic interactions into the system.

Furthermore, there could be a pinning effect on domain wall motion from the point defects. This is because point defects have to rearrange themselves during the domain wall motion. However, this arrangement process involves the migration of the point defects. The energy barrier for migration may be substantial in some materials, making the rearrangement process very difficult. Therefore, point defects can greatly limit the motion of domain walls.

**Ionic Conductivity:** The ionic conductivity in materials can also be tuned by point defects. In some cases, the ionic conductivity is obtained through defects that are thermally generated, such as Frenkel pairs or Schottky defects. In other cases, impurities are intentionally added to control the ionic conductivity of the materials. In the latter, the external impurities have to be in equilibrium with intrinsic point defects, since the defect reaction has to satisfy the requirements of charge balance, mass balance and site balance. Therefore, the concentration of one type of defects can be affected by the concentration of another.

The ionic conductivity is also a function of defect concentration. For example, as the defect concentration changes, the pre-factors are different. Furthermore, the activation energy of ionic conductivity consists of migration energy and association energy. The association energy takes into account the defect-defect interaction; therefore, it strongly depends on the defect concentrations. The ionic conductivity can be related with diffusivity through Nernst-Einstein equation, which is expressed as <sup>1</sup>:

$$\sigma_{ion} = \frac{Z^2 e^2 C_{ion} D_{ion}}{kT} \quad [1-11]$$

where  $\sigma_{ion}$  is the ionic conductivity,  $Z$  is valence of ion,  $e$  is the charge of electron,  $C_{ion}$  is the concentration,  $D_{ion}$  is the diffusivity of ions,  $k$  is the Boltzmann constant, and  $T$  is the temperature.

In experiments, desired conductivity is usually achieved by controlling the temperature and other thermodynamic parameters, such as oxygen partial pressure or impurities. In such system, many defect reactions are possible and multiple defect equilibrium will occur. The dependence of defect concentration of different species on the oxygen partial pressure is usually shown in a diagram, term as Brouwer diagram. The Brouwer diagram considers the net effect when all of the possible defect reactions simultaneously, therefore, providing a convenient way to represent the variation in defect concentration with changes the activity of a component of the compound. A exemplar case is given in Figure 1-5 for fluorite structure mixed ionic-electronic conductors.

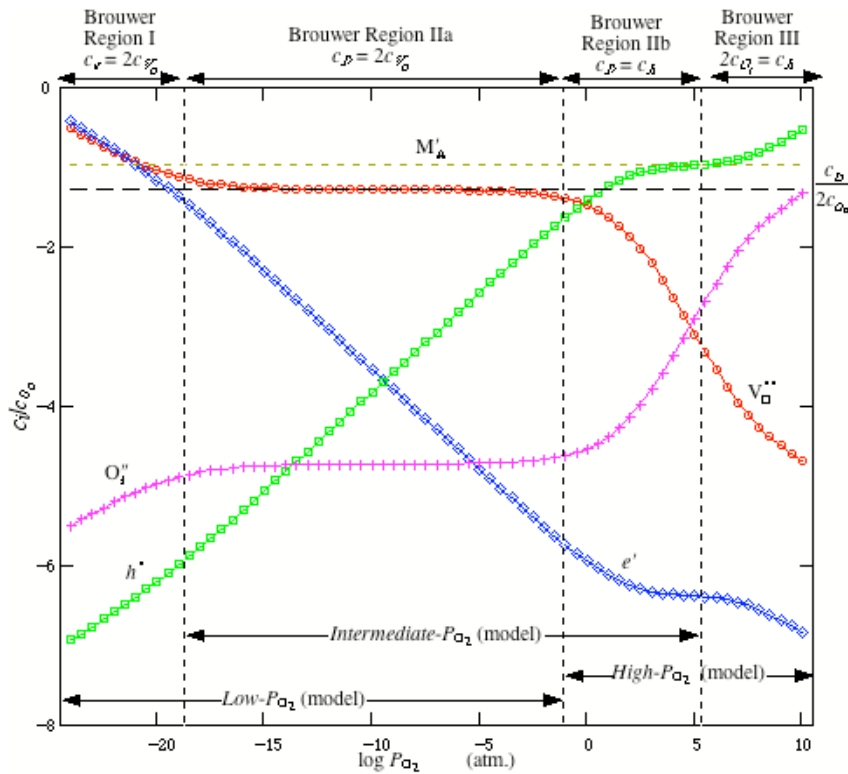


Figure 1-5. Brouwer diagram of fluorite structure mixed ionic-electronic conductor <sup>11</sup>.

## 1.2 Defect Stability in Lithium Niobate

LiNbO<sub>3</sub> is one of the most technologically important oxides with an extraordinary combination of ferroelectric, piezoelectric, acoustic, and optical properties <sup>10,12</sup>. For a very long

time work has focused on the congruent composition of  $\text{LiNbO}_3$ <sup>13-15</sup>. This is because only recently the stoichiometric  $\text{LiNbO}_3$  be synthesized using the double crucible Czochralski (DCCZ)<sup>16,17</sup> and vapor transport equilibration (VTE) methods<sup>18-20</sup>. This indicates that  $\text{LiNbO}_3$  has a strong tendency to form a lithium deficient structure. However, the reason why stoichiometric  $\text{LiNbO}_3$  is difficult to obtain is not yet clear.

The change of composition from the congruent (lithium poor) composition to the stoichiometric composition results in significant changes in the physical properties of the system, including the Curie temperature<sup>21</sup>, the ferroelectric coercive field<sup>21,22</sup>, and the photorefractive properties<sup>10</sup>. These changes in physical properties are thought to be due to the point defects and defect clusters. Yet, very little is known about the detailed structure and energetics of such clusters.

Three models for intrinsic point defect structures in  $\text{LiNbO}_3$  have been proposed. In the first model (Model I), two lithium vacancies are compensated by an oxygen vacancy<sup>23</sup>. In the second model (Model II), niobium antisites are compensated by niobium vacancies<sup>24</sup>. In the third model (Model III), niobium antisites are compensated by lithium vacancies<sup>10</sup>. For each model, different configurations of the defects are possible. Nevertheless, no fundamental understanding of either the local structure and these effects or their effects on the material properties is available.

In addition, to achieve the desired functionalities, various dopants are added to the system. For example, Mg is introduced to increase the resistance to photorefractive damage<sup>25,26</sup>; Fe doping is used for applications such as holographic storage and beam coupling<sup>27</sup>; Nd is added for solid-state laser applications<sup>28-31</sup>. In addition, dopant ions have also been employed as

probes to investigate the structure of domain walls and defect/domain-wall interactions<sup>32-34</sup>.

However, little is known about the incorporation site preference of these impurities.

To investigate the site selectivity of dopant ions, various experimental techniques, including electron-spin resonance<sup>4</sup>, electron nuclear double resonance (ENDOR)<sup>35</sup>, Mossbauer spectroscopy<sup>36,37</sup>, Rutherford backscattering<sup>38</sup>, X-ray standing wave analysis (XSW)<sup>39,40</sup>, extended x-ray absorption fine structure (EXAFS)<sup>41</sup>, and proton induced X-ray emission (PIXE)<sup>42</sup> have been employed. Moreover, several optical and magnetic resonance spectroscopy studies<sup>43-47</sup> have been used to determine the local environments and configurations around the dopant sites. However, a general consensus has not been reached as to what the dominant dopant configurations are. Furthermore, some of these studies used congruent LiNbO<sub>3</sub> samples grown by the Czochralski method<sup>13,14</sup>, others used stoichiometric LiNbO<sub>3</sub> produced through vapor transport equilibration (VTE)<sup>18-20</sup>. This makes it very difficult to compare results of experiments on samples from made with different synthesis technique; as a result the influence of the sample stoichiometry on the site selectivity and distribution is unclear.

### **1.3 Mechanical Properties of Ceria-based Materials**

The first test of a solid oxide electrolyte for solid oxide fuel cells (SOFCs) was carried out in the 1930s. Since then, much research has focused on finding an appropriate electrolyte<sup>48,49</sup>. To be used in practical applications, solid electrolytes need to satisfy several major requirements, including a high ionic conduction, negligible electronic conduction, and thermodynamic stability over a wide range of temperatures and oxygen partial pressures. In addition, solid electrolytes must have a thermal expansion compatibility with electrodes and suitable mechanical properties<sup>50</sup>.

Among various electrolytes, yttria-stabilized zirconia (YSZ)<sup>51-54</sup> has been investigated and used extensively. Compared with other solid electrolytes, YSZ exhibits very small electronic

contribution to total conductivity in the oxygen partial pressure range most important for practical applications<sup>50</sup>. However, YSZ electrolytes require a very high operating temperature (~1000 °C), which could cause many interface reactions such as the interaction between solid electrolytes and electrodes<sup>55</sup>. Thus, research focus on other potential electrolyte materials is of great interest.

As an alternative to YSZ, doped ceria<sup>56-59</sup> has been the subject of a great deal of attention due to its higher ionic conductivity than that of YSZ. The electrical conductivity of  $\text{Ce}_{0.80}\text{Gd}_{0.20}\text{O}_{1.9}$  (gadolinia-stabilized ceria) is about one order of magnitude higher than that of YSZ in the intermediate temperature (IT) range (500°C-700°C). Although  $\text{Bi}_2\text{O}_3$ -based materials showed higher ionic conductivity than YSZ and doped ceria, these materials are unstable at high temperatures and low partial pressures<sup>60</sup>, which severely limits its application.

The higher ionic conductivity of ceria-based electrolytes with respect to YSZ is the main advantage for use in SOFCs. However, doped ceria systems undergo reduction under low oxygen partial pressures, and the magnitude of electrical conductivity and stability are greatly dependent on the type and concentration of dopants<sup>55</sup>. Overall, ceria-based electrolytes show significant potential for practical application.

Due to the presence of oxygen vacancies in the doped ceria structure and important role of defect in determining physical properties of ceramics, the mechanical properties are quite different from that of the perfect structure. The mechanical property of doped ceria electrolytes are found to be inferior to YSZ<sup>52</sup>. Furthermore, the nanoindentation experiments indicate the elastic modulus decreases with increasing the oxygen vacancy concentration. However, the reason for this is yet fully understood.

## 1.4 Radiation Damage in Titanium

Titanium metal is widely used in industry, recognized for its high corrosion resistance and high strength with relatively less weight. Titanium is capable of withstanding acids and moist chlorine. Moreover, it is a very strong material with high ductility. The tensile strength of titanium is comparable to that of low-strength martensitic stainless steels and is better than that of austenitic or ferritic stainless steels.

Due to the relatively high strength and exceptional corrosion resistance, titanium has been considered as a potential material for nuclear reactor cladding. The degradation of thermo-mechanical behavior of cladding materials in the nuclear industry is a longstanding issue. The current cladding material is zircaloy. However, their corrosion resistance and ductility are poor compared with titanium.

The radiation process creates numerous point defects within a very short time, generating a dramatic thermal gradient and pressure gradient. The local structure is significantly modified and may be very unlike of the bulk structure. In addition, the defect generation has significant effects on the subsequent defect evolution and diffusion processes, substantially modifying the properties of materials. Therefore, it is critical to understand the effects of radiation on the structure and mechanical properties of titanium.

In addition, there are some indications that reducing the grain size will lead to an increase of resistance to the radiation damage<sup>61</sup>. However, the role of grain boundaries during the radiation process is poorly understood. The presence of grain boundaries may change the defect evolution process and subsequently change the mechanical behavior of the materials. Consequently, establishing the coupling between radiation damage, defect evolution, and mechanical properties is of great importance.

## 1.5 Overview of This Dissertation

This work is focused on the point defects energetics, dynamics, and their effects on the physical properties of lithium niobate, ceria-based materials, and titanium using density functional theory and molecular dynamic simulations.

In lithium niobate, the objective is to determine the dominant intrinsic defects/clusters under various experimental relevant conditions, such as for congruent and stoichiometric composition, as well as their local structures and configurations. Furthermore, the effects of such point defects and defect clusters on the polarization and ferroelectricity of the system will be explored. To determine whether the dominant defects are static or dynamic stable, the energy barrier of diffusion and corresponding mechanism will be elucidated. The details of intrinsic defects in lithium niobate are described in Chapter 3.

In addition to intrinsic point defects, various impurities have been introduced into the material to achieve functionalities. Therefore, the understanding of the incorporation site preference for different dopants and their charge compensation mechanisms is requisite. Furthermore, as impurities may introduce additional levels within the band gap of the bulk materials, the charge transfer levels of impurities need to be predicted to demonstrate the effects of impurities on the optical properties of the materials. The details of extrinsic defects in lithium niobate are given in Chapter 4.

In ceria-based materials, the objective of this work is to understand the effects of oxygen vacancies on the mechanical properties using molecular dynamic simulation. To achieve this, several empirical potentials have been evaluated first. Moreover, the effects of the dopant ionic radii on the mechanical properties will be established in order to search the optimal ionic radius of the dopants (Chapter 5).

For titanium metal, radiation effects on the materials will be investigated using cascade simulations, in order to understand the microstructure evolution of the materials under radiation damage. The survival Frenkel defects will be analyzed and their relationship with the primary knock-on atom energy will be investigated and compared with previous studies. Furthermore, the role of grain boundaries during the radiation process will be elucidated. The details of radiation damage in titanium are discussed in Chapter 6.

The summary of this work and envisioned future work are presented in Chapter 7.

## CHAPTER 2 SIMULATION METHODS

Electronic and atomic level simulations have been used extensively to study various properties and phenomena of materials, as they can provide information with atomic resolution that sometime is difficult to obtain from experiments. In the present study, electronic structure calculation at the level of density functional theory (DFT)<sup>62, 63</sup> and atomistic simulation at the level of molecular dynamics (MD)<sup>64</sup> are employed.

DFT is one of the most powerful and successful approaches to investigate the electronic structure in condensed matter materials. In numerous cases, the results predicted from DFT agree quite satisfactorily with the experimental results and observations<sup>63</sup>. Furthermore, in principle, DFT is an approach that does not require empirical parameters. In practice, certain approximations are needed. Therefore, due to this high fidelity, DFT is considered as a powerful tool in solid-state physics, chemistry and materials science. In general, DFT currently can only deal with up to hundreds of atoms and thousands of electrons. This prohibits many phenomena and properties at the larger scales from being considered, such as dislocations, phase transformations.

MD, on the other hand, can easily deal with millions of atoms at finite temperature using today's computational power. Moreover, MD can be used to study the nonequilibrium dynamic process of the system, which significantly broadens its applications. Unlike DFT, no electronic information is needed or provided by MD. Rather a classical interatomic potential<sup>64</sup> with a set of empirical parameters is used in order to describe the interactions between ions. In general, these empirical parameters are fitted to specific systems, which leads to poor transferability of the parameter and less material fidelity compared with DFT. As both DFT and MD have their

strengths and limitations, discretion is needed in choosing the appropriate method for a specific problem or process.

## 2.1 Density Functional Theory

### 2.1.1 Schrodinger Equation

The quantum state of a system consisting of electrons and nuclei is described using Schrödinger Equation. The time-independent, non-realistic Schrödinger Equation<sup>65</sup> is:

$$H\psi = E\psi \quad [2-1]$$

where  $H$  is the Hamiltonian operator,  $\psi$  is the eigenstate wave function and  $E$  is the eigenvalue. For atoms with electrons and nuclei,  $H$  can be expressed as:

$$H = -\frac{\hbar^2}{2m_e} \sum_i \nabla_i^2 + \sum_{i,l} \frac{Z_l e^2}{|r_i - R_l|} + \frac{1}{2} \sum_{i \neq j} \frac{e^2}{|r_i - r_j|} + -\frac{\hbar^2}{2M_l} \sum_l \nabla_l^2 + \sum_{l \neq j} \frac{Z_l Z_j e^2}{|R_l - R_j|} \quad [2-2]$$

where,  $m_e$  is the mass of electron,  $M_l$  is the mass of nuclei. The  $H$  consists of five terms, which are kinetic energy of electrons, the electron-nuclei interactions, the electronic-electron interactions, kinetic energy of nuclei, and interactions between nuclei and nuclei, respectively. However, analytical solutions are only available for very few simple cases, such as the one-dimensional potential well or the hydrogen atom<sup>62</sup>. For complex systems, only approximate solutions are possible. To obtain such approximate solutions, several assumptions have to be made.

### 2.1.2 Born-Oppenheimer Approximation

The Born-Oppenheimer approximation<sup>66</sup>, is based on the observation that electrons move much faster and weigh much less than the nuclei. It assumes the electronic motion and nuclear motion can be decoupled and that the electrons are in equilibrium with nuclei. This approximation is typically made although not all the methods employ it. In the Born-

Oppenheimer approximation, the electronic wavefunction depends on only the nuclear position but not the nuclear velocity. The Schrödinger Equation for electrons can then be written as:

$$\left[ -\frac{\hbar^2}{2m_e} \sum_i \nabla_i^2 + \sum_{i,I} \frac{Z_I e^2}{|r_i - R_I|} + \frac{1}{2} \sum_{i \neq j} \frac{e^2}{|r_i - r_j|} \right] \psi = E \psi \quad [2-3]$$

where only the first three terms in equation 2-2 remain, which are the kinetic energy of electrons, the electron-nuclei interactions, and the electronic-electron interactions. The kinetic energy of electrons and electron-nuclei term can be easily calculated. However, it is a tremendous challenge to describe the interaction between electrons and electrons, which is an interacting many-body problem.

All the above equations (2-1, 2-2, and 2-3) are expressed in term of wavefunctions. From wavefunctions, the probability of finding an electron at a given place or the electron density at a particular coordinate can be calculated by

$$n(r) = \sum_i \psi_i(r) \psi_i^*(r) \quad [2-4]$$

where, the  $\psi_i^*$  indicates the complex conjugate of the wave function. The link between wavefunction and electron density makes the electron density a fundamental variable of the system.

### 2.1.3 Hohenberg-Kohn Theorem

Two fundamental theorems in terms of electron density were established by Hohenberg and Kohn<sup>67</sup>. Theorem I states that “For any system of electrons in an external potential  $V_{\text{ext}}(\mathbf{r})$ , that potential is determined uniquely, except for a constant, by the ground state of electron density  $n(\mathbf{r})$ ”, which established a one-to-one mapping between the external potential and the ground-state electron density and allowed all properties of the system to be determined from the ground-state electron density. Theorem II states that “ A universal functional for the energy  $E[n]$

of the density  $n(r)$  can be defined for all electron systems. The exact ground state energy is the global minimum for a given  $V_{ext}(r)$ , and the density  $n(r)$  which minimizes this functional is the exact ground state density”, which is a direct consequence of variational principle. Although the Hohenberg-Kohn theorem are very powerful, neither theorem defined the functional of the electron density or indicated a systematic way of finding the functional.

#### 2.1.4 Kohn-Sham Equation

A route to actual calculations is provided by the Kohn-Sham equations<sup>68</sup>, which replaced the difficult the many-body problem with an auxiliary independent electron problem that can be exactly solved<sup>62</sup>. Since there is no unique way to define the auxiliary system, it is usually rephrased as an *ansatz*. The Kohn-Sham equations assume the exact ground state density can be represented by the ground state electron density of a non-interacting auxiliary system; the auxiliary Hamiltonian is chosen to have the usual kinetic operator and an effective local potential. Therefore, the Kohn-Sham equation can be expressed as:

$$\left[ \frac{-\hbar^2}{2m} \nabla^2 + V_{eff}(r) \right] \psi_i(r) = \varepsilon_i \psi_i(r) \quad [2-5]$$

$$V_{eff}(r) = V_{ext}(r) + V_{Hartree}(r) + V_{xc}(r) \quad [2-6]$$

where  $V_{ext}(r)$  is the external potential due to the nuclei and any other external potential,  $V_{ext}(r)$  is the Hartree potential,  $V_{xc}(r)$  is the exchange and correlation potential,  $\psi_i$  is the wave function of state  $i$ ,  $\varepsilon_i$  is the Kohn-Sham eigenvalue. The Hartree potential is defined as:

$$V_H(r) = e^2 \int \frac{n(r')}{|r-r'|} d^3 r' \quad [2-7]$$

The exchange and correlation potential is given as:

$$V_{xc}(r) = \frac{\delta E_{xc}(r)}{\delta n(r)}. \quad [2-8]$$

where,  $E_{xc}(r)$  is the exchange-correlation energy. This exchange-correlation functional is the only unknown term in the Kohn-Sham equations. Therefore, reasonable approximations, such as local density approximation (LDA) and generalized gradient approximation (GGA), are required to solve the equations <sup>62</sup>.

### 2.1.5 Exchange-Correlation Functionals

In LDA <sup>62</sup>, the exchange correlation energy per electron at a given point  $r$  is assumed to be equal to the exchange correlation energy per electron in a homogeneous electron gas that has the same density at  $r$ . Therefore, LDA does not consider the exchange correlation energy due to the inhomogeneities in system. Despite this, LDA works remarkably well for many systems, even in very inhomogeneous cases..

The GGA, on the other hand, includes not only the local density but also a density gradient term, which accounts for the inhomogeneities of the system. There are many forms of GGA, such as Perdew and Wang (PW92) <sup>69</sup>, Perdew, Burke, and Ernzerhof (PBE) <sup>70</sup>, and Lee-Yang-Parr (LYP). In general, GGA predicts lower binding energies than LDA, which improves the agreement with experiments, as LDA is well known to overbind the system. However, GGA does not lead to a consistent improvement over LDA, as it violates the sum rule and other relevant constraints. Sometimes, GGA even leads to worse results compared with LDA, making the selection of the appropriate functional a challenging task.

The wave functions ( $\Psi$ ) in Equation 2-5 can be generally represented using either plane waves or localized orbitals. Each method would be more appropriate for a particulate range of problems and applications. Localized orbitals provide an intuitive picture that captures the essence of atomic-like feature in solids, which is widely used in quantum chemistry.

Furthermore, localized orbitals allow, in principle, linear scaling of DFT calculations with system size. However, the localized orbitals basis set depends on the positions of the ions, which needs a Pulay correction added to the Hellman-Feynman forces<sup>62</sup>. The completeness and superposition errors of localized orbitals basis sets are very difficult to control. In general, plane waves provide general solutions of differential equations, such as the Schrödinger Equation. Therefore, plane waves are a natural choice for system with periodic boundary conditions (PBC)<sup>64</sup>. They provide important information about the band structures of many materials, including metal, semiconductors, and insulators. Moreover, the conversion between real and reciprocal space is easy and no Pulay correction is needed for the force calculations on atoms. However, the convergence of plane waves is very slow. To overcome this, the electron-ion interaction are usually represented by pseudopotentials

### **2.1.6 Pseudopotential Approximation**

The key idea of pseudopotentials<sup>71</sup> is to replace the strong Coulomb potential nucleus and the effects of tightly bounded core electrons with an effective ionic potential that acts on the valence electrons and has the same scattering properties as the all-electron potential beyond a given cut-off radius (Figure 2-1). The approximation is based on the fact that most of the properties of the materials are only determined by the valence electrons. Compared with all-electron method, the pseudopotential approach can significantly reduce the number of basis sets. The advent of norm-conserving pseudopotentials (NCPPs)<sup>72</sup> and ultrasoft pseudopotentials (USPPs)<sup>73,74</sup> has led to accurate electronic structure calculations that are the basis of modern research.

The PAW<sup>75</sup> method introduces a projector acting on the valence electrons and auxiliary localize functions that like USPP method. It is a combination of both augmented wave method (APM) and the pseudopotential approach<sup>76</sup>. Furthermore, it can be shown that NCPPs and

USPPs are approximations to the PAW method<sup>77</sup>. In general, the PAW method is expected to be as accurate as all electron methods and as efficient as pseudopotentials approach.

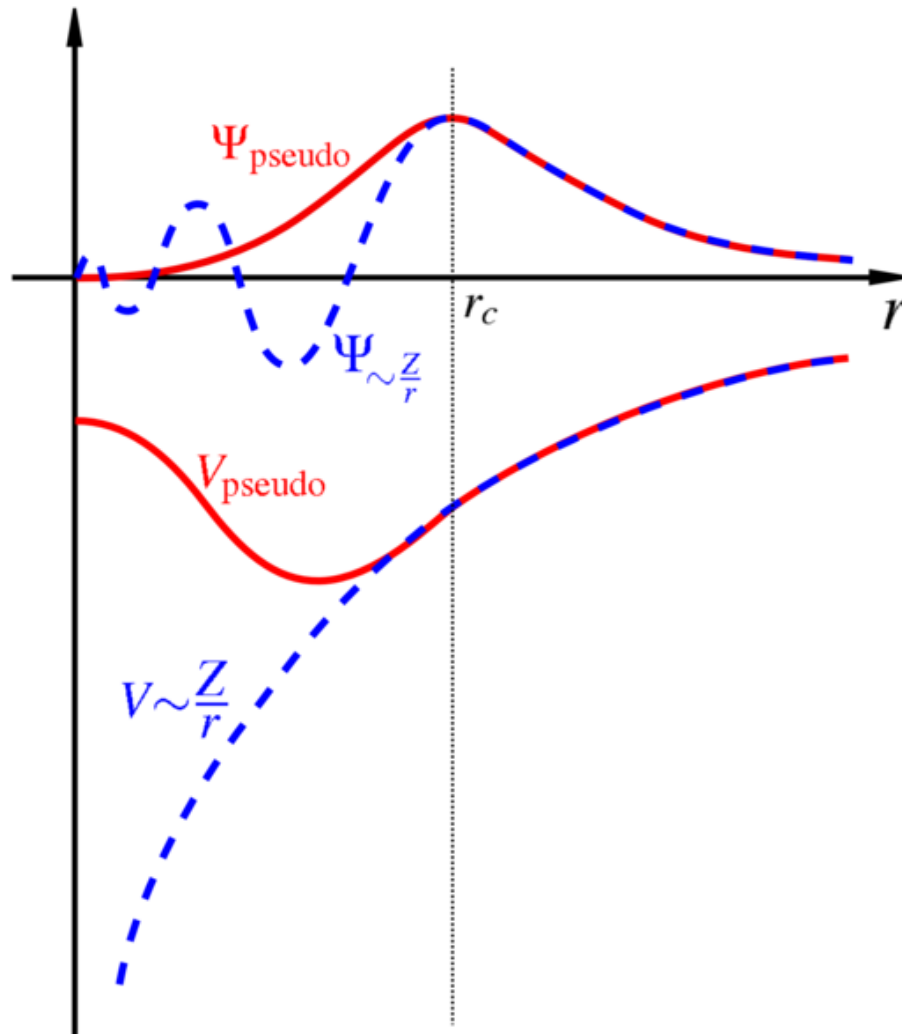


Figure 2-1. Illustration of the concept of pseudopotential. Picture taken with permission from Wikipedia: <http://en.wikipedia.org/wiki/Pseudopotential>

### 2.1.7 Limitations

In general, DFT is remarkably successful in determining a wide range of properties of the materials. However, there are certain limitations of the method. The best known problem of DFT is the underestimation of the band gap. The band gap of semiconductor and insulator is always underestimated by DFT. This is because DFT is the ground state theory while calculating

the band gap involves excited states. In addition, LDA usually predicts small lattice constants than experiments, which results in too large cohesive energies and too large bulk moduli. GGA, on the other hand, largely corrects this overbinding problem<sup>63</sup>. However, GGA has a tendency to overshoot this problem for the heavy elements. Furthermore, DFT neglects strong correlations and van der Waals interactions. Neglecting strong correlation causes DFT fail to predict the correct band structure of Mott insulator with *d* or *f* orbitals<sup>78</sup>.

### 2.1.8 DFT+U

To overcome these problems, many approaches have been developed, such as DFT+U<sup>78, 79</sup>. DFT+U attempts to improve the band structure of a Mott-insulator by adding an onsite repulsion term to the DFT Hamiltonian, which results in a localized feature of *d* or *f* electrons that DFT has failed to describe. Many versions of the DFT+U have been published in the literature. Among them, Dudarev's method<sup>79</sup> is probably the most widely used one due to easy implementation and lower computational effect requirement. In Dudarev's method, the total energy of the system is expressed as:

$$E_{DFT+U} = E_{DFT} + \frac{U - J}{2} \sum_{\sigma} n_{m,\sigma} - n_{m,\sigma}^2 \quad [2-9]$$

where  $n_{m, \sigma}$  is the occupation number of the *m*-th *d* or *f* state. The *U* and *J* are empirical parameters. It is noted that in Dudarev's method, only the difference between *U* and *J* (*U*-*J*) is meaningful.

## 2.2 Molecular Dynamics (MD) Simulation

MD is routinely used to investigate the structure, dynamics, and thermodynamics of various materials. In MD, the motion of atoms in the system is predicted by solving Newton's law of motion, which is

$$\mathbf{F}_i = m_i \mathbf{a}_i \quad [2-10]$$

where,  $\mathbf{F}_i$  is the force acting on an atom  $i$ ;  $m_i$  is the mass of atom  $i$ , and  $\mathbf{a}_i$  is the acceleration of atom  $i$ . The force on each atom can be calculated from the gradient of the potential energy:

$$\mathbf{F}_i = -\nabla_i V \quad [2-11]$$

where,  $V$  is the potential energy. Therefore, to describe the interaction between atoms, an appropriate potential is needed. For different types of materials, the potentials that have been used to describe the system may be in different forms. For any specific material, even using the same form of potential, different parameterizations may be used. Therefore, it is of great importance to evaluate the potential parameter before any practical calculations have been performed.

### 2.2.1 Interatomic Interactions

For ionic systems, one of the most widely used potential is the Buckingham potential combined with Coulombic interactions. The Buckingham potential is expressed as:

$$V_{Buck}(r_{ij}) = A_{ij} \exp\left(-r_{ij}/\rho_{ij}\right) - C_{ij}/r_{ij}^6 \quad [2-12]$$

where  $A_{ij}$ ,  $\rho_{ij}$  and  $C_{ij}$  are the empirical parameters that are fitted to the system, and  $r_{ij}$  is the separation between two ions  $i$  and  $j$ . The first term in Equation 2-12 is a repulsive interaction, which decreases exponentially with increase in distance between atoms  $i$  and  $j$ . The second term in Equation 2-12 is an attractive contribution due to the dipole interactions.

The Coulombic interaction is a long-range interaction and can be described as:

$$E_{Coul} = \frac{1}{2} \sum_{i=1}^N \sum_{j \neq i, 1}^N \frac{q_i q_j}{r_{ij}} \quad [2-13]$$

where,  $N$  is the total number of ions in the system,  $q_i$  and  $q_j$  are the charges on atom  $i$  and  $j$  respectively. The  $r^{-1}$  dependence makes the sum conditionally convergent. The summation of the Coulombic term over the system can be carried out using either Ewald sum<sup>64</sup> or direct sum<sup>80</sup>.

The embedded atom method (EAM) was developed for metallic system<sup>81</sup>. The potential energy of EAM consists of two parts: embedding energy and a two-body potential term. The embedding term, while the two-body term depends on the interatomic bond distances. The total energy is expressed as<sup>81</sup>:

$$E_i = \sum_i \left[ F_i(\rho_i) + \frac{1}{2} \sum_{j(\neq i)} \Phi_{ij}(R_{ij}) \right] \quad [2-14]$$

where  $F_i$  is the embedding function,  $\rho_i$  is the background electron density at the site  $i$ ,  $\Phi_{ij}$  is the pair function between atom  $i$  and atom  $j$ ,  $R_{ij}$  is the distance between atom  $i$  and  $j$ .

The modified embedded atom method (MEAM) is an extension of the EAM to include angular contributions<sup>82</sup>. In the present study, two types of MEAM potentials have been used. One is the traditional MEAM developed by Baskes<sup>82</sup>. The details of this MEAM potential are given in section 6.3.1. Another type of MEAM potential is in the function form of cubic spline<sup>83</sup>, thereafter named MEAM\_II. MEAM\_II removes the constraints of fixed angular feature and allows additional flexibility of the potential. The total energy in MEAM\_II is calculated by<sup>83, 84</sup>

$$E = \sum_{ij} \Phi(r_{ij}) + \sum_i U(\rho_i) \quad [2-15]$$

where  $\Phi(r_{ij})$  is the pair interaction between atom  $i$  and  $j$ .  $U(\rho)$  is the self energy function depending on the electron density of atom  $i$ . The electron density of atom  $i$  is calculated using

$$\rho_i = \sum_j \rho(r_{ij}) + \sum_{jk} f(r_{ij}) f(r_{ik}) g[\cos(\theta_{jik})] \quad [2-16]$$

where  $\theta_{jik}$  is the angle between atom  $j, i$ , and  $k$  centered on atom  $i$ . All five functions  $\Phi(r_{ij})$ ,  $U(\rho)$ ,  $\rho(r)$ ,  $f(r)$ , and  $g[\cos\theta]$  are represented by cubic spline functions, which are fitted to the

fundamental properties of the system. MEAM\_II can be related to the Stillinger-Weber potential [ $U(x)=x$  and  $\rho=0$ ] and EAM potential [ $f=0$  or  $g=0$ ]<sup>83</sup>. Examples of five cubic spline functions are given in Figure 2-2.

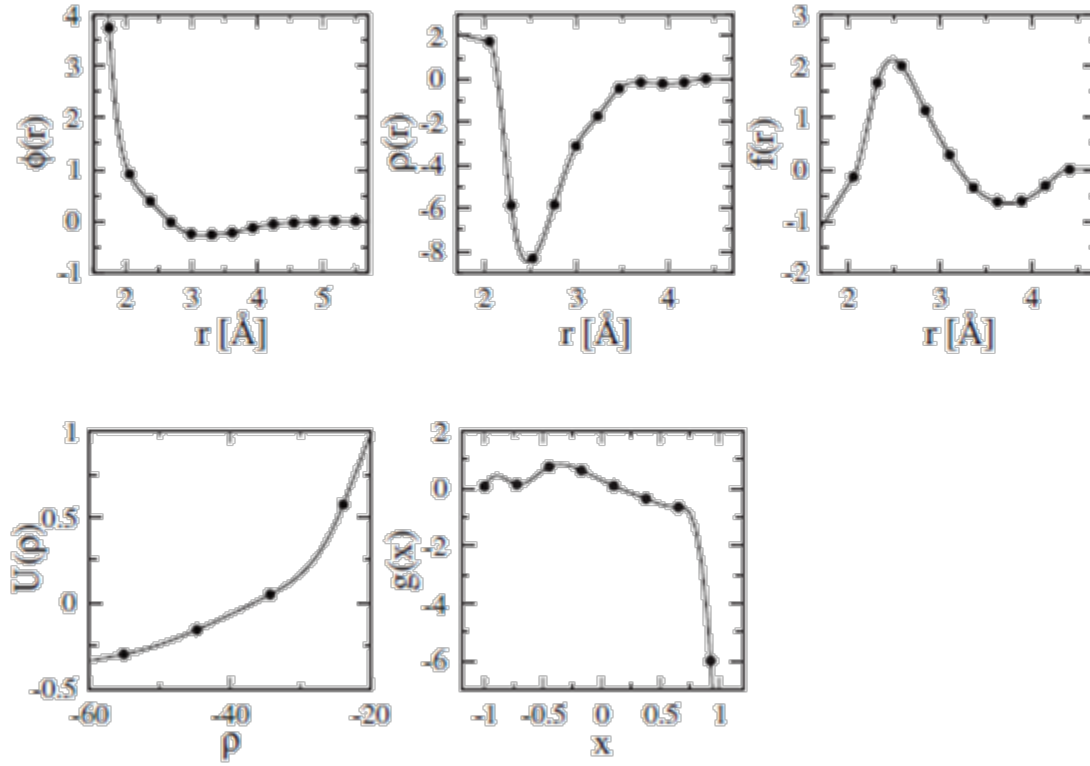


Figure 2-2. Cubic spline function of MEAM\_II, which are fitted for hcp titanium metal<sup>83</sup>.

### 2.2.2 Integration Scheme

The integration scheme of Newton's equation of motion is a central part of the MD simulations. At a small increment of time ( $\delta t$ ), referred as the time step, the position, velocity and accelerations of the atoms are calculated based on integration methods. There are several integration schemes available, such as Verlet algorithm<sup>64</sup>, which is one of the most widely used integration algorithms. In the current study, 5<sup>th</sup>-order Gear predictor-corrector method<sup>85</sup> is employed. This is because the Gear algorithm is faster than the Verlet algorithm when the

number of the system is large <sup>64</sup>. Moreover, the Gear algorithm is more accurate than the Verlet algorithm with a longer time step, therefore, achieving a higher degree of energy conservation <sup>64</sup>.

The central idea of the predictor-corrector is that a Taylor expansion is used to predict the positions, velocities, accelerations, and higher order derivatives of position at time  $t + \delta t$  then a correction term is added based on the predicted acceleration. For a fifth order predictor-corrector, the predictor formulas are given as <sup>64</sup>:

$$\begin{aligned}
 \vec{r}^p(t + \delta t) &= \vec{r}(t) + \delta t \vec{v}(t) + \frac{1}{2} \delta t^2 \vec{a}(t) + \frac{1}{6} \delta t^3 \vec{b}(t) + \frac{1}{24} \delta t^4 \vec{c}(t) + \frac{1}{120} \delta t^5 \vec{d}(t) \\
 \vec{v}^p(t + \delta t) &= \vec{v}(t) + \delta t \vec{a}(t) + \frac{1}{2} \delta t^2 \vec{b}(t) + \frac{1}{6} \delta t^3 \vec{c}(t) + \frac{1}{24} \delta t^4 \vec{d}(t) \\
 \vec{a}^p(t + \delta t) &= \vec{a}(t) + \delta t \vec{b}(t) + \frac{1}{2} \delta t^2 \vec{c}(t) + \frac{1}{6} \delta t^3 \vec{d}(t) \\
 \vec{b}^p(t + \delta t) &= \vec{b}(t) + \delta t \vec{c}(t) + \frac{1}{2} \delta t^2 \vec{d}(t) \\
 \vec{c}^p(t + \delta t) &= \vec{c}(t) + \delta t \vec{d}(t) \\
 \vec{d}^p(t + \delta t) &= \vec{d}(t)
 \end{aligned}
 \tag{2-17}$$

where  $\vec{r}$  is the position,  $\vec{v}$  is the velocity, and  $\vec{a}$  is the acceleration of each atom in the system.  $\vec{b}$ ,  $\vec{c}$  and  $\vec{d}$  are third, fourth and fifth derivatives of the position with respect to time. The superscript ‘p’ represents ‘predicted’ values.

The total energy of the system can be calculated based on the predicted positions of atoms. The interatomic forces at time  $t + \delta t$  are then calculated using the derivatives of potential energies with respect to the predicted atoms positions. With information on interatomic forces, accelerations are easily obtained. However, these predicted acceleration values are based on Taylor expansion rather than physics. Therefore, correction terms are needed in order to describe the physical behavior of atoms. The corrected positions and other derivatives are calculated by <sup>64</sup>:

$$\begin{aligned}
\vec{r}^c(t + \delta t) &= \vec{r}^p(t + \delta t) + c_0 \Delta \vec{a}(t + \delta t) \\
\vec{v}^c(t + \delta t) &= \vec{v}^p(t + \delta t) + c_1 \Delta \vec{a}(t + \delta t) \\
\vec{a}^c(t + \delta t) &= \vec{a}^p(t + \delta t) + c_2 \Delta \vec{a}(t + \delta t) \\
\vec{b}^c(t + \delta t) &= \vec{b}^p(t + \delta t) + c_3 \Delta \vec{a}(t + \delta t) \\
\vec{c}^c(t + \delta t) &= \vec{c}^p(t + \delta t) + c_4 \Delta \vec{a}(t + \delta t) \\
\vec{d}^c(t + \delta t) &= \vec{d}^p(t + \delta t) + c_5 \Delta \vec{a}(t + \delta t)
\end{aligned}
\tag{2-18}$$

The superscript ‘*c*’ corresponds to the ‘corrected’ values. The coefficients for a fifth order predictor-corrector are  $c_0 = 3/16$ ,  $c_1 = 251/360$ ,  $c_2 = 1$ ,  $c_3 = 11/18$ ,  $c_4 = 1/6$ , and  $c_5 = 1/60$ <sup>86</sup>.

These corrected values are then used to predict the positions and other higher order derivatives for the next iteration.

### 2.2.3 Thermostat

To simulate materials under realistic conditions, it is typically necessary to control the temperature. There are several commonly used approaches to achieve this. The simplest is probably the velocity-rescaling thermostat<sup>64</sup>. Within this method, the velocity of each atom, which is associated with the kinetic energy, is adjusted:

$$v_{target}(t) = \sqrt{\frac{T_{target}}{T_{current}}} v_{current}(t)
\tag{2-19}$$

where  $T_{current}$  is the current temperature,  $T_{target}$  is the target temperature,  $v_{current}$  is the current velocity, and  $v_{target}$  is the velocity after adjusting.

However, this method has several problems<sup>87</sup>. First, the energy and momentum conservation are not obeyed. Secondly, the rate of temperature adjustment depends on the MD time step. Furthermore, the ergodic theorem will not hold, which could lead to a failure of prediction of physical properties based on the ensemble average<sup>88</sup>. Due to these limitations, great caution is needed when velocity-rescaling method is used.

In the current study of cascade simulations in titanium, Berendsen thermostat is employed. The Berendsen thermostat<sup>89</sup> is found to be more reasonable in both the physics and statistical mechanics than velocity-rescaling. Within Berendsen thermostat, the velocity is adjusted by:

$$v_{target}(t) = \sqrt{1 + \frac{dt}{\tau} \left( \frac{T_{target}}{T_{current}} - 1 \right)} v_{current}(t) \quad [2-20]$$

where  $dt$  is the time step in the MD simulation, and  $\tau$  is the adjustable parameter for the thermal equilibration. It can be seen that the Berendsen thermostat is equivalent to velocity rescaling thermostat when  $\tau=dt$ . When  $\tau$  is infinity, the velocity will not be adjusted, which corresponds to the microcanonical ensemble. In general, the Berendsen thermostat is gentler than velocity rescaling. The Berendsen thermostat can be considered as the first order approximation of the Langevin thermostat<sup>64</sup>. Therefore, the dynamics of the system can be close to the realistic evolution.

#### 2.2.4 Barostat

In addition to temperature, controlling the supercell volume and shape is also requisite during the simulation under realistic conditions, such as under an external pressure. To achieve this, barostat schemes are needed, such as Andersen barostat<sup>90</sup> and Parrinello-Rahman barostat<sup>91</sup>.

The idea of the Andersen barostat is to assume the system in a container that can be compressed by piston with a mass of  $M$ . Then the Lagrangian can be written as:

$$L(\rho^N, \dot{\rho}^N, V, \dot{V}) = \frac{1}{2} V^{2/3} \sum_{i=1}^N m_i \dot{\rho}_i^2 - \sum_{i<j=1}^N U(V^{1/3} \rho_{ij}) + \frac{1}{2} M \dot{V}^2 - pV \quad [2-21]$$

where  $\rho_i$  is the scaled coordinates and defined as Cartesian coordinates divided by cubic root of the volume( $V$ ),  $p$  is the external pressure acting on the piston.

Then the motions of the atoms derived by Andersen can be expressed as:

$$\frac{dr_i}{dt} = \frac{P_i}{m_i} + \frac{1}{3} r_i \frac{d \ln V}{dt} \quad [2-22]$$

$$\frac{dP_i}{dt} = -\sum r_{ij} U'(r_{ij}) - \frac{1}{3} P_i \frac{d \ln V}{dt} \quad [2-23]$$

$$\frac{Md^2V}{dt^2} = p + \left[ \frac{2}{3} \sum \frac{P_i^2}{2m_i} - \frac{1}{3} \sum r_{ij} U'(r_{ij}) \right] / V \quad [2-24]$$

It is noted that Andersen barostat is isotropic, which means the external pressure is hydrostatic. In many cases, this is not a good approximation. The Parrinello-Rahman barostat extends the Andersen method by allowing the shape of the simulation cell to change. This is achieved by introducing a 3x3 matrix  $H$  so that

$$\begin{aligned} V &= \det(H) \\ r_i &= Hs_i \end{aligned} \quad [2-25]$$

The Lagrangian of Parrinello-Rahman barostat can be expressed as<sup>91</sup>:

$$L = \frac{1}{2} \sum_{i=1}^N m_i \dot{S}_i^T G \dot{S}_i - \sum U(r_{ij}) + \frac{1}{2} M \text{Tr}(\dot{h} \dot{h}^T) - pV \quad [2-26]$$

Both Andersen and Parrinello-Rahman barostats are used in the current study.

### 2.2.5 Ensembles

By controlling temperature, pressure, and other thermodynamic properties, such as volume, total number of atoms, and internal energy, simulations can be carried out under well-defined thermodynamic conditions, such as, in a well-defined thermodynamic ensemble. Simulation of a system with fixed  $N$ ,  $V$ , and  $E$  corresponds to the isochoric microcanonical ensemble (NVE)<sup>64</sup>. Similarly, NVT is canonical ensemble and NPT is isothermal-isobaric ensemble. These three are the most widely used ensembles in MD simulations, and have been employed in the current study. In addition, there are other types of ensembles, such as grand canonical ensemble, in

which the total number of the atoms ( $N$ ) in the system can be changed while a fixed uniform chemical potential has to be maintained.

## CHAPTER 3 INTRINSIC DEFECTS IN LITHIUM NIOBATE

### 3.1 Background of Intrinsic Defects

LiNbO<sub>3</sub> is an important ferro-, pyro-, and piezoelectric material with many promising physical properties<sup>12</sup>. Its applications include use as a second harmonic generator, a parametric oscillator, a transducer and nonvolatile memory<sup>18, 92</sup>. Non-stoichiometric, intrinsic defects and defect clusters have been identified as the origin of substantial differences in properties between materials with slightly different Li/Nb ratios. While a large body of experimental literature exists, and some theoretical investigations have been performed, many of the key conjectures in the literature, especially on defect clusters, remain unverified by either experiments or theory. The purpose of this work is to systematically analyze the intrinsic defects and defect-clusters in lithium niobate using density functional theory (DFT) calculations combined with thermodynamic calculations.

It appears that the growth process affects the type of defects produced. The typical composition of LiNbO<sub>3</sub> grown from congruent melting is  $\text{Li} / (\text{Li} + \text{Nb}) = 0.485$ , which indicates a lithium deficient defect structure<sup>10</sup>. More nearly stoichiometric compositions have been achieved through vapor transport equilibration (VTE)<sup>93, 94</sup> and double crucible Czochralski (DCCZ)<sup>16, 17</sup> methods. The change of composition from 0.485 (congruent) to 0.5 (stoichiometric) causes large shifts in the Curie temperature<sup>21</sup>, cohesive field for domain reversal<sup>17, 21, 22</sup>, built-in internal field<sup>95</sup>, and other properties<sup>10</sup>. In particular, it has been conjectured that the temperature stability and field dynamics of a defect cluster consisting of a niobium antisite surrounded by four lithium vacancies can explain much of the observed macroscale switching behavior in congruent lithium niobate<sup>10</sup>. However, no experimental verification or detailed

theoretical analysis of this intrinsic defect cluster has been presented to date. Thus, a fundamental understanding of this and other intrinsic defects in LiNbO<sub>3</sub> is essential.

Based on the experimental data, several defect models in congruent LiNbO<sub>3</sub> have been proposed. Prokhorov *et al.*<sup>23</sup> proposed that oxygen vacancies surrounded by two lithium vacancies (so-called, Model I) dominate at room temperature. However, it was soon determined from experiments that the density of LiNbO<sub>3</sub> increases with increasing Li<sub>2</sub>O deficiency<sup>96</sup>, which is inconsistent with Model I. Schirmer *et al.*<sup>24</sup> concluded that niobium antisites compensated by niobium vacancies (Model II) are the dominant defects, and that oxygen vacancies are present in negligible concentration.

However, Donnerberg *et al.*<sup>97</sup>, using atomic-level simulations, showed that the formation of niobium vacancies to compensate the niobium antisites is energetically less favorable than the formation of lithium vacancies. This leads to Model III consisting of  $\text{Nb}_{\text{Li}}^{\text{''''}} + 4\text{V}_{\text{Li}}^{\text{'}}$  (shown in Figure 3-1). Model III was supported by X-ray and neutron diffraction studies<sup>98-101</sup>. On the one hand, Schirmer *et al.*<sup>24</sup> pointed out that the niobium vacancy model (model II) and lithium vacancy model (model III) can be reconciled if it is assumed that there are ilmenite-type stacking faults in congruent LiNbO<sub>3</sub>. On the other hand, nuclear magnetic resonance (NMR) studies<sup>102, 103</sup> concluded that a combination of Model I and Model III provide both qualitative and quantitative agreement with Li NMR spectra. Inconsistent with this is the assumption that only Model III can be used to explain the temperature dependence of experimental Li and Nb NMR spectra<sup>102, 103</sup>. These contradictory experimental results demonstrate that the nature of intrinsic defect arrangements in LiNbO<sub>3</sub> is still not fully understood.

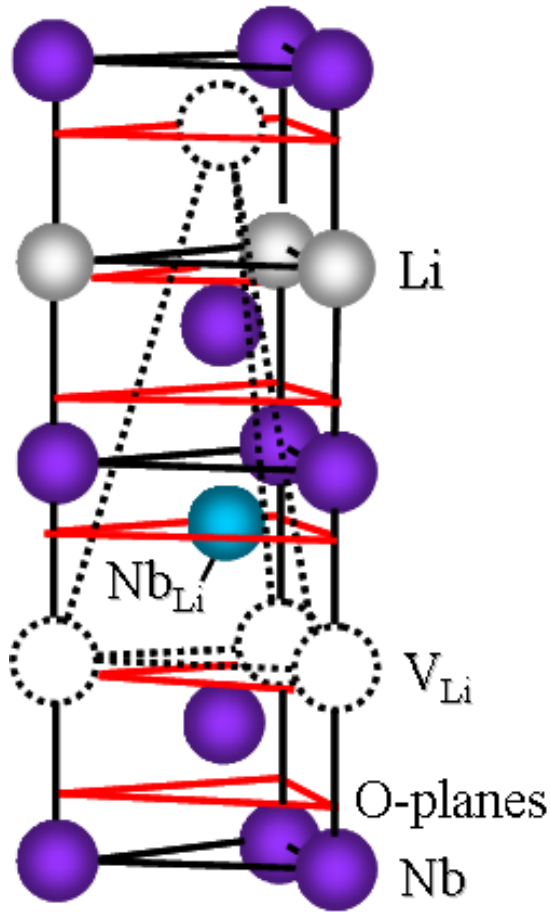


Figure 3-1. Schematic of possible defect arrangement involving one niobium antisite and four lithium vacancies (so-called Model III).

### 3.2 Structure of LiNbO<sub>3</sub> and Constituent Binary Oxides

Ferroelectric LiNbO<sub>3</sub> has an R3c structure, which belongs to the trigonal system. The lattice constants of LiNbO<sub>3</sub> are  $a = 5.1474$  and  $c = 13.8561$  Å. Both lithium and niobium sit on the 6a Wyckoff position while oxygen occupies 18 b. This indicates that there are six lithium, six niobium and eighteen oxygen in each unit cell. Compared with the paraelectric phase, which has a R-3c space group, the lithium and niobium ions are displaced along z direction, leading to spontaneous polarization of the system.

Li<sub>2</sub>O has an anti-fluorite structure (space group: Fm-3m), with a lattice constant of 4.57 Å<sup>104</sup>. For Nb<sub>2</sub>O<sub>5</sub>, several different structures have been reported, including R-Nb<sub>2</sub>O<sub>5</sub> (C2/m), P-

Nb<sub>2</sub>O<sub>5</sub> (I4<sub>1</sub>22), M-Nb<sub>2</sub>O<sub>5</sub> (I4/mmm), N-Nb<sub>2</sub>O<sub>5</sub> (C2/m), H-Nb<sub>2</sub>O<sub>5</sub> (P2/m), T-Nb<sub>2</sub>O<sub>5</sub> (Pbam), and B-Nb<sub>2</sub>O<sub>5</sub> (C2/c)<sup>105</sup>. Among these, T-Nb<sub>2</sub>O<sub>5</sub>, and B-Nb<sub>2</sub>O<sub>5</sub> are known to be high-pressure phases<sup>106</sup>; H-Nb<sub>2</sub>O<sub>5</sub> is observed to be stable at high temperatures (T > 1100°C)<sup>105</sup>; R-Nb<sub>2</sub>O<sub>5</sub> is metastable and transforms to P-Nb<sub>2</sub>O<sub>5</sub> on slow heating and to N-Nb<sub>2</sub>O<sub>5</sub> on rapid heating<sup>105</sup>. According to Holtzberg *et al.*<sup>107</sup>, the room-temperature phase of Nb<sub>2</sub>O<sub>5</sub> is amorphous. Here, metastable R-Nb<sub>2</sub>O<sub>5</sub> is used to determine the chemical potential range, since it is the only phase for which complete structural information is available from the literature<sup>105</sup>. Both lithium metal and niobium metal have Im-3m structure, whereas the molecular oxygen gas is simulated by putting an oxygen dimer in a vacuum box.

The coordination numbers of the ions in the three systems can be determined from examination of the crystal structures. As shown in Table 3-1, both of the structurally distinct Nb ions in LiNbO<sub>3</sub> structure are six-fold coordinated. Likewise, the two structurally distinct Nb ions in R-Nb<sub>2</sub>O<sub>5</sub> are also six-fold coordinated. Moreover, the bond lengths in the two systems determined from the DFT calculations are both close to each other and to the experimental values. The situation is different for Li<sub>2</sub>O. In particular, the Li in anti-fluorite structured Li<sub>2</sub>O is 4-fold coordinated, whereas it is six-fold coordinated in LiNbO<sub>3</sub>. Consistent with these differences in coordination, the calculated bond lengths are quite different.

Table 3-1. The comparison of bond lengths and coordination numbers between Li<sub>2</sub>O, Nb<sub>2</sub>O<sub>5</sub>, and LiNbO<sub>3</sub>.

		Bond Length		Coordination Number
		DFT	Experiment	
LiNbO <sub>3</sub>	Li-O (S)	2.02	2.05 <sup>15</sup>	6
	Li-O (L)	2.25	2.27 <sup>15</sup>	6
	Nb-O (S)	1.90	1.88 <sup>15</sup>	6
	Nb-O (L)	2.14	2.13 <sup>15</sup>	6
Li <sub>2</sub> O	Li-O	1.98	1.98 <sup>104</sup>	4
Nb <sub>2</sub> O <sub>5</sub>	Nb-O (S)	1.95	2.02 <sup>105</sup>	6
	Nb-O (L)	2.15	2.19 <sup>105</sup>	6

### 3.3 Computational Details

The Vienna *Ab Initio* Simulation Package (VASP)<sup>108, 109</sup> is employed to carry out all the calculations of crystallographic structures, electronic structures, and defect formation energies. The projected augmented wave (PAW) method<sup>75</sup>, which combines much of the accuracy of an all-electron method<sup>110</sup> with the flexibility of the pseudo-potential approach<sup>111</sup>, is used. The Li 2s<sup>1</sup>, Nb 4p<sup>6</sup>4d<sup>4</sup>5s<sup>1</sup>, and O 2s<sup>2</sup>2p<sup>4</sup> are treated as valence electrons. The cut-off energy for plane wave basis set is 400 eV<sup>74</sup>. The allowed error in energy from relaxation is 0.001 eV. The electronic minimization algorithm for energy calculation is based on residual minimization scheme-direct inversion in the iterative subspace (RMM-DIIS)<sup>112</sup>.

**LDA vs. GGA:** The results obtained from the local density approximation (LDA) and the general gradient approximation (GGA) for the lattice parameters of the ferroelectric phase of LiNbO<sub>3</sub> (R3c) are compared with experimental values in Table 3-2 for a supercell containing 2 x 2 x 2 conventional unit cells (240 atoms with a total of 1440 electrons). As is typical, GGA predicts larger lattice parameters than LDA.

Table 3-2. Lattice parameters calculated by PAW-LDA and PAW-GGA, compared with previous results. USPP denotes ultrasoft pseudopotentials; NCPP denotes norm-conserving pseudopotential.

	a (Å)	c (Å)	V (Å <sup>3</sup> )
PAW LDA	5.049	13.686	302.198
PAW GGA	5.138	13.914	318.119
USPP LDA <sup>74</sup>	5.064	13.667	303.523
USPP LDA <sup>73</sup>	5.086	13.723	307.420
NCPP LDA <sup>72</sup>	5.125	13.548	308.172
NCPP GGA <sup>72</sup>	5.255	13.791	329.816
Experiment	5.147 <sup>15</sup>	13.853 <sup>15</sup>	317.873 <sup>15</sup>
	5.151 <sup>113</sup>	13.876 <sup>113</sup>	318.844 <sup>72</sup>

As Table 3-2 shows, GGA gives excellent agreement with the experimental values, with the in-plane lattice parameter, *a*, being underestimated by 0.2% and the *c* lattice parameter being overestimated by 0.6%; as a result the calculated volume is within 0.1% of the experimental

value. The GGA-PAW calculations give considerably better agreement with experimental values than the LDA and GGA calculations with the norm-conserving pseudo-potentials (NCPP)<sup>72</sup> or LDA calculations with ultrasoft pseudopotentials (USPP)<sup>73,74</sup>.

The electronic densities of states (DOS) have been calculated using PAW-LDA and PAW-GGA. LDA yields a band gap of 3.42 eV, whereas the GGA value is 3.5 eV. These results are consistent with previous calculations using NCPPs of 3.48 and 3.50 eV for LDA and GGA respectively<sup>72</sup>. The calculated band gap is also in good agreement with the value of 3.5 eV, previously calculated using the orthogonalized-linear-combination-of-atomic-orbital method (OLCAO)<sup>114</sup>. The band gap calculated by GGA is 8% less than the experimental value of 3.78 eV<sup>115,116</sup>; this agreement can be considered as excellent, since DFT is widely known to underestimate band gaps<sup>62</sup>. The DOS calculated using GGA is given in Figure 3-2. The highest occupied valence band exhibits mainly O-2p features, whereas the lowest unoccupied conduction band mainly consists of Nb-4d electrons. This DOS is also consistent with calculations performed by OLCAO<sup>114</sup> and NCPP<sup>72</sup>. Based on this analysis of structure and band structure, GGA is chosen for the calculations of DFEs.

**K-point mesh:** The Monkhorst-Pack<sup>117</sup> method is used to carry out the integration in the Brillouin-zone. Since for LiNbO<sub>3</sub>, the length of *c* is approximately double that of *a* for a 2 x 2 x 2 system, we chose to have half the number of k-points in the z-direction (*c*-axis) as in the x- and y-directions. A 4 x 4 x 2 k-point mesh has been used in the current study for both the perfect structure and defect structure calculations. As discussed by Van de Walle and Neugebauer<sup>118</sup>, the  $\Gamma$  point should be avoided for an accurate calculation of the DFEs because the interaction between a defect and its mirror image through periodic boundary conditions is at its maximum at

the  $\Gamma$  point. Thus, the origin of the k-point mesh has been shifted from the  $\Gamma$  point to (0.5, 0.5, 0.5).

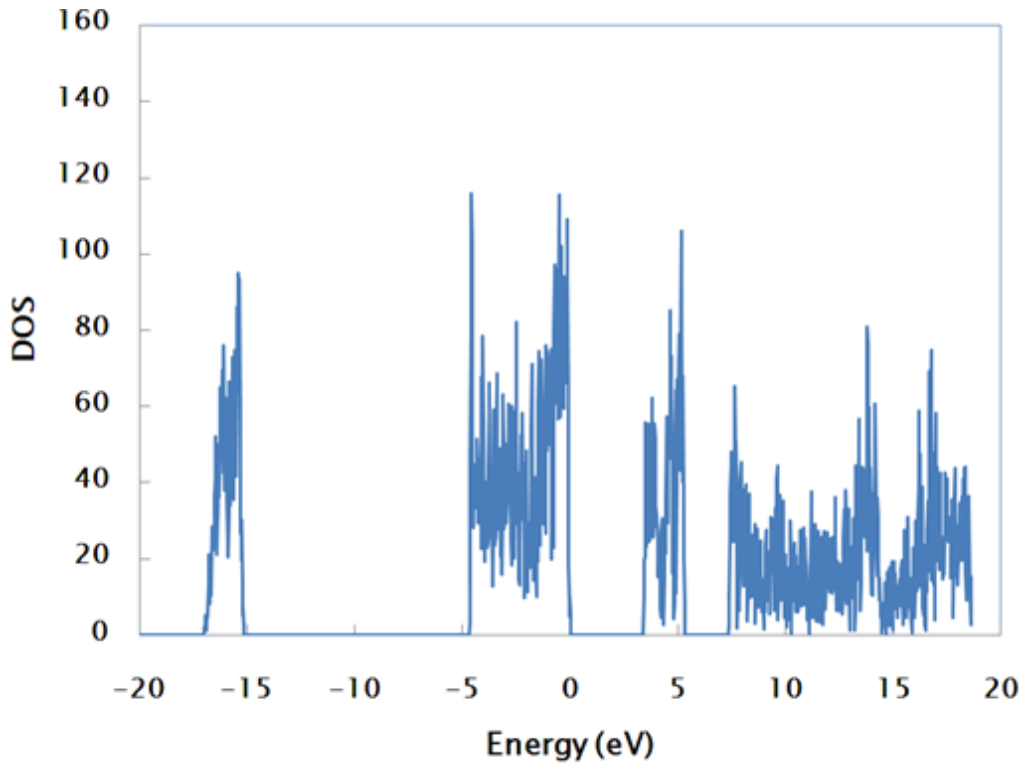


Figure 3-2. The density of state (DOS) and partial DOS (PDOS) using GGA for  $\text{LiNbO}_3$ .

**System size:** The supercell method<sup>119-121</sup>, containing a finite number of atoms and defects with periodic boundary conditions, is used to calculate the formation energies of both isolated defects and defect clusters. In general, the larger the supercell, the smaller the error due to the interaction between the defect and its mirror image, thereby more closely approximating the dilute limit that we wish to capture. Because larger supercells require a formidable amount of computational time, we have systematically analyzed the system-size convergence. To characterize the convergence, supercell sizes of  $1 \times 1 \times 1$ ,  $2 \times 1 \times 1$ ,  $2 \times 2 \times 1$ , and  $2 \times 2 \times 2$ , containing 30, 60, 120, and 240 atoms respectively, are considered. The difference in DFE as a function of supercell size is calculated; the results of typical cases are shown in Figure 3-3. The 120-atom supercell and 240-atom supercell produce similar results for various types of vacancies

and niobium antisite (see also Table 3-3). The larger size effects for the Nb vacancy and Nb antisite are presumably due to their larger charges, and point to the dominant effects of electrostatic charge on artificial defect-defect interactions. Based on the energies of the two larger system sizes, the error in the DFE from supercell size effects is estimated to be  $\sim 0.1 - 0.2$  eV.

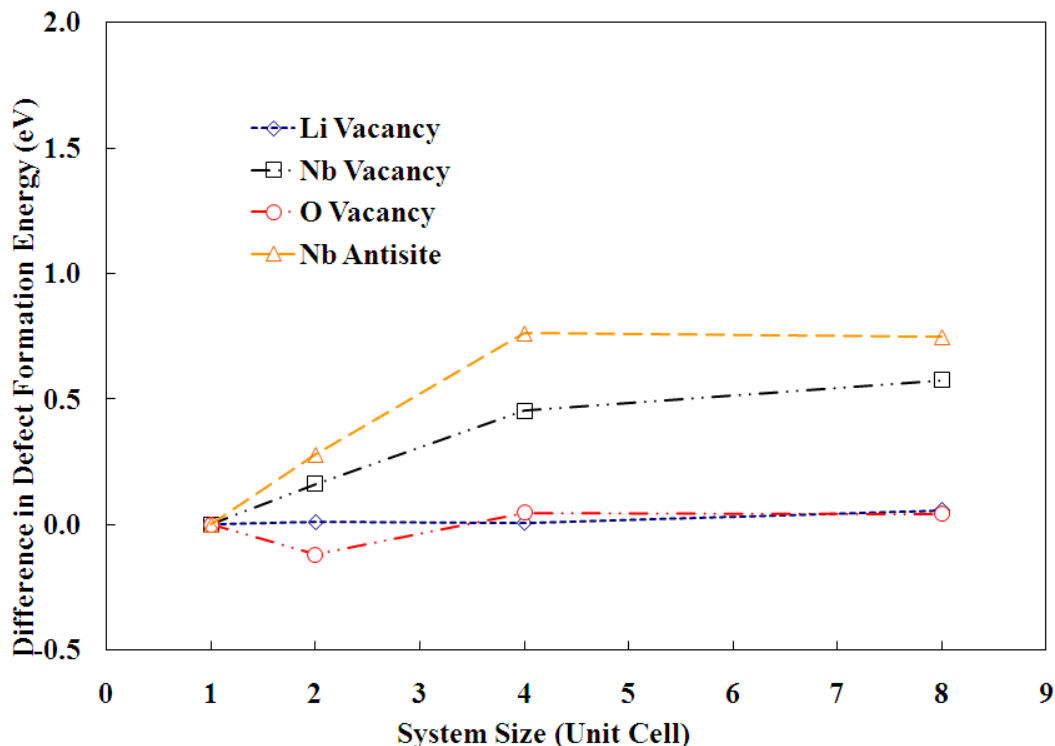


Figure 3-3. Difference in defect formation energy (relative to the  $1 \times 1 \times 1$  system) as a function of system size. Supercell sizes of  $1 \times 1 \times 1$ ,  $2 \times 1 \times 1$ ,  $2 \times 2 \times 1$ , and  $2 \times 2 \times 2$  correspond to 1, 2, 4, and 8 in the x-axis.

For the neutral defect clusters, the electrostatic contribution to the system size dependence can be expected to be rather small, and only due to dipole and higher multipole interactions; however, the strain contribution can be expected to be larger than for the point defects considered. As discussed below, from the analysis of the energy differences between defect reactions, the size dependence is expected to be weak enough that we can be confident in the

conclusions drawn. Therefore, all of the analyses reported are based on results obtained from the 2 x 2 x 2 (240 atom) supercell.

Table 3-3. Difference in DFE, and relative energy difference, between 2 x 2 x 1 system and 2 x 2 x 2 system for various defects.

	Li Vacancy	O Vacancy	Nb Vacancy	Nb Antisite
Difference (eV)	0.051	-0.005	0.121	-0.014

Even for the relatively large system used here, the precise optimization method can have an effect on the results obtained. The approach used here follows the scheme of Van de Walle and Neugebauer; in particular, the defects are added to an optimized perfect-crystal structure and then the positions of all atoms within 4.5 Å of the defect are optimized<sup>118</sup>. This implies that within a system of 240 atoms approximately 116 atoms are relaxed for all the defect cases. The DFE calculated in this manner differs from that obtained from a full optimization of all the atomic positions by 0.052 eV, 0.050 eV, and 0.140 eV for the Li vacancy, O vacancy and Nb antisite respectively. A similar approximation has been used for defects in GaN<sup>118</sup> and ZnO system<sup>122</sup>.

An alternative to using large system sizes to minimize the effects of the artificial interactions between defects and their images would be to compensate for them in an analytic manner. In particular, Makov and Payne<sup>123</sup> have developed a general approach to correct the calculation for cubic system. However, this approach has been found to lead to an overestimate of the correction term for some semiconductor systems<sup>118, 124, 125</sup>. We have not included a Makov-Payne correction in our charged supercell analysis, but rather rely on our system size being sufficiently large, an assumption that we justify by the data in Figure 3-3.

### 3.4 Thermodynamic Framework

The formation energy of a defect or a defect cluster depends on the chemical potential of the ions added or removed from the perfect crystal to form the defect. Below we outline a

thermodynamically consistent process to determine the physically possible range of chemical potentials. This was first developed in the context of binary oxides<sup>122,126</sup>. The extension to ternary oxides used here is substantially the same as that used previously for LiNbO<sub>3</sub><sup>74</sup>, BaTiO<sub>3</sub><sup>127</sup> and SrTiO<sub>3</sub><sup>128</sup>.

The stability of the system against decomposition into its constituent elements places upper limits on the chemical potential of each element in LiNbO<sub>3</sub>.

$$\mu_{Li}[LiNbO_3] \leq \mu_{Li}[Metal] \quad [3-1]$$

$$\mu_{Nb}[LiNbO_3] \leq \mu_{Nb}[Metal] \quad [3-2]$$

$$\mu_O[LiNbO_3] \leq \mu_O[O_2] \quad [3-3]$$

The total energy of a stoichiometric unit of LiNbO<sub>3</sub> can be expressed as:

$$\mu_{Li}[LiNbO_3] + \mu_{Nb}[LiNbO_3] + 3\mu_O[LiNbO_3] = E_{total}[LiNbO_3] \quad [3-4]$$

Thus lower limits of chemical potential for each element can then be obtained:

$$\mu_O[LiNbO_3] \geq \frac{1}{3}(E_{total}[LiNbO_3] - \mu_{Li}[Metal] - \mu_{Nb}[Metal]) \quad [3-5]$$

$$\mu_{Li}[LiNbO_3] \geq E_{total}[LiNbO_3] - 3\mu_O[O_2] - \mu_{Nb}[Metal] \quad [3-6]$$

$$\mu_{Nb}[LiNbO_3] \geq E_{total}[LiNbO_3] - 3\mu_O[O_2] - \mu_{Li}[Metal] \quad [3-7]$$

Furthermore, since neither Li<sub>2</sub>O nor Nb<sub>2</sub>O<sub>5</sub> precipitates from bulk LiNbO<sub>3</sub>, the ranges of chemical potentials are subject to the additional constraints:

$$2\mu_{Li}[LiNbO_3] + \mu_O[LiNbO_3] \leq E_{total}[Li_2O] \quad [3-8]$$

$$2\mu_{Nb}[LiNbO_3] + 5\mu_O[LiNbO_3] \leq E_{total}[Nb_2O_5] \quad [3-9]$$

The above sets of equations define the ranges of chemical potential consistent with the stability of LiNbO<sub>3</sub> against decomposition into binary oxides, or into its elemental components.

Knowing the boundary of chemical potential for each element, the range of possible values for the DFEs of single point defects can be calculated. To characterize the defect reaction, knowledge of the range of chemical potentials is not sufficient: the chemical potential of each element has to be known.

Physically, it is possible to change the oxygen chemical potential through the temperature and/or oxygen partial pressure. There are two limits on the oxygen chemical potential in  $\text{LiNbO}_3$ . Under extremely oxidizing conditions, the chemical potential of oxygen reaches its maximum. The criterion for the equilibrium of oxygen in  $\text{LiNbO}_3$  and  $\text{O}_2$  is:

$$\mu_o[\text{LiNbO}_3] = \mu_o[\text{O}_2] \quad [3-10]$$

Under reducing conditions, the Li and Nb in  $\text{LiNbO}_3$  must be in equilibrium with metallic Li and Nb. This places a lower limit on the oxygen chemical potential of:

$$\mu_o[\text{LiNbO}_3] = \frac{1}{3}(E_{total}[\text{LiNbO}_3] - \mu_{Li}[\text{Metal}] - \mu_{Nb}[\text{Metal}]) \quad [3-11]$$

As we shall see, these constraints actually correspond to unrealistically high and low oxygen partial pressures respectively, with the physically attainable range of partial pressures being much narrower.

Bringing all of these stability criteria together, we can construct the ternary chemical potential map shown in Figure 3-4, where the points in chemical-potential space should be analyzed in a manner analogous to that for the composition in a conventional ternary phase diagram<sup>129</sup>. In the following, the points and lines refer to the ternary chemical potential map in Figure 3-4.

**Case 1:  $\text{Li}_2\text{O}$  reference state (line AD):** When  $\text{Li}_2\text{O}$  is chosen as a reference state, the composition-weighted sum of the lithium and oxygen chemical potentials is equal to the total energy of  $\text{Li}_2\text{O}$ . Likewise the criterion for the equilibrium of Li in  $\text{LiNbO}_3$  and  $\text{Li}_2\text{O}$  is:

$$\mu_{Li}^{Li_2O} [LiNbO_3] = \frac{1}{2} (E_{total} [Li_2O] - \mu_O) \quad [3-12]$$

The chemical potential of Nb in LiNbO<sub>3</sub> can then be determined:

$$\mu_{Nb}^{Li_2O} [LiNbO_3] = E_{total} [LiNbO_3] - 3\mu_O - \mu_{Li}^{Li_2O} [LiNbO_3] \quad [3-13]$$

**Case2: Nb<sub>2</sub>O<sub>5</sub> reference state (line BC):** In this case, the Nb in LiNbO<sub>3</sub> and Nb<sub>2</sub>O<sub>5</sub> are in equilibrium:

$$\mu_{Nb}^{Nb_2O_5} [LiNbO_3] = \frac{1}{2} (E_{total} [Nb_2O_5] - 5\mu_O) \quad [3-14]$$

The chemical potentials of Li in LiNbO<sub>3</sub> can then be determined as:

$$\mu_{Li}^{Nb_2O_5} [LiNbO_3] = E_{total} [LiNbO_3] - 3\mu_O - \mu_{Nb}^{Nb_2O_5} [LiNbO_3] \quad [3-15]$$

**Reconciliation of the two reference states:** One might think that these separate analyses would be equivalent. To explore this, we can take  $\mu_{Li} [LiNbO_3]$  in Equation 3-12 and 3-15 in terms of individual energy contributions. From Equation 3-12 we get the chemical potential for Li in LiNbO<sub>3</sub>, with a Li<sub>2</sub>O reference as:  $\mu_{Li}^{Li_2O} [LiNbO_3]$  as:

$$\mu_{Li}^{Li_2O} [LiNbO_3] = \mu_{Li} [Metal] + \frac{1}{2} \Delta H_f (Li_2O) \quad [3-16]$$

Likewise from Equation 3-15, we can determine the chemical potential of Li in LiNbO<sub>3</sub> with an Nb<sub>2</sub>O<sub>5</sub> reference as:

$$\mu_{Li}^{Nb_2O_5} [LiNbO_3] = \mu_{Li} [Metal] + \Delta H_f (LiNbO_3) - \frac{1}{2} \Delta H_f (Nb_2O_5) \quad [3-17]$$

Thus:

$$\mu_{Li}^{Nb_2O_5} [LiNbO_3] - \mu_{Li}^{Li_2O} [LiNbO_3] = \Delta H_{diff} \quad [3-18]$$

where

$$\Delta H_{diff} \equiv \Delta H_f (LiNbO_3) - \frac{1}{2} (\Delta H_f (Nb_2O_5) + \Delta H_f (Li_2O)) \quad [3-19]$$

As Table 3-4 shows, both experimental data and our GGA calculations show that  $H_{diff}$  is non-zero. As a result, the two reference states are thermodynamically different from each other.

Table 3-4. The heats of formation of  $\text{Li}_2\text{O}$ ,  $\text{Nb}_2\text{O}_5$ , and  $\text{LiNbO}_3$  calculated from the GGA calculations, compared with experimental results. Both experimental and calculated values are at  $T=0$  K.

	GGA(eV)	Experiment(eV)
$\Delta H(\text{Li}_2\text{O})$	-6.280	-6.139 <sup>130, 131</sup>
$\Delta H(\text{Nb}_2\text{O}_5)$	-18.262	-19.202 <sup>130</sup> -19.943 <sup>130</sup> -19.687 <sup>130</sup> -19.735 <sup>130</sup> -19.666 <sup>130</sup> -19.813 <sup>130</sup> -19.687 <sup>131</sup>
$\Delta H(\text{LiNbO}_3)$	-14.433	-14.149 <sup>132</sup>
$\Delta H_{diff}$	-2.162	-1.236

The result of this analysis is that the chemical potentials of all three elements are constrained. The bounds that these constraints impose could be determined from experiments on the range of stability of the various oxides; unfortunately, the complete experimental data set required is not available. We therefore chose to use the results of GGA calculations to determine these constraints, as we are then able to develop a completely consistent data set of chemical potentials and DFEs.

**Calculation of chemical potentials: application to  $\text{LiNbO}_3$ :** Using the method outlined above, the GGA calculations allow us to explicitly define the domain of possible chemical potentials. To accurately calculate the ranges of chemical potential for each element, the energy of lithium metal, niobium metal, oxygen gas,  $\text{Li}_2\text{O}$ ,  $\text{Nb}_2\text{O}_5$  and  $\text{LiNbO}_3$  have been determined using GGA (Table 3-5).

The heats of formation for  $\text{Li}_2\text{O}$ ,  $\text{Nb}_2\text{O}_5$  and  $\text{LiNbO}_3$  have been calculated from the difference between energies of the oxides and composition-weighted sum of the energies of the elements. From the data shown in Table 3-4, the error associated with experimental results for

Nb<sub>2</sub>O<sub>5</sub> is significantly larger than for Li<sub>2</sub>O and LiNbO<sub>3</sub>. In particular, the calculated  $\Delta H_f$  values for Li<sub>2</sub>O and LiNbO<sub>3</sub> are within 2.3 % of the experimental values (Table 3-4), whereas for Nb<sub>2</sub>O<sub>5</sub> the error is between 4 and 10 % of the experimental values. This larger deviation  $\Delta H_f$  for Nb<sub>2</sub>O<sub>5</sub> is not surprising due to the experimental uncertainties in the structure discussed above.

Using the values shown in Table 3-5 and Equation 3-1 to Equation 3-10, the ranges of possible chemical potential of each element are calculated. We then consider the chemical potential of oxygen. The dependence of  $\mu_O$  on temperature and partial pressure can be calculated if the dependence of  $\mu_O [T, P^o]$  at one particular pressure  $P^o$  is known<sup>126</sup>:

$$\mu_o[T, P] = \mu_o[T, P^o] + \frac{1}{2} kT \ln\left(\frac{P}{P^o}\right) \quad [3-20]$$

Table 3-5. The energy of lithium metal, niobium metal, oxygen gas, Li<sub>2</sub>O, Nb<sub>2</sub>O<sub>5</sub>, and LiNbO<sub>3</sub> as calculated by GGA.

	Space Group	Energy (eV) per Atom
Li (Metal)	Im-3m	-1.895
Nb (Metal)	Im-3m	-10.049
O <sub>2</sub> (Gas)		-4.392
	Space Group	Energy (eV) per Formula Unit
LiNbO <sub>3</sub>	R3c	-39.552
Li <sub>2</sub> O	Fm-3m	-14.461
R-Nb <sub>2</sub> O <sub>5</sub>	C2/m	-60.319

Thus high values of  $\mu_O$  correspond to high oxygen partial pressures and conditions that tend to favor oxidation. Similarly, low values of  $\mu_O$  correspond to low partial pressures of oxygen and conditions that favor reduction. The value of  $\mu_O$  calculated by DFT is at 0 K. Its dependence on temperature can be derived from experimental thermodynamic data, yielding:

$$\mu_o[T, P] = \mu_{o(O_2)}[0 K, P^o] + \frac{1}{2} \Delta G(\Delta T, P^o, O_2) \quad [3-21]$$

The experimentally determined temperature dependence of the oxygen chemical potential at 1 atm is given in Table 3-6<sup>130</sup>. The requirements of stability of LiNbO<sub>3</sub> discussed above, place limits on the oxygen partial pressures which, at 298 K, can lie in range of  $4.9 \times 10^{-139}$  to  $2.6 \times 10^{18}$

atm. Of course, both of these limits are physically unreasonable. Thus in Figure 3-4, the more physically reasonable pressure range of  $10^{-20}$  atm to 10 atm is also indicated.

Table 3-6. Change in oxygen chemical potential with respect to 0 K value from experiment <sup>130</sup>.

Temperature (K)	Change in $u_O$ (eV)
100	-0.150
200	-0.341
298.15	-0.544
300	-0.548
400	-0.765
500	-0.991
600	-1.233
700	-1.460
800	-1.702
900	-1.949
1000	-2.199

Referring to the ternary stability map in Figure 3-4, at any point within the triangle, the sum of the chemical potentials of each element yields the total energy of  $\text{LiNbO}_3$ . Furthermore, considering the constraints imposed by Equation 3-8 and Equation 3-9, we can further narrow down the range of chemical potentials. The region enclosed by points A, D, and  $P_{\text{Li-Nb}}$  satisfies Equation 3-8, while the region enclosed by points B, C,  $P_{\text{O-Li}}$ , and  $P_{\text{O-Nb}}$  satisfies Equation 3-9. The intersection of these two regions defines the thermodynamically allowable range of chemical potentials; this stability region is thus defined by the shaded quadrilateral enclosed by the points A, B, C, and D. Therefore, to study the general case, the DFE calculations for all points within the stability range are performed.

At this point, all of the methods needed for defect-energy calculations are defined. In the next Section, we present the results.

### 3.5 Defect Formation Energy

The current paper focuses on following intrinsic defects: Li-Frenkel, Nb-Frenkel, O-anti-Frenkel,  $\text{Li}_2\text{O}$  pseudo-Schottky,  $\text{Nb}_2\text{O}_5$  pseudo-Schottky,  $\text{LiNbO}_3$  Schottky, and three defect

clusters that have been discussed in the literature:  $5 \text{Nb}_{\text{Li}}^{\bullet\bullet\bullet} + 4 \text{V}_{\text{Nb}}^{\bullet\bullet\bullet}$ ,  $2 \text{Nb}_{\text{Li}}^{\bullet\bullet\bullet} + 3 \text{V}_{\text{Li}}^{\bullet} + \text{V}_{\text{Nb}}^{\bullet\bullet\bullet}$  and  $\text{Nb}_{\text{Li}}^{\bullet\bullet\bullet} + 4 \text{V}_{\text{Li}}^{\bullet}$ .<sup>10</sup>

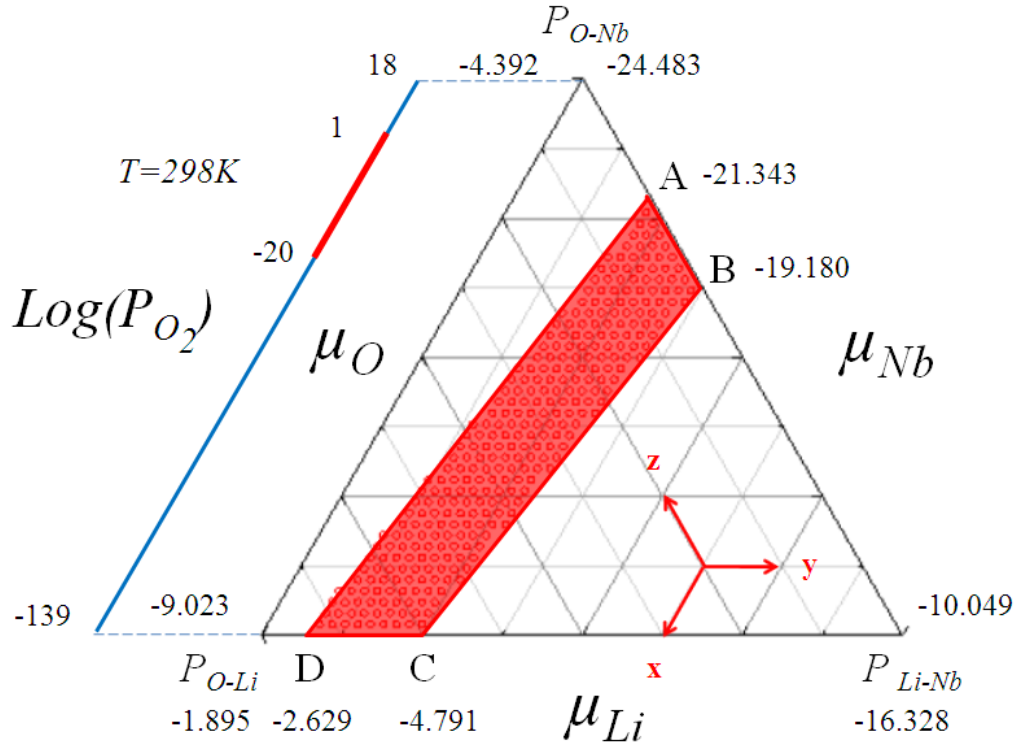


Figure 3-4. Stability range of chemical potentials (in eV) of the elements in  $\text{LiNbO}_3$ . The region enclosed by points A, D, and  $P_{\text{Li-Nb}}$  satisfies Equation 3-8, while the region enclosed by points B, C,  $P_{\text{O-Li}}$ , and  $P_{\text{O-Nb}}$  satisfies Equation 3-9. The intersection of these two regions defines the thermodynamically allowable range of chemical potentials. This stability region is thus defined by the shaded quadrilateral enclosed by the points A, B, C, and D. Line AD represents using  $\text{Li}_2\text{O}$  as reference state; line BC represents using  $\text{Nb}_2\text{O}_5$  as reference. The oxygen partial pressure range (in atm) is that for room temperature. The chemical potential unit is in eV/atom.

For computational efficiency, the DFEs of these intrinsic defect complexes are first determined from the formation energies of the individual charged defects that make up the complex. Thus, the formation energy of  $\text{Li}_2\text{O}$  pseudo-Schottky comes from separate calculations on the formation energy of lithium vacancy and oxygen vacancy. The association energy resulting from the interaction of the individual charged defects in these neutral defect clusters will be discussed in section 3.6.

Before characterizing the defect clusters, it is important to analyze the individual defects with various charge states. The following section will discuss all the results obtained for individual defects followed by the neutral charged clusters.

### 3.5.1 Formalism

The DFE of a defect or defects, denoted as  $\alpha$ , with charge state  $q$  is defined as <sup>118</sup>

$$\Delta E_f(\alpha, q, T, P) = E^{total}(\alpha, q) - E^{total}(perfect) + \sum_i n_i \mu_i - q(\varepsilon_F + E_v + \Delta V) \quad [3-22]$$

where  $E^{total}(\alpha, q)$  is the total energy obtained from DFT calculation of a supercell with the defect(s);  $E^{total}(perfect)$  is the total energy of the supercell without any defects.  $n_i$  is the number of atoms of species  $i$  that have been added to ( $n_i > 0$ ) or removed from ( $n_i < 0$ ) the supercell when the defects are created;  $\mu_i$  is the chemical potential of element  $i$ .  $T$  is temperature and  $P$  is the oxygen partial pressure.  $\varepsilon_F$  is the Fermi energy with respect to the valence band maximum in the bulk single crystal.  $E_v$  is the valence band maximum of the bulk single crystal system. Therefore, as discussed by Van de Walle and Neugebauer <sup>118</sup>, a correction term  $\Delta V$ , which is the difference in the electrostatic potentials of the defected and un-defected systems, is needed to align the band structures.

Strictly speaking, the free energy rather than the total energy should be used in Equation 3-22 for the calculation of the DFEs. The total internal energies of a supercell obtained from DFT calculations correspond to the Helmholtz free energy at zero temperature, neglecting zero-point vibrations <sup>126</sup>. These calculations thus neglect the contributions from the vibrational entropy; fortunately, experimental and theoretical results for entropies of point defects typically fall between 0 to  $10k$  (0 to 0.26 eV at 300 K), where  $k$  is the Boltzmann constant <sup>118</sup>. As a consequence, we do not expect this neglect of the entropy term to qualitatively change our

conclusions. Detailed analyses by He *et al.*<sup>133</sup> and Kohan *et al.*<sup>122</sup> also concluded that entropic effects can be neglected.

### 3.5.2 Point Defects

The DFEs of all the native point defects with various charge states in LiNbO<sub>3</sub> have been calculated using Equation 3-22. The interstitial sites are assumed to be at (0.0, 0.0, 0.13936) for individual defects, which corresponds to the center of an empty oxygen octahedron. Since the DFE depends on the location of the Fermi energy, the influence of the Fermi energy on the stability of each individual defect is considered. In the current study, the reference zero of Fermi energy is assigned to be the valence band maximum (VBM) of the perfect structure; the highest Fermi energy thus corresponds to the conduction band minimum (CBM). As discussed by Van de Walle *et al.*<sup>118</sup>, it is necessary to implement an additional procedure to calculate the shift of bands caused by the presence of defects. Thus, to calculate this shift, the average electrostatic potential difference ( $\Delta V$  in Equation 3-22) between the perfect structure and the defected structure has been determined using the approach of Kohan *et al.*<sup>122</sup>.

For pure stoichiometric LiNbO<sub>3</sub>, which is an insulator, the Fermi energy is expected to be at the middle of the band gap. In the present paper, we are simulating the dilute limit of pure stoichiometric system; therefore the shift of Fermi energy is considered negligible. The dependence of DFEs on the Fermi level is shown in Figure 3-5, using Nb<sub>2</sub>O<sub>5</sub> (the BC line in Figure 3-4) as the reference state. For each individual defect, Figure 3-5 includes only the charge states with lowest DFE values over the corresponding Fermi level range. The slopes of the lines in the Figure 3-5 represent the charge states of the defects. When Fermi energy is at middle of the band gap,  $V_{Li}^{\cdot}$ ,  $V_{Nb}^{''''}$ ,  $V_{O..}$ ,  $Nb_{Li}^{''''}$ ,  $Li_i^{\cdot}$ ,  $Nb_i^{''''}$ , and  $O_i^{''}$  are the energetically favored charge state for each defect. It is also observed that, as the Fermi energy increases (i.e., moves from the

VBM towards the CBM), the thermodynamically stable charge of the positive defects decreases. Correspondingly, the charge states of the negative defects decrease as the Fermi energy increases. This order of stability is broadly consistent with that determined in the DFT calculations of Li *et al.*<sup>74</sup>

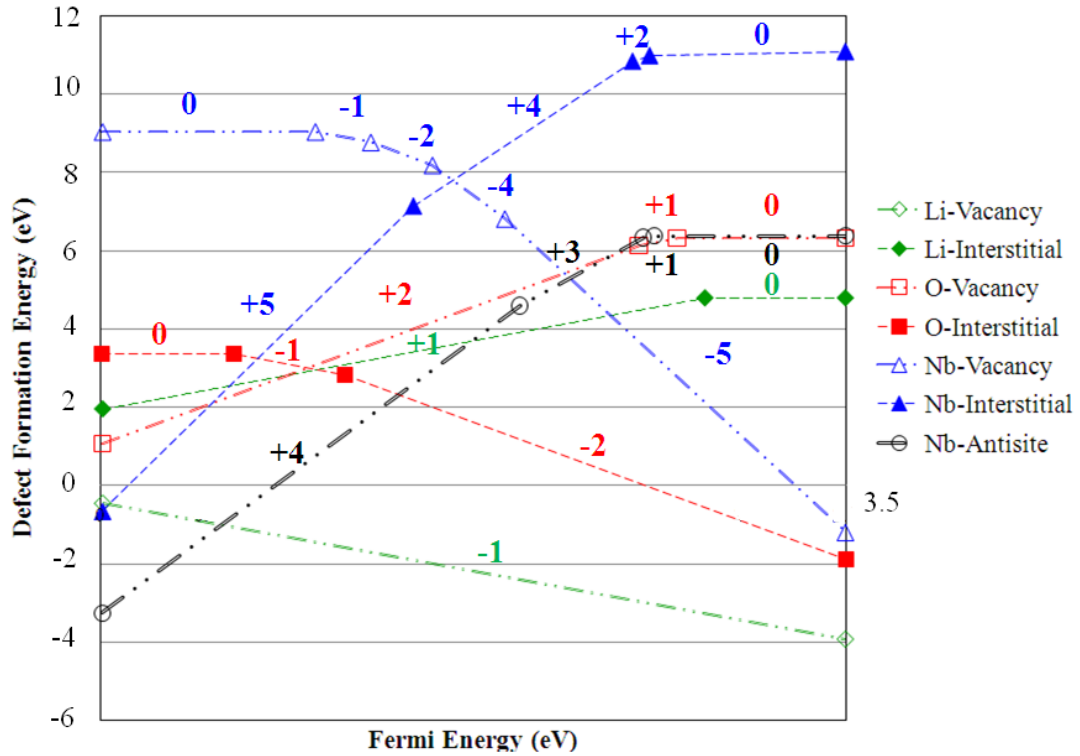


Figure 3-5. Defect formation energies of various point defects as a function of Fermi energy; the lowest-energy charge state is given in each case. The Fermi energy ranges from  $E_F=0$  (left) at the VBM to  $E_F=3.5\text{eV}$  at the conduction band minimum (right).

In Figure 3-5, the points at which the slopes change are the thermodynamic transition levels,  $\epsilon(q_1/q_2)$ . At these transition points the Fermi level of the charge state  $q_1$  and  $q_2$  have the same energy. For Nb-related defects, the stable Nb antisite changes from 3+ to 1+ directly without passing through the 2+ charge state. Correspondingly, the Nb interstitial changes from 2+ to 0, and Nb vacancy changes from 2- to 4-. To characterize this phenomenon, the thermodynamic transition level of adjacent charge state of Nb-related and O-related defects are calculated and shown in Figure 3-6.

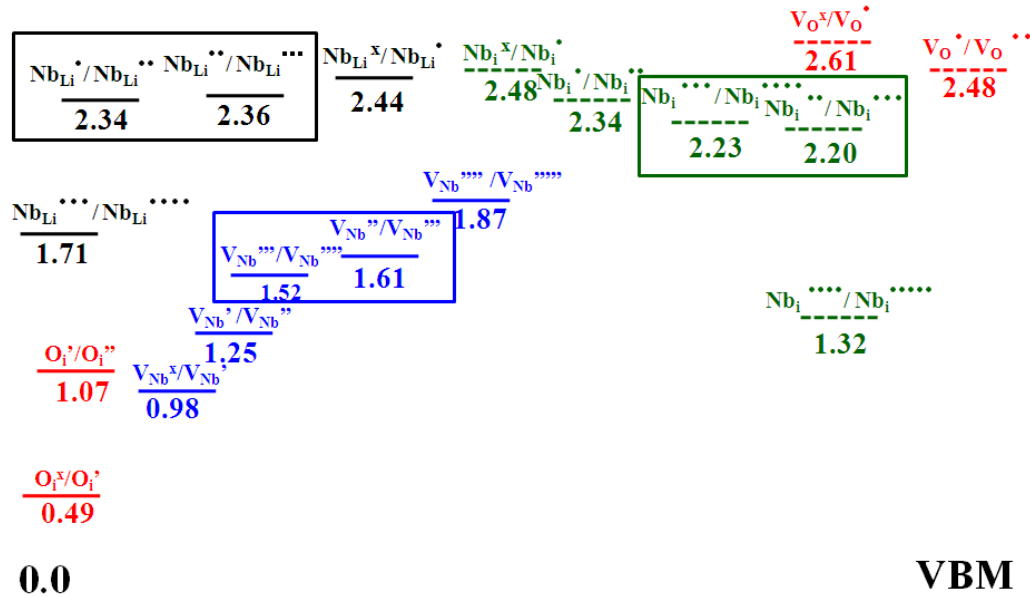


Figure 3-6. Thermodynamic transition levels of O-related and Nb-related defects. The values under the line are with respect the valence band maximum (VBM). The transitions enclosed by squares have a negative U character.

It can be seen that there are order switching for the Nb antisite, Nb interstitial and Nb vacancy. The Nb antisite  $\epsilon$  (1+ / 2+) is lower than Nb antisite  $\epsilon$  (2+ / 3+). For the Nb interstitial,  $\epsilon$  (2+ / 3+) is lower than  $\epsilon$  (3+ / 4+). For the Nb vacancy,  $\epsilon$  (3- / 4-) is lower than Nb vacancy  $\epsilon$  (2- / 3-). These switchings of the order of thermodynamic transition levels are indicative of the so-called negative U effects<sup>134</sup>. However, as Figure 3-6 shows, the energies for the thermodynamic transition levels for the respective Nb-related defects discussed above are extremely close to each other; indeed they are close to the estimated uncertainties in the present calculations.

The electron-lattice interaction result in different atomic relaxations for different charge state of the defects. Taking the Nb antisite as an example, the average bond length of 0, 1+, 2+,

3+ and 4+ are 2.130 Å, 2.092 Å, 2.063 Å, 2.038 Å, and 2.011 Å respectively. These decreases in bond lengths as the charge state of Nb antisite increases are due to the increasing electrostatic interactions.

### 3.5.3 Defect Clusters

The constraint of charge neutrality means that only neutral defect complexes will be present in the system. While this leads to a need to consider a plethora of different defect clusters, it does provide the simplification of not having to consider the effects of the Fermi energy, since this term drops out in Equation 3-22. In the current section, the charged defect that make the neutral defect are assumed to be infinitely far away from each other. The association effects are added in section 3.6.

From Figure 3-7, it can be seen that formation energy of the Li-Frenkel, O-anti-Frenkel, Nb-Frenkel, and LiNbO<sub>3</sub> Schottky are independent of the choice of the chemical potential. This is because these defects preserve the stoichiometry of the system, obviating any chemical potential term. By contrast, the Li<sub>2</sub>O pseudo-Schottky, Nb<sub>2</sub>O<sub>5</sub> pseudo-Schottky,  $5 \text{Nb}_{\text{Li}}^{\bullet\bullet\bullet\bullet} + 4 \text{V}_{\text{Nb}}^{\bullet\bullet\bullet\bullet}$ ,  $2 \text{Nb}_{\text{Li}}^{\bullet\bullet\bullet\bullet} + 3 \text{V}_{\text{Li}}^{\bullet} + \text{V}_{\text{Nb}}^{\bullet\bullet\bullet\bullet}$  and  $\text{Nb}_{\text{Li}}^{\bullet\bullet\bullet\bullet} + 4 \text{V}_{\text{Li}}^{\bullet}$  defect clusters change the stoichiometry of the system. Thus, their formation energies are influenced by the reference state of chemical potential. The calculations show that the formation energy for Nb-antisite compensated purely by Nb-vacancies ( $5 \text{Nb}_{\text{Li}}^{\bullet\bullet\bullet\bullet} + 4 \text{V}_{\text{Nb}}^{\bullet\bullet\bullet\bullet}$ ) is different for the two reference states; however it is energetically unfavorable under both conditions. The DFE for  $\text{Nb}_{\text{Li}}^{\bullet\bullet\bullet\bullet} + 4 \text{V}_{\text{Li}}^{\bullet}$  clusters is positive with the Li<sub>2</sub>O (AD in Figure 3-4) reference state but negative for the Nb<sub>2</sub>O<sub>5</sub> (BC in Figure 3-4) reference state, indicating that this defect cluster will occur spontaneously under these conditions.

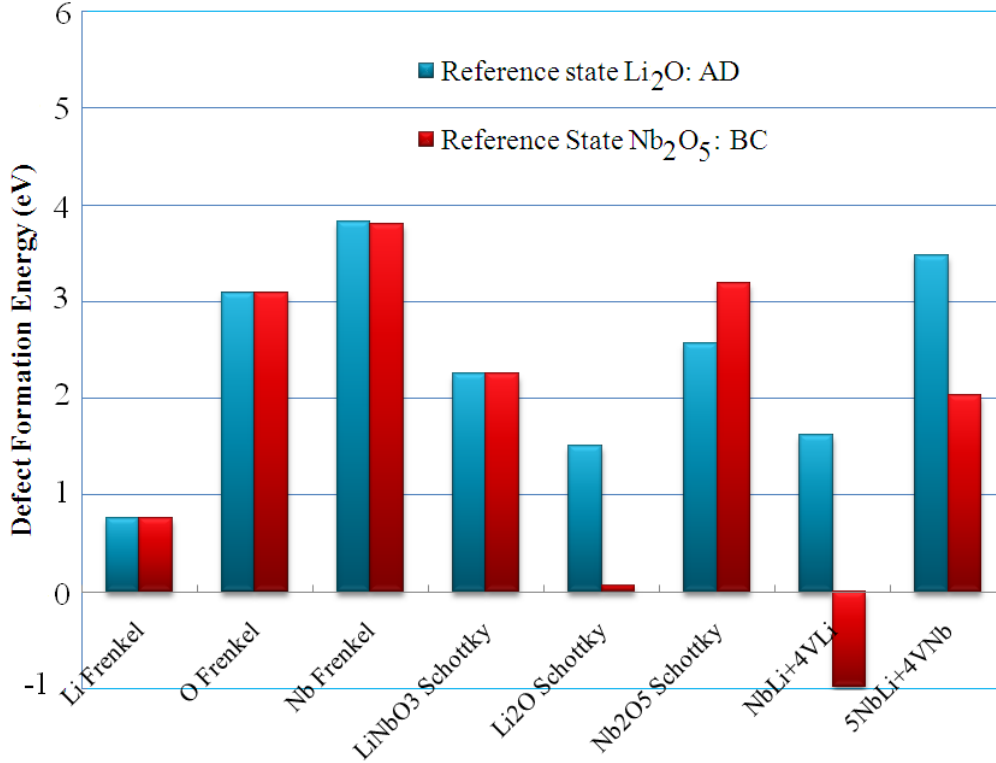


Figure 3-7. Formation energies of neutral defects and defect clusters under  $\text{Nb}_2\text{O}_5$  rich conditions (blue) and  $\text{Li}_2\text{O}$  rich conditions (red).

The Frenkel defects analyzed above consist of individual fully charged defects. Frenkel defects with partial charged or neutral individual defects can also be considered. However, the formation energies of Frenkel defects with partial charged or neutral individual defects all turn out to have higher energies than those formed from normal fully charged individual defects. For example, the formation energy of the Frenkel defects consisting of  $\text{Li}_{i-x} + \text{V}_{\text{Li}x}$  is 1.9 eV higher than the Frenkel defect formed from  $\text{Li}_i + \text{V}_{\text{Li}}$ .

Table 3-7 compares the results of our DFT calculations with the previous DFT calculations and with calculations using empirical potentials. For the purposes of comparison, it is instructive to distinguish between those neutral defects that maintain the systems stoichiometry (Li-Frenkel, Nb-Frenkel, O-Frenkel, and  $\text{LiNbO}_3$ -Schottky) and those defects and defect clusters that do not maintain the system stoichiometry. For the stoichiometric defects, all four calculations conclude

that the Li-Frenkel defect has the lowest formation energy. They also all predict that the Nb-Frenkel has the highest DFE. Three of the four calculations conclude that the LiNbO<sub>3</sub> Schottky has a lower DFE than the O-Frenkel, with only the older atomistic calculations of Donnerberg *et al.*<sup>97</sup> giving the opposite order.

Table 3-7. Defect formation energies for various defects, compared with previous electronic-structure and atomistic simulations.

Defects (eV/defect)	Jackson (Atomistic)	Donnerberg (Atomistic)	USPP-LDA	PAW- GGA	PAW-GGA
Reference State	None	None	Nb <sub>2</sub> O <sub>5</sub>	Nb <sub>2</sub> O <sub>5</sub>	Li <sub>2</sub> O
Li-Frenkel	1.37	0.93	1.78	0.77	0.77
Nb-Frenkel	11.72	6.26	6.43	3.80	3.80
O-Frenkel	4.76	3.42	5.80	3.10	3.10
LiNbO <sub>3</sub> Schottky	3.95	3.91	4.84	2.25	2.25
Li <sub>2</sub> O Pseudo-Schottky	1.81	1.94	-0.89	0.07	1.51
Nb <sub>2</sub> O <sub>5</sub> Pseudo-Schottky	5.09	2.85	7.29	3.19	2.57
Nb <sub>Li</sub> <sup>••••</sup> + 4V <sub>Li</sub> <sup>'</sup>	1.51	2.74	-4.40	-0.98	1.62
Nb <sub>Li</sub> <sup>••••</sup> + 4 V <sub>Nb</sub> <sup>•••••</sup>	10.23	5.06	2.08	2.03	3.47

With respect to the non-stoichiometric defects, it is difficult to compare the results from the atomistic simulations with the DFT calculations, since the atomistic calculations neither include an explicit reference nor take into account the chemical potential. However, the results of the DFT calculations<sup>74</sup> can be compared, despite the concerns with the previous DFT calculations mentioned in the Introduction. In particular the USPP and PAW calculations yield the same order of stability of defects for the Nb<sub>2</sub>O<sub>5</sub> reference state, with the Nb<sub>Li</sub><sup>••••</sup> + 4V<sub>Li</sub><sup>'</sup> cluster having the lowest energy which, importantly, both analyses predict to be negative. This is strong evidence that this defect cluster should form spontaneously in Nb<sub>2</sub>O<sub>5</sub> rich environments. Although they agree in the order of stability of the defects, the corresponding USPP and PAW calculations yield considerably different specific values for DFEs. Unfortunately the paper of Li *et al.*<sup>74</sup> does not break down the final DFEs into the contributions from the presence of the

defect and the contributions from the chemical potentials; it is thus not possible to analyze these differences further.

### 3.5.4 Defect Stability Range

The DFEs calculated so far using DFT are based on specific chemical potentials. Knowledge of the defect formation dependence over the complete chemical potential stability range is also of considerable importance. The lowest-energy defect as a function of chemical potential of each element is given in Figure 3-8. It is observed that Li-Frenkel and  $\text{Nb}_{\text{Li}}^{\text{''''}} + 4\text{V}_{\text{Li}}^{\text{'}}$  are the two important defects. The Li-Frenkel is the dominant defect within region AEFD (in Figure 3-4), whereas the  $\text{Nb}_{\text{Li}}^{\text{''''}} + 4\text{V}_{\text{Li}}^{\text{'}}$  cluster is the dominant defects within region EBCF (in Figure 3-4).

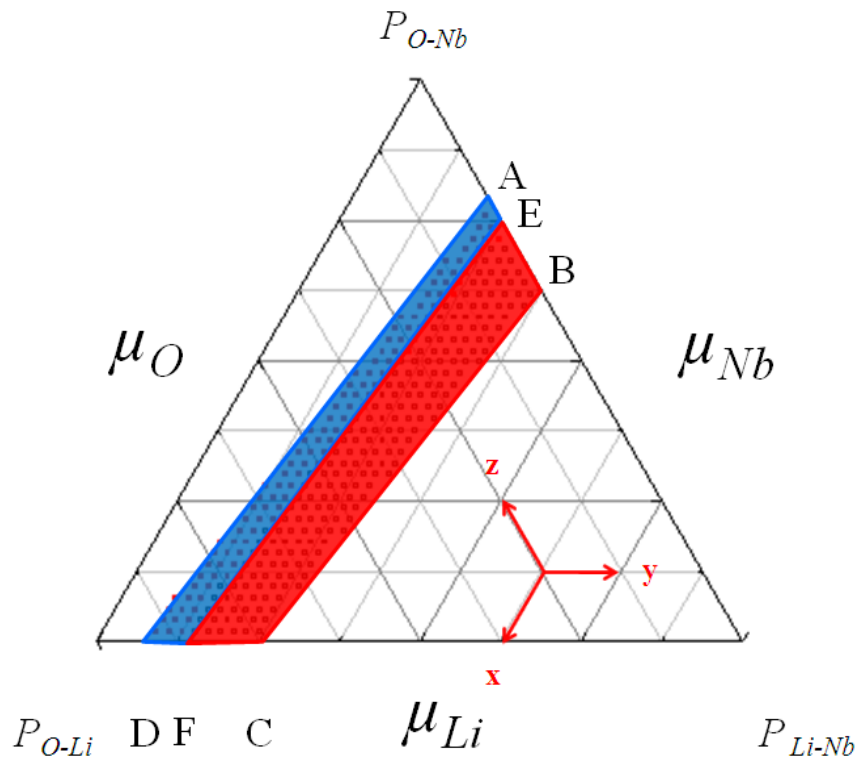


Figure 3-8. Defect stability range: in the region AEFD, the Li-Frenkel is the dominant defect reaction; whereas in EBCF, the niobium antisite compensated by lithium vacancies is dominant. The Li-Frenkel is the dominant defect throughout the whole range of  $\mu_O$  along the AD line, while the defect cluster consists of niobium antisite compensated and four lithium vacancies cluster dominates along BC for all oxygen partial pressures.

As discussed above, the dominant defects might change as  $\mu_O$  transitions from its maximum (oxidizing conditions) to its minimum (reducing conditions). Remarkably, however, the Li-Frenkel is the dominant defect throughout the whole range of  $\mu_O$  along the AD line, while the  $\text{Nb}_{\text{Li}}^{\text{''''}} + 4\text{V}_{\text{Li}}^{\text{'}}$  cluster dominates along BC for all oxygen partial pressures.

### 3.6 Association Effects and Defect Configurations

The above defect reaction analysis is based on the formation energies of individual point defect; that is, the defects are assumed to be so far away from each other that there is no interaction between them. Here, the validity of this approximation is examined by calculating the formation energies of the clustered defects. The change in energy relative to the well-separated defects is the association energy: negative association energy corresponds to the preference for the defects to cluster. Calculations of such associated clusters require the choice of specific defect arrangements. For the Frenkel defects, the vacancy and interstitial are assumed to be first neighbors. For the  $\text{Li}_2\text{O}$ -pseudo-Schottky, an oxygen atom and two lithium atoms in its first nearest neighbor have been removed from the system. For the  $\text{Nb}_2\text{O}_5$ -pseudo-Schottky, two nearest Nb atoms are removed along with five oxygen atoms that are the first nearest neighbor to the removed Nb atoms. The arrangement for the  $\text{Nb}_{\text{Li}}^{\text{''''}} + 4\text{V}_{\text{Li}}^{\text{'}}$  follows the model of Kim *et al.*<sup>135</sup>, which assumes the defect complexes composed of a niobium antisite surrounded by three Li vacancies in the nearest neighbor plus one independent vacancy along the z direction. We analyze different possible arrangements for these defects. For  $5 \text{Nb}_{\text{Li}}^{\text{''''}} + 4 \text{V}_{\text{Nb}}^{\text{''''}}$ , initially a Li-site is chosen and replaced with an Nb atom. Then four of the first nearest Li-atom sites are replaced with Nb to obtain the  $5 \text{Nb}_{\text{Li}}^{\text{''''}}$  configuration. Four Nb sites which are the nearest neighbor of the first Li-atom replaced are then removed from the system to create  $4 \text{V}_{\text{Nb}}^{\text{''''}}$ .

In all cases shown in Table 3-8, the defects have a tendency to cluster, as evidenced by the negative association energies. Since, this association does not change any of the thermodynamics of the system; these differences in energy are independent of the reference state. Interestingly, although association lowers the energy of all of the defect clusters analyzed, it does not change their relative order. This gives us high confidence that the conclusions drawn from the isolated defect calculations are valid. The simulations of Li, Nb and O Frenkel pairs resulted in the perfect structure with no defects, since the vacancies and interstitials of the corresponding pairs were too close to each other.

Table 3-8. Association energy of Li<sub>2</sub>O-Pseudo Schottky, Nb<sub>2</sub>O<sub>5</sub> Pseudo-Schottky, 5 Nb<sub>Li</sub><sup>''''</sup> + 4 V<sub>Nb</sub><sup>''''</sup>, and Nb<sub>Li</sub><sup>''''</sup> + 4 V<sub>Li</sub><sup>'</sup>.

	Association Energy
Li <sub>2</sub> O Schottky	-0.23
Nb <sub>2</sub> O <sub>5</sub> Schottky	-1.20
Nb <sub>Li</sub> <sup>''''</sup> + 4V <sub>Li</sub> <sup>'</sup>	-0.25
Nb <sub>Li</sub> <sup>''''</sup> + 4 V <sub>Nb</sub> <sup>''''</sup>	-1.12

Previously, the DFE of the Nb<sub>Li</sub><sup>''''</sup> + 4 V<sub>Li</sub><sup>'</sup> cluster without considering association effects was determined from the sum of the DFEs of its isolated constituent defects<sup>136</sup>. That is, each defect was assumed to be at an extremely long distance from others. However, there may be a significant difference between the energy of isolated defects and any specific structural variant of the cluster arising from the electrostatic and elastic interaction among the defects. To explore the association of the lithium vacancies around the niobium antisite, several carefully chosen arrangements are considered. Since both the Nb antisite and the lithium vacancies lie on the Li sub-lattice, the specific structure can be characterized in terms of this sub-lattice alone; the energetics are governed by the structural relaxation of all the ions in the cluster and in its vicinity. Because there are so many possibilities, it is not feasible to characterize all the possible arrangements of the Li vacancies. However, the most important distinction is between those in

which the vacancies are very close to the Nb antisite and those in which defects are a considerable distance apart. Thus, the clusters can be categorized in terms of the number of first nearest neighbors (FNNs), with the remaining vacancies further away.

- (i) 0 lithium vacancy as FNN and 4 far away (A0).
- (ii) 1 lithium vacancy as FNN and 3 far away (A1)
- (iii) 2 lithium vacancies as FNNs and 2 far away (A2)
- (iv) 3 lithium vacancies as FNNs and 1 far way (A3)
- (v) 4 lithium vacancies as FNNs (A4)

In the A0 structure, there is no association of the vacancies; this is the case analyzed previously and found to have negative formation energy for the  $\text{Nb}_2\text{O}_5$  reference state<sup>136</sup>. For A1 and A2, only the lithium vacancies in the first nearest neighbor positions are explicitly included in the supercell calculation. Thus, taking A2 as an example, two lithium vacancies are included in the supercell; the DFE of the other two lithium vacancies are assumed to be the same as that of an isolated single lithium vacancy. The DFE of isolated lithium vacancies are 1.13 eV and 3.29 eV under  $\text{Nb}_2\text{O}_5$  and  $\text{Li}_2\text{O}$  reference states, respectively. The effects of Fermi level on the DFE of lithium vacancy are given by Xu *et al*<sup>136</sup>. The total formation energy of the entire defect cluster is the sum of the DFEs the partial cluster and any isolated Li vacancies. For A3 and A4, to maintain the overall charge neutrality and characterize possible local charge effects, all the lithium vacancies are explicitly included in the supercell calculation. Thus, taking A3 as an example, three lithium vacancies are in the FNN position while the fourth lithium vacancy is far away from defect cluster. The dependence of the DFE on the number of lithium vacancies in the FNNs of niobium antisite is given in Figure 3-9.

As illustrated in the figure, the energy decreases with the number of FNNs. Thus, A1 and A2 cases are not considered further. The discussion is focused on the A3 and A4 cases. Since there are six possible sites for the vacancies in the first neighbor shell, there are a number of structurally distinct variants of the A3 and A4 clusters. Each data point in Figure 3-9 corresponds

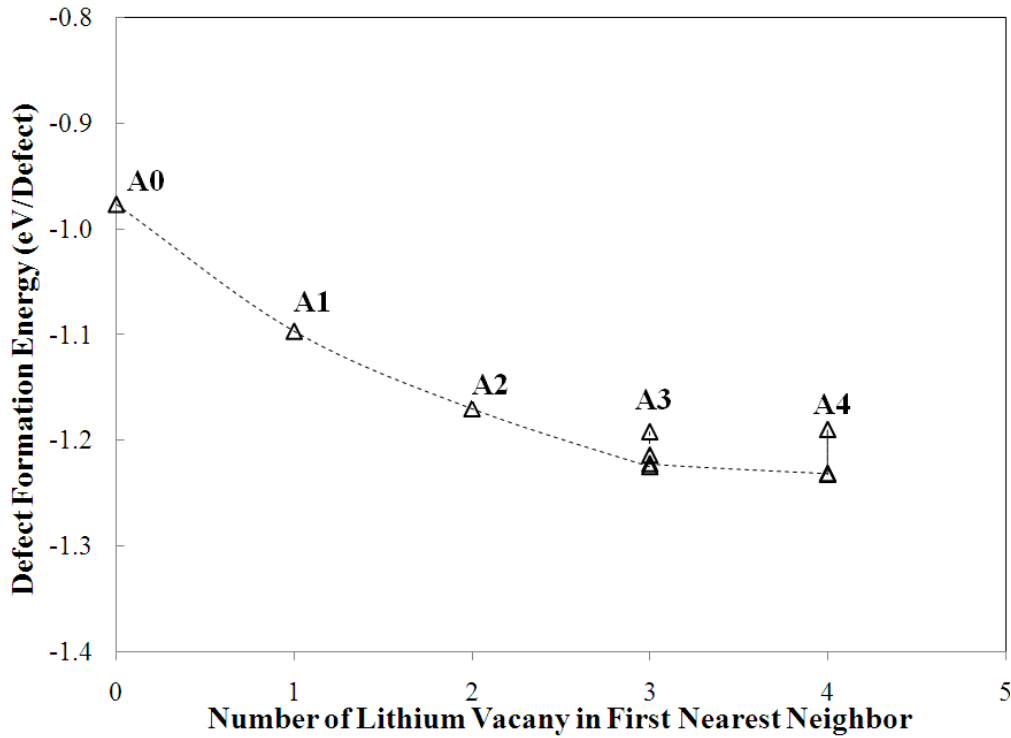


Figure 3-9. Defect formation energies dependence on the number of lithium vacancies in the first nearest neighbor positions of niobium antisite. For A3 and A4, different points represent different configurations, as discussed in Section.3.6.

to a distinct configuration. Indeed, for the energy of the A4 the association energy is  $\sim -0.25$  eV/defect, which characterizes the attractive interaction among these charged defects. Because the association energies of the A3 and A4 structures are very similar, the energetics of a number of variants of each is examined in detail below.

**Configuration A3:** While there are a finite number of crystallographically distinct arrangements

of the three FNN vacancies, the fourth ‘far away’ vacancy could be in an almost unlimited number of distinct locations. One particular A3 model was proposed by Kim *et al.*<sup>135</sup>,

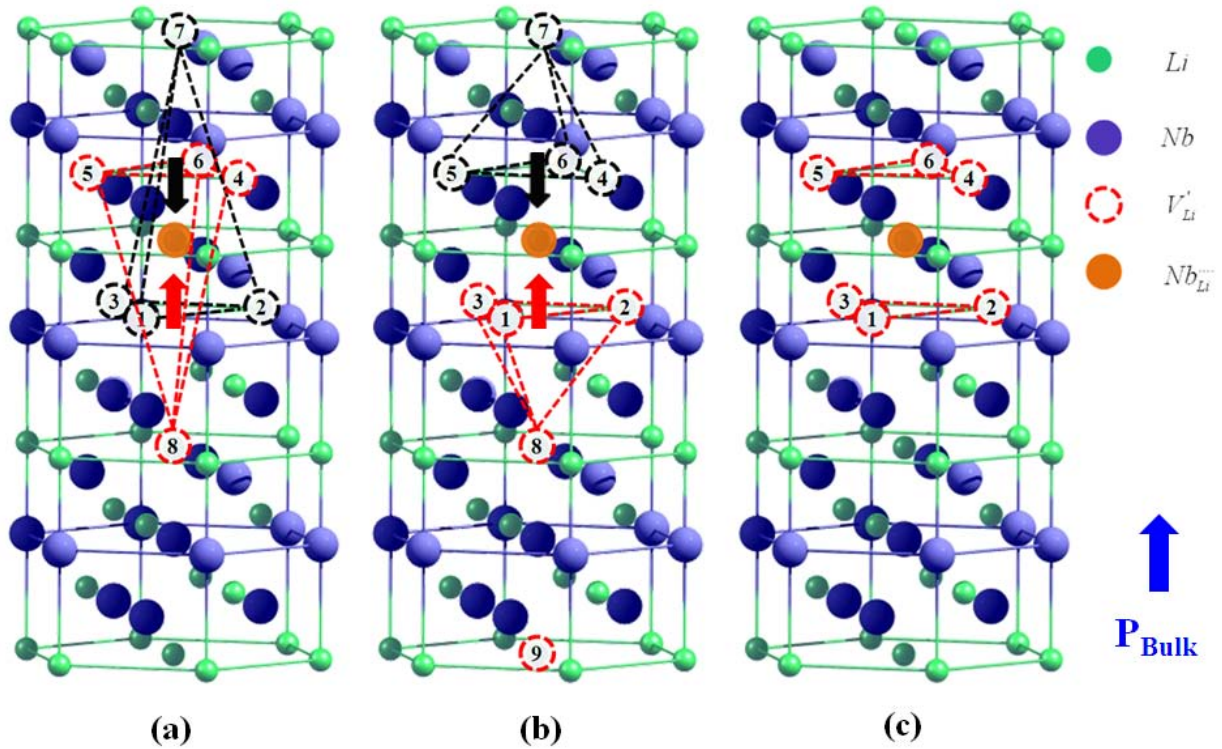


Figure 3-10. Local structure of niobium antisite. A. Kim’s model: Defect cluster 4-5-6-8 (red) is parallel to the bulk polarization direction; cluster 1-2-3-7 (black) is anti-parallel to the bulk polarization direction. B. Proposed configuration Defect clusters 1-2-3-8 and 1-2-3-9 (red) are parallel to the bulk polarization direction with different value of dipole moment. Defect cluster 4-5-6-7 (black) is anti-parallel to the bulk polarization direction. The bulk polarization direction is shown in blue. The oxygen sublattice is not shown for clarity. C. Configurations of A4. 1-6 represent the six possible positions of lithium vacancies in the first near neighbors (FNNs). The dipole moment direction is from negative charged defect center (lithium vacancies) to positive charged defect center (niobium antisite). The bulk polarization is set to in the figure.

in which the fourth Li vacancy lies along the z direction on the opposite side of the niobium antisite, as shown in Figure 3-10(a). Two different configurations using Kim’s model are considered in the present study: one in which the dipole moment of the cluster is parallel to the ferroelectric polarization (4-5-6-8, Kim-parallel), the other with the defect dipole is anti-parallel to the ferroelectric polarization (1-2-3-7, Kim-antiparallel). The polarization of each system is

shown in Table 3-9, the Kim-parallel structure in which the defect and bulk polarization are parallel has a slightly lower energy (by 0.03 eV) than Kim-antiparallel structure in which defect and bulk polarization are anti-parallel. Because both of the structures preserve the rhombohedra symmetry of the system, there are no components of polarization orthogonal to the bulk uniaxial polarization; as a result, the polarization remains purely uniaxial.

In Figure 3- 10 (b), three configurations have been proposed, which could yield much larger electric dipole moments than Kim’s model (Table 3-9). These correspond to vacancies on the 1-2-3-8, 1-2-3-9 and 4-5-6-7 sites, respectively. Cases 1-2-3-8 and 1-2-3-9 have dipole moments parallel to the bulk polarization direction while the dipole moment of 4-5-6-7 is antiparallel to the bulk polarization. These configurations are similar to Kim’s model, in that three lithium vacancies lie in an FNN plane, (1, 2, and 3 in Figure 3-10 (c)). However, they differ in the position of the fourth lithium vacancy (8 or 9), which in all cases lies on the same side of the Nb antisite as the plane of three Li FNN vacancies. The polarization and DFEs calculated based on these proposed configurations are given in Table 3-9.

Table 3-9. Defect formation energies and polarization of various A3 configurations. Kim-parallel represents that both defect and bulk have the same direction of polarization. Kim-antiparallel represents that the polarization direction of defect and bulk is opposite. The 1-2-3-8 and 4-5-6-7 configurations are illustrated in Figure 3- 10(a) and Figure 3- 10(b). All these models only possess polarization along [0001] direction. The bulk polarization is calculated to be  $63.7 \mu\text{C}/\text{cm}^2$ , which is in excellent agreement with experimental value  $62 \pm 4 \mu\text{C}/\text{cm}^2$  base on near-stoichiometric sample <sup>137</sup> The polarization of congruent LiNbO3 is  $\sim 71 \mu\text{C}/\text{cm}^2$  <sup>138</sup>.

Defect Cluster	DFE (eV/Defect)	System Polarization ( $\mu\text{C}/\text{cm}^2$ )	Polarization Change Caused by Defect Clusters( $\mu\text{C}/\text{cm}^2$ )
4-5-6-8 (Kim-parallel) <sup>135</sup>	-1.222	60.5	-3.2
1-2-3-7 (Kim-antiparallel) <sup>135</sup>	-1.191	59.8	-3.9
1-2-3-8 (parallel)	-1.224	69.2	5.5
1-2-3-9 (parallel)	1.201	74.5	10.8
4-5-6-7 (antiparallel)	-1.223	60.6	-3.1

The comparison of the DFEs and polarizations of both Kim's model and the variants of the proposed configuration are given in Table 3-9. There is only ~0.03 eV per defect difference between the highest and lowest energy variants. According to Gopalan *et al.*<sup>10</sup>, when the dipole moment of the defect and polarization of the bulk are in the same direction, the system has a lower energy. Gopalan *et al.*<sup>10</sup> considered this to be the equilibrated state. When the dipole moment of the defects is in the opposite direction from the bulk ferroelectric polarization, the polarization of the defected system is lower than the bulk value and the energy is higher. This may be considered to be a frustrated state. Table 3-9 does not show any clear relationship between the polarization and DFE. For the corresponding structures, such as parallel vs. anti-parallel Kim's model, the DFE decreases as the local polarization of the system (ferroelectric plus defect dipole) increases, which is consistent with the prediction of Gopalan *et al.*<sup>10</sup> However, it is not possible to compare inequivalent structures because the difference can be caused by both polarization and structure.

**Configuration A4:** Taking four lithium atoms from six possible FNN positions yields fifteen ( $C_6^4 = 15$ ) possible defect clusters. However, due to the three-fold symmetry of  $\text{LiNbO}_3$  basal plane, only four of these configurations are distinct; these are listed in Table 3-10 and illustrated in Figure 3-10 (c). All of the A4 structures have lower energies than the lowest energy A3 structure. The energy range among these four structures is only 0.047 eV, which is equivalent to the thermal energy at 545 K. This indicates that all such configurations are likely to be present at room temperature. All of these defect arrangements break the symmetry of the ferroelectric phase, thereby leading to non-uniaxial contributions to the polarization (see Table 3-10). These non-uniaxial components are not negligible, amounting to up to 7.9% of the uniaxial component (for the A4-A structure). However, since all the symmetry equivalent structures of

each of the four structures are equally likely, the system maintains the overall, though not local, polarization of a bulk system as uniaxial, as the non-uniaxial contributions of an ensemble of defect clusters can be expected to cancel out.

Table 3-10. Defect formation energies and polarization of various A4 configurations (see Figure 3- 10 (c). D\* represents degeneracy. Change in Polarization represents that polarization changes caused by the defect cluster in [0001] direction using bulk as reference.

Defect Cluster	Vacancy positions	D*	DFE (eV/Defect)	System Polarization ( $\mu\text{C}/\text{cm}^2$ )			Change in Polarization ( $\mu\text{C}/\text{cm}^2$ )
				[2-1-10]	[-12-10]	[0001]	
A4-A	1 -3 -5 -6	6	-1.296	3.5	3.4	61.6	-2.1
A4-B	1 -2 -3 -5	3	-1.254	1.3	2.3	58.2	-5.5
A4-C	3 -4 -5 -6	3	-1.294	0.3	0.0	61.6	-2.1
A4-D	1 -2 -5 -6	3	-1.301	2.3	1.1	64.5	0.8

All of these configurations considered have a negative DFE, indicating spontaneous formation of the defects. However, the current study is based on the assumption of a dilute solution of defects; presumably the formation energies will increase with increasing concentration, such that the system remains stable. A previous study and Li *et al.*<sup>74</sup> also observed negative formation energies for this material. Furthermore, the energy difference between different configurations is rather small. This indicates that all the configurations could exist in the system. Therefore, the polarization of the system, such as congruent  $\text{LiNbO}_3$ , is an overall effect of different configurations. The polarization of the 1-2-3-8 system is very similar to the experimental values for the polarization. However, the comparison between simulation and experiments should be treated with caution because the dipole moments calculated in the present study represent an average over the simulation supercell. Thus, it represents a local polarization rather than the experimental polarization over a macroscopic region.

### 3.7 Diffusion Mechanisms

As the above analysis has shown, the DFEs of all of the A3 and A4 complexes are within 0.11 eV of each other. It is therefore of considerable interest to determine whether these structures can be expected to be essentially static or whether the energy barriers to Li-vacancy migration are sufficiently low that they might be highly dynamic with Li vacancies diffusing among the various nearly energetically equivalent sites. If the defects are indeed dynamic, the non-uniaxial components of the polarization of each individual cluster may dynamically cancel out locally.

To set the context for this analysis, the diffusion of an isolated Li vacancy through the Li-sublattice in  $\text{LiNbO}_3$  is first considered. Based on a qualitative structural analysis, the energy barriers of several diffusion paths have been calculated (Figure 3-11).

Path A: Diffusion of a lithium vacancy directly to its first nearest neighbor in the Li-sublattice. Each Li ion has six first Li neighbors at a distance of 3.771 Å. Therefore, the jump direction for an individual Li ion can be any one of the following six directions:  $[0\ 2\ -2\ 1]$ ,  $[-2\ 0\ 2\ 1]$ ,  $[2\ -2\ 0\ 1]$ ,  $[0\ -2\ 2\ -1]$ ,  $[2\ 0\ -2\ -1]$ , and  $[-2\ 2\ 0\ -1]$ . As the diffusion directions maintain the three-fold symmetry, for both the plane above and below, the overall effect would lead to an isotropic diffusion mechanism. It is noted that such diffusion is not in the basal (0001) plane.

Path B: Diffusion of a Li through the neighboring vacant site, then to its first nearest neighbor in the Li-sublattice. For example, in Figure 3-11(b), lithium vacancy first move towards  $[1\ -1\ 0\ 0]$  then to  $[0\ 0\ 0\ 1]$  to reach  $[2\ -2\ 0\ 1]$ .

Path C: Diffusion within the basal plane. The diffusion distance for lithium vacancy within the basal plane (0001) is 5.138 Å along  $[-2110]$ . The coordination number of a vacancy is also six. However, this diffusion direction is perpendicular to the  $[0001]$  direction, which leads to anisotropic diffusion mechanism.

Path D: Along the  $[0001]$  direction, the stacking of cations follows the order: Li-Nb-vacant site-Li-Nb-vacant site; thus, diffusion of a lithium vacancy directly along the z direction will not be favorable as the niobium ions block the diffusion path. This path is not considered further.

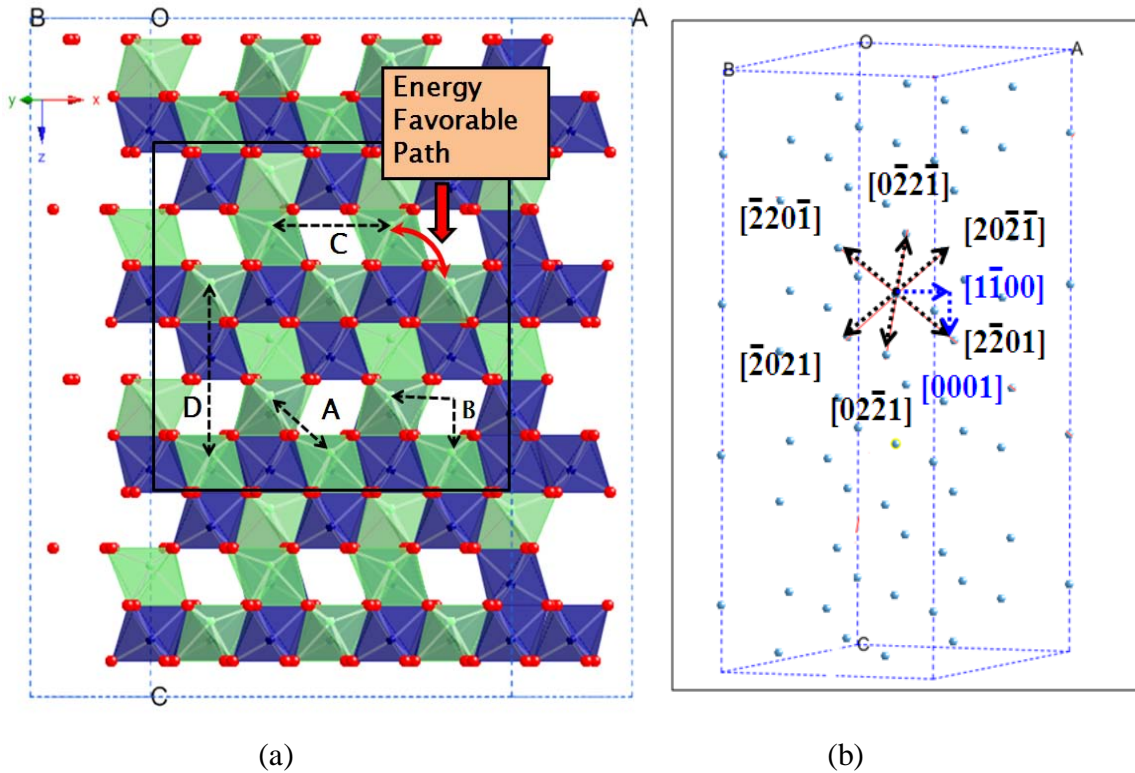


Figure 3-11. (a) Schematics of possible diffusion paths in the  $\text{LiNbO}_3$ , vertical direction is  $[000-1]$ . Diffusion path A represents the diffusion of lithium vacancy directly to its first nearest neighbor in the Li-sublattice. Path B represents the diffusion through the vacant site then to its first nearest neighbor in the Li-sublattice. Path C represents the diffusion within the basal plane. Path D is the diffusion of lithium vacancy directly along z direction, which is blocked by the niobium ions. The energy favorable path is highlighted with red and in solid line. (b) The diffusion direction of lithium vacancy to its six first nearest neighbor shown in three dimensions. This corresponds to the diffusion path A in the figure left (black). The diffusion path B is shown in blue. Only Li-sublattice is shown.

The energy barriers associated with each of path A, B and C are given in Figure 3-11. It is found that the migration energy for diffusion within the basal plane (Path C) is much higher than the values for diffusion between the first nearest neighbors of the Li-sublattice (Paths A and B). It is also observed that the diffusion path between the first nearest neighbors in the Li-sublattice

is neither in a straight line nor exactly through the vacant site, but is a compromise between the two. Furthermore, the diffusion barriers for this path is calculated to be 1.63 eV (Figure 3-12), which is in excellent agreement with the experimental values of the Li migration energy of 1.55 eV<sup>139</sup>, 1.62 eV<sup>140</sup>, and 1.17 eV<sup>141</sup> (Table 3-11). This result is consistent with the conjecture that the diffusion mechanism in LiNbO<sub>3</sub> is through the migration of lithium vacancies on the Li-sublattice<sup>142</sup>.

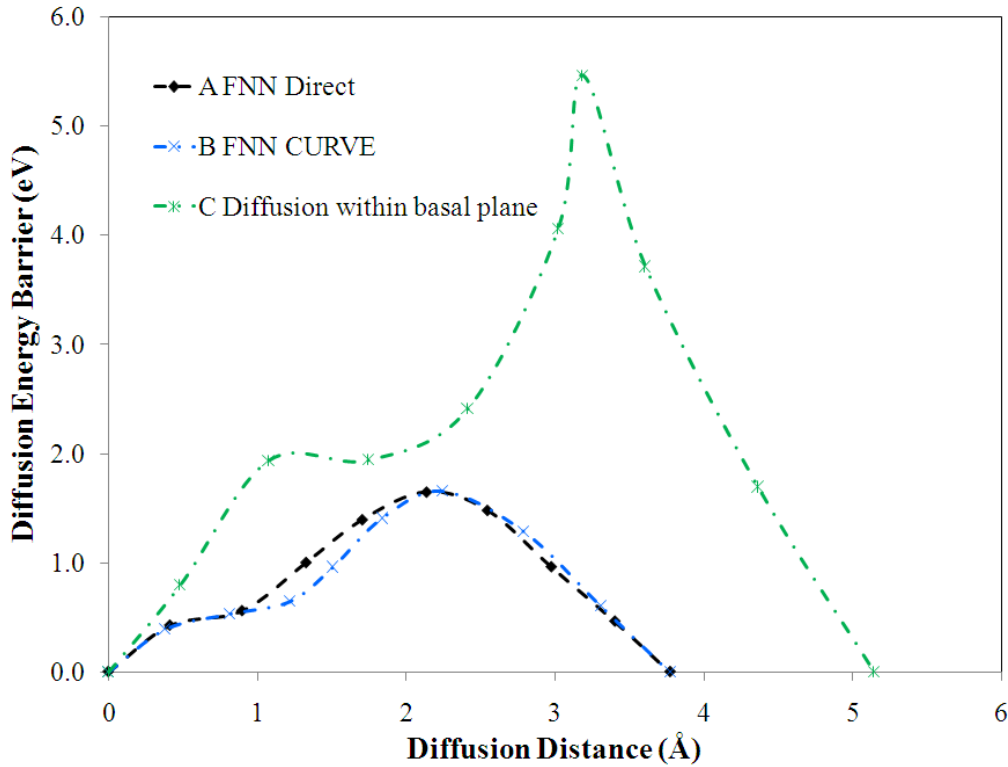


Figure 3-12. NEB calculations of diffusion barriers for lithium vacancy for several diffusion paths. Path A: *FNN Direct* represents diffusion of lithium vacancy directly to its first nearest neighbor in the Li-sublattice. Path B: *FNN curve* represents the diffusion through the vacant site then to its first nearest neighbor in the Li-sublattice. Path C: represents the *diffusion within the basal plane*. Both path A and B converge to the energy favorable path indicated in Figure 3-11 during the NEB calculation, in which the relaxation of the ions is considered.

The diffusivity of lithium vacancy can be calculated using the standard diffusion formula<sup>1</sup>

$$D_{vac} = \alpha \zeta \lambda^2 \nu_0 \exp\left(\frac{-\Delta H}{k_B T}\right) \quad [3-23]$$

where  $\alpha$  is a geometric constant depending on crystal structure,  $\alpha=1/\zeta$ ,  $\zeta$  is the coordination number of the vacancy,  $\lambda$  is the jump distance,  $\nu_0$  is the vibration frequency of the atoms,  $\Delta H$  is the migration energy,  $k_B$  is the Boltzmann constant, and  $T$  is the temperature. Making the standard assumption, the vibration energy  $h\nu_0$  is assumed to be the same as the thermal energy  $k_B T$ , where  $h$  is the Plank constant. At 1200 K, in which most diffusivity are experimentally measured,  $\nu_0 \approx 2.5 \times 10^{13} \text{ s}^{-1}$ . The jump distance between the first nearest Li neighbors is 3.771 Å. This yields a diffusivity at 1200 K of  $4.2 \times 10^{-9} \text{ cm}^2/\text{s}$  for an activation enthalpy of 1.63 eV, as obtained from DFT. The diffusivity calculated from experimental data at 1200 K is  $1.6 \times 10^{-7} \text{ cm}^2/\text{s}$  (Mehta *et al.* <sup>139</sup>),  $2.8 \times 10^{-8} \text{ cm}^2/\text{s}$  (Halstead *et al.* <sup>140</sup>), and  $2.6 \times 10^{-7} \text{ cm}^2/\text{s}$  (Schmidt *et al.* <sup>141</sup>) respectively (Table 3-11).

Table 3-11. Activation Energy ( $E_a$ ) obtained from first principles calculations, compared with the experimental results. The pre-factor ( $D_0$ ) of the calculation is based on the assumption that the vibration frequency  $\nu_0 \approx 2.5 \times 10^{13} \text{ s}^{-1}$  and a jump distance between the first nearest neighbors of 3.771 Å. The diffusivity is calculated at  $T=1200\text{K}$ .

	Calculation	Experiment		
	(This Work)	Mehta <i>et al.</i> <sup>139</sup>	Halstead <i>et al.</i> <sup>140</sup>	Schmidt <i>et al.</i> <sup>141</sup>
$D_0$ ( $\text{cm}^2/\text{s}$ )	$3.56 \times 10^{-2}$	$5.10 \times 10^{-1}$	$1.80 \times 10^{-1}$	$2.10 \times 10^{-2}$
$E_a$ (eV)	1.63	1.55	1.62	1.17
Diffusivity ( $\text{cm}^2/\text{s}$ )	$5.10 \times 10^{-9}$	$1.58 \times 10^{-7}$	$2.84 \times 10^{-8}$	$2.57 \times 10^{-7}$

These variations in diffusivity mainly reflect the differences in the activation energies. In particular, the activation energy obtained by Schmidt *et al.* is significantly smaller than the others are, which lead to a higher diffusivity. The difference is even larger at low temperatures. At room temperature (298 K), the diffusivity is  $2.4 \times 10^{-30} \text{ cm}^2/\text{s}$ , based on the DFT results. The diffusivity calculated from experimental data at room temperature is  $3.2 \times 10^{-27} \text{ cm}^2/\text{s}$  (Mehta *et al.* <sup>139</sup>),  $7.4 \times 10^{-29} \text{ cm}^2/\text{s}$  (Halstead *et al.* <sup>140</sup>), and  $3.6 \times 10^{-22} \text{ cm}^2/\text{s}$  (Schmidt *et al.* <sup>141</sup>) respectively. These are extremely low diffusion constants, which indicate that the defect clusters are rather stable at such temperature.

The average diffusion distance can then be calculated using the standard random walk equation:

$$x = \sqrt{6Dt} \quad [3-24]$$

where  $x$  is the diffusion distance,  $D$  is the diffusivity and  $t$  is the time. At room temperature, for lithium vacancy to diffuse in the order of angstroms, it requires the diffusion time to be in the range of years. This indicates that each configuration of the defect complex should be very stable at room temperature, which may lead to significant local dipole moments, even including non-uniaxial contributions. However, the average diffusion distance is predicted to be in the order of tens of nanometers after five hours of annealing at 250 °C<sup>143</sup>, which indicates the lithium vacancy should still be able to diffuse and change the configurations of the defect complexes. This is in agreement with the experimental observation that the relative peak emission intensities measured by combined excitation emission spectroscopy can be modified by the annealing of the sample<sup>143</sup>.

### 3.8 Discussion

As discussed in the section 3.1, the X-ray and NMR measurements do not provide a consistent picture of the defects in LiNbO<sub>3</sub>. The X-ray data indicate that the oxygen vacancy concentration is negligible, i.e., that there are no Model I defects ( $V_{O..} + 2V_{Li}'$ ); by contrast, NMR suggests that there are almost equal numbers of Model I and Model III defects ( $Nb_{Li}^{''''} + 4V_{Li}'$ ). It is of considerable interest to analyze our results to see if they can shed any light on this issue.

With reference to the thermodynamics analysis, it is clear that room temperature and standard pressure, ( $\mu_O [LiNbO_3] = \mu_O [gas]$ ), are most relevant for applications; thus the following analysis is performed under these conditions. However, the DFE still cannot be

uniquely determined since the separate values of chemical potential of Li and Nb cannot be determined uniquely, but are coupled.

Our calculations are consistent with the experiments in that they indicate that both Model I and Model III are energetically favorable relative to most other defect structures. In particular, as shown in Figure 3-13(a), Model III and the Li-Frenkel are the dominant defects under different conditions, while Model I has the second lowest DFE through most of the chemical potential stability range. The error bars of 0.2 eV/defect represent our estimated uncertainty in the formation energies. The Li-Frenkel defects do not, of course, change the stoichiometry of the system and are thus not relevant with regards to interpreting the X-Ray and NMR data.

The concentrations of each defect can be calculated from:

$$C_d = N_{site} \exp(-\Delta G_f / kT) \quad [3-25]$$

where  $C_d$  is the number of the defects,  $N_{sites}$  is the number of sites in the crystal where the defect could occur,  $k$  is the Boltzmann constant, and  $T$  is the temperature in Kelvin. The calculated defect concentrations are shown in Figure 3-13(b). This figure must be interpreted with caution, since negative formation energy would apparently lead to a concentration of unity for the corresponding defect, which is not reasonable, since the calculations on which Figure 3-13 are based assume a dilute solution of defects; presumably the formation energies will increase with increasing concentration, such that the system remains stable. For low Nb chemical potentials (Li-rich conditions), the Li-Frenkel is the dominant defect, with a small admixture of Model I. At higher Nb chemical potentials, Model III is dominant and produces a concentration of lithium vacancies that is at least two orders of magnitude larger than produced by Model I. Since Model I defects lead to oxygen vacancies while Model III defects do not, this would be consistent with the experimental finding<sup>24</sup> that for Nb-rich conditions, oxygen vacancies

concentration is much smaller than the lithium vacancy concentrations. However, it should be noted that although the defect concentration of Model I is much smaller than Model III, it may still reach substantial levels under these Nb-rich conditions. In order to achieve the experimentally postulated ratio of 1.1: 1 for Model I and Model III, the DFEs of these two defect reactions would have to be much more similar in magnitude than they are calculated to be; thus this study does not support this scenario.

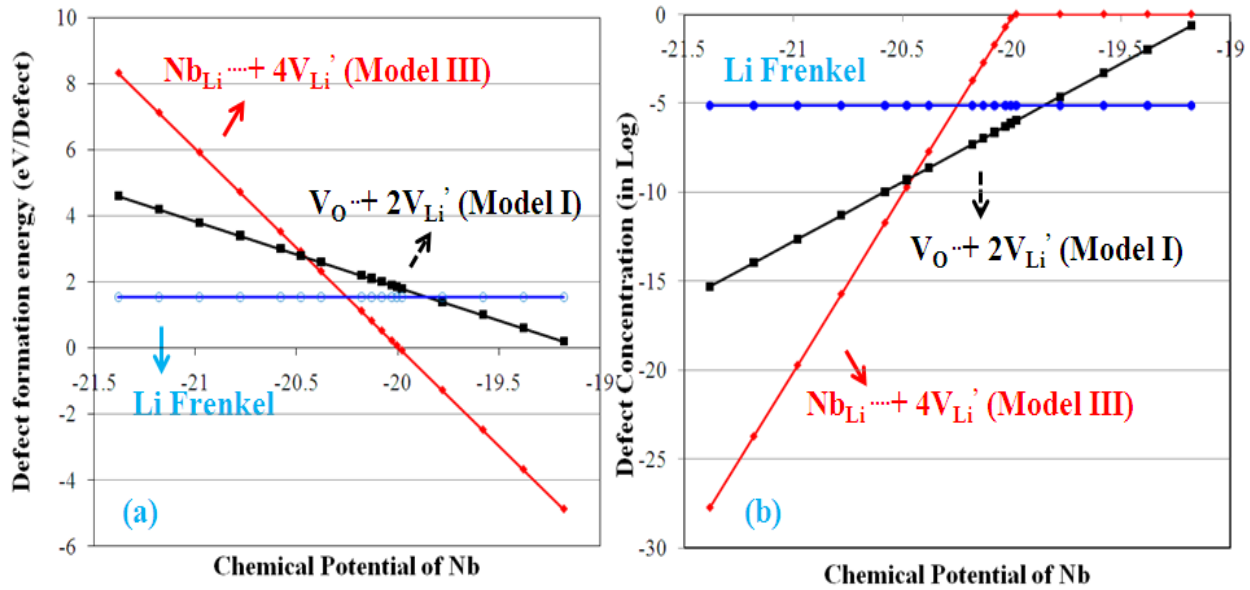


Figure 3-13. The DFEs of Model III, Li-Frenkel and Model I as a function of niobium chemical potential. (b) The defect concentration caused by model III, Li-Frenkel and model I as a function of niobium chemical potential. The chemical potential unit is in eV/atom.

We finally address the mechanism for the vapor transport equilibration (VTE) method<sup>18</sup> used widely in transforming a congruent composition of lithium niobate into a stoichiometric composition. In the vapor transport equilibration method<sup>20</sup>, a target wafer is exposed to  $Li_2O$  vapor produced by decomposition of  $Li_2CO_3$  at high temperature ( $> 730$  °C)<sup>144</sup>. This produces a constant vapor pressure of  $Li_2O$  equal to the vapor pressure of stoichiometric  $LiNbO_3$ . The wafer, which is congruent  $LiNbO_3$  and deficient in  $Li_2O$ , absorbs  $Li_2O$  from the vapor until it

reaches the stoichiometric composition. Then Li diffuses into a considerable depth due to the high diffusivity. The whole growth procedure is thus under Li<sub>2</sub>O-rich conditions. In the language of our calculations, this experimental VTE procedure thus corresponds to using Li<sub>2</sub>O as the reference state. Therefore, according to the analysis in section 3.5, the lithium Frenkel defect is predicted to be the most stable, with a positive DFE. Using Equation 3-25, the concentration of defect is predicted to be negligible, which result in a stoichiometric composition.

Our calculations thus indicate that the relative energetics of the defect clusters can change under variations of temperatures and chemical potentials during annealing experiments, which may result in different relative abundances<sup>143</sup>. Furthermore, these results strongly suggest that the defect chemistry can be expected to be sensitive to the thermal and chemical history of the sample, making direct comparisons among experimental results difficult; indeed, this sensitivity could be the origin of some of the experimental inconsistencies.

In summary, the intrinsic defects and defect clusters in LiNbO<sub>3</sub> have been characterized using DFT-PAW approach. The formation energies of various types of defects and defect clusters have been reported and the dominant defects are determined over the chemical potential stability range. The association effects have also been investigated. The Li-Frenkel was found to have the lowest DFE under Li<sub>2</sub>O-rich conditions, while the cluster consisting of a niobium antisite compensated by lithium vacancy ( $\text{Nb}_{\text{Li}}^{\bullet\bullet\bullet\bullet} + 4\text{V}_{\text{Li}}^{\cdot}$ ) was found to be energetically stable under Nb<sub>2</sub>O<sub>5</sub>-rich conditions.

These results are consistent with experimental observations. In particular, for the first time, the intrinsic defect cluster mentioned above, which was conjectured before to play a critical role in domain structure and dynamics, has been verified using first principles calculations to indeed have the lowest formation energy. The defect analysis also sheds light on the mechanism by

which a congruent composition of  $\text{LiNbO}_3$  can be transformed into a stoichiometric composition by the widely used VTE method today.

## CHAPTER 4 EXTRINSIC DEFECTS IN LITHIUM NIOBATE

### 4.1 Background of Extrinsic Defects

During the past decades, there have been numerous studies of doped  $\text{LiNbO}_3$ <sup>43, 45, 143, 145-147</sup> for optical lasers, optical amplifiers, and integrated optical circuits<sup>148-151</sup>. Various dopants have been added to the system for different purposes. For example, Mg has been introduced into the system to increase the resistance to photorefractive damage<sup>25, 26</sup>; Er and Nd have been added for solid-state laser applications<sup>28-31</sup>. Dopant ions have also been employed as probes to investigate the structure of domain walls and defect/domain-wall interactions<sup>32-34</sup>.

Various experimental techniques, including electron-spin resonance<sup>4</sup>, X-ray standing wave analysis (XSW)<sup>39, 40</sup>, Rutherford backscattering<sup>38</sup>, extended x-ray absorption fine structure (EXAFS)<sup>41</sup>, and ion beam channeling<sup>152</sup> have been employed to investigate the site selectivity of dopant ions. Moreover, several optical and magnetic resonance spectroscopy studies<sup>43-47</sup> have been used to determine the local environments and configurations around the dopant sites. While some of these studies used congruent  $\text{LiNbO}_3$  samples grown by the Czochralski method<sup>13, 14</sup>, others used stoichiometric  $\text{LiNbO}_3$  produced through vapor transport equilibration (VTE)<sup>18-20</sup> from congruent samples. The influence of the sample stoichiometry on the site selectivity and distribution is also unknown, which makes the comparison between experiments on samples from different synthesis technique problematic.

In addition to understanding how the dopants are incorporated into the structure, an understanding of the associated charge compensation mechanisms is also necessary. Atomic-level simulations<sup>153</sup> using an empirical potential have been used to predict the dominant defect for various dopant ions. However, the empirical potentials did not explain the discrepancies between experiments. For instance, erbium sitting on lithium site compensated by erbium sitting

on niobium site is predicted to be dominant at 0 K by the empirical potential. However, at room temperature, the same potential predicted that  $\text{Er}^{3+}$  ions occupy the Nb site, compensated by  $\text{Nb}_{\text{Li}}^{\dots}$ . It is not clear how such a small temperature change (300 K = 0.026 eV) could cause such a qualitative change in the dominant crystal defect. The experimental and theoretical results thus indicate that the charge compensation mechanisms for dopant ions in  $\text{LiNbO}_3$  are still not well understood.

In the present study, the formation energies of several dopants with different valance charges ( $\text{Mg}^{2+}$ ,  $\text{Fe}^{2+}$ ,  $\text{Er}^{3+}$ ,  $\text{Nd}^{3+}$ , and  $\text{Fe}^{3+}$ ) have been determined using DFT to predict the site preference and corresponding charge compensation mechanisms. The influences of the composition and growth condition on the defect chemistry have been assessed based on thermodynamic analysis under  $\text{Nb}_2\text{O}_5$  and  $\text{Li}_2\text{O}$  reference states respectively. Furthermore, the charge transfer level of iron with regard to the band structure has been calculated to elucidate the effects of coexistence of both 2+ and 3+ charged ions on the optical properties of  $\text{LiNbO}_3$ .

## 4.2 Structure of Reference Binary Oxides

In order to calculate the formation energies and to determine the dominant defects, the chemical potentials of the dopants are needed. However, it is extremely difficult to determine the exact value of the chemical potential, as it is a variable depending on many factors, including partial pressure, temperature, and compositions. Therefore, appropriate reference states are needed, such as the metallic or oxides phase of the dopants. For the metallic phase to be used, it is assumed that materials are in an extremely reducing environment, which is far from the condition of dopants in  $\text{LiNbO}_3$ . A more general and plausible way is to use the corresponding binary oxides as reference state, in which the bonding environments of dopants is more similar to

that in  $\text{LiNbO}_3$ . Therefore, the structures of the binary oxides need to be clarified first. In current study, the thermodynamic stable and most common phase for each binary oxide is used.

#### 4.2.1 Crystal Structure of MgO and FeO

Both MgO and FeO has a rock-salt structure (Space Group:  $\text{Fm-3m}$ )<sup>1</sup>, in which both cations and anions form a separate FCC sub-lattice with lattices interpenetrating with each other. The ionic radii of  $\text{Mg}^{2+}$ ,  $\text{Fe}^{2+}$ , and  $\text{O}^{2-}$  are 0.86 Å, 0.75 Å, and 1.26 Å, respectively<sup>154</sup>. The ratio of cation/anion radii of MgO and FeO are 0.683 and 0.595 respectively, which fall into the range between 0.414 and 0.732. Therefore, each cation or anion has a coordination number of six and is at the vertices of an octahedron. An illustration of atomic arrangement for rock-salt structure is shown in Figure 4-1.

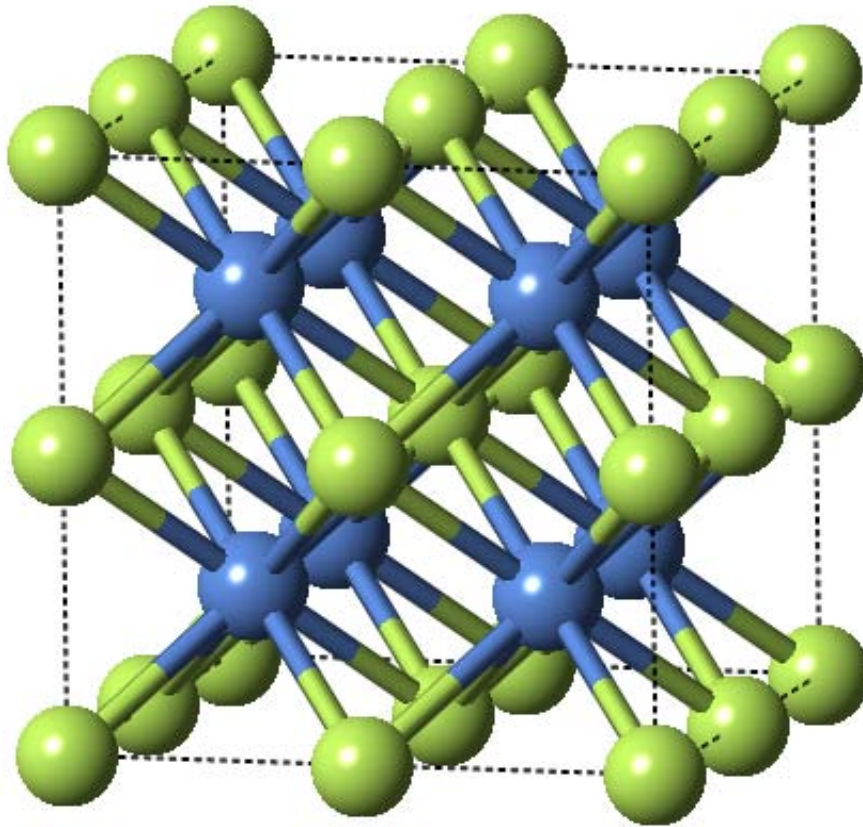


Figure 4-1. Crystal structure of MgO and FeO.

#### 4.2.2 Crystal Structure of $\text{Er}_2\text{O}_3$ , $\text{Nb}_2\text{O}_3$ , and $\text{Fe}_2\text{O}_3$

Erbium oxide has a cubic structure, with space group of  $Ia\bar{3}$ <sup>155</sup>. The lattice constant of  $\text{Er}_2\text{O}_3$  is  $10.5 \text{ \AA}$ <sup>155</sup>. There are 32 erbium and 48 oxygen in each unit cell (Figure 4-2), resulting in a total number of 80 ions. Erbium ions sit on two different Wyckoff positions, 8a and 24d<sup>155</sup> respectively. The details about the Wyckoff positions and fraction coordinates are given in Table 4-1.  $\text{Er}^{3+}$  is coordinated with six oxygen ions and in a distorted octahedron. Oxygen has a coordination number of four and occupies a tetrahedral site.

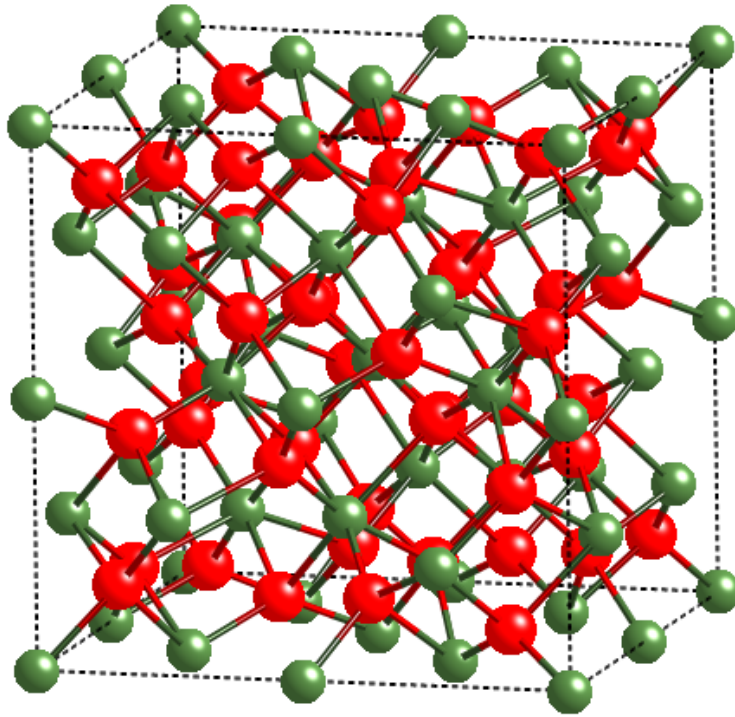


Figure 4-2. Crystal structure of  $\text{Er}_2\text{O}_3$ .

Table 4-1. Wyckoff position and fraction coordinates of  $\text{Er}_2\text{O}_3$ <sup>155</sup>.

$\text{Er}_2\text{O}_3$	Wyckoff	x	y	z
Er (1)	8a	0.0000	0.0000	0.0000
Er (2)	24d	0.2855	0.0000	0.2500
O	48e	0.1293	0.1471	0.9165

The structure of neodymium oxide belongs to the trigonal system (Space Group:  $P\bar{3}m1$ <sup>156</sup>, Figure 4-3). The lattice constants in the  $[1000]$  and  $[0001]$  direction are  $3.8277 \text{ \AA}$  and  $5.9908 \text{ \AA}$

<sup>156</sup>. The Wyckoff position of Nd<sup>3+</sup> is 2d while the oxygen occupy two different Wyckoff site, 2d and 1a respectively. The details of the Wyckoff position and fraction coordinates are given in Table 4-1.

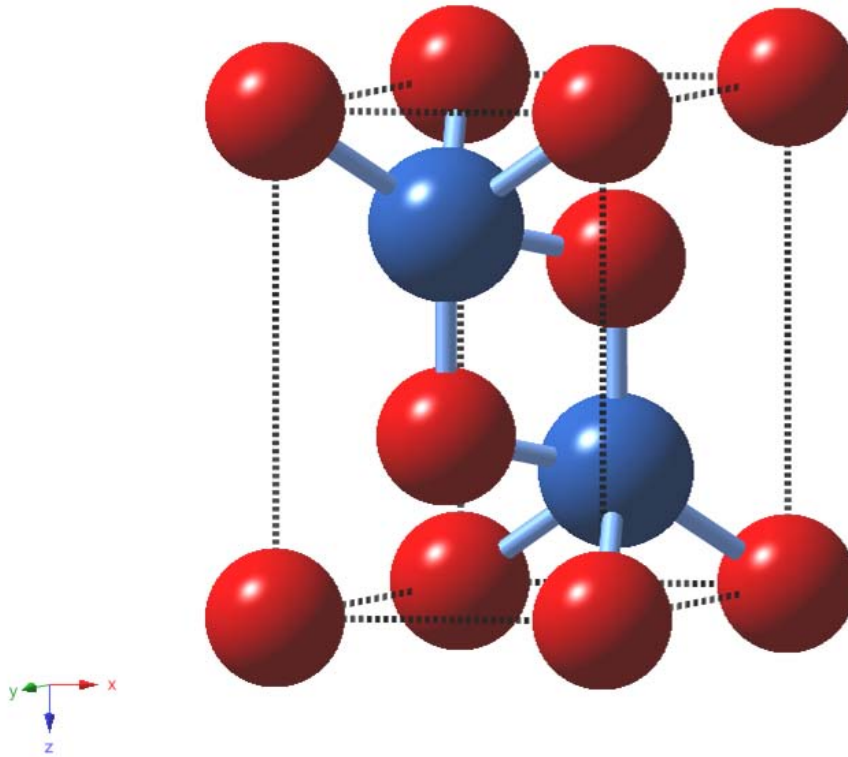


Figure 4-3. Crystal structure of Nd<sub>2</sub>O<sub>3</sub>.

Table 4-2. Wyckoff position and fraction coordinates of Nd<sub>2</sub>O<sub>3</sub> <sup>156</sup>.

Nd <sub>2</sub> O <sub>3</sub>	Wyckoff	x	y	z
Nd	2d	0.3333	0.6667	0.2462
O	2d	0.3333	0.6667	0.6646
O	1a	0.0000	0.0000	0.0000

Fe<sub>2</sub>O<sub>3</sub> has several phases <sup>157</sup>, with corundum α- Fe<sub>2</sub>O<sub>3</sub> being the most common form <sup>158</sup>. It has a trigonal Barvais lattice with space group: R-3c . The oxygen ions form hexagonal close packed array with iron sitting on two thirds of the octahedral sites. There are six formulas of units in each unit cell (Figure 4-4). β- Fe<sub>2</sub>O<sub>3</sub> is a metastable cubic face centered phase, which converts to the alpha phase at ~500 °C. γ- Fe<sub>2</sub>O<sub>3</sub> is also metastable and cubic and converts to the

alpha phase at even higher temperature. To be used as reference state,  $\alpha$ -Fe<sub>2</sub>O<sub>3</sub> is chosen because it is the most common and thermodynamically stable phase.

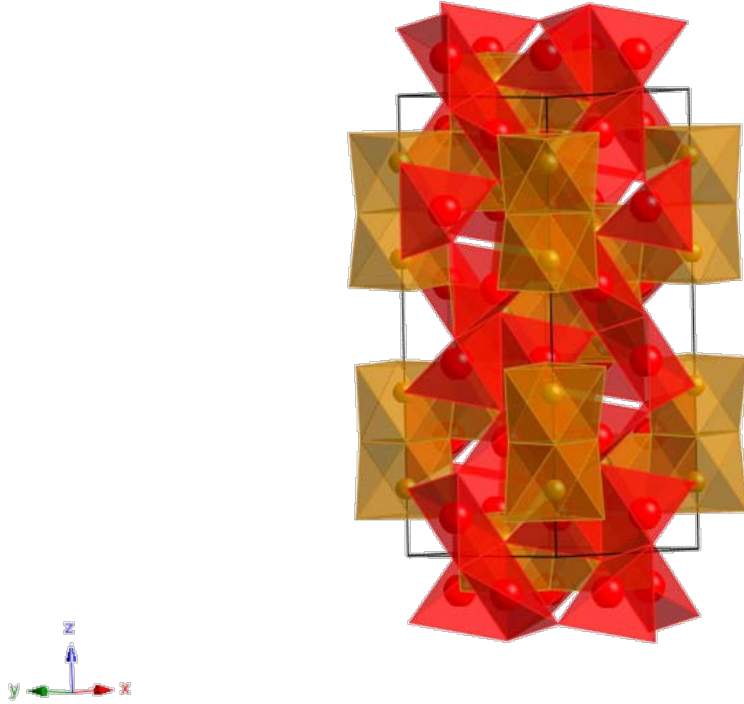


Figure 4-4. Crystal structure of  $\alpha$ -Fe<sub>2</sub>O<sub>3</sub>.

### 4.3 Computational Details

The system size for doped LiNbO<sub>3</sub> study is 2 x 2 x 1 unit cells (each of 30 atoms), which for perfect LiNbO<sub>3</sub> contains 120 atoms and 720 electrons; periodic boundary conditions are applied in all three dimensions. The integration over the Brillouin-zone uses a 4 x 4 x 2 Monkhorst-Pack<sup>117</sup> k-point mesh. Mg has an electronic configuration of [Ne].3s<sup>2</sup>, in which the two s electrons are considered as valence electrons. This electronic configuration is much simpler than that of the Fe, which is a transition metal with d orbitals. For iron, the electronic structure is [Ar].3d<sup>6</sup>.4s<sup>2</sup>. Both 3d and 4s electrons are treated as valence electrons.

Er and Nd are rare earth elements. The electronic structure of Er is [Xe] 4f<sup>12</sup>6s<sup>2</sup>. Due to the localized nature of 4f electrons<sup>159, 160</sup>, the frozen core approximation<sup>161, 162</sup> is used. For Er,

eleven of twelve  $f$  electrons are treated as the frozen core in VASP, with only a single  $f$  electron treated as a valence electron<sup>163</sup>. In addition, the  $6s^2$  and  $5p^6$  are also treated as valence electrons, resulting in nine Er valence electrons in total. The electronic configuration of Nd is  $[\text{Xe}] 4f^3 6s^2$ , similar to Er; frozen core approximation has also been implemented in VASP.

The localized nature of  $4f$  and  $3d$  electrons results in strong correlation effects. In general, mean field theories, such as the local density approximation (LDA) and GGA, cannot accurately describe the strong correlations of  $d$  and  $f$  electrons<sup>163-165</sup>. Therefore, in addressing this problem, either a higher level theory, or a correction to LDA or GGA, such as DFT+U approach<sup>78, 79</sup> is required. The effect of the +U term on defect energetics needs to be assessed. To evaluate the effects of +U, several fundamental properties, which include lattice constants, band gap, and magnetic moments, have been calculated using GGA and GGA+U for the reference binary oxides. To perform GGA+U calculations, reasonable values for the U and J parameters are needed. In this study, Dudarev's approach<sup>79</sup> has been used, in which only the difference between U and J is meaningful.

There are no parameters of + U for  $\text{Nd}_2\text{O}_3$  in the literature. Only one parameter of +U, in which  $U - J = 6.5$  eV, has been applied to Nd, in that case  $\text{TiO}_2$  using LDA+U.<sup>166</sup> For  $\text{Fe}_2\text{O}_3$ , there are several studies focusing on parameterization of U and J values.  $U - J = 4$  eV has been chosen based on the analysis of heat of formation data<sup>167</sup>, which is also probably the most widely used value in the literature. However, this value is used with LSDA+U. As for GGA+U, both  $U - J = 4$  eV and  $U - J = 6$  eV have been used in the previous studies<sup>168, 169</sup>. Since this section is trying to evaluate the effects of +U, both values have been employed to calculate the fundamental properties of FeO and  $\alpha\text{-Fe}_2\text{O}_3$ .

The fundamental properties of FeO and Fe<sub>2</sub>O<sub>3</sub> are calculated using GGA and GGA+U and compared with experimental data. For FeO, it is observed that GGA underestimates the lattice constant by ~ 0.21 Å, while GGA+U using both values overestimates it by 0.08 Å. GGA predicts its band structure to be metallic, which is a well known failure of this method<sup>62</sup>. On the other hand, GGA+U predicts FeO to be semiconductor, with a band gap of 1.7 eV and 2.02 eV respectively using U - J = 4 eV and U - J = 6 eV. Although the calculated band gap using GGA+U is lower than the experimental value (2.4 eV<sup>170</sup>), it correctly predicts the material to be semiconductor and with an typical of GGA. In addition, GGA also severely underestimates the magnetic moments while GGA+U improves it significantly.

Table 4-3. Fundamental properties comparison between GGA, GGA+U and experiments for FeO.

FeO	GGA	GGA+(U=4)	GGA+(U=6)	Experiment
Crystal Structure	Fm-3m	Fm-3m	Fm-3m	Fm-3m <sup>1</sup>
Lattice Constants (Å)	4.088	4.382	4.382	4.334 <sup>171</sup>
Magnetic Structure	AFM	AFM	AFM	AFM <sup>172</sup>
Magnetic moments	1.009	3.755	3.8	4.2 <sup>173</sup>
Band Gap (eV)	Metallic	1.7	2.02	2.4 <sup>170</sup>

For α-Fe<sub>2</sub>O<sub>3</sub>, GGA+U has a similar effect. GGA predicts a lower value for the lattice parameter than the experimental results. The lattice constant predicted using GGA+U is in excellent agreement with experimental value. The magnetic moment calculated using GGA is too low while GGA+U improves it to 80% of the experimental value.

Table 4-4. Fundamental properties comparison between GGA, GGA+U and experiments for Fe<sub>2</sub>O<sub>3</sub>.

Fe <sub>2</sub> O <sub>3</sub>	GGA	GGA+U(4 eV)	GGA+U(6 eV)	Experiment
Crystal Structure	R-3c	R-3c	R-3c	R-3c <sup>174</sup>
Lattice Constants (Å)-a	4.698	5.02	5.018	5.0355 <sup>175</sup>
Lattice Constants (Å)-c	13.376	13.716	13.685	13.7471 <sup>175</sup>
Magnetic Structure	AFM	AFM	AFM	AFM <sup>174</sup>
Magnetic moments	0.734	4.071	4.222	4.9 <sup>176</sup>

It is observed that GGA+U using both values generate similar results and the difference between two sets of parameters is relatively small. Since U - J = 6 eV generally provides slightly

better lattice constants, band gap, and magnetic moments. Therefore, this value is used for the further defect formation energies calculations.

The comparison of fundamental properties between GGA, GGA+U and experiments for  $\text{Nd}_2\text{O}_3$  is given in Table 4-5. Unlike iron oxides, no significant difference in lattice constants and band gap has been observed between GGA and GGA+U. The lattice constants predicted by GGA and GGA+U are very close to the experimental value, while both methods underestimate the band gap by  $\sim 1.6$  eV. Therefore, there is no need to use GGA+U for  $\text{Nd}_2\text{O}_3$ .

Table 4-5. Fundamental properties comparison between GGA, GGA+U and experiments for  $\text{Nd}_2\text{O}_3$ .

$\text{Nd}_2\text{O}_3$	GGA	GGA+U (6.5 eV)	Experiment
Crystal Structure	P-3m1	P-3m1	P-3m1 <sup>156</sup>
Lattice Constants (Å)-a	3.839	3.934	3.8827 <sup>156</sup>
Lattice Constants (Å)-c	5.998	6.107	6.077 <sup>156</sup>
Band Gap (eV)	4.12	4.24	5.8

No +U parameters have been determined for Er in either  $\text{LiNbO}_3$  or  $\text{Er}_2\text{O}_3$ . However, there are several sets of parameters available for Er in GaN and in  $\text{Er}_x\text{Ga}_{1-x}\text{N}$ <sup>177, 178</sup>. For Er in GaN using the density functional based tight banding (DFT-TB) method<sup>177</sup>,  $U - J = 10.3$  eV was used. However, it is known that the DFT-TB method yields higher estimates for U and J than does regular DFT<sup>177</sup>. For  $\text{Er}_x\text{Ga}_{1-x}\text{N}$  using LSDA+U<sup>178</sup>,  $U=8.6$  eV and  $J=0.75$  eV have been used. Since there are no accepted values for U and J for  $\text{LiNbO}_3$ , we have explored a range in order to map out the possible magnitude of the effects of electron localization: (i)  $U - J = 4$  eV; (ii)  $U - J = 7.85$ eV<sup>178</sup>, and (iii)  $U - J = 10.3$  eV<sup>177</sup>. Although none of these parameters may actually be the best physical representation of electron localization for Er in  $\text{LiNbO}_3$ , they do span the range of reasonable values, and should thus enable us to assess the importance of the localization of electrons on the defect energetics. Because the GGA+U has to be used for both the reference

state  $\text{Er}_2\text{O}_3$  and for Er in  $\text{LiNbO}_3$ , its effects on  $\text{Er}_2\text{O}_3$  are discussed first, followed by its effects of Er in  $\text{LiNbO}_3$ .

For  $\text{Er}_2\text{O}_3$ , the band gap calculated using pure GGA is 4.37 eV, which is about 13% less than the experimental value of  $\sim 5$  eV<sup>179</sup>. This agreement can be considered to be good, because it is well known that for many systems GGA fails to predict the band gap of a material with partially filled *d* or *f* orbital<sup>163-165</sup>. There is no significant change in the band gap or electronic density of states for any of the parameter sets for U-J, which indicates that the Er is reasonably described by GGA (Figure 4-5).

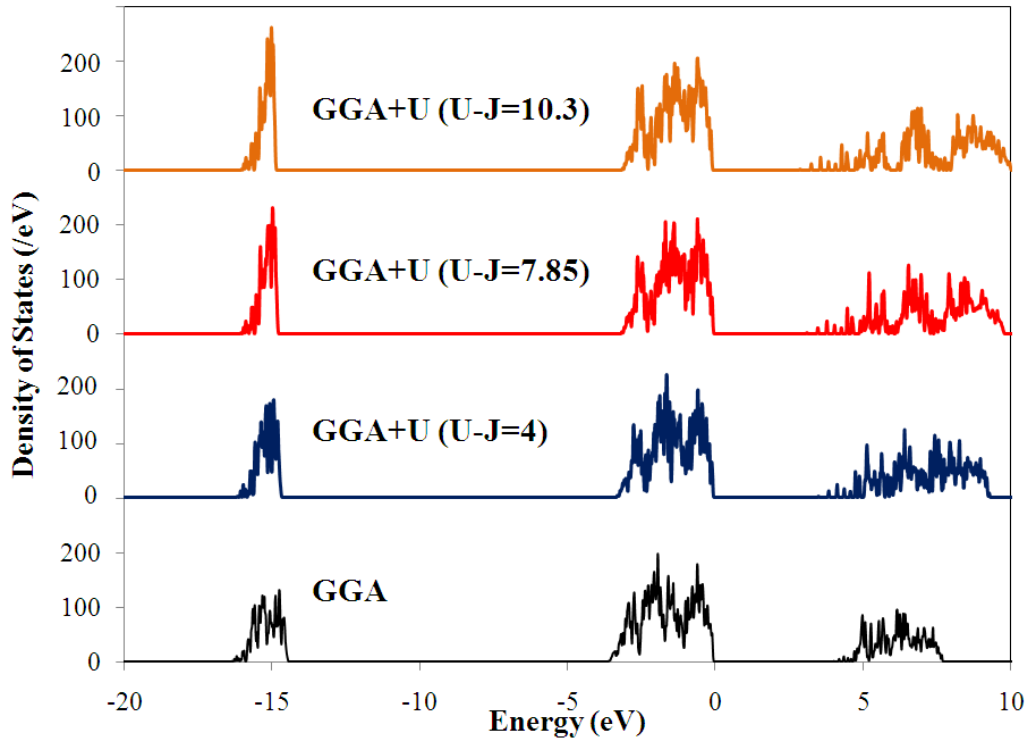


Figure 4-5. Electronic density of States of  $\text{Er}_2\text{O}_3$  calculated using GGA and GGA+U. The parameters  $U - J = 4$  eV,  $U - J = 7.85$  eV, and  $U - J = 10.3$  eV are considered.

For Er in  $\text{LiNbO}_3$ , the representative case of  $\text{Er}_{\text{Li}''} + 2\text{V}_{\text{Li}'}'$  is chosen to illustrate the effects of +U, in which the association effect is also considered. For  $U - J = 4$  eV,  $U - J = 7.85$  eV, and  $U - J = 10.3$  eV, the DFE increases by 0.067 eV/defect, 0.102 eV /defect and 0.072 eV/defect,

respectively. Thus, the stability order predicted from the GGA calculations is correct and the energy values can be considered reliable to within  $\sim 0.1$  eV/defect. We thus conclude that electron localization as captured by the +U term has no significant effect on either the electronic structure or the defect energetics for Er systems.

In summary, for MgO, no +U is needed as Mg does not have any *f* or *d* electrons. For iron oxides, it is necessary to use the GGA+U method to predict reasonable band gap and magnetic moments. Based on the analysis of the lattice constants, band gap and magnetic moments of FeO and  $\alpha$ -Fe<sub>2</sub>O<sub>3</sub>,  $U - J = 6$  eV is chosen to carry out the formation energies calculations. For Er<sub>2</sub>O<sub>3</sub> and Nd<sub>2</sub>O<sub>3</sub>, no significant effects of the +U on the lattice constants and band gap of the reference binary oxides or on the formation energy of the impurities in LiNbO<sub>3</sub> has been observed. Therefore, GGA will be continued to perform the formation energy calculations.

#### **4.4 Formation Energies and Site Preference**

While defect structures are generally written in terms of fully charged constituent defects, partially charged and charge-neutral defects are also possible<sup>118</sup>. For example, many experiments on TiO<sub>2</sub> have concluded that as the oxygen partial pressure decreases from moderately reducing conditions to extremely reducing conditions, there is a transition from a fully charged oxygen vacancy to a singly charged oxygen vacancy or triply charged titanium interstitial<sup>133</sup>. Thus, before characterizing the defect clusters, it is important to analyze the individual defects with various charge states. The following sub-sections will discuss the results obtained for individual defects of various charges, followed by the defect clusters. For the defect clusters, the constraint of charge neutrality leads to the simplification of not having to consider the effects of the location of the Fermi energy<sup>136</sup>.

#### 4.4.1 Single Defects

Single isolated point defects in the 2x2x2 supercell are investigated, which corresponds to the situation of the charge-compensating defects being far from both the impurities and each other. Assuming the impurities are +3 charged, depending on the position of ions, two different types of point defects could be formed, which are  $M_{Li}$  and  $M_{Nb}$  respectively. To explore how the Fermi level may affect the point defects in the system, an exemplar case of Er in  $LiNbO_3$  is discussed in detail in the following.

The DFEs of  $Er_{Li}$  and  $Er_{Nb}$  defects with various charge states in  $LiNbO_3$  have been calculated using Equation 3-22. The influence of the Fermi energy on the stability of each individual defect is considered. The reference zero of the Fermi energy is assigned to be the valence band maximum (VBM) of the perfect structure; the highest Fermi energy thus corresponds to the conduction band minimum (CBM), which for GGA is 3.5 eV, close to the experimental value of 3.78 eV<sup>115, 116</sup>. A Fermi energy at the center of the gap corresponds to the pure system, while p-type and n-type correspond to Fermi energies closer to the valence and the conduction bands, respectively<sup>180</sup>. As the Fermi level could shift in the presence of impurities and defects, two extreme cases corresponds to  $\epsilon_f=0$  and  $\epsilon_f=3.5$ .

The dependence of DFEs on the Fermi level is shown in Figure 4-6, using  $Nb_2O_5$  (the BC line in Figure 3-4) as the reference state. At each value of the Fermi level, Figure 4-6 includes only the charge state with the lowest DFE of each individual defect. The slopes of the lines in Figure 4-6 represent the charge states of the defects. As the Fermi energy increases, the thermodynamically stable charge of the cations decreases.  $Er_{Li}^{2+}$  has a lower energy than its singly charged counterpart  $Er_{Li}^{3+}$  for most of the range of Fermi level, while  $Er_{Nb}^{3+}$  has the lowest DFE throughout the entire range. The partial density of states of Li, Nb, O, and Er for  $Er_{Li}^{2+}$  and  $Er_{Nb}^{3+}$

have been also generated and are given in Figure 4-7. No significant effect of Er on the PDOS of lithium, niobium and oxygen is observed. From Figure 4-7, it can be seen that there is a greater overlap in the PDOS of the Er and O ions for  $\text{Er}_{\text{Nb}}''$  than that for  $\text{Er}_{\text{Li}}''$ , indicating stronger covalent bonding.

In the unit cell of  $\text{LiNbO}_3$ , six closed-packed planes are stacked<sup>10</sup>. The cations lie in the oxygen octahedral in repeating sequence: Li, Nb, vacant site, Li Nb, vacant site...<sup>10</sup>. Within a single plane of cations, there is an ordered arrangement of Li ions, Nb ions, and vacant sites. For  $\text{Er}_{\text{Li}}''$  the DFT calculations show that the Er is shifted along  $\langle 0001 \rangle$  towards the vacant site by  $\sim 0.17 \text{ \AA}$ . The observation by Gog *et al.* using x-ray standing-wave (XSW) spectroscopy<sup>39, 40</sup> showed the Er to be in a position near a Li site but displaced normal to the basal plane by  $0.46 \text{ \AA}$ <sup>39</sup>. This difference between the experimental measurement and calculated value for the displacement may have several origins. First, the experiments were performed using congruent  $\text{LiNbO}_3$ , while the simulations were carried out for stoichiometric material. Second, the experiments measured the near-surface region where Er is incorporated through diffusion, while the calculations are for the bulk. Both the composition and surface effects could cause a change in the position of the Er ions. Third, the difference may be also due to the limitation of the current calculation method, which simulates the defects in a finite size supercell and assumes that the defect concentration is in the dilute limit. For partial charged defects,  $\text{Er}_{\text{Li}}'$  and  $\text{Er}_{\text{Li}}^x$ , the displacements are  $0.14 \text{ \AA}$  and  $0.08 \text{ \AA}$ , respectively. By comparison, the DFT calculations of  $\text{Er}_{\text{Nb}}''$  yield a displacement of only  $\sim 0.02 \text{ \AA}$  towards the vacant site. The displacements for  $\text{Er}_{\text{Nb}}'$  and  $\text{Er}_{\text{Nb}}^x$  are less than  $0.005 \text{ \AA}$ .

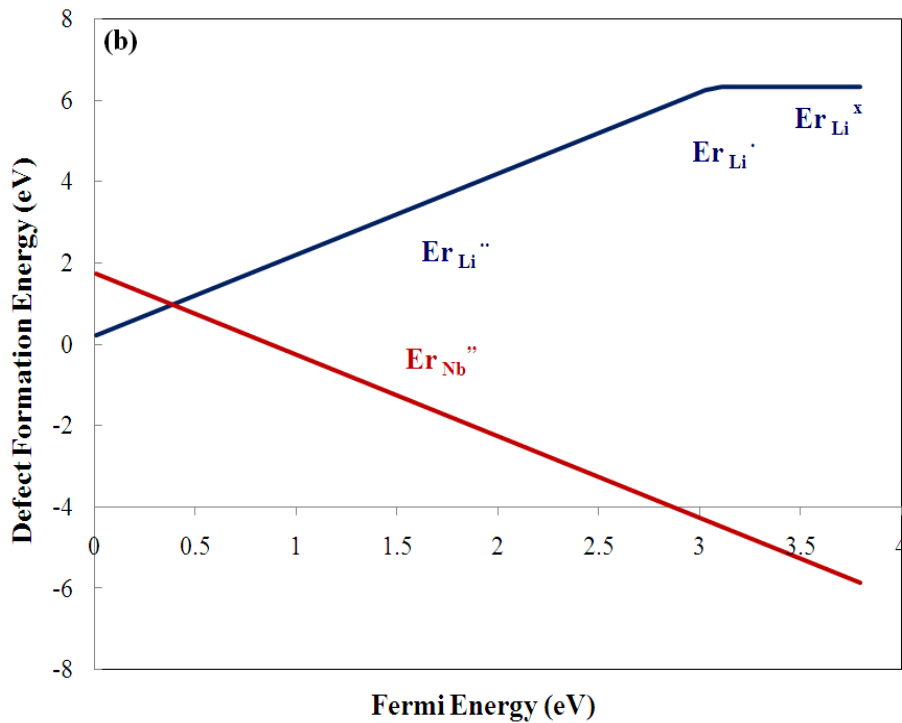
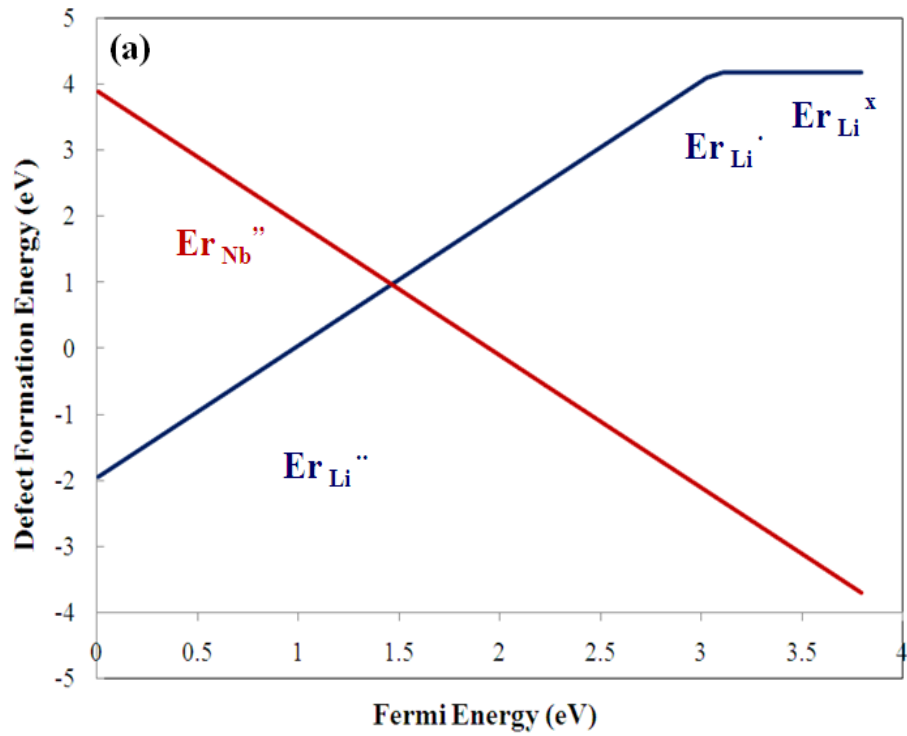


Figure 4-6. Defect formation energies of the lowest energy charge state of  $Er_{Li}$  and  $Er_{Nb}$  as a function of Fermi energy; the lowest-energy charge state is given in each case. The Fermi energy ranges from  $E_F=0$  (left) at the VBM to  $E_F=3.5$  eV at the conduction band minimum (right). (a), using  $Nb_2O_5$  as reference state. (b) using  $Li_2O$  as reference state.

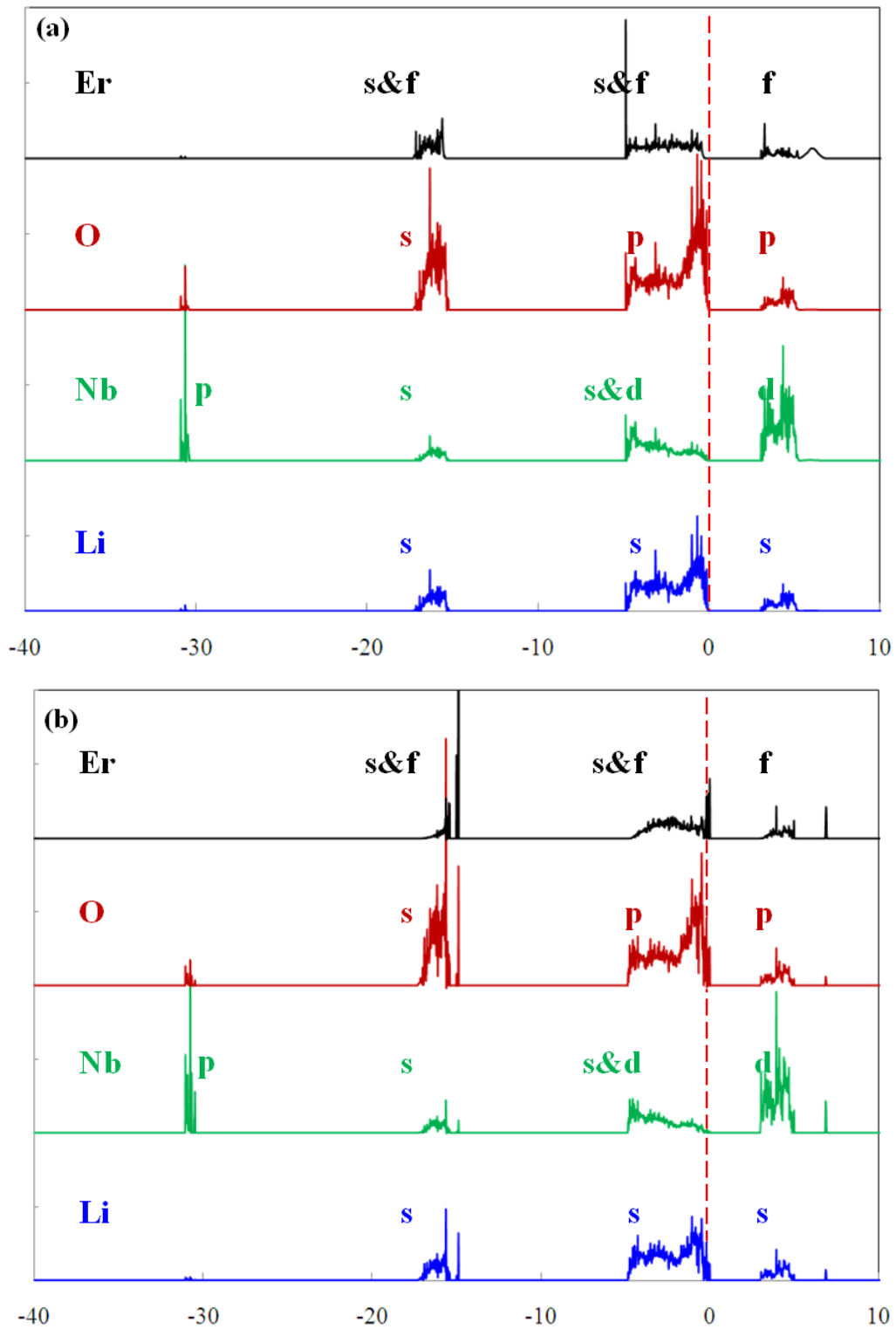
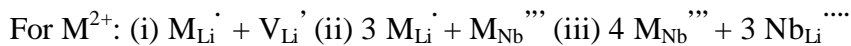


Figure 4-7. (a) Partial density of state (PDOS) for  $\text{ErLi}$ ; (b) PDOS for  $\text{ErNb}$ . The absolute values of the number of the DOS in the two figures have been rescaled to make the comparison easier.

These results are readily understood in terms of the electrostatic and elastic interactions within the system. Thus, when Er substitutes on a Li site, the repulsive electrostatic interaction between Nb and Er is greater than that between Nb and Li and thus forces the Er towards the vacancy. The ionic radii of  $\text{Li}^+$ ,  $\text{Nb}^{5+}$  and  $\text{Er}^{3+}$  are 0.76 Å, 0.64 Å, and 0.89 Å, respectively<sup>154</sup>. Therefore, the larger size of the Er ion also tends to push it closer to the vacancy; thus, both interactions push the Er towards the vacant site. By contrast, when Er substitutes on a Nb site, the smaller Er charge leads to weaker repulsion from the Li, thus tending to move the Er ion away from the vacant site. However, the larger ionic radii will again push the Er towards the vacant site. The electrostatic and elastic interactions thus tend to counteract each other, resulting in only a small net displacement.

#### 4.4.2 Defect Clusters

There are two different charge states of the impurities considered in current paper, which are  $M^{+2}$  ( $\text{Mg}^{2+}$  and  $\text{Fe}^{2+}$ ) and  $M^{+3}$  ( $\text{Er}^{3+}$ ,  $\text{Nd}^{3+}$ , and  $\text{Fe}^{3+}$ ). Depending on the charge states, different defect reactions are needed in order to maintain the overall charge balance of the system, resulting in different ratio of the charge compensation species in the system. Based on the previous studies and literatures, the following defect clusters have been considered in this study.



As in the cases of the single point defect analysis, an exemplar case of Er is presented below in full detail. Similar analyses for Mg, Nd, and Fe are given in the later part of this section, with comparison between these impurities.

For Er related defects, the current paper focuses on the following four extrinsic defect clusters that have been discussed in the literature:  $2 \text{Er}_{\text{Li}}^{\bullet\bullet} + 4\text{V}_{\text{Li}}^{\bullet} = 2(\text{Er}_{\text{Li}}^{\bullet\bullet} + 2\text{V}_{\text{Li}}^{\bullet})$ ,  $\text{Er}_{\text{Li}}^{\bullet\bullet} + \text{Er}_{\text{Nb}}^{\bullet\bullet}$ , and  $2 \text{Er}_{\text{Li}}^{\bullet\bullet} + \text{Nb}_{\text{Li}}^{\bullet\bullet\bullet\bullet}$ <sup>10, 153</sup>. Two completely separated  $\text{Er}_{\text{Li}}^{\bullet\bullet} + 2\text{V}_{\text{Li}}^{\bullet}$  cluster are considered because this approach allows all of the defect clusters to be analyzed independently of the chemical potential of the Er.

The energies of neutral defect complexes are first determined from the formation energies of the individual defects. As mentioned above, because these defects are charge neutral, their energies are independent of the location of the Fermi level. However, the DFEs of the clusters do depend on the choice of reference state. From Figure 4-8, it is can be seen that the formation energies of the  $\text{Er}_{\text{Li}}^{\bullet\bullet} + \text{Er}_{\text{Nb}}^{\bullet\bullet}$  and  $2 \text{Er}_{\text{Li}}^{\bullet\bullet} + \text{Nb}_{\text{Li}}^{\bullet\bullet\bullet\bullet}$  clusters are the independent of the reference state. This is because within  $\text{LiNbO}_3$ , the sum of chemical potentials of Li and Nb is constant for any given value of the chemical potential for oxygen. By contrast, the DFE of the  $2 \text{Er}_{\text{Li}}^{\bullet\bullet} + 4\text{V}_{\text{Li}}^{\bullet}$  and  $2 \text{Er}_{\text{Nb}}^{\bullet\bullet} + 4\text{V}_{\text{Li}}^{\bullet} + 2 \text{Nb}_{\text{Li}}^{\bullet\bullet\bullet\bullet}$  clusters do depend on the chemical potential of oxygen. Thus, their formation energies are directly influenced by the reference state of chemical potential.

Table 4-6. Defect formation energies for defect reactions under different reference states. The chemical potential of Er is assumed to be the same as the value in  $\text{Er}_2\text{O}_3$ . These value are calculated based on the single defect energy without considering association effects.

Defect Reaction	DFE(eV)	
Fully Charged	$\text{Li}_2\text{O}$	$\text{Nb}_2\text{O}_5$
$2 \text{Er}_{\text{Li}}^{\bullet\bullet} + 4\text{V}_{\text{Li}}^{\bullet}$	8.369	-4.607
$\text{Er}_{\text{Li}}^{\bullet\bullet} + \text{Er}_{\text{Nb}}^{\bullet\bullet}$	1.939	1.939
$2 \text{Er}_{\text{Li}}^{\bullet\bullet} + \text{Nb}_{\text{Li}}^{\bullet\bullet\bullet\bullet}$	4.274	4.274
$2\text{Er}_{\text{Nb}}^{\bullet\bullet} + 4\text{V}_{\text{Li}}^{\bullet} + 2 \text{Nb}_{\text{Li}}^{\bullet\bullet\bullet\bullet}$	13.039	0.064

The calculations show that the formation energy for  $2 \text{Er}_{\text{Li}}^{\bullet\bullet} + 4\text{V}_{\text{Li}}^{\bullet}$  is negative for the  $\text{Nb}_2\text{O}_5$  reference state. This result is similar to the previously studied intrinsic  $\text{Nb}_{\text{Li}}^{\bullet\bullet\bullet\bullet} + 4 \text{V}_{\text{Li}}^{\bullet}$  cluster.

Under  $\text{Nb}_2\text{O}_5$ -rich conditions, the  $2 \text{Er}_{\text{Nb}}^{\bullet\bullet} + 4\text{V}_{\text{Li}}^{\bullet} + 2 \text{Nb}_{\text{Li}}^{\bullet\bullet\bullet\bullet}$  cluster has a very small positive

formation energy, and might thus be expected to also be observed. The calculations also predict that for the  $\text{Li}_2\text{O}$  reference state,  $\text{Er}_{\text{Li}}^{\bullet\bullet} + \text{Er}_{\text{Nb}}^{\bullet\bullet}$  has the lowest DFE. However, the DFE is positive, which indicates energy is required to create the defects under conditions such as VTE. Based on the thermodynamic calculation, the concentration of such defects at room temperature should be very low.

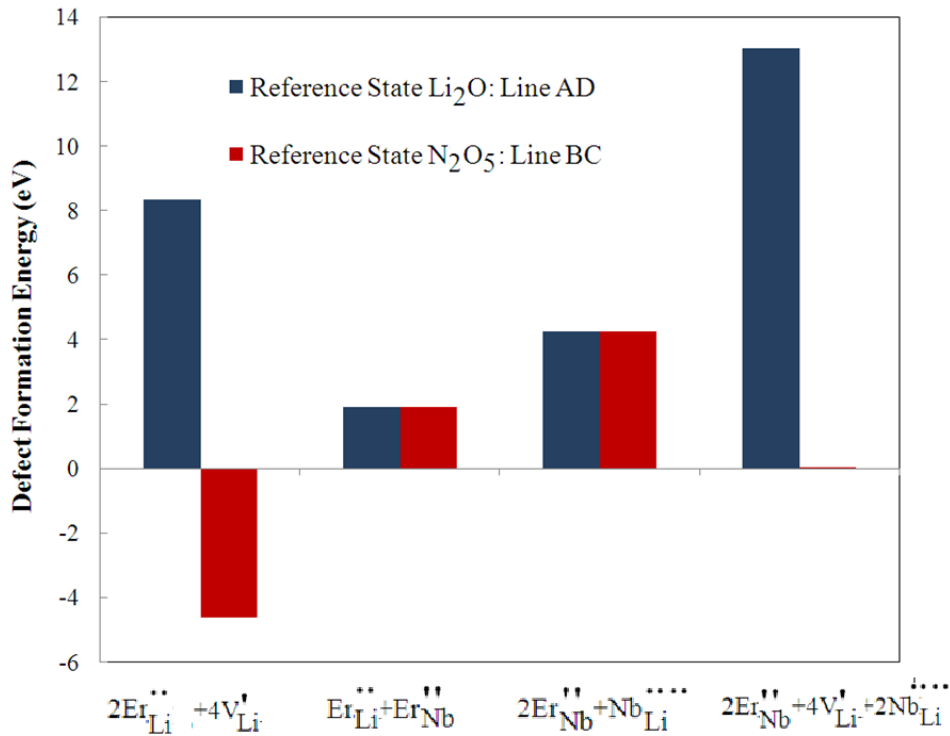


Figure 4-8. Formation energies of Er-related defect clusters under  $\text{Li}_2\text{O}$  rich conditions (blue) and  $\text{Nb}_2\text{O}_5$  rich conditions (red).

To this point, the calculations have assumed that the individual defects that form a defect cluster are infinitely far away from each other; that is, there are no interactions between them. However, due to the charge and elastic interactions induced by the differences in ionic radii, defect association can be expected to change the DFEs. Here, the case of  $\text{Er}_{\text{Li}}^{\bullet\bullet} + 2\text{V}_{\text{Li}}^{\bullet}$  is analyzed. While there are an almost innumerable number of possible different compensating structures, it is only necessary to analyze the limiting case of association, in which some of the compensating

vacancies are in the first neighbor shell while all of the others are far from the Er defect. Cases in which vacancies lie in the second or third shell or beyond can be assumed to have lower association energies. There are six Li sites in the first nearest neighbor (FNN) shell around the Er-occupied Li site, as indicated in Figure 4-9.

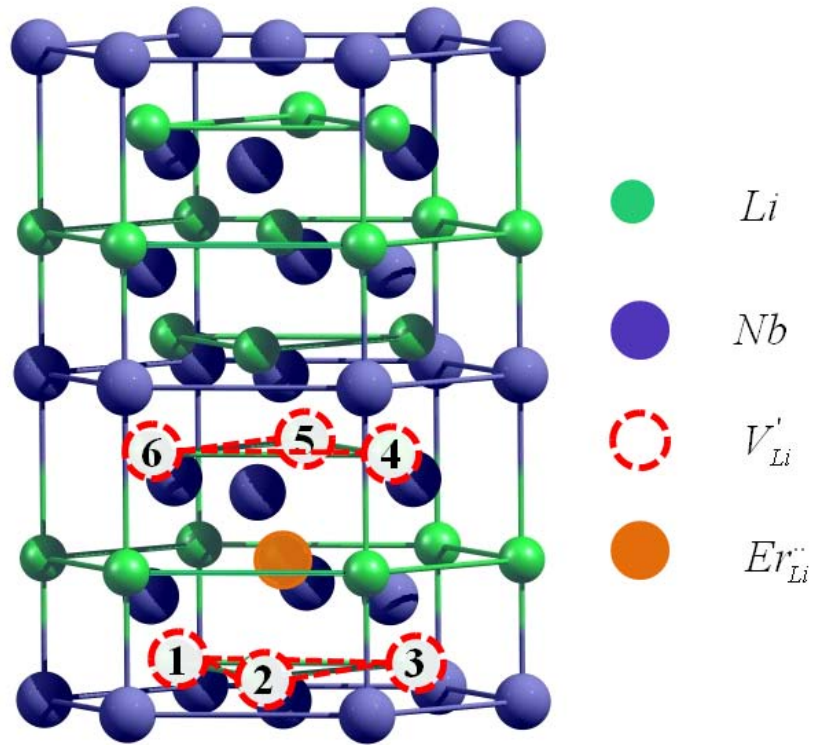


Figure 4-9. Possible lithium vacancy positions in the first nearest neighbor (FNN) around Er sitting on lithium site. The oxygen sub-lattice is not shown.

The arrangement of the Li vacancies can conveniently be divided into three categories:

A0: No lithium vacancies in the FNN shell;

A1: One lithium vacancy in the FNN shell;

A2: Two lithium vacancies in the FNN shell;

In the A0 structure there is no association of the vacancies; this is the case analyzed above and found to have negative formation energy for the  $Nb_2O_5$  reference state. For A1, there are two distinct configurations for one lithium vacancy sitting around the Er site. The lithium

vacancy could lie above the Er ion (4 or 5 or 6 in Figure 4-9) or below the Er ion (1 or 2 or 3 in Figure 4-9). For the A2 case, there are  $C_6^2 = 15$  possible configurations of vacancies. However, due to the three-fold rotational symmetry around the  $\text{Er}_{\text{Li}}''$  only four of these configurations are crystallographically distinct. The four different arrangements are 1-2, 1-4, 4-5, and 2-5 in Figure 4-9.

As illustrated in Figure 4-10, the energy of the A1 structure is lower than that of the A0 structure, while the energy of the A2 structures are lower yet by 0.068 eV/defect (i.e., -0.204 eV for the total cluster). These results indicate an attractive interaction between  $\text{Er}_{\text{Li}}''$  and  $\text{V}_{\text{Li}}'$ , which is consistent with the conjecture of Dierolf *et al.*<sup>143</sup> that  $\text{Er}_{\text{Li}}''$  is compensated by a  $\text{V}_{\text{Li}}'$  close to  $\text{Er}_{\text{Li}}''$ .

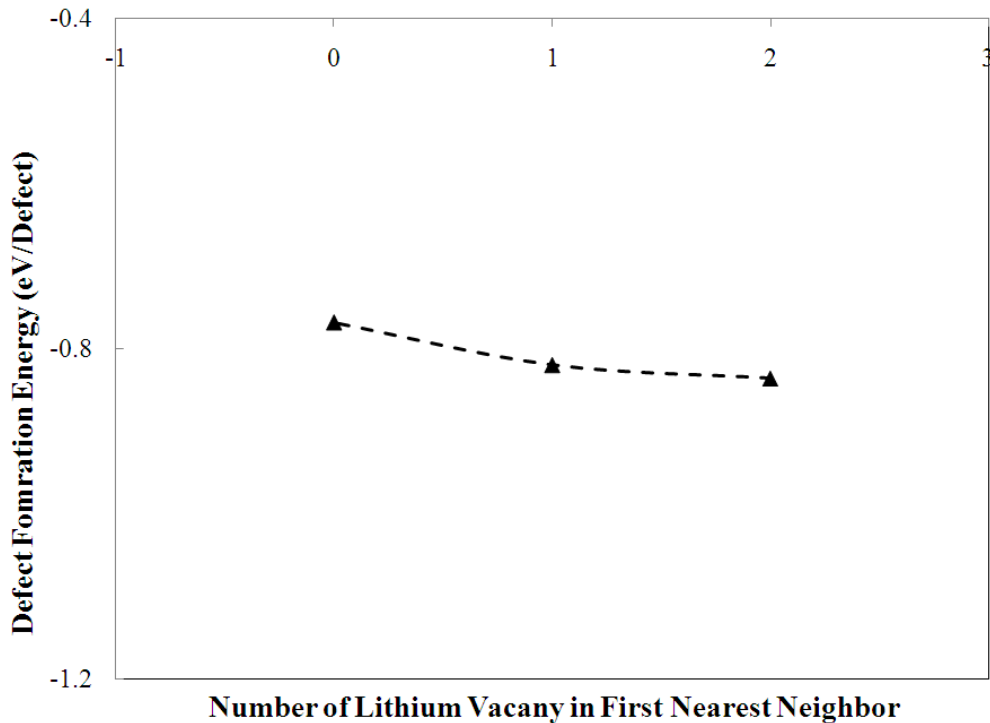


Figure 4-10. Defect formation energy for  $\text{Er}_{\text{Li}}'' + 2\text{V}_{\text{Li}}'$  shows the effects of association of the lithium vacancies around  $\text{Er}_{\text{Li}}''$  site.

Since this association energy is relatively small ( $\sim 2.5 k_B T$ ), it might be supposed that the structures of a defect cluster could fluctuate dynamically among various symmetry equivalent configurations. However, our DFT calculations show that the migration barrier for the diffusion of a lithium vacancy between the first nearest neighbor in the lithium sublattice is 1.63 eV, which is consistent with the experimental value of 1.55 eV<sup>139</sup> and 1.62 eV<sup>140</sup> for the ionic conductivity. These values of activation energies indicate that the transitions among configurations are relatively difficult. However, lithium vacancy can still move a considerable distance during long time annealing. For example, experimentally stoichiometric LiNbO<sub>3</sub> has been annealed at 250 °C for 5 hours<sup>143</sup>. It is assumed that the vibration energy  $h\nu_0$  is equal to the thermal energy  $k_B T$ . The jump distance between first nearest neighbors is 3.771 Å. Under such condition, the diffusivity of lithium vacancy is calculated to be  $7.07 \times 10^{-18}$ , which compares reasonably well with previous estimates of  $5.97 \times 10^{-16}$ , (Mehta *et al.*<sup>139</sup>) and  $4.46 \times 10^{-17}$  (Halstead *et al.*<sup>140</sup>). The average diffusion distance can then be calculated in the usual manner:

$$x = \sqrt{6Dt} \quad [4-1]$$

where  $x$  is the average diffusion distance,  $D$  is the diffusivity and  $t$  is the diffusion time. Using the above value of diffusivity, the average diffusion distance is 5.7 nm (this work), 80.3 nm (Mehta *et al.*<sup>139</sup>), and 21.9 nm (Halstead *et al.*<sup>140</sup>). The average diffusion distance in the order of tens of nanometers indicates the lithium vacancy can still travel and change the configurations of the defect complex. The calculation is in agreement with the experimental observation that the relative peak emission intensities have been modified by the annealing of the sample<sup>143</sup>.

Similar analyses have been applied to Mg, Nd, and Fe impurities. A summary of the formation energies of these impurities under Nb<sub>2</sub>O<sub>5</sub> reference state with possible different charge states is given in Figure 4-11.

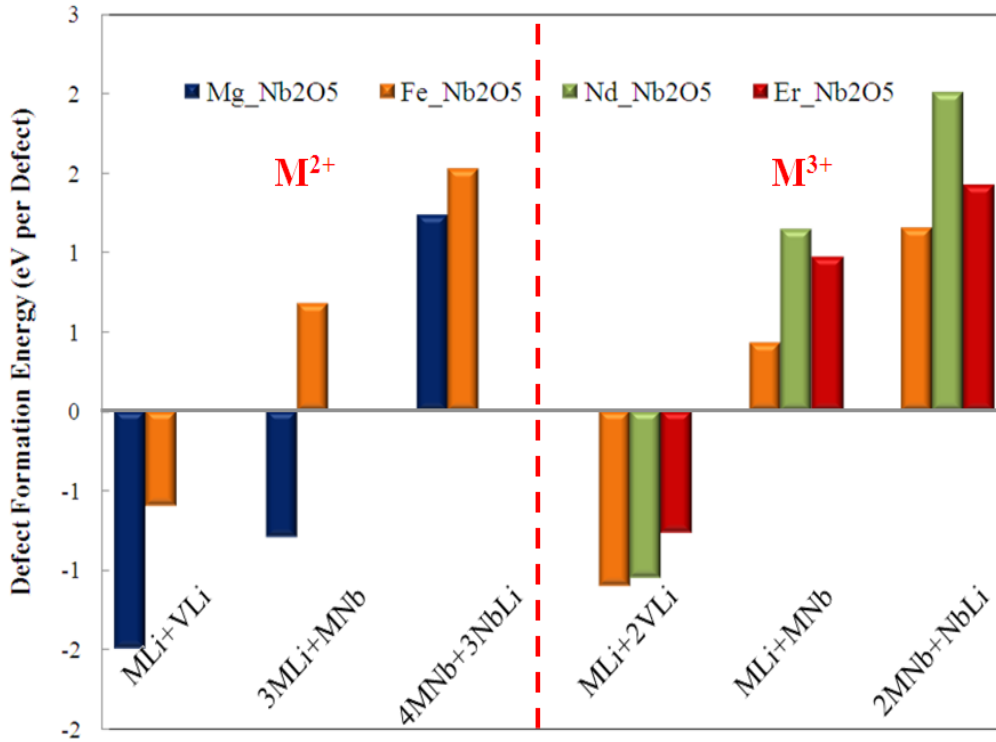


Figure 4-11. Defect formation energies of various possible defect reactions for impurities under Nb<sub>2</sub>O<sub>5</sub> reference state.

It is noted that under Nb<sub>2</sub>O<sub>5</sub> reference state, the impurities sitting on the lithium site compensated by the lithium vacancies have the lowest formation energies compared with other types of defect clusters. Similar to the intrinsic defects situation, the formation energies are negative, which indicates the Nb<sub>2</sub>O<sub>5</sub> may not accurately represent the experimental conditions. However, as the reference state moves from Nb<sub>2</sub>O<sub>5</sub> towards Li<sub>2</sub>O, the formation energies of the defect clusters increases and impurities on lithium site compensated by lithium vacancies remains dominant over a certain range of the chemical potentials. This is because the relative stability orders of defects will remain as chemical potential change all of them in a similar way.

It is found that the formation energy for Mg sitting on both sites is also negative albeit less negative than the defect cluster consisting of Mg on lithium site compensated by lithium vacancies, unlike the other impurities. This indicates the tendency for Mg to sit on both sites is higher than for Fe, Er and Nd impurities. As for iron, both  $\text{Fe}^{2+}$  and  $\text{Fe}^{3+}$  on lithium site compensated by lithium vacancies are possible, as formation energies of both defect reactions are negative. However,  $\text{Fe}^{3+}$  is more energetically favorable. This suggests that Fe-doped  $\text{LiNbO}_3$  may have different charge states of iron and the concentration of  $\text{Fe}^{3+}$  is higher than  $\text{Fe}^{2+}$ .

The formation energies of impurities given in Figure 4-12 are under  $\text{Li}_2\text{O}$  reference state, which corresponds to the experimental condition of stoichiometric  $\text{LiNbO}_3$ .

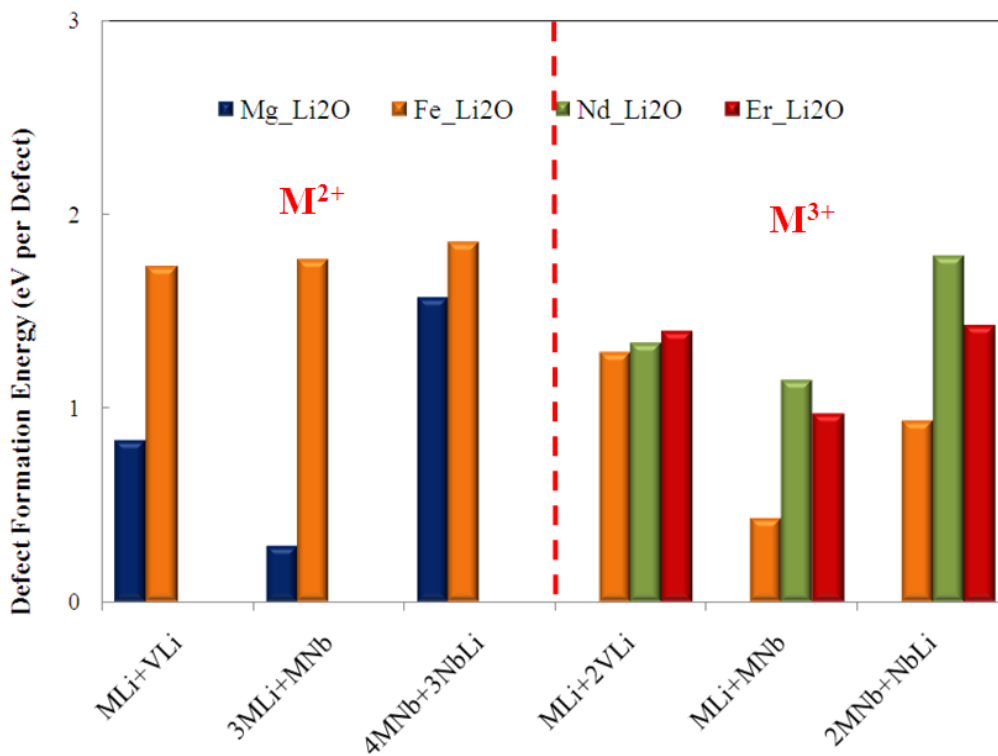


Figure 4-12. Defect formation energies of various possible defect reactions for impurities under  $\text{Li}_2\text{O}$  reference state.

As the figure shows, all the defects have positive formation energies, which is consistent with the stoichiometric composition as the defect concentration is very small based on energy

calculations. By comparing different defect clusters, it is found that impurities occupying both sites have the lowest energy for both  $M^{2+}$  and  $M^{3+}$ . Similar to the  $Nb_2O_5$  cases,  $Fe^{3+}$  is more energetically favorable than  $Fe^{2+}$ . The detailed discussion between these calculation and experimental evidence is given in section 4.6.

#### 4.5 Charge Transfer Levels

A charged crystallographic defect associated with one or more electrons could absorb visible light, so that usually transparent materials could become colored. This involves a charge transfer process, which generally absorbs or emits certain wavelength of light. The charge transfer level, also called the optical level, is similar to the thermodynamic transition level defined previously. However, they differ in the atomic configuration of final charge state. For the thermodynamic transition level, the atomic configuration of final charge state is fully relaxed. For the charge transfer level, the final state is calculated based on the configuration of the initial charge state. This is because the electron movement is much faster than the atomic relaxation and the transition from one charge state to the other can be considered spontaneous.

The concept of calculating charge transfer levels is shown in Figure 4-13. Electrons in the conduction band can recombine with a hole on the acceptor, which leads to emission of a photon with energy  $E_{PL}$ . This photon can be experimentally observed and measured, for instance, using photoluminescence or absorption spectroscopy. During this process, the atomic configuration of the donor remains unchanged. The energy difference between this configuration and fully relaxed configuration is the relaxation energy,  $E_{rel}$ , which is also termed as Franck-Condon shift<sup>118</sup>.  $E_A$  is the thermal ionization energy of the acceptor<sup>118</sup> and  $E_g$  is the band gap of the bulk material.

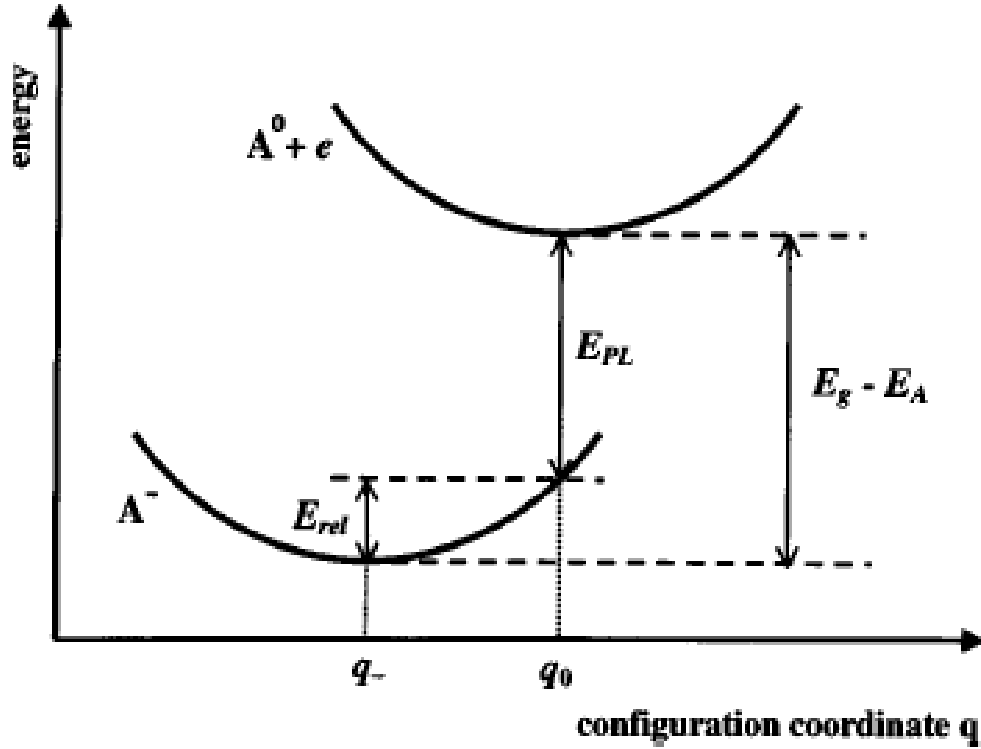


Figure 4-13. Schematics of calculations of charge transfer levels.  $E_{PL}$  is the charge transfer energy,  $E_{rel}$  is Franck-Condon shift,  $E_g$  is the band gap, and  $E_A$  is the thermal ionization energy<sup>118</sup>.

The thermal ionization energy, or the energy required to remove one electron from dopant at a particular charge state in  $\text{LiNbO}_3$ , can be calculated using the following equation:

$$E_A = E_{tot}[M_{Li}^{2+}] - E_{tot}[M_{Li}^{3+}] + E_{corr} - E_v - \Delta V \quad [4-2]$$

where  $E_{tot}[Er_{Li}^{2+}]$  is the energy of the supercell containing an dopant at lithium site with +2 charged.  $E_{tot}[Er_{Li}^{3+}]$  is energy of the supercell containing an dopant at lithium site with +3 charged.  $E_{corr}$  is the energy difference between the highest occupied state at the  $\Gamma$  point and the special k-point, where the band energy is lower than at the  $\Gamma$  point<sup>118</sup>. This term is needed because the electrons should be removed from the top of the valence band at the  $\Gamma$  point while the electron is actually taken out of the highest occupied Kohn-Sham level at the special k point in the supercell calculations.  $E_v$  is the valence band maximum of the bulk materials in the

calculation, and  $\Delta V$  is the electrostatic potential difference between the two supercells. The thermal ionization energy of  $\text{Fe}^{2+}$  in  $\text{LiNbO}_3$  is calculated to be 1.836 eV, which is consistent with the previous estimates <sup>181</sup>.

The comparison between theoretical calculations and experimental PL measurement of Fe-doped  $\text{LiNbO}_3$  is given in Table 4-7. It is seen that the value of  $E_{\text{PL}}$  measured from PL experimental is  $\sim 1.4$  eV <sup>182</sup>. The charge transfer level ( $E_{\text{PL}}$ ) of  $\text{Fe}^{2+}/\text{Fe}^{3+}$  has been calculated to be 1.34, which is in excellent agreement with experimental value. This confirms the long-time conjecture that there is a charge transfer effect in the Fe-doped  $\text{LiNbO}_3$ . However, due to the well-known problem of underestimation band gap using DFT, the results have to be treated with caution. A detailed discussion is given in section. 4.6.2.

Table 4-7. Charge transfer level of impurities calculated by GGA with comparison of experiments.

All units in eV	$\text{Fe}^{2+}/\text{Fe}^{3+}$	$\text{Mg}^{1+}/\text{Mg}^{2+}$	$\text{Nd}^{2+}/\text{Nd}^{3+}$	$\text{Er}^{2+}/\text{Er}^{3+}$
$E_{\text{A}}$	1.84	3.42	3.38	2.75
$E_{\text{g}}$	3.5	3.50	3.50	3.50
$E_{\text{PL}}$	1.34	0.06	0.12	0.75
$E_{\text{rel}}$	0.33	0.04	0.01	0.00
Experiment	1.4 <sup>182</sup> /1.6 <sup>183</sup>	No Associated Peak <sup>184</sup>	No Associated Peak <sup>185</sup>	0.80 <sup>186</sup>

Using a similar approach, the charge transfer levels are calculated for Mg, Nd, and Er. The results of the calculations are given in Table 4-7. It is noted that for both Mg and Nd, the thermal ionization energies are relatively large and close to the calculated band gap, which result in the  $E_{\text{PL}}$  being very small. These small values of  $E_{\text{PL}}$  correspond to very long wavelengths, beyond those experimentally accessible. Consistent with this, no associated peak has been experimentally reported.

The Er charge transfer levels are an interesting case. It is found that the calculated value of  $E_{\text{PL}}$  is 0.75 eV while there is a experimental peak at 0.80 eV, which is equivalent to 1540 nm <sup>186</sup>. <sup>187</sup>. However, the calculation and experiments are believed to describe different process. The

experimental peak at 1540 nm has been concluded to be the transition from  ${}^4I_{15/2}$  to the ground state  ${}^4I_{13/2}$ . These two states differ only in the total spin number. Therefore, it can be considered as the local rearrangement of the electrons, which does not involve any charge transfer effects.

On the other hand, the calculated  $E_{PL}$  simulate a process in which electrons in the conduction band jump into the charge transfer level. Therefore, in order for this process to happen, it is necessary for conduction band to have electrons. For Fe-doped, there are both  $Fe^{2+}$  and  $Fe^{3+}$  in the materials<sup>182, 183</sup>, therefore, there are electrons at the charge transfer level, which is relatively close to the conduction band and which can be excited easily. For Er charge transfer, there is no  $Er^{2+}$  in the system. Thus the incident light energy should have an energy equal to or higher than the band gap to excite electron from the valence band to conduction to conduction band. However, the experimental incident light usually has a wave length longer than 440nm<sup>182, 186</sup>, which is less than the band gap. Thus, there are no electrons in the conduction band and the charge transfer level can not be observed from experiments.

## 4.6 Discussions

### 4.6.1 Er Doped $LiNbO_3$

The principal conclusions of this work are that (i) the Er dopant sits on the Li sites, (ii) various slightly different microstructural configurations of Er sites exist<sup>143</sup>, and (iii) charge compensation is provided by Li vacancies for  $Li_2O$ -rich conditions or (iv) by Er on Nb sites under  $Nb_2O_5$ -rich conditions. We briefly examine the experimental evidence relevant to each of these predictions.

(i) XSW studies<sup>39, 40</sup> found that Er occupies a Li site with C3 point symmetry, but that it is shifted from the ferroelectric Li position by 0.46 Å along the uniaxial direction of the hexagonal structure. ESR<sup>4</sup> identified a single site for  $Er^{3+}$  ions, but could not distinguish whether it is Li site or Nb site. Rutherford backscattering<sup>38</sup> and EXAFS<sup>41</sup> also yielded  $Er^{3+}$  substituting

for Li ions, while ion beam channeling<sup>152</sup> indicate that Er may occupy both Li and Nb sites. The DFT calculations predicted that Er primarily sits on the Li site under both Li<sub>2</sub>O-rich and Nb<sub>2</sub>O<sub>5</sub>-rich conditions, but with different concentrations based on the difference values of the DFEs. The site is predicted to be shifted along the -Z direction by 0.17 Å. This is consistent with the experimental data measured using XSW and EXAFS which show Er occupies the Li site and moves along -Z direction. However, the magnitude of displacement is quite different. Possible reasons for this is discussed in section 4.4. The case of Er site on both Li and Nb site, which is relevant to ion beam channeling, is discussed in (iv).

(ii) Optical and magnetic resonance spectroscopy revealed multiple slightly different sites for the Er ion.<sup>143, 188</sup> Baumann *et al.* using XSW and optical spectroscopy<sup>43</sup> found that there are four energetically distinguishable sites for Er, resulting from different local environments. Gill *et al.*<sup>45, 46</sup> using total site selective spectroscopy reported six different sites. Furthermore, Dierolf *et al.*,<sup>143</sup> by combining excitation emission as well as absorption, emission, and Raman spectroscopy (CEES), found a large number (>11) of different Er<sup>3+</sup> sites. Moreover, the results of Dierolf *et al.*<sup>143</sup> suggest that the charge compensation can be classified into two categories: a first close compensation which influences the local symmetry of the Er-defect and a secondary probably somewhat further away which influences the local electric field along the z-axis. The inclusion of a second more distant charge compensating Li vacancy further increases the number of potential sites as well. These different arrangements are associated with different local and distant charge compensation species. A2 arrangements (see Sec. 3.B) are considered as the first category while A1 and A0 arrangements fall into the second category. The experimental structure analysis supports there are many slightly different sites for Er<sup>3+</sup>. When considering only lithium vacancies around the Er<sup>3+</sup> site, seven different configurations could be identified using

DFT calculations. If the presence of impurities, niobium antisites, Er-Er cluster or even domain walls were to be considered, the number of different  $\text{Er}^{3+}$  site would be considerably larger. The optical spectroscopy measurements show that the relative number of differently charge compensated Er ions depends on the stoichiometry of the sample. While in congruent samples the more perturbed A2 type arrangements dominate, in stoichiometric samples the less perturbed arrangements are more prominent. Furthermore, under domain inversion at room temperature during which the charge compensating defects are immobile, drastic changes are observed for some defect configurations and no changes are observed for others. In particular, the majority defect configuration in stoichiometric samples remains unchanged (aside from a small spectral shift). For this reason, it is likely that this defect has distant charge compensation as described by configuration A0.

(iii) A consensus as to the precise nature of the charge compensation mechanism for  $\text{Er}_{\text{Li}}^{\bullet\bullet}$  has not yet been achieved. It has been reported by Gill *et al.*<sup>46</sup> that the site redistribution associated with an increase in Er concentration is very similar to that associated with an increase in Li deficiency, which indicates that  $\text{Er}_{\text{Li}}^{\bullet\bullet}$  is compensated by lithium vacancies<sup>143, 189</sup>. This is based on the fact that for congruent  $\text{LiNbO}_3$ , lithium vacancies already exist in the material<sup>136, 190</sup>. Therefore, it is much easier for  $\text{Er}^{3+}$  to occupy a vacant site. The DFT calculations predicted that under  $\text{Nb}_2\text{O}_5$ -rich conditions, which includes ambient temperature and oxygen partial pressure, the dominant defect are  $\text{Er}_{\text{Li}}^{\bullet\bullet}$  compensated by  $\text{V}_{\text{Li}}^{\bullet}$  based on the formation energies, which provides theoretical support to this conjecture. It could also explain the observation that increasing the Er concentration tends to increase the Li deficiency in the crystal.

(iv) No direct observation for  $\text{Er}_{\text{Nb}}^{\bullet\bullet}$  has been reported, although ion beam channeling indicates that Er may occupy a Nb site<sup>152</sup> and electron paramagnetic resonance (EPR) indicates

Er sits on both Li and Nb site <sup>191</sup>. This absence may be partially due to the methods to incorporate the Er ions into the crystal. The Er<sup>3+</sup> doping is often achieved during Czochralski growth or diffusion-doping <sup>43</sup>, the latter involving the diffusion of Er ions into congruent LiNbO<sub>3</sub>. It has been reported that the diffusion of Er<sup>3+</sup> is through the Li-sublattice <sup>142, 192</sup>. The diffusion of Nb was also found to be much slower than that of lithium vacancies <sup>142, 193, 194</sup>. Therefore, it is probably much easier for a Er ion to move into a Li sublattice and stay there rather than to push Nb ions off their lattice sites during these kinetic processes; this would make the incorporation of Er on a Nb site difficult.

Furthermore, both Czochralski growth and diffusion doping predetermine the dominant defects to Er on Li site compensated by lithium vacancies. These existing defects can be expected to play a significant role when the sample is converted to the stoichiometric composition using VTE under Li<sub>2</sub>O rich conditions. Taking nearly stoichiometric Li<sub>0.498</sub>Nb<sub>0.5+x</sub>O<sub>3</sub> for example, after VTE process the concentration of lithium vacancy is still 0.4 %. If we assume that the lithium vacancies are primarily compensated by Er<sub>Li</sub><sup>••</sup>, 0.2 % of Er<sub>Li</sub><sup>••</sup> would be required. The system would thus be equivalent to 0.2 mol % Er:LiNbO<sub>3</sub>. Since the concentration of Er<sub>Li</sub><sup>••</sup> and Er<sub>Nb</sub><sup>••</sup> is a constant, the concentration Er<sub>Nb</sub><sup>••</sup> of can be calculated from the mass-action law as:

$$[Er_{Li}^{••}] \times [Er_{Nb}^{••}] = \exp(-\Delta G_f / kT) \quad [4-3]$$

where,  $\Delta G_f$  is the defect formation energy,  $k$  is the Boltzmann constant, and  $T$  is the temperature in Kelvin. At the room temperature, the concentration of Er<sub>Nb</sub><sup>••</sup> is estimated to be  $9.7 \times 10^{-26}$ , which are  $\sim 23$  orders of magnitude smaller than Er<sub>Li</sub><sup>••</sup>. Increasing the temperature will increase the concentration of Er<sub>Nb</sub><sup>••</sup>, such that at 800 K, the concentration of Er<sub>Nb</sub><sup>••</sup> is calculated to be  $1.01 \times 10^{-5}$ . However, this is still two orders of magnitude smaller than the concentration of

$\text{Er}_{\text{Li}}^{\bullet\bullet}$ . Thus, compared to the concentration of  $\text{Er}_{\text{Li}}^{\bullet\bullet}$ , the  $\text{Er}_{\text{Nb}}^{\bullet\bullet}$  concentration is negligible. These calculations indicate that even a small lithium vacancy concentration could significantly affect the defect chemistry of the system. Furthermore, it may provide an explanation why the Er on Nb site has not been observed.

#### 4.6.2 Fe Doped LiNbO<sub>3</sub>

The key findings about Fe-doped LiNbO<sub>3</sub> from DFT calculations are the following. (i) Fe prefers to occupy a lithium site, compensated by lithium vacancies for the Nb<sub>2</sub>O<sub>5</sub> reference state and by Fe on a niobium site for the Li<sub>2</sub>O reference state; (ii) Fe<sup>3+</sup> is more energetically favorable than Fe<sup>2+</sup>; (iii) There is a charge transfer level provided by iron at the position of 1.4 eV below the conduction band.

(i) In spite of extensive efforts to determine the occupied site of iron using various techniques, such as optical absorption<sup>195</sup>, electron spin resonance (EPR)<sup>196</sup>, Mossbauer spectroscopy<sup>36,37</sup>, and Proton Induced X-ray Emission (PIXE)<sup>42</sup>, no experimental consensus has yet emerged. Most of the studies suggest that iron occupies a lithium site, which is supported by electron nuclear double resonance (ENDOR)<sup>35</sup>, PIXE<sup>42</sup>, X-ray standing waves<sup>197</sup>, and X-ray absorption fine structure analysis<sup>198</sup>. On the contrary, several studies using EPR and ESR claim that iron occupies the niobium site<sup>196,197</sup>. In addition, there are some studies that support a two-site model, in which iron occupies both lithium and niobium sites<sup>199</sup>. Our calculations have shown that iron on a lithium site is favorable under both Nb<sub>2</sub>O<sub>5</sub> and Li<sub>2</sub>O rich conditions, but with different charge compensation mechanisms. Under Nb<sub>2</sub>O<sub>5</sub> reference state, in which the intrinsic defects are predicted to be niobium antisites compensated by lithium vacancies and a congruent composition is formed, the compensating defects are lithium vacancies. This supports the studies using ENDOR, PIXE, X-ray related techniques<sup>35,42,197</sup>. Under Li<sub>2</sub>O rich conditions, which

correspond to growth condition of stoichiometric  $\text{LiNbO}_3$ , the compensation mechanism is considered as Fe on a niobium site. However, since the dopants are usually introduced into system through a diffusion process on a congruent sample, it is very difficult to observe iron on a niobium site due to existing intrinsic defects. Similar discussions about how the growth method, impurities introduction process, and the intrinsic defects may affect the dominant defects have been given in section 4.6.1. Overall, the DFT calculations indicate that by controlling the experimental condition or the composition of the material, the site occupancy of the iron can be altered.

(ii) As a transition metal, iron ions have different valence charges ( $\text{Fe}^{2+}$  and  $\text{Fe}^{3+}$ ), which is also the case in Fe-doped  $\text{LiNbO}_3$ . In most of the studies, the concentration of iron is very low<sup>182, 183</sup>. Furthermore, the concentration of  $\text{Fe}^{2+}$  is usually at least one order of magnitude lower than  $\text{Fe}^{3+}$  concentration<sup>182</sup>. Although the concentration ratio of  $\text{Fe}^{2+}/\text{Fe}^{3+}$  can be varied using thermal treatments or other types of technique<sup>182, 200</sup>, the naturally occurred concentration ratio of  $\text{Fe}^{2+}$  and  $\text{Fe}^{3+}$  indicates that  $\text{Fe}^{3+}$  is more stable. DFT calculations show that the defect reactions involved with  $\text{Fe}^{3+}$  have lower formation energies than the reactions involve with  $\text{Fe}^{2+}$ , which corroborates experimental observation.

(iii) The  $\text{Fe}^{2+}/\text{Fe}^{3+}$  charge transfer level is then calculated to be 1.34 eV below the conduction band using the calculated band gap of 3.5 eV. (Figure 4-14) However, as indicated previously, the band gap is 0.28 eV lower than the experimental value. The difference also represents the possible error bar in the charge transfer level. Using the experimental value of the band gap (3.78 eV<sup>115, 116</sup>), the charge transfer level will be 1.62 eV. The experimental photoluminescence measurement of peak associated with iron is determined to be 1.4 eV at temperatures below 300K and for various iron concentrations<sup>182</sup>. With treatment at 520 °C in

lithium carbonate, a luminescence band at 770 nm (which is equivalent to 1.7 eV) due to iron center has been observed<sup>183</sup>. The difference between the experiments also indicates the difficulty of determining this value. However, both values fall into the range predicted by DFT calculations. Therefore, the DFT calculations confirm the long-time conjecture that the peak is associated with charge transfer between Fe<sup>2+</sup> and Fe<sup>3+</sup>.

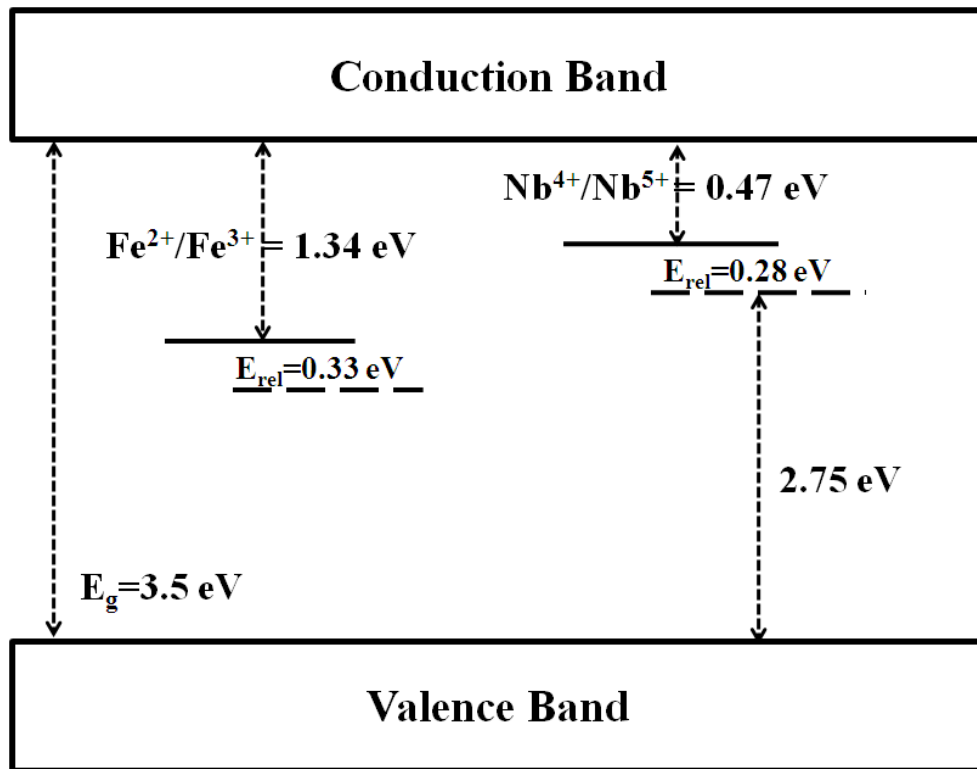


Figure 4-14. The relative position of Fe<sup>2+</sup>/Fe<sup>3+</sup> charge transfer level with regard to the band gap.

## CHAPTER 5 POINT DEFECTS IN CERIA-BASED ELECTROLYTES

### 5.1 Solid Oxide Fuel Cell Electrolytes

The first test of a solid oxide electrolyte for solid oxide fuel cells (SOFCs) was carried out in the 1930s. Since then, research has focused on finding an appropriate electrolyte. To be used in practical applications, solid electrolytes need to satisfy several major requirements, which include a high ionic conduction, negligible electronic conduction, and thermodynamic stability over a wide range of temperature and oxygen partial pressure. In addition, solid electrolytes must have a thermal expansion compatibility with electrodes and suitable mechanical properties<sup>50</sup>.

Among various electrolytes, yttria-stabilized zirconia (YSZ)<sup>51-54</sup> has been most extensively investigated and is widely used. Compared with other solid electrolytes, YSZ exhibits a very low electronic contribution to total conductivity in the oxygen partial pressure range most important for practical applications<sup>50</sup>. However, YSZ electrolytes require a very high operating temperature (~1000 °C), which could cause many interface reactions such as the interaction between solid electrolytes and electrodes. Thus, research focus on other potential electrolyte materials is of great interest.

As an alternative to YSZ, doped ceria<sup>56-59</sup> has been the subject of a great deal attention due to its higher ionic conductivity than that of YSZ. The electrical conductivity of  $\text{Ce}_{0.80}\text{Gd}_{0.20}\text{O}_{1.9}$  (gadolinia-stabilized ceria) is about one order of magnitude higher than that of YSZ in the intermediate temperature (IT) range (500°C-700°C) (Figure 5-1). Although  $\text{Bi}_2\text{O}_3$ -based materials showed even higher ionic conductivity than YSZ and doped ceria, these materials are unstable at high temperatures and low partial pressures<sup>60</sup>, which have severely limited their applications.

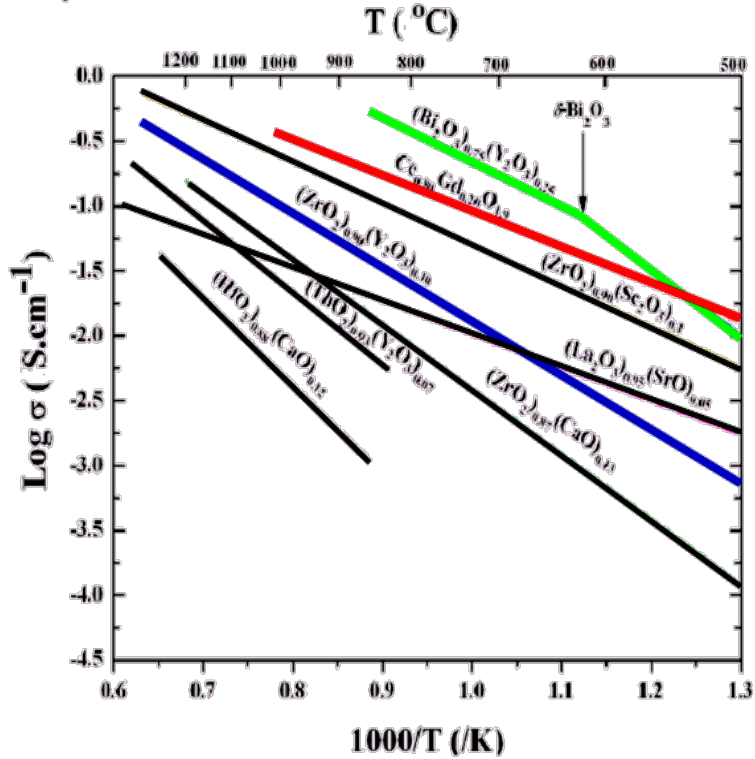


Figure 5-1. Electrical conductivity of various electrolytes as a functional of temperature <sup>201</sup>.

The higher ionic conductivity of ceria-based electrolytes with respect to YSZ is the main advantage for their use in SOFCs. However, the doped ceria systems undergo reduction under low oxygen partial pressures, and the magnitude of electrical conductivity and stability are greatly dependent on the type and concentration of dopants <sup>55</sup>. Overall, ceria-based electrolyte shows considerable potential for practical application.

## 5.2 Structure of Ceria-Based Materials

Ceria has a fluorite structure (space group: Fm-3m, Figure 5-2) which can be considered as an anion cube cage encapsulated in a face centered cubic (FCC) cation lattice (Fig 5-2). In the lattice, Ce-atoms sit at the corner of the cubic lattice, while the O-atoms sit at the tetrahedral sites. This indicates that each Ce-atom is coordinated with eight O-atoms and each O-atom is coordinated with four Ce-atoms. From the radius ratio calculation  $r_{\text{Cation}} / r_{\text{Anion}} = 0.8347$  (crystal radius for cerium and oxygen are 1.01 and 1.21 Å respectively <sup>202</sup>), which falls in the 0.732-1

regime. Therefore, the cubic arrangement of the O-atoms around the Ce is consistent with the model established by Pauling<sup>203</sup>.

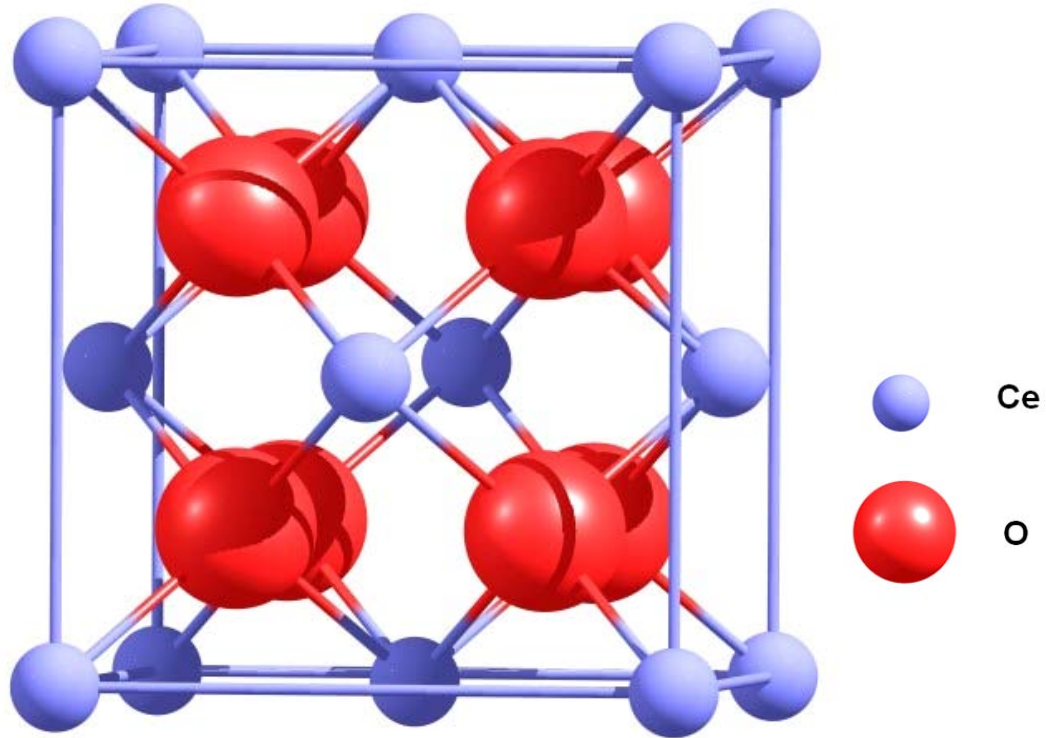


Figure 5-2. Schematics of fluorite structure for CeO<sub>2</sub>.

Another instructive way of describing the crystal structure is by looking at the stacking sequence through different planes. Figure 5-3 shows the Kagome<sup>204, 205</sup> net formed by Ce-atoms. As the Ce-atoms forming the net are in different planes, a shift vector is needed to relate the projected positions of Ce-atoms in different planes. Thus, from the atomic positions, one can identify Ce-atoms belonging to different planes in the net.

The ceria unit cell contains four ceria-molecules ( $Z = 4$ ). Considering the cation as reference, the location of the atoms, site symmetry, multiplicity and Wyckoff letter in an ideal fluorite structure are given in the Table 5-1. In reality, the atomic positions may vary a little from the ideal lattice position. A neutron diffraction study on ceria by Yashima *et al.* showed that the

O-atoms are distributed at 8c and 32f positions<sup>206</sup>. The structural details of the neutron diffraction study are summarized in Table 5-2.

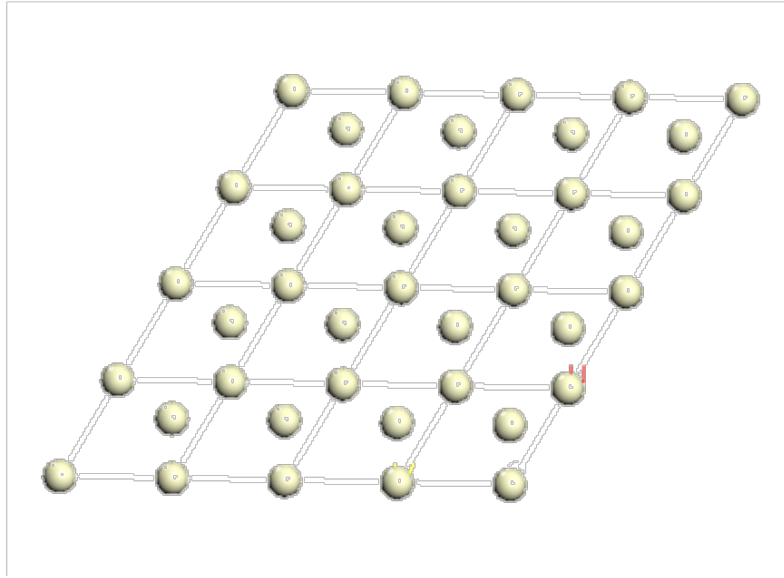


Figure 5-3. Kagome net formed by Ce from  $\langle 1\ 1\ 1 \rangle$  view. Only the Ce-sublattice is shown.

Table 5-1. Potential Fluorite structure data from International Tables of Crystallography, Volume A: space-Group Symmetry, Fourth Edition<sup>207</sup>.

Atom	Site	Site symmetry	Coordinates		
O	8c	43m	1/4,	1/4,	1/4
			1/4,	1/4,	3/4
Ce	4b	m3m	1/2,	1/2,	1/2
	4a	m3m	0.0	0.0	0.0

Table 5-2. Atomic position of ceria from neutron diffraction<sup>206</sup>.

Atom	Site	U(Å <sup>2</sup> )	x	y	z
Ce	4a	0.0340	0.0	0.0	0.0
O1	8c	0.041	0.25	0.25	0.25
O2	32f	0.041	0.325	0.325	0.325

Doped ceria has a very open structure and it exhibits large tolerance for high levels of atomic disorder. Oxygen vacancies can be introduced by doping with oxides of metals with low valences. For instance the elements with 2+ or 3+ valence as MO and M<sub>2</sub>O<sub>3</sub>:





Many studies suggest that vacancies introduced by doping are bound to dopant cations to form some complex defect associates<sup>55, 208</sup>. This association energy is mainly due to the electrostatic interaction of the defects caused by their charge. The association energy is also dependent on the ionic radii and dielectric polarizability of the doped cations, which may cause elastic strain in the system<sup>58</sup>. Because of the presence of oxygen vacancies in the doped ceria structure and because of the role of defect in determining physical properties of ceramics, the mechanical properties are quite different from that of the perfect structure. This is supported by the study of Atkinson *et al.*<sup>209</sup> using a simulation approach, which showed that ceria based electrolytes will be mechanically unstable above 700°C. This indicates that the mechanical property of doped ceria is inferior to YSZ<sup>52</sup>. However, the origins of this are not fully understood.

### 5.3 Computational Details

Molecular dynamics simulations and lattice-statics calculations are carried out in the present study. The interatomic interactions between cations and anions are described by combining both long-range Coulombic interaction and short-range repulsive contributions. The long-range Coulombic interactions are:

$$E_{LR}(r_{ij}) = \frac{1}{2} \sum_{i=1}^N \left\{ \sum_{j \neq i} \frac{q_i q_j}{r_{ij}} \right\} \quad [5-3]$$

where  $N$  is the total number of ions in the system,  $q_i$  and  $q_j$  are the charge on ion  $i$  and  $j$  respectively,  $r_{ij}$  is the distance between ion  $i$  and  $j$ . The summations over the system are carried out using the Ewald method. All of the potentials used in the present study employ the formal ionic charge for cerium and oxygen (i.e.,  $q_{Ce} = +4$  and  $q_O = -2$ ).

Short-ranged interactions are typically described by one of two types of potentials. The first one is the Buckingham potential:

$$E_{Buck}(r_{ij}) = Ae^{(-r_{ij}/\rho)} - C/r_{ij}^6 \quad [5-4]$$

where  $A$ ,  $\rho$  and  $C$  are adjustable parameters, chosen to reproduce pertinent physical properties of the real material.

The other one used is the Born-Mayer-Huggins (BMH) potential:

$$E_{BMH}(r_{ij}) = f_0(b_i + b_j) \exp\{(a_i + a_j - r_{ij})/(b_i + b_j)\} - c_i c_j / r_{ij}^6 \quad [5-5]$$

Here  $a_i$ ,  $b_i$  and  $c_i$  are parameters for individual atom species. Although the BMH form can be simply recast into the Buckingham form, it does have the advantage that, at least in principle, parameters for individual ions can be defined, rather than for ion pairs as in the Buckingham form. For ceria-based systems, parameters in both the Buckingham and BMH forms have been developed. Since the quality of the simulations is directly determined by the quality of the potential, an evaluation of the available potentials is given in Section 5.4.

The calculations used in the evaluation of the potentials are carried out using General Utility Lattice Program (GULP)<sup>210, 211</sup>. All simulations are performed on a 6 x 6 x 6 supercell of cubic non-primitive fluorite unit cells, each of which contains four CeO<sub>2</sub> formula units, for a total of 2592 ions. Periodic boundary conditions are applied in all three spatial directions. To simulate sub-stoichiometry, Ce<sup>4+</sup> ions are randomly replaced by Ce<sup>3+</sup> (q=+3) ions. Within a single simulation the arrangement of Ce<sup>4+</sup> and Ce<sup>3+</sup> ions is fixed; this is a limitation of the current approach, since experimentally electron transfer allows the Ce<sup>3+</sup> ions to develop an equilibrium arrangement, which may not be random. An appropriate number of oxygen ions are then removed to maintain charge neutrality. Computational annealing of the system by MD at high temperature allows the oxygen vacancies to diffuse to form a structure in which the anion and

vacancy arrangements are in equilibrium with respect to the fixed cation sublattice. For sub-stoichiometric ceria and doped ceria, since the properties may depend on the arrangements of dopant cations and oxygen vacancies, several random cation structures are generated and the properties of each structure are calculated to capture the range of effects. For  $T > 0$  K calculations, the free energy is calculated using the quasi-harmonic approximation to lattice dynamics, as implemented in the GULP code.

## 5.4 Interatomic Potentials Evaluation

Five different parameterizations of the Buckingham potential and one parameterization of the BMH potentials are currently available for the ceria-based systems. The parameters for the five Buckingham potentials, denoted as Grimes<sup>212</sup>, Vyas<sup>213</sup>, Butler<sup>214</sup>, Gotte (2004)<sup>215</sup>, and Gotte (2007)<sup>216</sup>, are given in Table 5-3. The Grimes, Gotte (2004) and Gotte (2007) potentials have also been parameterized for  $\text{Ce}^{3+}$ , allowing the effects of off-stoichiometry to be assessed. In addition, the Grimes potential has been parameterized for a number of rare earth ions, allowing doping effects to be determined. The parameters for Inaba's BMH potential are given in Table 5-4. All of the Buckingham potentials have shell model parameters; unless otherwise indicated all of the simulation results for these systems are based on shell-model calculations. Inaba's BMH potential is a rigid-ion potential. To evaluate the quality of each potential, the lattice constant, thermal expansion, chemical expansion, oxygen migration energy and dielectric properties are determined. The detailed comparison for these properties is given in the following subsections.

### 5.4.1 Lattice Constant and Thermal Expansion

The zero-temperature lattice constants calculated using these potentials are listed in Table 5-5. The values are all essentially identical and in excellent agreement with the experimental data. This is to be expected since the potentials were fitted to the lattice parameter and some

other fundamental properties. However, it should be noted that the experimental data is 293 K while simulation data are for 0 K.

Table 5-3. Parameters of the five Buckingham potentials for ceria-based systems.

	Species	A (eV)	r (Å)	C (eV Å <sup>6</sup> )	Y <sub>e</sub> (e)	K <sub>1</sub> (eVÅ <sup>-2</sup> )	Ref
Grimes	O <sup>2-</sup> -O <sup>2-</sup>	9547.96	0.2192	32.0	-2.04	6.3	217 218
	Ce <sup>4+</sup> -O <sup>2-</sup>	1809.68	0.3547	20.40	-0.20	177.84	213
	Ce <sup>3+</sup> -O <sup>2-</sup>	2010.18	0.3449	23.11			58
	In <sup>3+</sup> -O <sup>2-</sup>	1495.65	0.3327	4.33			219
	Y <sup>3+</sup> -O <sup>2-</sup>	1766.40	0.33849	19.43			217
	Gd <sup>3+</sup> -O <sup>2-</sup>	1885.75	0.3399	20.34			58
	La <sup>3+</sup> -O <sup>2-</sup>	2088.79	0.3460	23.25			58
Vyas	O <sup>2-</sup> -O <sup>2-</sup>	9547.92	0.2192	32.0	-2.04	10.3	213
	Ce <sup>4+</sup> -O <sup>2-</sup>	2531.5	0.335	20.40	-0.20	177.84	
Butler	O <sup>2-</sup> -O <sup>2-</sup>	22764.3	0.149	45.83	-6.10	419.9	214
	Ce <sup>4+</sup> -O <sup>2-</sup>	1986.8	0.3511	20.40	7.7	291.8	
Gotte (2004)	O <sup>2-</sup> -O <sup>2-</sup>	9547.92	0.2192	32.0	60.78	-3.0	215
	Ce <sup>4+</sup> -O <sup>2-</sup>	1809.68	0.3547	24.40	166.021	7.0	
	Ce <sup>3+</sup> -O <sup>2-</sup>	1809.68	0.3547	24.40	166.021	7.0	
Gotte (2007)	O <sup>2-</sup> -O <sup>2-</sup>	9533.421	0.234	224.88	1759.8	-6.5667	216
	Ce <sup>4+</sup> -O <sup>2-</sup>	755.1311	0.429	0.0	43.451	4.6475	
	Ce <sup>3+</sup> -O <sup>2-</sup>	1140.193	0.386	0.0	2172.5	15.092	

Table 5-4. Parameters of the Inaba<sup>220</sup> Born-Huggins-Mayer potential for CeO<sub>2</sub>. No shell model is available for this potential.

		z	a (Å)	b (Å)	c (J <sup>0.5</sup> (nm) <sup>3</sup> mol <sup>0.5</sup> )
Inaba	Ce <sup>4+</sup>	2.700	1.33	0.0454	0.00
	O <sup>2-</sup>	-1.350	1.847	0.166	1.294

To determine the thermal expansion, the temperature dependence of the lattice parameter for each potential (normalized to the corresponding T = 0 K values) is shown in Figure 5-4. The quasi-harmonic approximation used for these calculations includes quantum effects, which leads to zero thermal expansion at T = 0 K. The coefficient of thermal expansion values given in Table 5-5 are taken from T= 400 K to T= 1400 K over which the lattice parameter is approximately linear in temperature and over which quantum effects are no longer important.

None of these potentials is able to reproduce the experimental value quantitatively. It is found that the Butler potential overestimates the experimental thermal expansion, whereas the others underestimate the thermal expansion. The thermal expansion calculated by the Butler and

Gotte (2007) potentials, which are 112% and 82% of the experimental value, are better than other values. The thermal expansion calculated using Gotte (2007), Gotte (2004), Vyas and Grimes potentials predict values that are 63%, 57%, 10% and 11% of the experimental value, respectively.

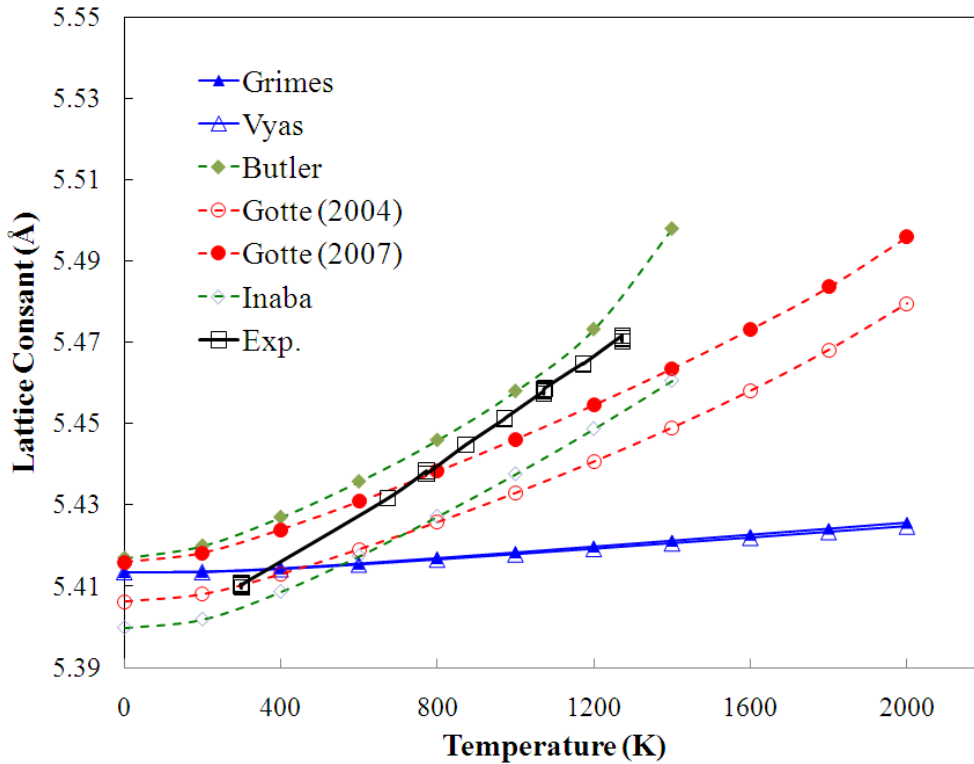


Figure 5-4. Temperature dependence of the lattice parameter of  $\text{CeO}_2$  obtained from MD simulation using different potentials, compared with experiment data<sup>221</sup>.

## 5.4.2 Chemical Expansion

The chemical expansion measures the lattice expansion produced by off-stoichiometry. To simulate this, we introduced oxygen vacancies into the pure ceria system and replaced the requisite number of  $\text{Ce}^{4+}$  ions with  $\text{Ce}^{3+}$  ions. The effect of this sub-stoichiometry on the lattice parameter is four-fold. (i) The larger ionic radius of the  $\text{Ce}^{3+}$  compared to the  $\text{Ce}^{4+}$  ions (1.143 Å vs. 0.97 Å) tends to increase the lattice parameter. (ii) The lower charge of the  $\text{Ce}^{3+}$  reduces the strength of the attractive Coulombic interactions, thereby also tending to increase the lattice

parameter. (iii) the presence of oxygen vacancies decreases the attractive Coulombic interactions, also tending to an increased lattice parameter. (iv) The oxygen vacancies also have the effect of lowering the atomic density, thereby tending to decrease the lattice parameter. We note that three of these four effects can be expected to lead to an increase in the lattice parameter with increasing sub-stoichiometry.

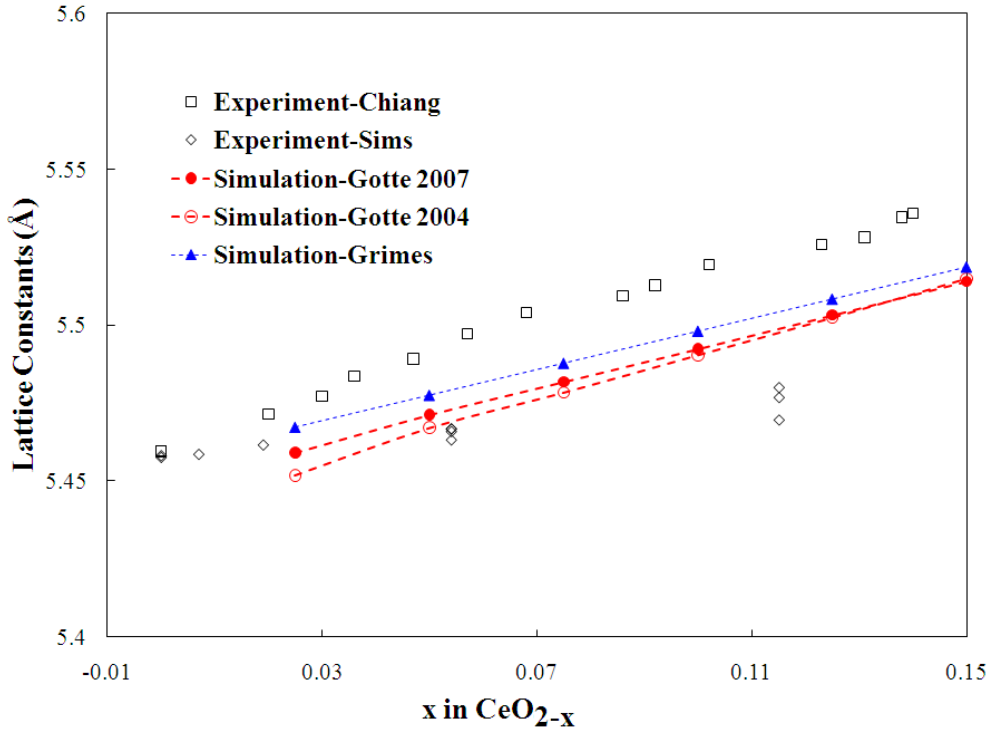


Figure 5-5. The effect of composition on the lattice constants of CeO<sub>2-x</sub> obtained from MD simulations at 1073K. The values are compared with experimental results<sup>221, 222</sup>.

As mentioned above in section 5.4 only three of the potentials have parameters for Ce<sup>3+</sup>: Grimes, Gotte (2004) and Gotte (2007). Figure 5-5 compares the simulated lattice parameters at 1073 K using the Grimes, Gotte (2004) and Gotte (2007) potentials with the experimental value for CeO<sub>2-x</sub> (x = 0.0 – 0.15)<sup>222, 223</sup>. The simulation results at each temperature show that the lattice parameter increases with increasing vacancy concentration, consistent with the qualitative argument above. The slope of the chemical expansion line with respect to x in CeO<sub>2-x</sub> is given in

Table 5-5. It is found that the both Grimes and Gotte (2007) potential give a chemical expansion close to the experimental results, which indicates that both potentials successfully capture the effects of sub-stoichiometry.

Table 5-5. Properties of CeO<sub>2</sub> from experiment and from various interatomic potentials.

	Exp.	Empirical Potential					
		Grimes <sup>58</sup>	Vyas <sub>213</sub>	Butler <sub>214</sub>	Gotte (2004) <sup>215</sup>	Gotte (2007) <sup>216</sup>	Inaba <sub>220</sub>
Lattice Constant (Å)	5.411	5.411	5.414	5.411	5.411	5.411	5.414
Coefficient of Thermal Expansion (X 10 <sup>-6</sup> K <sup>-1</sup> )	11.6	1.27	1.16	13.1	6.65	7.31	9.58
Coefficient of Chemical Expansion @ 1173K (Å/Oxygen Vacancy Concentration)	0.535	0.41	-	-	0.505	0.43	-
Static Relative Permittivity	18.6 - 20.0	18.6	12.71	19.53	16.2	18.6	-
High Frequency Dielectric	4	4.54	3.98	4	5.59	4	-
Oxygen Migration Energy (eV)	0.7±0.1	0.3 (shell) 0.63 (rigid ion)	0.54	0.74	0.41(shell) 0.58(rigid ion)	0.58	0.54

### 5.4.3 Dielectric Properties and Oxygen Migration Energy

As shown in Table 5-5, all the potentials reasonably reproduce both the static and high-frequency dielectric constants. The oxygen migration energy predicted by Grimes and Gotte (2004) are significantly smaller than the experimental value. Interestingly, using the Grimes potential in the rigid ion approximation, rather than with a shell model, the predicted oxygen migration energy is in excellent agreement with the experimental results. The Gotte (2004)

potential also predicts higher migration energy when the shell model is not used. Physically, this is quite reasonable since the polarizability of the ions in the shell model allows charges of ions to polarize in a manner that lowers the energy barriers. The oxygen migration energy calculated using Vyas, Butler, Gotte (2007) and Inaba are also in reasonably good agreement with experimental data.

#### **5.4.4 Elastic Constants**

Table 5-6 compares the zero-temperature elastic constants, as determined directly from GULP for the various potentials, with the experimental results and with DFT. The experimental values for the elastic properties are also given in Table 5-6. The values of  $C_{11}$ ,  $C_{12}$  and  $C_{44}$  were obtained from Raman scattering, which probes the fundamental vibrations of the system<sup>224</sup>. The value of the bulk modulus determined from these values is in quite good agreement with independent determinations from pressure-volume curves<sup>225</sup>. Likewise, the Young's modulus obtained from analysis of the Raman scattering results is in good agreement with the value from nanoindentation<sup>226</sup>.

For the simulations, the values of  $C_{11}$ ,  $C_{12}$  and  $C_{44}$  were determined in GULP, from which all of the moduli and the anisotropic factor  $Z$  were determined using standard analytic elastic relationships. The values predicted by the Grimes, Vyas, Butler, Inaba and Gotte (2004) potentials are all larger than the corresponding experimental values. The values obtained for the Gotte (2007) are in essentially perfect agreement with the experimental values. Although not discussed in their paper, it can reasonably be assumed that the experimental elastic properties were part of the fitting set for the potential. The bulk modulus,  $B$ , tetragonal shear modulus,  $G$ , and Young's modulus,  $Y$ , show corresponding levels of agreement with experiment.

Table 5-6. Comparison of elastic properties, including the bulk modulus, B, Young's modulus, Y, and shear modulus,  $G = \frac{1}{2}(C_{11} - C_{12})$ , of CeO<sub>2</sub> from experiment, DFT calculations and as predicted by empirical potentials. Those experimental and simulated values that were independently determined are given in bold. Others were determined using standard relationships among elastic properties.

Exp.	Buckingham					BMH	DFT	
All units in GPa	Grimes <sup>58</sup>	Vyas <sup>213</sup>	Butler <sup>214</sup>	Gotte (2004) <sup>215</sup>	Gotte (2007) <sup>216</sup>	Inaba <sup>220</sup>		
C <sub>11</sub>	<b>403.0</b> <sub>224</sub>	<b>554.2</b>	<b>573.0</b>	<b>504.4</b>	<b>554.0</b>	<b>403.0</b>	<b>451.0</b>	<b>399.5</b> <sub>227</sub>
C <sub>12</sub>	<b>105.0</b> <sub>224</sub>	<b>124.6</b>	<b>147.7</b>	<b>143.1</b>	<b>125.0</b>	<b>105.0</b>	<b>103.6</b>	<b>127.5</b> <sub>227</sub>
C <sub>44</sub>	<b>60.0</b> <sup>224</sup>	<b>123.6</b>	<b>146.8</b>	<b>16.1</b>	<b>71.7</b>	<b>60.0</b>	<b>99.1</b>	<b>63.5</b> <sub>227</sub>
B	204 <b>236±4</b> <sub>225</sub> <b>230±10</b> <sub>228</sub>	267.9	289.4	263.6	268.0	204.3	207.0	218
G	149.0	215.0	212.6	180.7	214.5	149.0	173.7	136
Y	-	508.0	512.5	439.7	511.2	362.4	412.3	338
G <sub>Po</sub>	96.0	160.2	173.4	81.8	128.2	96.0	124.3	92.5
ly Y <sub>Po</sub>	248.95 <b>255</b> <sup>226</sup>	400.7	433.6	222.4	331.7	249.0	310.6	243.1
ly Z	0.40	0.58	0.69	0.09	0.19	0.40	0.57	0.46

Also included in this table are the results of previous electronic-structure calculations at the level density functional theory (DFT) using the local density approximation (LDA) with the projector augmented wave (PAW) method<sup>62</sup>.

Both the atomistic simulations and the electronic-structure calculations were performed on ideal crystals. We therefore used the Voigt-Reuss-Hess method<sup>229</sup> to determine polycrystalline-average elastic constants from the single-crystal values. Because  $C_{11} = C_{33}$  and  $C_{12} = C_{13} = C_{23}$

for a cubic system, the polycrystalline average of the bulk modulus is identical to the single crystal value. The Hess average is shown in Table 5-6.

The polycrystalline averaged shear modulus lies within the bounds <sup>229</sup>:

$$G_R = \frac{5(C_{11} - C_{12}) \times C_{44}}{4C_{44} + 3(C_{11} - C_{12})} < G < G_v = \frac{C_{11} - C_{12} + 3C_{44}}{5} \quad [5-6]$$

The elastic anisotropy of the material can be characterized by the directionality of the Young's modulus, E, can also be determined using:

$$E^{-1} = \frac{C_{11} + C_{12}}{(C_{11} - C_{12})(C_{11} + 2C_{12})} - C_{44} [Z - 1] \left[ \sin^2 \theta \cos^2 \theta + \frac{1}{4} \sin^4 \theta \sin^2 2\Phi \right] \quad [5-7]$$

where  $\theta$  is the angle between [100] axis and the chosen direction and  $\Phi$  is the angle between [010] axis and the projection of the chosen direction on the (100) plane. Here Z is the Zener anisotropy ratio:

$$Z = \frac{2C_{44}}{C_{11} - C_{12}} \quad [5-8]$$

For Z=1, the system is isotropic, and the Young's modulus is independent of direction. For Ceria, the Young's modulus along different crystallographic directions is shown in Table 5-7. Since all of these metrics of the elastic properties were determined analytically from the elastic constants, they show corresponding degrees of agreement with experimental values.

Table 5-7. Anisotropy in the Young's modulus of CeO<sub>2</sub> using different methods. Numbers in brackets indicate fractional value relative to that in the <001> direction.

Directions	Grimes <sup>58</sup>	Gotte(2007) <sup>216</sup>	DFT <sup>227</sup>	Exp.
<0 0 1>	504.9 (1.0)	359.6 (1.0)	355.9 (1.0)	359.6 (1.0)
<1 1 0>	351.6 (0.70)	189.8 (0.53)	196.7 (0.55)	189.8 (0.53)
<1 1 1>	319.3 (0.63)	163.9 (0.46)	171.2 (0.48)	163.9 (0.46)

#### 5.4.5 Potential Summary

None of the potentials is able to reproduce all of the experimental properties evaluated. Overall, the Gotte (2007) has the highest materials fidelity. In particular, the elastic and dielectric

properties are in essentially perfect agreement with experiment, and the predicted oxygen migration energy is in good agreement with experiment. The chemical expansion is also in reasonable agreement with the experimental data. However, the predicted thermal expansion is smaller than the experimental value, indicating that the potential is significantly less anharmonic than the experimental system.

Interestingly, the Grimes potential predicts the chemical expansion to within 20%. It also yields dielectric properties and the oxygen migration energy in good agreement with experiment. However, it does a very poor job in predicting the coefficient of thermal expansion, predicting a value that is only 11% of the experimental value. In terms of the elastic properties, the Grimes potential is clearly not as good as the Gotte (2007) or Inaba potentials, but has a similar level of fidelity as the other potentials. To its advantage, the Grimes potential is the only potentials providing parameters for some rare-earth ions, which allows the study of doped ceria system.

In the next section, we evaluate the effects of off-stoichiometry on the elastic properties. Because both the Grimes and Gotte (2007) potentials do predict some of the salient properties with reasonable accuracy, we will compare the results predicted for each. In Section 5.5, we examine the effects of rare earth doping on the elastic properties, for which the Grimes potential is the only one with potentials parameters.

## 5.5 Mechanical Softening Effects

A key finding in the experimental measurements of Wang *et al.*<sup>226</sup> for the Young's modulus of ceria was that there is significant elastic softening with decreasing oxygen partial pressure ( $P_{O_2}$ ), i.e., with increasing sub-stoichiometry<sup>226</sup>. The open square symbols in Figure 5-6 denote the room temperature Young's modulus for different levels of sub-stoichiometry, determined from their data. The experiments were actually performed at fixed  $PO_2$ , at which the lattice parameter was determined. The corresponding degree of off-stoichiometry can be

calculated from the method developed by Bevan<sup>230</sup> and Panlener<sup>231</sup>. Figure 5-6 also shows the corresponding results predicted from the Grimes and Gotte (2007) potentials at 300 K. In Figure 5-6, the Young's moduli are plotted as a function of lattice constants rather than of the composition. There are differences between the predicted chemical expansions and the experimental value; it thus turns out that the direct calculated Young's moduli agree with the experimental values quite well for the Gotte (2007) potential. The Grimes potential agrees less well, mainly due the significant over-estimate in the elastic constants of the pure system.

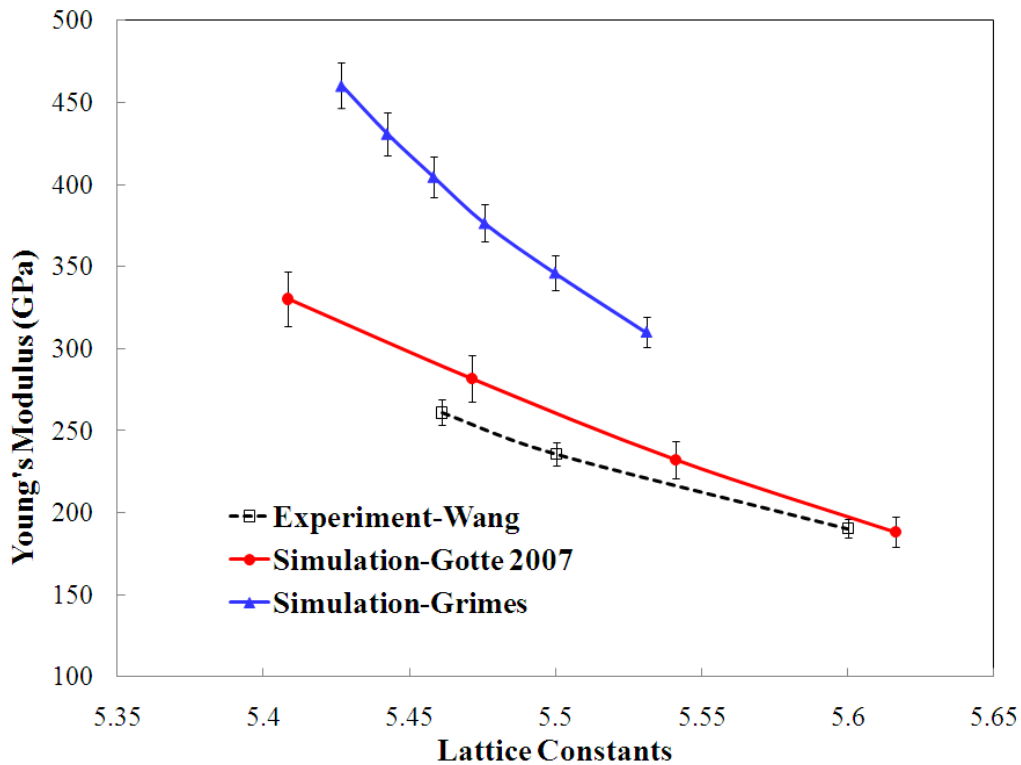


Figure 5-6. Composition dependence on the room temperature Young's modulus of  $\text{CeO}_{2-x}$  obtained from MD simulation using Gotte (2007) potential, Grimes potential and from experiment<sup>226</sup>.

In contrast to the Raman scattering experiments, the DFT calculations and the MD simulations, the nanoindentation experiments of Wang *et al.*<sup>226</sup> did not show significant elastic anisotropy. It is possible that microstructural factor in the indented samples led to effectively

isotropic elastic behavior, rather than the anisotropic behavior seen in the spectroscopy experiments<sup>224</sup>, which probe the intrinsic atomic-level elastic response.

We have also used atomic simulations to determine the effect of temperature on the elastic properties of CeO<sub>2</sub> using the Gotte (2007) potential, which has the highest fidelity for elastic properties. Figure 5-7 shows the temperature dependence of Young’s modulus (Y) in the <001> direction, the shear modulus (G), the bulk modulus (B), and the anisotropy factor (Z). The trends are in accord with conventional trends for the softening of the elastic properties with temperature. The elastic anisotropy factor also decreases with increasing temperature.

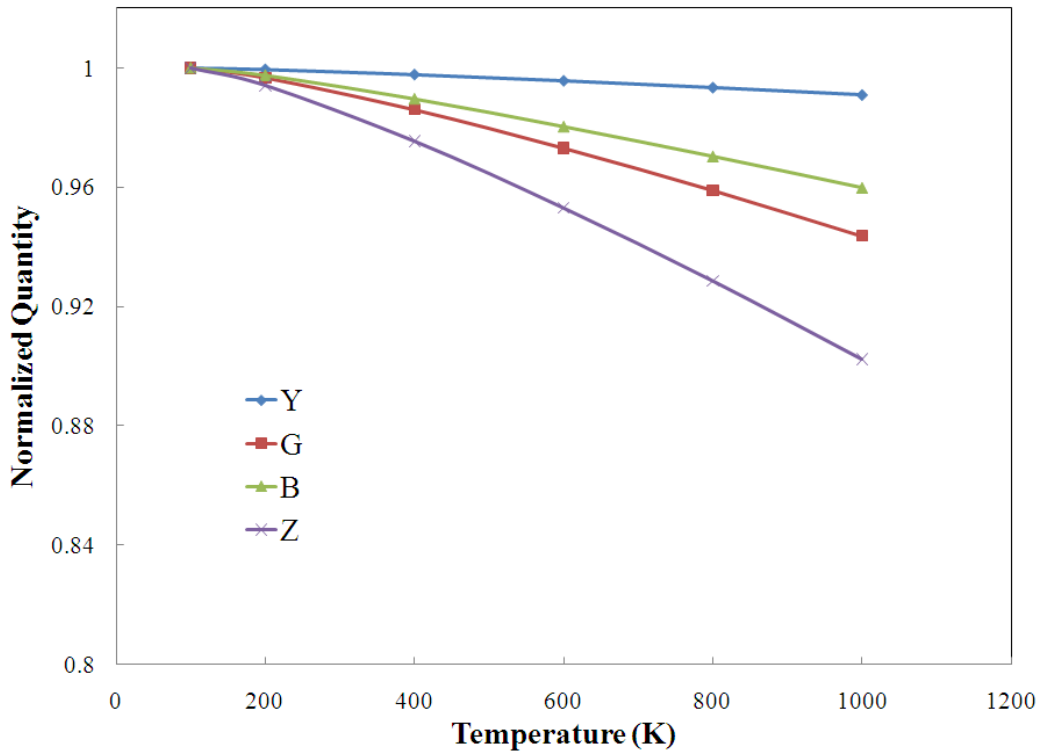


Figure 5-7. The effects of temperature on the normalized bulk modulus (B), shear modulus (G), Young’s modulus (Y), and anisotropic factor (Z) for CeO<sub>2</sub>, as determined by MD simulation using Gotte (2007) potential.

We have determined the effects of doping of ceria doped with In<sup>3+</sup>, Y<sup>3+</sup>, Gd<sup>3+</sup>, La<sup>3+</sup> ions, for which the potential parameters compatible with the Grimes potential were provided by Minervini *et al.*<sup>58</sup>. The ionic radii of these dopant ions are given in Table 5-8. Even though the

Grimes potential cannot accurately reproduce the thermal expansion, dielectric constant, and oxygen migration energy accurately; it does accurately reproduce the most two important properties for addressing the effects of doping are the chemical expansion, for which it does a good job, and the elastic constants, for which it captures the trends, albeit being overall too stiff.

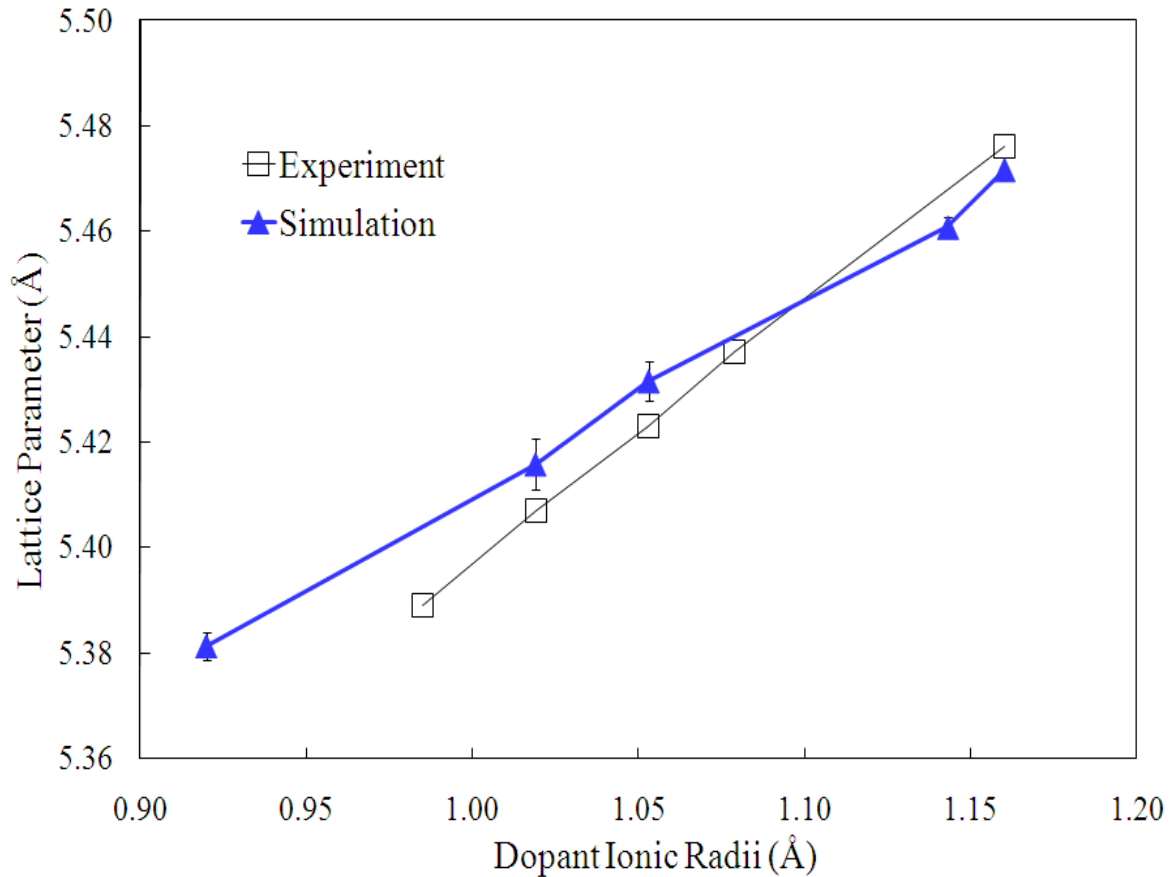


Figure 5-8. The effect of dopant ion size on the lattice parameter of  $\text{Ce}_{0.8}\text{M}_{0.2}\text{O}_{1.9}$  (where  $\text{M} = \text{In}^{3+}, \text{Y}^{3+}, \text{Gd}^{3+}, \text{Ce}^{3+}, \text{La}^{3+}$ ) obtained from MD simulation, compared with the experimental results<sup>232</sup>.

Table 5-8. Ionic Radii for relevant ions from Shannon Table<sup>154</sup>.

Dopant Ions	Ionic Radius (VIII)
$\text{Ce}^{4+}$	0.97 Å
$\text{In}^{3+}$	0.92 Å
$\text{Y}^{3+}$	1.019 Å
$\text{Gd}^{3+}$	1.053 Å
$\text{Ce}^{3+}$	1.143 Å
$\text{La}^{3+}$	1.16 Å

We compared the lattice constants of various doped-ceria systems with the experimental values. In a manner analogous to that for  $\text{CeO}_{2-x}$ , the doped structures are generated by randomly replacing the  $\text{Ce}^{4+}$  ions by dopant cations and compensating the charge by creating appropriate number of oxygen vacancies in the system.

Since the experimental results for dopants are already available at 298 K and the effect is more pronounced for a larger dopant concentration, room temperature  $\text{Ce}_{0.8}\text{M}_{0.2}\text{O}_{1.9}$  was simulated, where  $\text{M} = \text{In}^{3+}, \text{Y}^{3+}, \text{Gd}^{3+}, \text{La}^{3+}$  ions. Figure 5-8 compares the simulated lattice parameters using the Grimes potential with the experimental values<sup>232</sup>. The simulated values are within  $0.2\text{\AA}$  of the experimental values over the full range of ionic radii<sup>154</sup>, which can be considered to be in a adequate agreement, As is evident from Figure 5-8, the simulations show a consistently weaker dependence of the lattice parameter on the ionic radius of the dopant ion. This is consistent with the calculated lower chemical expansion in  $\text{CeO}_{2-x}$  (see Table 5-5).

For fuel-cell electrolyte applications, it is also important to understand the effect of dopants on the Young's modulus of doped ceria system. From the point of view of the atomic-level simulation, the approach is essentially identical to that for sub-stoichiometric  $\text{CeO}_2$  since the  $\text{Ce}^{3+}$  ions and  $\text{M}^{3+}$  ions act in the same manner. Experimentally, the Young's modulus of  $\text{Ce}_{0.8}\text{Gd}_{0.2}\text{O}_{1.9}$  at room temperature is determined to be  $147.2 \pm 16.1 \text{ GPa}$ <sup>233</sup>, whereas the Grimes potential predict twice this value. This indicates that Grimes potential overestimates the Young's modulus of pure and reduced ceria system by similar amounts. However, the relative trend of Young's modulus dependence on ionic radii is considered should be more reliable than the absolute values. As Figure 5-9 shows, the system becomes elastically softer with increasing ionic radius of the dopant. Similar elastic softening effects have been observed experimentally in doped ceria systems<sup>226</sup>.

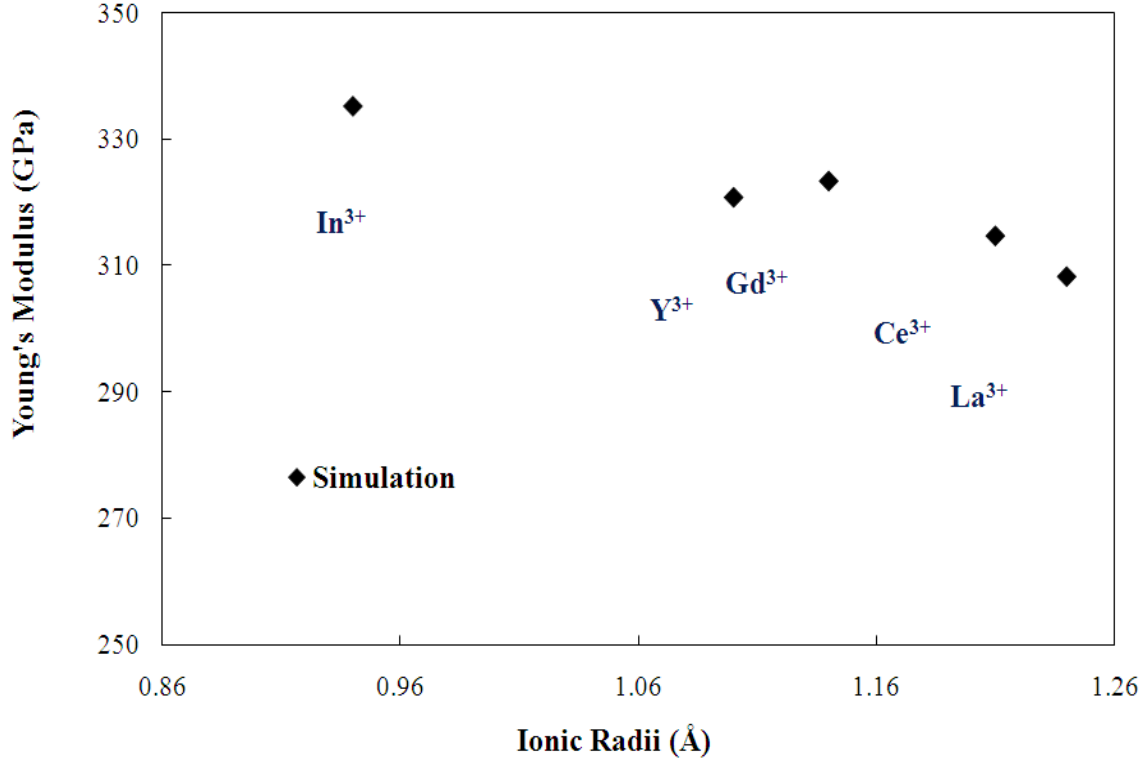


Figure 5-9. Dopant size dependence on the Young's modulus of  $\text{Ce}_{0.8}\text{M}_{0.2}\text{O}_{1.9}$  (where  $\text{M} = \text{In}^{3+}$ ,  $\text{Y}^{3+}$ ,  $\text{Gd}^{3+}$ ,  $\text{Ce}^{3+}$ ,  $\text{La}^{3+}$ ) obtained using Grimes Potential.

## 5.6 Oxygen Diffusion

The diffusivity of doped-ceria system is calculated based on the positions of oxygen ions at different time in the MD simulation. The mean square displacement (MSD) of cations and anions in the system can be extracted from the position of oxygen ions in the usual manner as:

$$MSD = \langle |r(t) - r(0)|^2 \rangle \quad [5-9]$$

where  $r(t) - r(0)$  is the distance traveled by an oxygen ion over time  $t$ . To calculate the diffusivity, this quantity needs to be averaged over all the oxygen ions in the system for a long period. Then, the diffusivity ( $D$ ) can be obtained from

$$D = \lim_{t \rightarrow \infty} \frac{1}{6t} \langle |r(t) - r(0)|^2 \rangle \quad [5-10]$$

After determining the diffusivity at different temperatures, the activation energy are calculated from the Arrhenius equation:

$$D = D_0 \exp(-E_a / RT) \quad [5-11]$$

where  $D_0$  is the pre-factor and  $E_a$  is the activation energy. The conductivity can be then calculated from diffusivity by Nernst-Einstein equation<sup>234</sup> and compared with experiment data.

For doped-ceria systems, the diffusivities at different temperatures are given in Figure 5-10. From Equation 5-11, the activation energy of each system is calculated and compared with DFT results and experimental value (Figure 5-11). It can be seen that DFT predict  $\text{Sm}^{3+}$  and  $\text{Pm}^{3+}$  have the lowest activation energies, unlike experimental results. The values predicted by DFT are also lower than experiments. It is noted that Gd-doped ceria has the lowest activation energy among the trivalent-doped systems that have been studied in the present paper, which is consistent with the experimental observation. The underlying reason that Gd-doped ceria is energetically favorable is attributed to the small mismatch of ionic radii between the host cations and dopant ions.

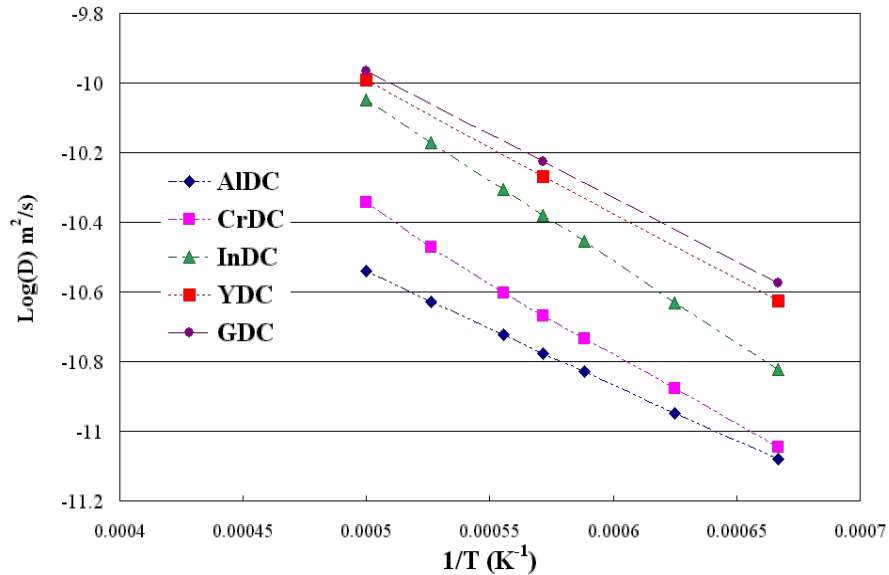


Figure 5-10. Diffusivity dependence on temperature for various doped-ceria systems.

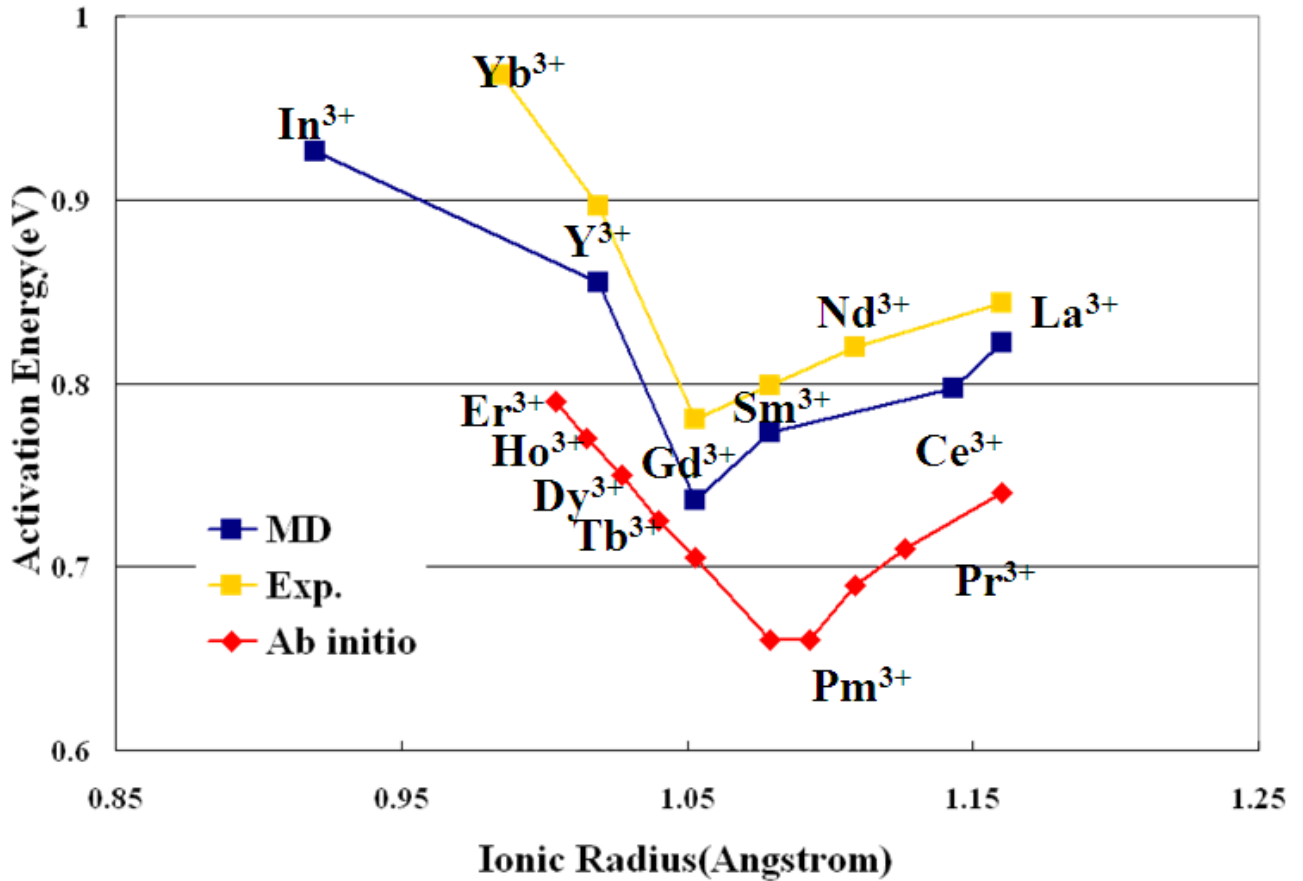


Figure 5-11. Activation energies of oxygen diffusion of various ceria-based electrolytes. The results are compared with experimental values and DFT results.

Since activation energy consists of the migration energy and association energy, to separate these two factors, the migration energies along different diffusion paths:  $\langle 100 \rangle$ ,  $\langle 110 \rangle$ , and  $\langle 111 \rangle$  have been calculated using the nudged elastic band (NEB) method (Figure 5-12). It is the observed that the migration energy along  $\langle 100 \rangle$  path is smaller than the other two, which indicated  $\langle 100 \rangle$  is the favorable path. Furthermore, the migration energy barrier is calculated to 0.62 eV, which is in excellent with experimental value of 0.5-0.6 eV<sup>49</sup>. The association energy, which is due to the elastic and electrostatic interactions between dopant and host cations, can be calculated by taking the difference between activation energy and migration energy.

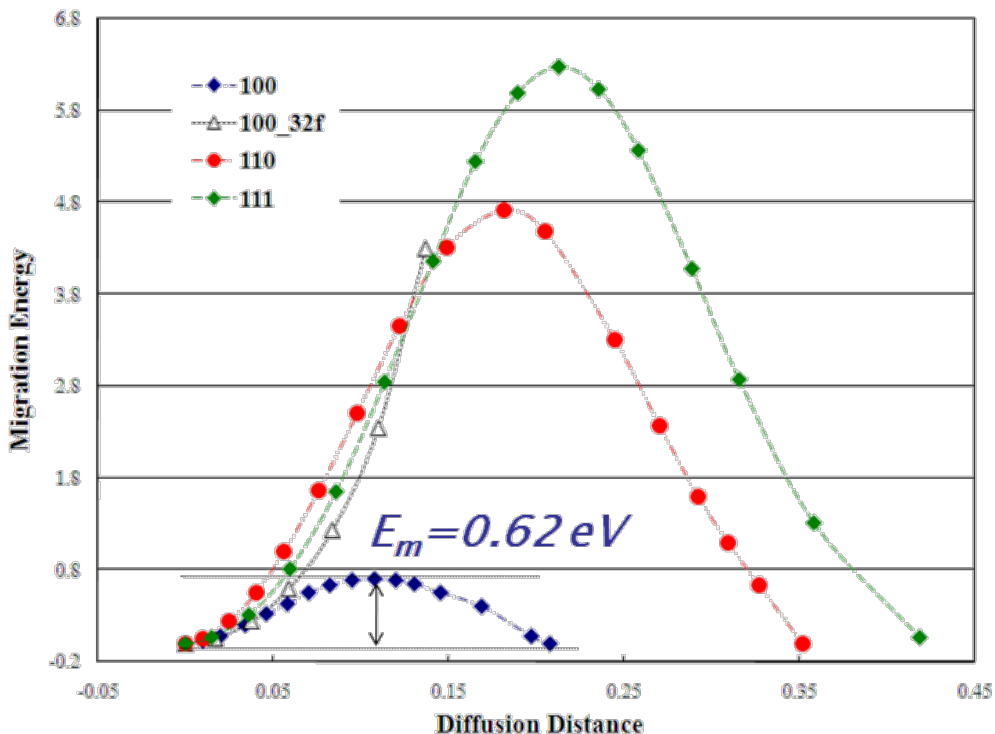


Figure 5-12. Migration barrier along [001], [110], and [111] directions obtained from NEB calculations.

## 5.7 Summary

The materials fidelity of six different empirical potentials have been evaluated, based on lattice constants, thermal expansion, chemical expansion, dielectric properties, oxygen migration energy and mechanical properties. No single potential can reproduce all fundamental properties. Therefore, choosing the appropriate potential(s) for specific applications is critical. Overall, the Gotte (2007) has the highest overall fidelity, while the Grimes can be applied to the widest range of systems.

The simulations, using the best available potential(s) for each physical property, show that both sub-stoichiometry and aliovalent doping of ceria leads to large decreases in the elastic constants of the material. These decreases arise from the significantly reduced strength of ionic interactions. If this elastic softening were to be so large as to threaten the mechanical integrity of

the system, then it would pose a challenging problem for the design of ceria-based electrolytes. It appears that the only way to mitigate this softening would be to strengthen the ionic interactions in the system. Of course, reducing the amount of doping or the sub-stoichiometry would do this; however it would also significantly reduce the ionic conductivity of the system, which is the key performance metric of the material. It would thus be of significant value to identify a strategy for increasing the ionic conductivity that does not result in a significant softening in the elastic properties.

## CHAPTER 6 CASCADE SIMULATIONS IN TITANIUM

### 6.1 Background

A fast reactor is a specific type of nuclear reactor, which has no moderator and relies on fast neutrons alone to sustain the fission chain reaction<sup>235, 236</sup>. Compared with thermal reactors, fast reactors produce more neutrons per fission, resulting in more neutrons than required to sustain the chain reaction. These extra neutrons can be used to produce extra fuels or to transmute long-half-life waste to less troublesome isotopes<sup>237</sup>. In fast reactors, the key component is the nuclear fuel, which can be enriched uranium or plutonium. In addition to nuclear fuel, there are many components in fast reactors, such as coolant, control rods, cladding materials.

Cladding is the outer layer of the fuel rods. The current standard material for cladding is zircaloy<sup>238 239</sup>, which is corrosion-resistant and is able to maintain the mechanical integrity during the operation. Zircaloy mainly consists of zirconium; other elements can be tin, niobium, iron, chromium, and nickel<sup>240</sup>. Similar to zirconium, titanium also has a HCP structure, with even better corrosion resistance and mechanical properties. Therefore, titanium has been considered as a potential cladding material for the next generation of fast reactors. However, before any practical applications, it is of great importance to understand how radiation effects may affect its physical properties.

Radiation effects in nuclear materials are of great complexity, as they are coupled with various microstructural phenomenon and processes. Therefore, it is quite challenging to disentangle each process and to understand the corresponding mechanism. For instance, high-energy radiation can knock the atoms off their equilibrium sites with extremely high kinetic energy, generating an extremely high local temperature and pressure. Accordingly, thermal and

pressure gradients can be formed. In addition, the electrons can be stimulated from the ground state to an excited state, initiating charge transfer processes or chemical reactions. All of these processes are entangled with each other, and the complexity is overwhelming.

Cascade simulations offer a powerful means of characterizing the details of some of these sophisticated processes and decoupling some of the phenomena<sup>241, 242</sup>. The typical spatial and time resolutions of cascade simulations match very well with the dimensions and lifetime of experimental cascades by neutrons or heavy ions. Moreover, cascade simulations can provide information about production, evolution and subsequent diffusion of the defects, information which proves to be of great importance in determining the microstructure evolution and mechanical properties of the materials.

Based on previous studies of cascade simulations in a number of materials, some consistent trends have been identified<sup>243</sup>: The total number of stable surviving point defects is found to have a power-law dependence on the cascade energy; it is also noted that the efficiency of generating stable defects decreases with cascade energy until sub-cascade becomes prominent. In addition, the temperature dependence is rather weak. However, previous cascade simulations of metallic materials mainly focused on cubic structure, such as iron<sup>241, 244</sup>. Few studies are available for HCP structure<sup>245</sup>, which has the potential to show anisotropy under the radiation. Therefore, it is of great importance to carry out cascade simulations in HCP metals. In addition, improvements, particularly with the accuracy of the interatomic potential, are also needed for cascade simulations.

In the present study, cascade simulations in  $\alpha$ -titanium have been carried out using high fidelity modified embedded atom method (MEAM)<sup>83, 246</sup> potentials combined with the potential developed by Ziegler, Biersack and Littmark (ZBL)<sup>247</sup> for short range interactions. The

simulations are performed with energies of primary knock-on atom (PKA) ranging from 0.1 keV up to 30 keV at 100K. To obtain statistically meaningful results, for each value of PKA energy, cascade simulations using several crystallographic directions and positions of PKA have been carried out. The results are then compared with Norgett-Robinson-Torrens (NRT) model and previous simulation studies using a Finnis-Sinclair potential<sup>245</sup>. The effects of PKA orientation and grain boundaries are also discussed.

## 6.2 Structure of Titanium

Titanium has several phases (Figure 6-1). Among these,  $\alpha$ -titanium is the stable phase at room temperature and atmosphere;  $\beta$  is a high temperature body-centered cubic phase;  $\omega$  is a high-pressure phase, with hexagonal structure. In addition, the phase transformation between  $\alpha$ -phase and  $\omega$ -phase is martensitic and strongly hysteretic, as indicated in Figure 6-1.

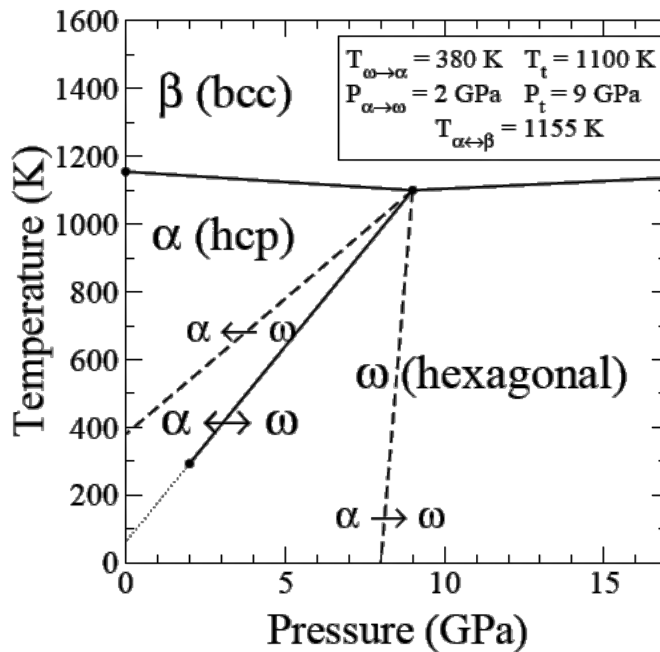
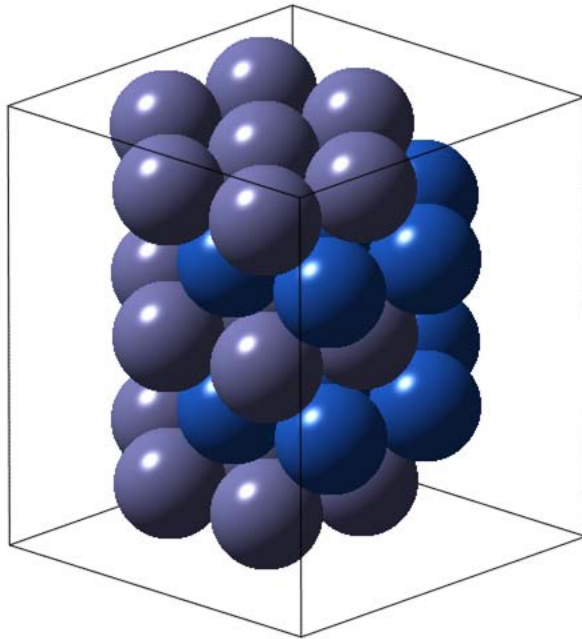


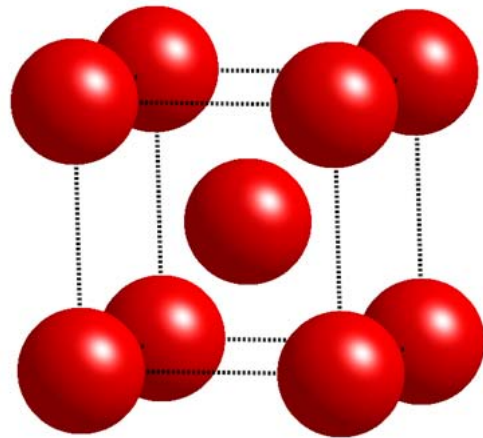
Figure 6-1. Phase diagram of titanium<sup>248</sup>.

$\alpha$ -titanium has a hexagonal close-packed (HCP) structure, with lattice constants of 2.95 Å and 4.68 Å in a and c directions. The three planes with the highest densities are basal plane

(0001), prismatic plane (10-10), and pyramidal plane (10-11), respectively. The closed packed directions are  $\langle 11-20 \rangle$ . Along the [0001] direction, the structure forms alternating layer with ABAB sequence. There are two atoms in each unit cell, with Wyckoff positions of  $(1/3, 2/3, 1/4)$  and  $(2/3, 1/3, 3/4)$  respectively. The ratio of  $c/a$  is 1.588, which is slightly lower than the ideal ratio 1.633, resulting in six neighbors at 2.90 Å and six at 2.95 Å.  $\alpha$ -titanium transforms to body centered cubic (BCC)  $\beta$ -titanium at high temperature, which has a lattice constant of 3.32 Å at 900 °C<sup>248</sup>. The most densely packed planes and directions for BCC are (110) and  $\langle 111 \rangle$  respectively.



**$\alpha$ -titanium: HCP structure**



**$\beta$ -titanium: BCC structure**

Figure 6-2. Structure of  $\alpha$  and  $\beta$  phase of titanium<sup>248</sup>.

$\omega$ - titanium has a hexagonal structure, with space group  $P6/mmm$ <sup>248</sup>. Each unit cell contains three atoms.  $\omega$  phase also forms a layered structure along the  $c$  axis. The first layer consists of atoms in the  $(0, 0, 0)$  Wyckoff position. The second layer is formed from atoms at  $(2/3, 1/3, 1/2)$  and  $(1/3, 2/3, 1/2)$ . The atoms in the first layers have a coordination number of

fourteen whereas the atoms in the next layer have eleven neighbors. The density of the  $\omega$  phase is higher than that of  $\alpha$ -titanium, as it is a high-pressure phase. As the  $\beta$  phase has a BCC structure, the (111) planes in  $\beta$  are hexagonal layers. The collapse of bcc planes in the [111] direction can generate the  $\omega$  structure.

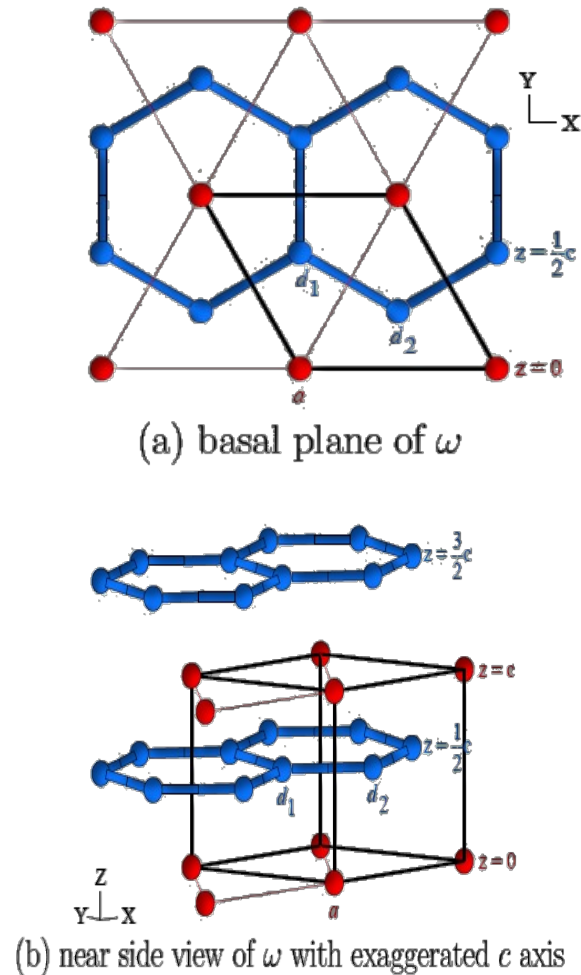


Figure 6-3. Structure of  $\omega$  phase of titanium<sup>248</sup>.

### 6.3 Computational Details

The cascade simulations are carried out using an in-house MD code and two MEAM potentials, one of which is especially accurate in describing the transformations among the phases of titanium. The details of the MEAM potential are given in section 6. 3.1. Since the

interatomic distances in cascade simulations are sometimes very short, the MEAM potentials are used in combination with the ZBL potential, whose details are presented in section 6.3.2.

Periodic boundary conditions are applied in three dimensions with a Parrinello-Rahman<sup>91</sup> barostat. The Berendsen thermostat, which is more reasonable in both physics and statistical mechanics than velocity rescaling, is employed to maintain the temperature of the system. The motions of the atoms are integrated via fifth order predictor-corrector algorithm<sup>64</sup>. The time step is chosen to be 0.2 fs, to balance accuracy with the computational efficiency. A time step less than that does not have a significant effect on the number of surviving Frenkel defects (Figure 6-4). Prior to the cascade simulations, the systems are equilibrated at 100K for 20 ps. Typical cascade simulations times are 20 ps, which is considered to be long enough for the system to reach a stable state, based on the analysis of the time evolution of the defects.

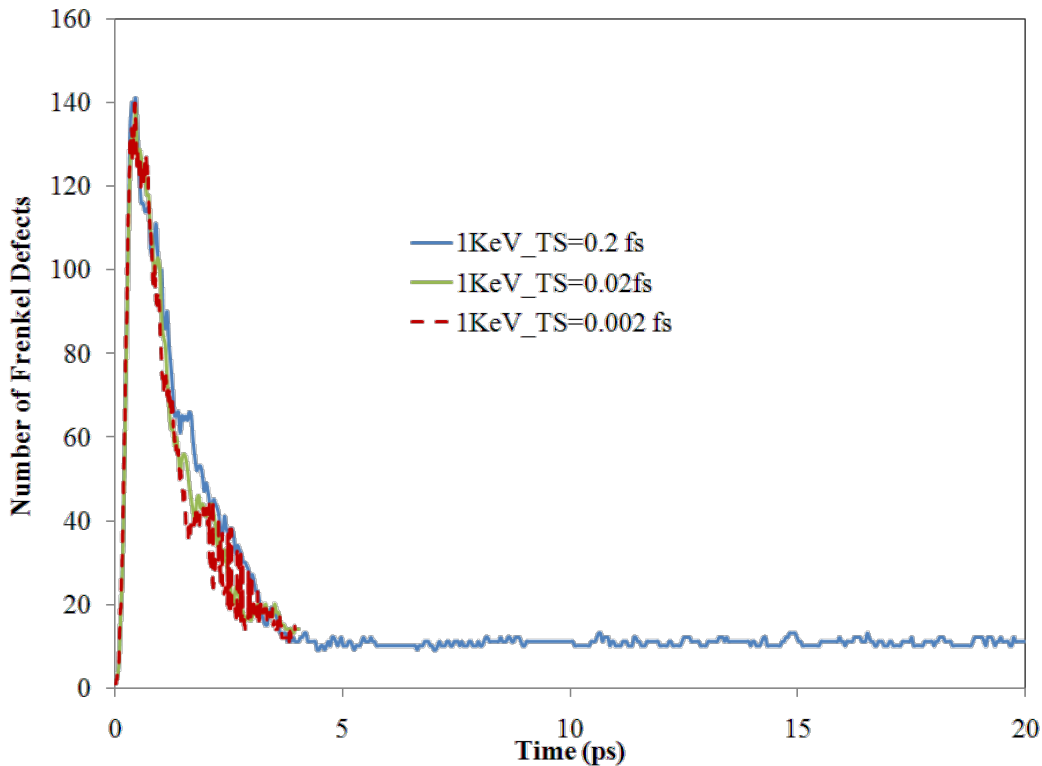


Figure 6-4. The evolution of number of Frenkel defect with time in cascade simulations at 100K with PKA = 1 keV using different time steps.

The number of point defects (vacancies and interstitials) and defect clusters are analyzed using two different approaches: common neighbor analysis and lattice matching analysis respectively (section 6.4). To achieve reasonable statistics, several cascade simulations are simulated for each case. The number of simulations performed for each PKA energy and corresponding system size are given in Table 6-1. The equivalent neutron energies to PKA energies are also listed, assuming elastic collisions between two species.

Table 6-1. The system size and number of simulations performed for each PKA energy. The neutron energy that is equivalent to average PKA energy is also listed.

Neutron Energy (MeV)	Average PKA Energy (KeV)	Atoms in Simulations	No. of Simulations Performed
0.0025	0.1	64000	6
0.0125	0.5	64000	6
0.025	1	64000	12
0.075	3	64000	12
0.125	5	216000	12
0.25	10	216000	18
0.75	30	216000	3

### 6.3.1 MEAM Potential

In the present study, two types of MEAM potentials have been used. One is the traditional MEAM, named MEAM\_I hereafter. The total energy of the system is given as<sup>246</sup>:

$$E_i = \sum_i \left[ F_i(\rho_i) + \frac{1}{2} \sum_{j(\neq i)} \Phi_{ij}(R_{ij}) \right] \quad [6-1]$$

where  $F_i$  is the embedding function,  $\rho_i$  is the background electron density at the site  $i$ ,  $\Phi_{ij}$  is the pair function between atom  $i$  and atom  $j$ ,  $R_{ij}$  is the distance between atom  $i$  and  $j$ . The embedding function is given as<sup>82</sup>:

$$F(\rho_i) = AE_c \frac{\rho_i}{\rho^0} \ln \frac{\rho_i}{\rho^0} \quad [6-2]$$

where  $A$  is an adjustable parameter,  $E_c$  is the cohesive energy,  $\rho^0$  is the background electron density for a reference structure, which is usually the equilibrated structure of  $\alpha$ -titanium.  $\rho_i$  is the background electron density at given site, which consists of several partial electron densities for different angular contributions, corresponding to  $s$ ,  $p$ ,  $d$ , and  $f$  orbital respectively. The partial electron density term are expressed as <sup>82</sup>:

$$(\rho_i^{(0)})^2 = \left[ \sum_{j \neq i} \rho_j^{a(0)}(R_{ij}) \right]^2 \quad [6-3]$$

$$(\rho_i^{(1)})^2 = \sum_{\alpha} \left[ \sum_{j \neq i} \frac{R_{ij}^{\alpha}}{R_{ij}} \rho_j^{a(1)}(R_{ij}) \right]^2 \quad [6-4]$$

$$(\rho_i^{(2)})^2 = \sum_{\alpha, \beta} \left[ \sum_{j \neq i} \frac{R_{ij}^{\alpha} R_{ij}^{\beta}}{R_{ij}^2} \rho_j^{a(2)}(R_{ij}) \right]^2 - \frac{1}{3} \left[ \sum_{j \neq i} \rho_j^{a(2)}(R_{ij}) \right]^2 \quad [6-5]$$

$$(\rho_i^{(3)})^2 = \sum_{\alpha, \beta, \gamma} \left[ \sum_{j \neq i} \frac{R_{ij}^{\alpha} R_{ij}^{\beta} R_{ij}^{\gamma}}{R_{ij}^3} \rho_j^{a(3)}(R_{ij}) \right]^2 - \frac{3}{5} \sum_{\alpha} \left[ \sum_{j \neq i} \frac{R_{ij}^{\alpha}}{R_{ij}} \rho_j^{a(3)}(R_{ij}) \right]^2 \quad [6-6]$$

where  $\rho_j^{\alpha}$  is the atomic electron density from atom  $j$  at distance  $R_{ij}$ ,  $R_{ij}^{\alpha}$  is the  $\alpha$  component ( $\alpha = x, y, z$ ) of the distance vector between atom  $i$  and  $j$ . There are several ways of combining the partial densities to give the total background electron densities <sup>249</sup>. The following formula is widely used <sup>246</sup>:

$$\rho_i = \rho_i^{(0)} G(\Gamma) \quad [6-7]$$

$$G(\Gamma) = \frac{2}{1 + e^{-\Gamma}} \quad [6-8]$$

$$\Gamma = \sum_{h=1}^3 t_i^h \left[ \frac{\rho_i^{(h)}}{\rho_i^{(0)}} \right]^2 \quad [6-9]$$

where  $t_i^h$  are adjustable parameters.

The atomic electron density from atom  $j$  is calculated by

$$\rho_j^{a^{(h)}}(R_{ij}) = e^{-\beta^{(h)}(R_{ij}/r_e-1)} \quad [6-10]$$

where  $\beta^{(h)}$  are the decay lengths and adjustable parameters;  $r_e$  is the near neighbor distance in the equilibrium reference structure.

Although the embedding function is given in the specific form above, the pair-interaction function given in Equation 6-1 is not uniquely defined. Instead, the total energy per atom of the equilibrated reference structure is given from a universal functional proposed by Rose *et al.*<sup>250</sup>.

The functional is expressed as

$$E^u(R) = -E_c(1 + a^* + da^{*3})e^{-a^*} \quad [6-11]$$

where  $d$  is an adjustable parameter and

$$a^* = \alpha(R/r_e - 1) \quad [6-12]$$

$$\alpha = \left( \frac{9B\Omega}{E_c} \right)^{\frac{1}{2}} \quad [6-13]$$

where  $B$  is the bulk modulus and  $\Omega$  is the equilibrium volume.

Once the total energy per atom and embedding function are computed for the reference structure, the pair interaction as a function of the nearest neighbor distance can be computed using Equation 6-1.

It is noted that the formulas above only consider nearest neighbor interactions. The second and more distant neighbor interaction are described using a many-body-screening function<sup>251-253</sup>. For given atom  $i, j$  and  $k$ , a unique plane can be defined. An ellipse passing through atom  $i$  and  $j$  can be also defined using the following equation:

$$x^2 + \frac{1}{C}y^2 = \frac{1}{2}(R_{ij})^2 \quad [6-14]$$

The central idea of this screening function is to define two limiting values, which are  $C_{max}$  and  $C_{min}$  respectively. If the atom  $k$  is outside the ellipse defined by  $C_{max}$ , it is assumed that atom  $k$  does not have any effect on the interactions between atom  $i$  and  $j$ . If atom  $k$  is inside the ellipse defined by  $C_{min}$ , it is assumed that the atom  $k$  completely screens the interaction between atom  $i$  and  $j$ . Between  $C_{max}$  and  $C_{min}$ , the screening interaction gradually changes.

The screening function is defined as

$$S_{ij} = \prod_{k \neq i, j} S_{ikj} \quad [6-15]$$

$$S_{ikj} = f_c \left[ \frac{C - C_{min}}{C_{max} - C_{min}} \right] \quad [6-16]$$

where

$$f_c(x) = 1 \quad x \geq 1$$

$$f_c(x) = [1 - (1-x)^4]^2 \quad 0 < x < 1 \quad [6-17]$$

$$f_c(x) = 0 \quad x \leq 0$$

Another type of MEAM potential is in the function form of cubic spline<sup>83</sup>, thereafter named MEAM\_II, which removes the constraints of fixed angular feature and allows additional flexibility of the potential.

The total energy in MEAM\_II is calculated by<sup>84</sup>

$$E = \sum_{ij} \Phi(r_{ij}) + \sum_i U(\rho_i) \quad [6-18]$$

where  $\Phi(r_{ij})$  is the pair interaction between atom  $i$  and  $j$ .  $U(\rho)$  is the self energy function depending on the electron density of atom  $i$ . The electron density of atom  $i$  is calculated using

$$\rho_i = \sum_j \rho(r_{ij}) + \sum_{jk} f(r_{ij}) f(r_{ik}) g[\cos(\theta_{jik})] \quad [6-19]$$

where  $\theta_{jik}$  is the angle between atom  $j, i$ , and  $k$  centered on atom  $i$ . All five functions  $\Phi(r_{ij})$ ,  $U(\rho)$ ,  $\rho(r_{ij})$ ,  $f(r_{ij})$ , and  $g[\cos(\theta_{jik})]$  are represented by cubic spline functions, which are fitted to the fundamental properties of the system. MEAM\_II can be related to the Stillinger-Weber<sup>254</sup> potential [ $U(x)=x$  and  $\rho=0$ ] and EAM potential [ $f=0$  or  $g=0$ ]. The parameters of MEAM\_II are given in Table 6-2.

Table 6-2. The parameters of spline function for MEAM\_II<sup>83</sup>.

	$t$	$t_{min}$	$t_{max}$	$N$	
phi	r [Å]	1.742693	5.5	13	
rho	r [Å]	2.055802	4.41	11	
f	r [Å]	2.055802	4.41	10	
U	rho <sub>tot</sub>	-55.1423	-23.9383	4	
g	cos(theta)	-1	0.928437	8	
i	phi(r_i)	rho(r_i)	f(r_i)	U(rho_i)	g(x_i)
0	3.7443	1.7475	-0.1485	-0.2975	0.0765
1	0.9108	-5.8678	1.6845	-0.1545	0.1416
2	0.3880	-8.3376	2.0113	0.0510	0.7579
3	-0.0188	-5.8399	1.1444	0.5734	0.6301
4	-0.2481	-3.1141	0.2862	0.0905	
5	-0.2645	-1.7257	-0.3459	-0.3574	
6	-0.2272	-0.4429	-0.6257	-0.6529	
7	-0.1293	-0.1467	-0.6120	-6.0091	
8	-0.0597	-0.2096	-0.3112		
9	-0.0311	-0.1442	0.0000		
10	-0.0138	0.0000			
11	-0.0032				
12	0.0000				
i	phi'(r)	rho'(r)	f'(r)	U'(rho)	g'(x)
0	-20	-1	2.773275	0.007769	8.336423
N	0	0	0	0.105198	-60.4025

Several properties are calculated using these two MEAM potential and compared with other types of approaches, which includes EAM<sup>255</sup> and FS potential<sup>256</sup>, DFT<sup>83</sup>, and experimental results. The calculated properties include lattice constants, elastic constants and modulus, defect formation and migration energies, surface energies, stacking fault energy, thermal expansion coefficient, specific heat, melting point and enthalpy of melting. The comparisons are given in Table 6-3 and Table 6-4. In general, both MEAM potentials have a

very high fidelity for  $\alpha$ -titanium. However, further tests show that MEAM\_I predicts a very low activation energy of transformation from  $\alpha$ -titanium to  $\beta$ -titanium, which results in incorrect structures during the MD tensile test. On the other hand, MEAM\_II provides a reasonable description of the transformation among different phases.

Table 6-3. The fundamental properties calculated using MEAM\_I and MEAM\_II, compared with EAM, FS, DFT and experimental data.

Ti	EAM <sup>255</sup>	F-S <sup>256</sup>	MEAM_I <sup>246</sup>	MEAM_II <sup>83</sup>	DFT <sup>83</sup>	Exp.
$E_c$	-4.855	—	-4.873	-4.831	—	-4.870 <sup>257</sup>
a	2.922	—	2.945	2.931	2.948	2.951 <sup>258</sup>
c	4.772	—	4.687	4.678	5.171	4.679 <sup>258</sup>
c/a	1	0.975	0.974	1.596	1.583	0.971 <sup>258</sup>
B	1.099	—	1.097	—	—	1.097 <sup>259</sup>
$C_{11}$	1.954	1.8	1.701	1.74	1.72	1.761 <sup>259</sup>
$C_{12}$	0.737	0.873	0.804	0.95	0.82	0.869 <sup>259</sup>
$C_{44}$	0.481	0.514	0.421	0.58	0.45	0.508 <sup>259</sup>
$C_{33}$	2.067	2.17	1.871	1.88	1.90	1.905 <sup>259</sup>
$C_{13}$	0.609	0.766	0.748	0.72	0.75	0.683 <sup>259</sup>
$E_{hcp \rightarrow bcc}$	—	—	0.024	—	—	0.07 <sup>260</sup>
$E_{hcp \rightarrow fcc}$	—	—	0.048	—	—	0.06 <sup>260</sup>

Table 6-4. The fundamental properties calculated using MEAM\_I and MEAM\_II, compared with EAM, FS, DFT and experimental data.

Ti	EAM <sup>255</sup>	F-S <sup>256</sup>	MEAM_I <sup>246</sup>	MEAM_II <sup>83</sup>	DFT <sup>83</sup>	Exp.
$E_v$	1.48	1.43	1.79	2.24	2.03	>1.50 <sup>261</sup>
$E_m$	0.82	—	1.09	—	—	—
	0.96	—	0.87	—	—	—
$E_{dv}$	2.73	—	3.87	4.00	2.58	—
C	3.82	3.07±0.2	3.9	2.21	2.87	—
O	3.45	3.07±0.2	4.53	2.64	2.58	—
T	3.39	3.07±0.2	unstable	unstable	unstable	—
Basal (0001)	—	993	2144	1474	1939	2100 <sup>261</sup>
Prism(1-100)	—	1061	2145	1554	2451	1920 <sup>261</sup>
Prism(11-20)	—	1187	2352	1682	1875	—

### 6.3.2 ZBL Potential

The interatomic distances in the cascade simulations may be very short compared with traditional MD, due to the extremely high kinetic energy of the atoms. Therefore, to reproduce a realistic potential surface energy under such extreme conditions, a short-range interaction has

been developed by Ziegler, Biersack and Littmark (ZBL) <sup>247</sup>, in which the interatomic interactions are described by a universal form over a large number of the materials. The ZBL potential is based on the Thomas-Fermi and Linhard model and can be considered as a screened electrostatic potential of the nucleon-nucleon interaction <sup>262</sup>. The form of the ZBL potential is:

$$V(r) = \frac{Z_i Z_j e^2}{r_{ij}} \Phi(r_{ij}) \quad [6-20]$$

where  $Z_i$  and  $Z_j$  are the atomic number of the atoms,  $e$  is the charge of electron,  $r_{ij}$  is the interatomic distance, and  $\Phi(r_{ij})$  is the screen function. The screening function can be expressed as

$$\Phi(r_{ij}) = \sum_{i=1,4} A_i \exp(-b_i r_{ij} / a_u) \quad [6-21]$$

$$a_u = \frac{0.8854}{Z_i^{0.23} + Z_j^{0.23}} a_{Bohr} \quad [6-22]$$

where  $A_i$  and  $b_i$  are predefined parameters,  $a_{Bohr}$  is the Bohr radius (0.539177 Å).

Table 6-5. The predefined parameters of the ZBL potential <sup>247</sup>.

$i$	$A_i$	$b_i$
1	0.1818	3.2000
2	0.5099	0.9423
3	0.2802	0.4028
4	0.02817	0.2016

## 6.4 Defect Analysis Method

In the current studies, both common neighbor analysis (CNA) and lattice matching analysis (LMA) have been employed. In essence, these two methods characterize similar aspects of the bonding and local environments of the vacancies and interstitials. The numbers of surviving stable defects using both methods are found to be consistent with each other. However, they differ in several aspects, which are discussed in details in the following.

### 6.4.1 Common Neighbor Analysis

The CNA<sup>263</sup> method identifies a given atom's nearest neighbors within a certain cutoff radius. In  $\alpha$ -titanium, a cutoff value of 3.37 Å has been used to identify the first nearest neighbors. This is much longer than the bond length even with consideration of the thermal vibrations, but shorter than the second nearest neighbor distance. In general, CNA examines the common neighbors of specific atom and provides the following information: (1) the total number of the atoms in the system, (2) the total number of the bonds of each atom, (3) the number of the atoms in each subset with a different coordination number.

Furthermore, CNA has been extended to distinguish the stacking sequence of HCP and FCC<sup>263</sup>. In both structures, the numbers of first nearest neighbors and second nearest neighbors are the same. Therefore, third nearest neighbor information is needed to achieve this. It is noted this extended analysis has been solely applied to the atoms with twelve neighbors. If an atom with twelve coordination number is neither HPC nor FCC, it is indicated as “\*Others”. A typical analysis results is given in Table 6-6.

Unfortunately, CNA cannot directly provide either the accurate positions for or the number of vacancies and interstitials. For instance, if a titanium vacancy is created in the system, CNA characterizes a certain number of the atoms having a less neighbor than they should, providing the local environment of vacancy position, from which the position of vacancy may be indirectly extracted. However, at finite temperature, the thermal vibration and diffusion process will make the detection of the accurate position of a vacancy very difficult. Furthermore, if many vacancies are present, there is no systematic way to determine how many vacancies are in the system, as the number depends on the spatial distribution of the vacancies and interstitials. Overall, the number of the defects can be indirectly estimated using CNA, the accurate number and positions are yet very difficult to obtain.

Table 6-6. Coordination number distributions provided by CNA with distinguishing HPC and FCC stacking sequence. \*Others means other types of stacking sequence, not FCC and HCP.

A) Value of cut-off: 3.370	
B) # of Coordination	# of atoms
10	: 12
11	: 110
12	: 63835
13	: 43
14	: 0
15	: 0
Total	: 64000
C) Types of structure # of atoms among 12 coordination	
HCP	: 63779
FCC	: 2
Others*	: 54
Total	: 63835

#### 6.4.2 Lattice Matching Analysis

LMA is an approach that compares the positions of atoms with reference lattice sites. The reference lattice is usually chosen to be the structure after long time equilibration at certain temperature. The schematic of LMA is illustrated in Figure 6-5. For a given lattice site of reference structure, LMA searches atoms within a certain radius of that site, typically 40% of the bond length. If there is an atom within the radius, the site is considered as being occupied.. Otherwise, the site is regarded as a vacancy. If an atom does not belong to any site, then it is considered as an interstitial.

Therefore, LMA provides the positions of vacancies and interstitial. Moreover, the number of defects is easily calculated within LMA. Nevertheless, the quality of LMA depends on the reference lattice, unlike CNA, which solely relies on the positions of atoms. In some cases, the reference lattice is difficult to define, such as polycrystalline systems with grain boundaries, in which CNA is more straightforward. Therefore, LMA and CNA are complementary to each other. Due to this, both methods are employed in this study.

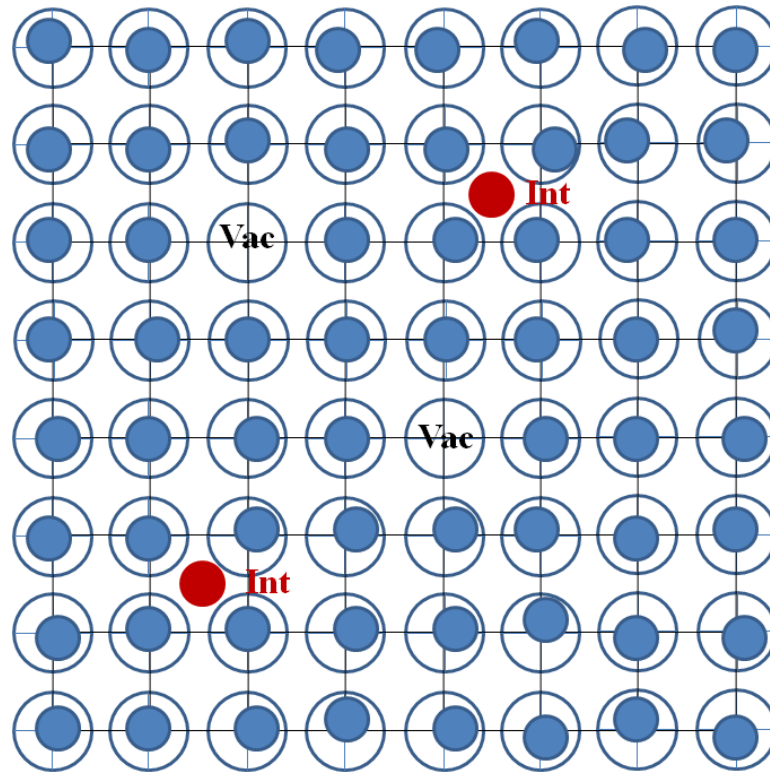


Figure 6-5. The schematics of lattice matching analysis (LMA). Both interstitials and vacancies are shown.

## 6.5 Single Crystal Results and Discussions

The threshold energy,  $E_d$ , is probably the most important single parameter that can be used to provide estimates about the production of survival Frenkel defects in cascade simulations<sup>245</sup>. If the PKA energy is less than the threshold energy, atoms undergo large amplitude vibrations, without forming stable Frenkel pairs. To obtain its value, cascade simulations are carried out along various crystallographic directions. The orientation dependence of  $E_d$  in  $\alpha$ -titanium using MEAM\_I potential is shown in Figure 6-6, compared with a previous study using the FS potential.

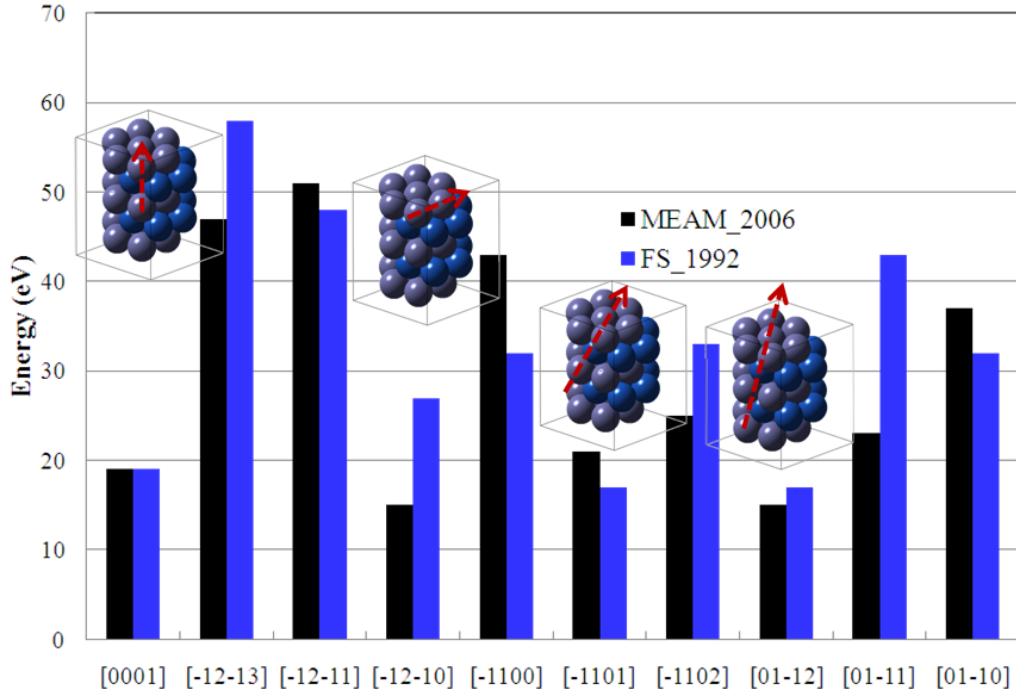


Figure 6-6. Threshold energies at various crystallographic orientations using MEAM\_I, compared with previous results using FS potential.

It is found that there is a significant variation in the threshold energy, ranging from a minimum value of 14 eV in [01-22] direction to the maximum number of 52 eV in [-12-11] direction using MEAM\_I. In addition, several orientations have threshold energies less 20 eV. It is found that there is a head-on collision between atoms when PKA follows these low energy directions. In the case of high-index PKA directions, such collision does not happen. Since the displacements in the cascade simulations are easily affected by these directions, this can be used to estimate the upper limit of the surviving defects.

$$N_{NRT} = 0.8E_{dam} / 2E_d \quad [6-23]$$

where  $E_{dam}$  is the damage energy and  $E_d$  is the average threshold energy. It is noted that the damage energy is only a portion of the PKA, which is lost during the elastic collision process. The other part energy lost is due to the electronic excitation and ionization. However, MD

simulations do not consider such electronic effects. Therefore, in MD simulations, the damage energy is approximated equivalent to the PKA energy.

Overall, MEAM\_I and FS potentials predict similar trend, although certain differences exist in different orientations. The average value of the threshold energy is estimated to be approximately 25 eV with MEAM\_I, which is smaller than value predicted using the FS potential (30 eV). Therefore, from the NRT relationship (Equation 6-23), the number of stable survival Frenkel defects predicted by MEAM\_I is estimated to be higher than that of FS potential.

Once the threshold energy is obtained, the cascade simulations are carried out in single crystal titanium. During such simulations, a PKA with high kinetic energy is introduced into the system after long time equilibration, creating a large number of defects within a short period of time. Initially, high-index directions of PKA, such as [13-45], [11-24], and [11-21], are chosen to avoid channeling effects. However, to explore anisotropic effects, some low-index direction simulations are also carried out. For a particular PKA energy at a specific orientation, the position of the PKA is also varied to achieve average effects. For all cascade simulations in a single crystal system, the defect production and evolution process are very similar. A detailed description of cascade simulation when  $E_{\text{PKA}} = 1 \text{ keV}$  at 100K is given below. The snapshot of cascade simulation with  $\text{PKA} = 1 \text{ keV}$  at 100 K is shown in Figure 6-7. It is observed that initially the number of defects increases very rapidly until a maximum number of Frenkel defect reached. This is the ballistic phase of the cascades usually last 0.3 ~ 0.4 ps. A highly disordered region is formed around the PKA within such phase. After ~ 0.4 ps, recombination of vacancies and interstitial begins, which results in a decrease in the number of defects. This subsequent process is considered as the relaxation phase. Soon after, the number of surviving Frenkel defects

reaches a steady state, accompanied by lattice restoration, leaving a small amount of defects and defect clusters inside the system.

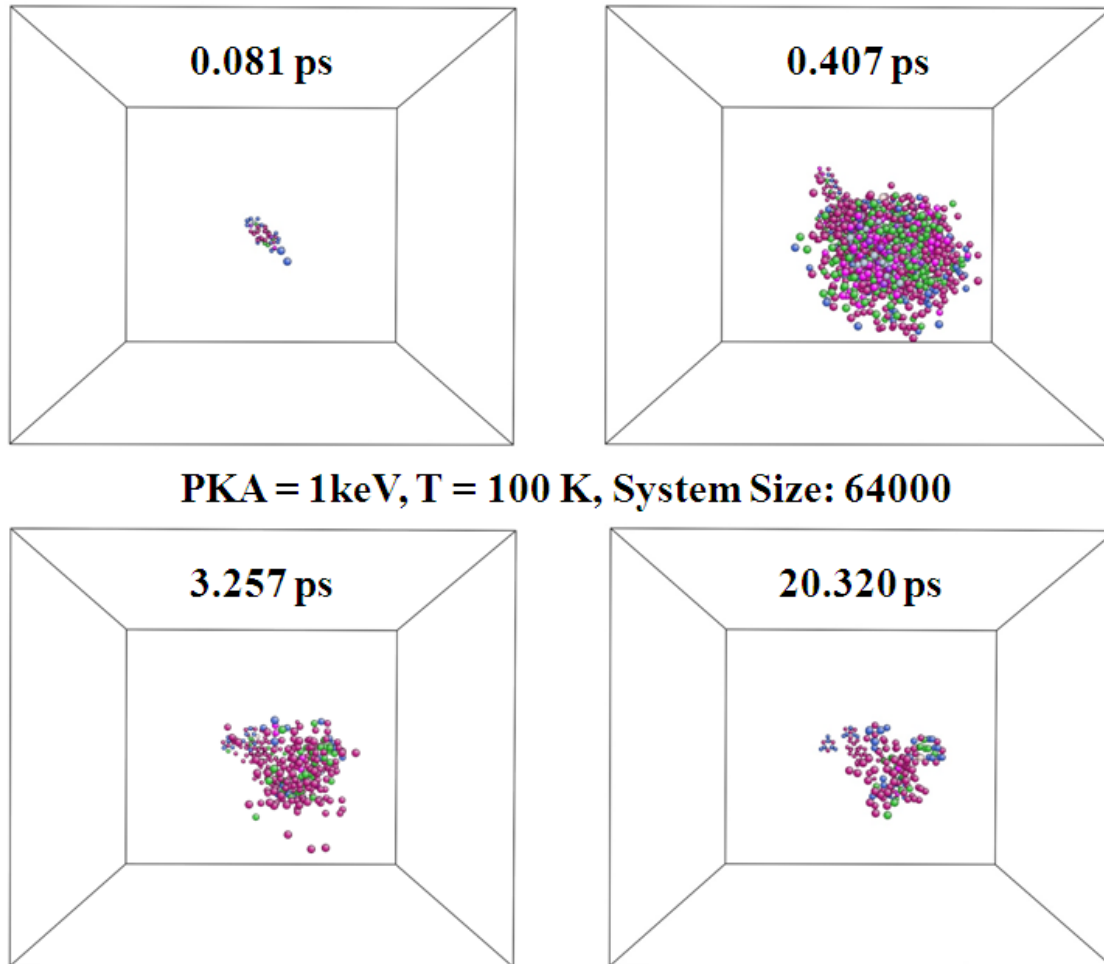


Figure 6-7. Snapshot of cascade simulation in single crystal system at different simulation time. Only the atoms with coordination rather than 12 are shown.

To achieve statistically meaningful results, several cascades simulations with different PKA directions and positions have been carried out for a given value of PKA energy. The numbers of Frenkel defects as a function of simulation time for PKA energy of 1 keV, 3 keV, 5 keV and 10 keV of PKA are shown in Figure 6-8. It can be seen that there is a peak for each curve, which defines the transition from the ballistic phase to relaxation phase. The height of the peak, which is the maximum number of Frenkel defects created during the simulations, increases

with increases in the PKA energy. The time to reach a steady state also increases as a function of PKA energy. For instance, for PKA energy with 1keV, the numbers of surviving Frenkel defects reach a steady state after 4 ps. For 10 keV simulations, it requires approximately 6 ps to reach steady state. From Figure 6-8, it can be also seen that all simulations with the same PKA energy nearly overlap with each other, indicating reasonable statistics has been achieved. The average value for a given PKA energy has been taken to establish the relationship between PKA energy and surviving Frenkel defects.

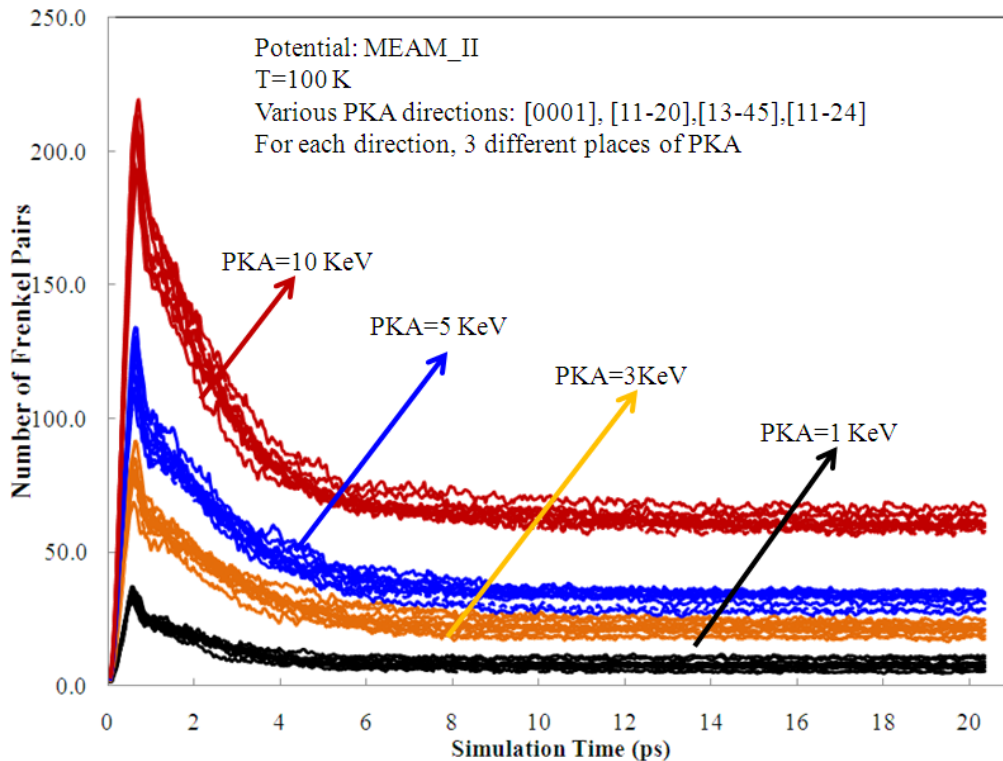


Figure 6-8. The number of survival Frenkel defects as a function of simulation time with various directions, positions, and energies of primary knock-off atom.

In principal, high index directions for the PKA should be used to avoid channeling effects. To investigate the effects of orientations and lattice symmetry, simulations with low index directions have also been carried out. For each value of PKA energy, PKA with different positions along [13-45], [11-24], [0001], [11-21] and [11-20] are simulated. The average

numbers of survival Frenkel defects with various PKA energies are shown in Figure 6-9. No significant variation is observed at any energy. Therefore, the effects of anisotropy of the HCP structure are rather weak, which indicates that the cascade feature is insensitive to anisotropy of the crystal structure.

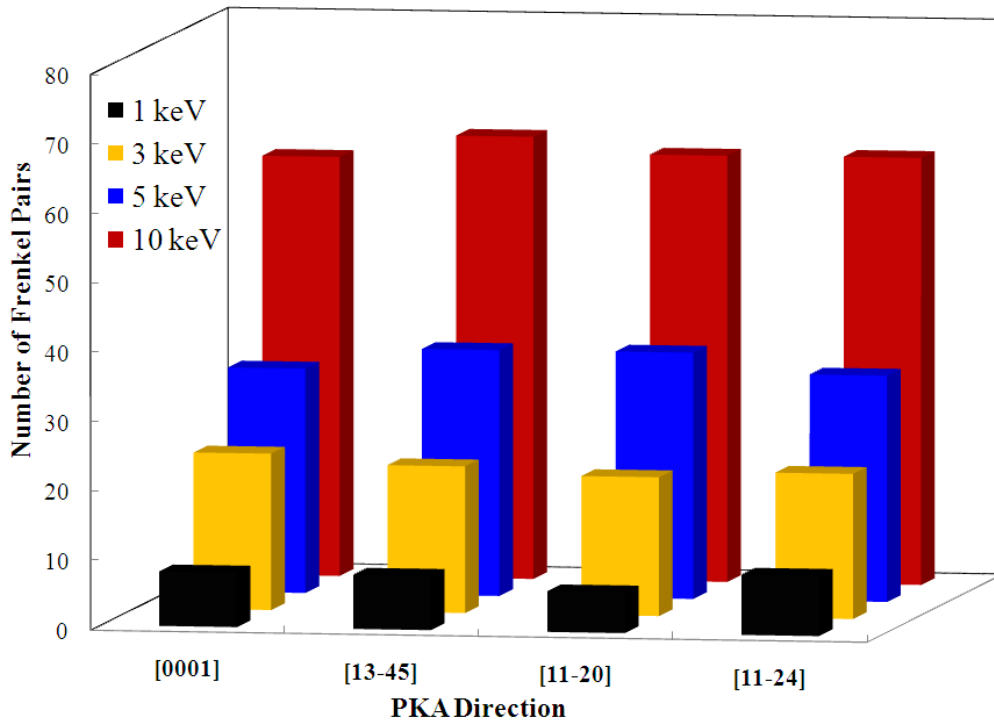


Figure 6-9. The effect of PKA directions on survival Frenkel defects.

The dependence of the number of surviving Frenkel defects on the PKA energy is shown in Figure 6-10. It is seen that the number of Frenkel pairs using MEAM\_I and MEAM\_II is higher than that of FE potential at given PKA energy. This is expected, as the threshold energy is lower for FS potential. Since the number of Frenkel defects and the number predicted by NRT model have a definite relationship,  $N_{NRT}$  prediction is also shown in Figure 6-10. It is found that the relative ratio of  $N_F$  with respect to  $N_{NRT}$  using MEAM potentials is higher than FS potential.

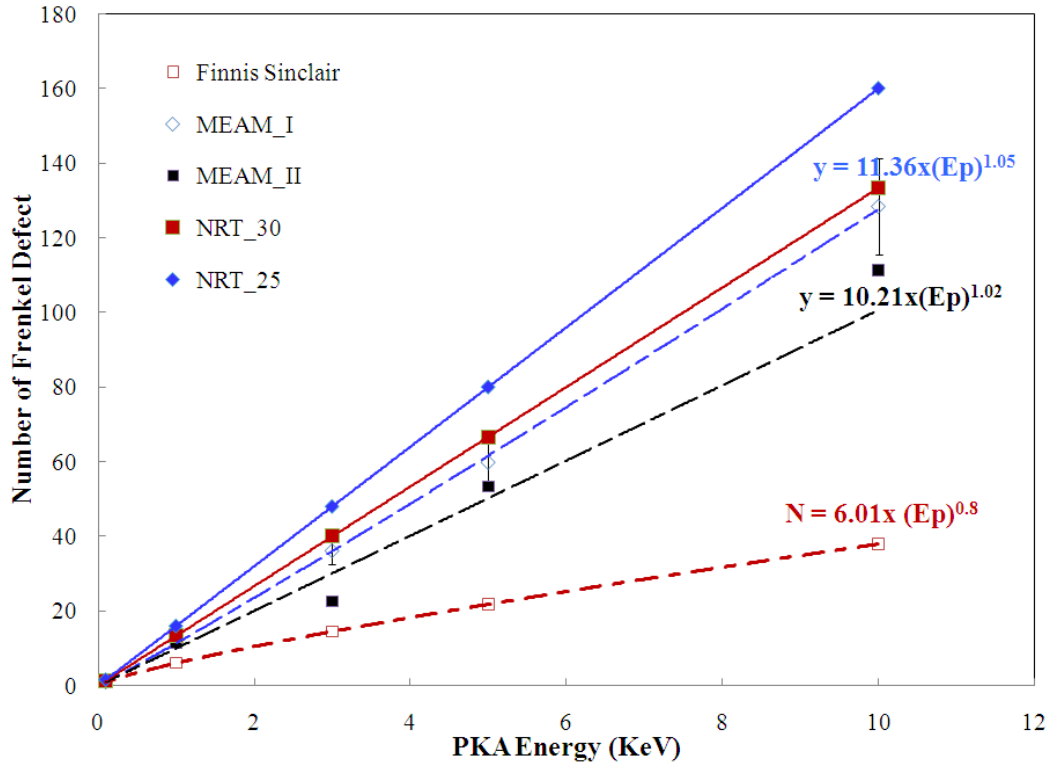


Figure 6-10. The comparison of number of survival Frenkel defects as a function of PKA energies between MEAM\_I, MEAM\_II, and FS potentials. The numbers predicted by NRT model with difference threshold energies are also indicated.

Detailed analysis leads to the conclusion that the large difference in surviving Frenkel defects is considered to be caused by the potentials. Although these three potential predict similar values of cohesive energy, lattice parameters,  $c/a$  ratio, elastic constants, vacancy and interstitial energy, and surface energies for equilibrium structure of Ti, they are different in several aspects.

First, the potentials were fitted to different structures and data. The FS potential was fitted to an imaginary FCC lattice, which does not exist in the phase diagram of titanium, with the nearest neighbor distance equal to the lattice parameter,  $a$ , of the hexagonal lattice and with a negative stacking fault energy, assuming the third-nearest-neighbor interaction is just a small perturbation compared with first and second nearest neighbor interactions. This can be done

because the first and second nearest neighbor environment of FCC and ideal HCP structure are identical; the negative stacking fault energy assures the preference for the HCP structure. By contrast, the MEAM\_I parameters were determined by fitting to the fundamental properties of HCP structure of titanium, which includes elastic constants, surface energy, stacking fault energy, and vacancy formation energy. In addition, the stability of the HCP structure at finite temperatures was verified by considering a thermal expansion coefficient for MEAM\_I. For MEAM\_II, the parameters were fitted to the physical properties of several phase of titanium, including  $\alpha$ ,  $\beta$ ,  $\omega$ , FCC, and simple hexagonal phases, to improve the accuracy and extend the applicability. In addition, a DFT database for test of the potential was employed during the fitting process of MEAM\_II. It included additional interstitial defects in  $\alpha$  and  $\omega$ , phonon spectra for  $\alpha$ ,  $\beta$ , and  $\omega$ , surface energies for  $\alpha$  and  $\omega$ , and stacking fault energy in  $\alpha$ . As a result, the phase transformation is reasonably described by MEAM\_II.

Second, the short-range interactions of these potentials are very different. The potential energy ( $E^u$ ) as a function of nearest-neighbor distance is given in Figure 6-11. It is noted that the  $E^u$  (in Equation 6-11) is function for uniform expansion or contraction in the reference structure. From Figure 6-11, it can be seen that MEAM\_I is least repulsive at short range. Consistent with this, MEAM\_I predicts the highest number of stable Frenkel pair after cascade simulations. MEAM\_II is more repulsive than MEAM\_I, especially in the range of 1 - 1.5 Å. However, it is less repulsive than FS when the interatomic distance is shorter than  $\sim 0.7$  Å or larger than  $\sim 1.6$  Å. The FS potential is the most repulsive one when the first-nearest neighbor distance is larger than  $\sim 1.6$  Å. In agreement with this, FS predicts the least number of stable Frenkel defects in the cascade simulations.

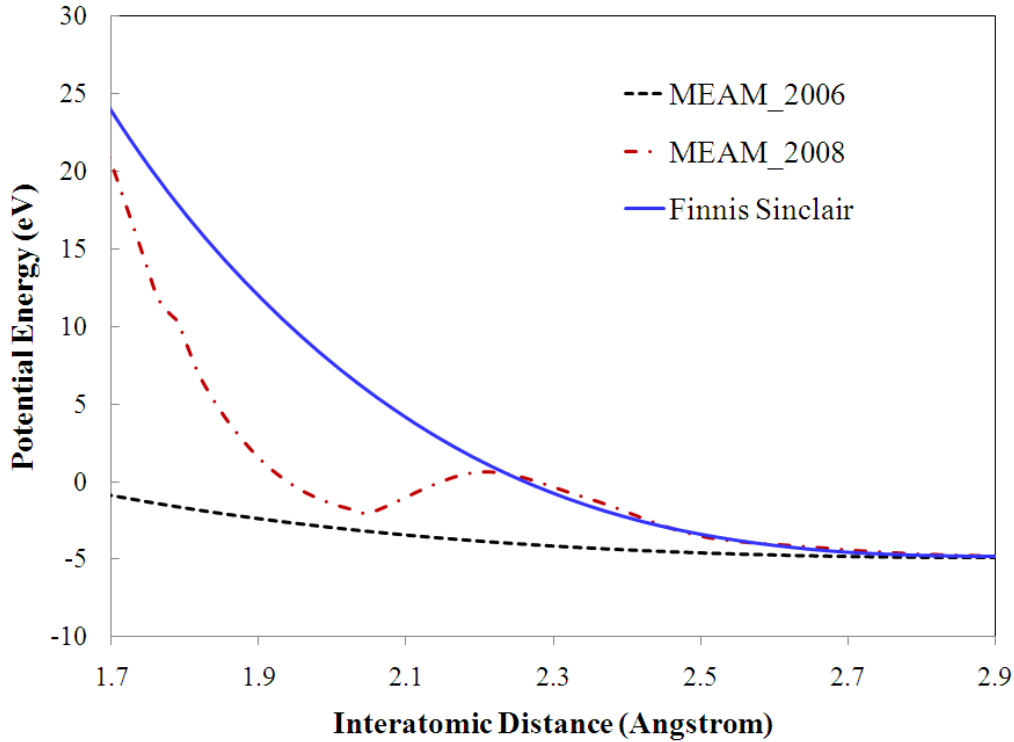


Figure 6-11. The potential energy as a functional of nearest neighbor distance using FS, MEAM\_2006 and MEAM\_2008 potentials.

In addition, different cutoffs have been used when connecting these potentials with ZBL potential. For the FS potential, the ZBL potential is used for spacing less than 1.1 Å and FS potential is used when spacing greater than 2.09 Å. An exponential potential with four parameters is employed to join these two potential. For MEAM\_2008, the potential is used when interatomic distance is larger than 1.7427 Å and ZBL is used when distance is shorter than 1.5 Å. From Figure 6-11, it is also observed that MEAM\_2008 and FS are very similar when interatomic distance is longer than 2.2 Å. Therefore, if this is used as a cutoff for both MEAM\_2008 and FS, they are expected to predict similar results. In summary, the differences in the cutoff and connecting functions lead to significant changes in the overall potential energy functions, which have a significant effect on the radiation damage and defect distributions

## 6.6 Effects of Grain Boundaries

Grain boundaries can be considered as sources and sinks of defects. Therefore, they can have a significant influence on the defect generation, evolution, and distribution, which will further determine the microstructures and mechanical properties of materials. There are experimental indications that metals with grain sizes in the nano scale may be more radiation resistant than that with coarse-grains<sup>264</sup>. However, the underlying reasons are not fully understood. Therefore, it is of great importance to perform cascade simulations with the presence of grain boundaries.

Polycrystalline titanium is generated with four grains for cascade simulations, with a 2D hexagonal texture. Each hexagonal is filled with a single crystal titanium orientated with [0001] along the columnar direction. The in-plane orientations are chosen in such a way that the grain boundaries between grains are high-energy tilt grain boundaries, ensuring the microstructure is stable. The grain size of polycrystalline system is approximately 20 nm, with 252838 atoms in the system.

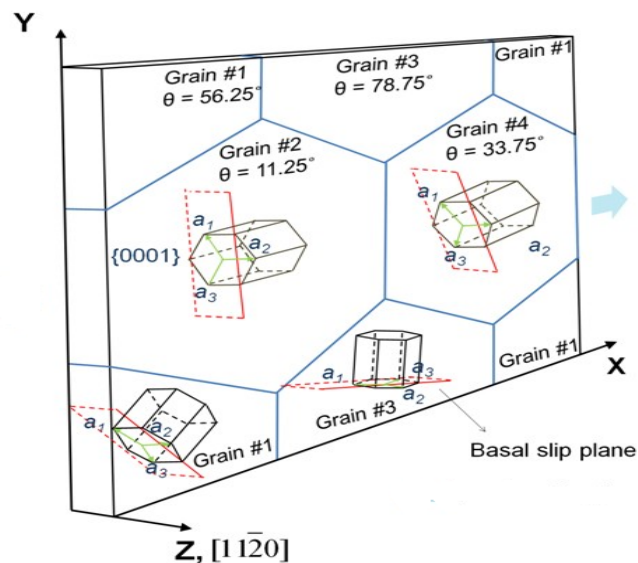


Figure 6-12. Polycrystalline structure of titanium in the cascade simulations. Courtesy of D. H. Kim.

Similar to the single crystal study, various direction and position of PKA have been simulated for a given value PKA energy. It is found that the effects of grain boundaries can be classified into two cases. First, when the PKA energy is low ( $\sim 1$  keV), if the PKA is located at the center region of one grain, the effects of grain boundaries are insignificant. This case is very similar to that in the single crystal, as the amorphous region created by the PKA does not interact with the grain boundaries. Consistent with this, the number of surviving Frenkel defects is similar to that in the single crystal.

Second, there are significant effects of the grain boundaries. This could happen when the PKA energy is larger than 3 keV or the position of PKA is close to the grain boundaries. For example, when PKA = 10 keV, the defect evolution process is shown in Figure 6-13. It can be seen that the defects created by PKA quickly reach the grain boundaries and interact with them. Furthermore, it is found that grain boundaries also have a significant effect on the relaxation phase, limiting the ability of atoms to return to their equilibrium positions. Therefore, the number of surviving Frenkel defects in polycrystalline system for such case is much higher than that in the single crystal. In addition, a portion of the defects created by PKA become part of the grain boundaries, leading to a grain boundary growth. The cascade morphologies are found to be strongly influenced by the structure of grain boundaries.

In summary, cascades simulations have been carried in polycrystalline titanium systems, including various PKA energies, directions, and positions. It is found that when the PKA energy is small and PKA is far from the grain boundaries, there is no strong interaction between them, generating similar number of surviving Frenkel defects as in the single crystal. However, when PKA energy is relatively large or PKA is close to the grain boundaries, numerous points defects are created along the interfaces, leading to a grain boundary growth. The numbers of surviving

Frenkel defects in such cases are much higher than that in single crystal cascade simulations. It is also found that grain boundary structures in the polycrystalline systems after cascade simulations are highly disordered and the morphologies strongly depend on these grain boundary structures.

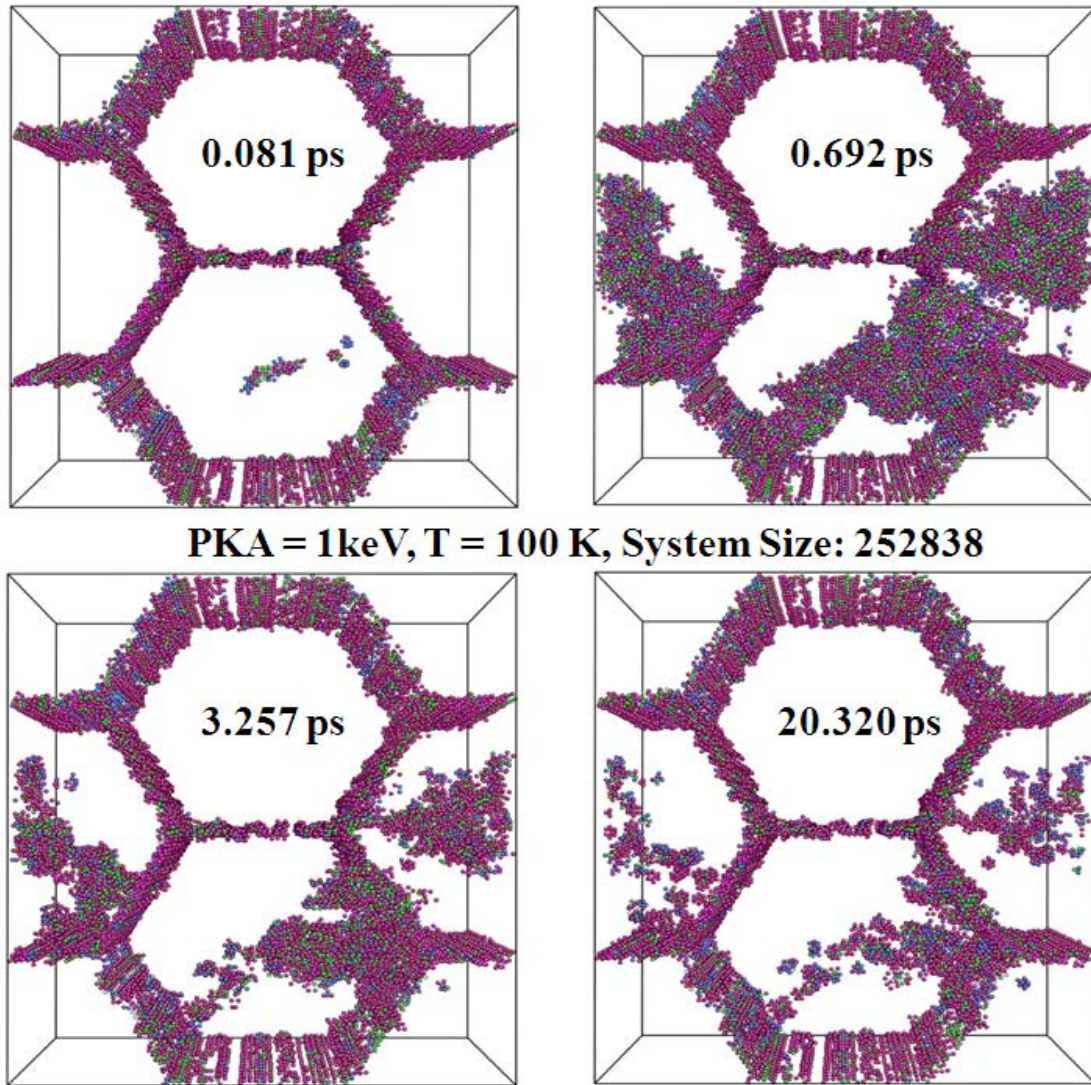


Figure 6-13. Snapshot of cascade simulation of polycrystalline system when PKA = 10 keV at 100K. Only the atoms with coordination rather than 12 are shown.

## CHAPTER 7 SUMMARY AND FUTURE WORK

In this dissertation, the structure and stability of defects in structurally complex materials have been determined and predicted using atomic level simulations. The production, evolution, and dynamic behavior of defects have been explored. A great effort has been focused on establishing the relationship between fundamental properties of bulk materials and effects of point defects.

### 7.1 Lithium Niobate

A large experimental body of literature on lithium niobate, a technologically important ferroelectric, suggests that non-stoichiometric defects dominate its physical behavior, from macroscale switching to nanoscale wall structure. The exact structure and energetics of such proposed intrinsic defects and defect-clusters remained unverified by either first principles calculations or experiments. Here, density-functional theory (DFT) was used to determine the dominant intrinsic defects in  $\text{LiNbO}_3$  under various conditions. In particular, in an  $\text{Nb}_2\text{O}_5$ -rich environment, a cluster consisting of a niobium antisite compensated by four lithium vacancies was predicted to be the most stable defect structure, thereby verifying a conjecture in the literature. Under  $\text{Li}_2\text{O}$ -rich conditions, the lithium Frenkel defect was predicted to be the most stable, with positive defect formation energy (DFE). This was proposed as the underlying reason that the vapor transport equilibration (VTE) method can grow stoichiometric  $\text{LiNbO}_3$ . The effects of temperature and oxygen partial pressure were also explored by combining the DFT results with thermodynamic calculations. The relative stabilities of various defect cluster arrangements of lithium vacancies around a niobium antisite in  $\text{LiNbO}_3$  were determined. Their effects on the ferroelectricity of the system were also discussed. It was found that at room temperature the non-uniaxial dipole moments associated with the defect clusters could locally

affect the properties of the system. The diffusion mechanism was predicted to be through first nearest neighbor jumps on the Li-sublattice. The diffusivity of lithium vacancy was found to be extremely low at room temperature, which indicated that the defect complexes should be rather stable. These predictions provided a picture of a very rich defect structure in lithium niobate, which has important effects on its physical behavior at the macroscale.

The incorporation site preference and corresponding charge compensation mechanisms of several impurities in  $\text{LiNbO}_3$  were predicted based on DFT calculations of possible defect clusters at congruent and stoichiometric growth conditions respectively. In general, it was found that impurities occupy lithium sites compensated by lithium vacancies under  $\text{Nb}_2\text{O}_5$  reference state. In addition, impurities on both lithium and niobium site were predicted to be dominant under  $\text{Li}_2\text{O}$  reference state. However, due to the effects of intrinsic defects and method of incorporation impurities, the concentration of impurities on niobium site was predicted to be negligible for stoichiometric sample. Interestingly, it was found that Mg had a strong tendency to occupy both lithium and niobium sites even under  $\text{Nb}_2\text{O}_5$  rich conditions. Increasing the concentration of Mg would lead to an increase in the value of its chemical potential, which would further result in a switch of dominant defects from Mg on lithium site compensated by intrinsic lithium vacancies to Mg on both sites. The prediction is consistent with the experimental observation that Mg is mainly on lithium sites at low dopant concentration and on both sites at high concentrations. It was also found that  $\text{Fe}^{3+}$  is more energetically favorable than  $\text{Fe}^{2+}$  under both reference states. Therefore, without special treatment, the  $\text{Fe}^{3+}$  was predicted to be the majority species. In agreement with this, the experimental concentration of  $\text{Fe}^{2+}$  is usually at least one order of magnitude lower than the  $\text{Fe}^{3+}$  concentration. The thermal ionization energies and charge transfer levels of impurities were calculated, especially for transition metal

iron. The charge transfer level of  $\text{Fe}^{2+}/\text{Fe}^{3+}$  was calculated to be 1.34 eV, which corroborated the long-time conjecture that there was a charge transfer effect in the Fe-doped  $\text{LiNbO}_3$ . The relative position of this charge transfer level with regard to the band structure was illustrated, with consideration of the effects of intrinsic defects  $\text{Nb}_{\text{Li}}^{4+}/\text{Nb}_{\text{Li}}^{5+}$ . The charge transfer levels of Mg, Nd, and Er and were also calculated and discussed.

The suggested future work is to investigate the effects of defects at interfaces, such as polarization domain walls. It is known that domain walls are atomic sharp from simulations, usually a few unit cells wide. However, the experimental measurements of such width are of the order of dozens nanometers. Studies of point defects and defect clusters would contribute to resolving this discrepancy. These point defects could introduce both short range electrostatic interaction and long range elastic interaction into the system, which could locally change the domain wall structure and may cause a broadening effects. Therefore, it is of great significance to simulate the defects at domain wall to determine how they may affect the domain wall width.

Another direction would be to explore the effects of external fields, in particular, electrical field. In experiments, the cohesive field of congruent materials is almost an order of magnitude larger than that of stoichiometric lithium niobate. The hypothesis is that such differences are caused by point defects. DFT calculations can provide theoretical evidence to corroborate or refute such a conjecture. It has been shown that the defect clusters have dipole moments. For switching the polarization, first nearest neighbor jumping is requisite for defect clusters. Due to the high-energy barrier, this jumping process is rather difficult at room temperature. Nevertheless, only short distance movements are needed for polarization inversion of bulk atoms, which is relatively easy. Therefore, by simulating defects under electrical field, the

polarization reversal process can be elucidated. The corresponding structural changes of defect clusters and their effects on the other fundamental properties on the materials can be determined.

## **7.2 Ceria-based Materials**

We critically assessed the materials fidelity of six interatomic potentials for ceria, based on predicted lattice constants, thermal expansion, chemical expansion, dielectric properties, oxygen migration energy and mechanical properties. While, no potential can reproduce all fundamental properties, the Gotte (2007) and Grimes potentials display the combination of highest fidelity widest range of applicability. The simulations showed that sub-stoichiometry lead to a significant softening of the elastic constants, which was consistent with experimental results. Similar results were observed for doped ceria systems. The simulations showed that both sub-stoichiometry and aliovalent doping of ceria lead to large decreases in the elastic constants of the material, using the best available potential(s) for each physical property. These decreases arise from the significantly reduced strength of ionic interactions. If this elastic softening were to be so large as to threaten the mechanical integrity of the system, then it would pose a challenging problem for the design of ceria-based electrolytes.

It would thus be of significant value to identify a strategy for increasing the ionic conductivity that does not result in a significant softening in the elastic properties. A co-doping strategy is a possible solution to achieve both high ionic conductivity and mechanical strength. Using multiple trivalent dopants could suppress the ordering effects of oxygen vacancy and increase in the configurational entropy of the system, which results in enhancement of the ionic conductivity. In addition, due to the mismatch between host cations and dopant ions, strains can be created, which may strengthen the materials.

### 7.3 Titanium

Cascade simulations were carried out in  $\alpha$ -titanium, including various energies, positions and orientations of primary knock-on atoms to obtain statistically meaningful results. The dependence of Frenkel defects on the time was established and two different phases during the cascade simulation were observed: the ballistic and relaxation phase. The effects of PKA energies on survival Frenkel defects were evaluated and compared with previous study using FS potentials. It was found that both MEAM potential in this study predicted higher value of the survival Frenkel defects. This is because both MEAM potentials predict lower average threshold energies, which results in a higher number of defects in the NRT model. The orientation effects of the PKA were also evaluated and no significant effect were found. The effects of grain boundaries were evaluated.

For the practical application of titanium as a cladding materials, the fundamental understanding of the mechanical properties, especially the plastic deformation behavior of the initial stage during the radiation, is required. There are some experimental indications that nano-crystalline materials have a higher tolerance of radiation damage. Therefore, it is crucial to perform mechanical test on the polycrystalline system after cascade simulations. Some simulations might predict microstructure evolution with atomic resolution. Furthermore, these simulations might also provide useful insights about the deformation mechanisms, such as dislocation and twinning.

## LIST OF REFERENCES

- 1 M. W. Barsoum, *Fundamentals of Ceramics* (Taylor & Francis, Bodmin, Cornwall, UK, 2002).
- 2 W. D. Callister, *Materials Science and Engineering: An Introduction* (John Wiley & Sons Inc., 2002).
- 3 J. H. Spaeth and H. Overhof, *Point Defects in Semiconductors and Insulators* (Springer, New York, USA, 2003).
- 4 J. Garcia Sole, L. E. Bausa, and D. Jaque, *An Introduction to the Optical Spectroscopy of Inorganic Solids* (John Wiley & Sons Ltd., West Sussex, England, 2005).
- 5 G. H. Dieke, *Spectra and Energy Levels of Rare Earth Ions in Crystals* (Interscience Publishers, New York, USA, 1968).
- 6 Y. Tanabe and S. Sugano, *J. Phys. Soc. Jpn.* **9**, 753 (1954).
- 7 Y. Tanabe and S. Sugano, *J. Phys. Soc. Jpn.* **9**, 766 (1954).
- 8 H. Holleck, *Journal of Vacuum Science & Technology a-Vacuum Surfaces and Films* **4**, 2661 (1986).
- 9 X. Jiang, M. Wang, K. Schmidt, E. Dunlop, J. Haupt, and W. Gissler, *J. Appl. Phys.* **69**, 3053 (1991).
- 10 V. Gopalan, V. Dierolf, and D. A. Scrymgeour, *Annu. Rev. Mater. Res.* **37**, 449 (2007).
- 11 K. Duncan, in *Department of Materials Science and Engineering* (University of Florida, Gainesville, 2001), Vol. Ph.D.
- 12 K. K. Wong, *Properties of Lithium Niobate* (INSPEC, Stevenage, Herts, UK, 2002).
- 13 S. Erdei and V. T. Gabrieljan, *Cryst. Res. Technol.* **24**, 987 (1989).
- 14 H. L. Wang, Y. Hang, J. Xu, L. H. Zhang, S. N. Zhu, and Y. Y. Zhu, *Mater. Lett.* **58**, 3119 (2004).
- 15 S. C. Abrahams and P. Marsh, *Acta Crystallogr., Sect. B: Struct. Sci.* **42**, 61 (1986).
- 16 K. Kitamura, J. K. Yamamoto, N. Iyi, S. Kimura, and T. Hayashi, *J. Cryst. Growth* **116**, 327 (1992).
- 17 K. Kitamura, Y. Furukawa, K. Niwa, V. Gopalan, and T. E. Mitchell, *Appl. Phys. Lett.* **73**, 3073 (1998).
- 18 F. S. Chen, *Journal of Applied Physics* **40**, 3389 (1969).

- 19 R. J. Holmes and D. M. Smyth, *J. Appl. Phys.* **55**, 3531 (1984).
- 20 R. L. Holman, *Processing of Crystalline Ceramics*, (Plenum, New Yourk, 1978).
- 21 V. Gopalan and M. C. Gupta, *Appl. Phys. Lett.* **68**, 888 (1996).
- 22 V. Gopalan, T. E. Mitchell, Y. Furukawa, and K. Kitamura, *Appl. Phys. Lett.* **72**, 1981 (1998).
- 23 A. Prokhorov and I. Kuzminov, *Physics and Chemistry of Crystalline Lithium Niobate* (Hilger, Bristol, New York, 1990).
- 24 O. F. Schirmer, O. Thiemann, and M. Wohlecke, *J. Phys. Chem. Solids* **52**, 185 (1991).
- 25 R. Mouras, M. D. Fontana, P. Bourson, and A. V. Postnikov, *J. Phys.: Condens. Matter* **12**, 5053 (2000).
- 26 D. A. Bryan, R. Gerson, and H. E. Tomaschke, *Appl. Phys. Lett.* **44**, 847 (1984).
- 27 D. L. Staebler and W. Phillips, *Appl. Opt.* **13**, 788 (1974).
- 28 E. Lallier, *Appl. Opt.* **31**, 5276 (1992).
- 29 E. Lallier, J. P. Pocholle, M. Papuchon, C. Grezesbesset, E. Pelletier, M. Demicheli, M. J. Li, Q. He, and D. B. Ostrowsky, *Electron. Lett.* **25**, 1491 (1989).
- 30 L. F. Johnson and A. A. Ballman, *J. Appl. Phys.* **40**, 297 (1969).
- 31 S. J. Field, D. C. Hanna, D. P. Shepherd, A. C. Tropper, P. J. Chandler, P. D. Townsend, and L. Zhang, *Opt. Lett.* **16**, 481 (1991).
- 32 V. Dierolf, T. Morgus, C. Sandmann, E. Cantelar, F. Cusso, P. Capek, J. Spirkova, K. Polgar, W. Sohler, and A. Ostendorf, *Radiat. Eff. Defects Solids* **158**, 263 (2003).
- 33 V. Dierolf, C. Sandmann, S. Kim, V. Gopalan, and K. Polgar, *J. Appl. Phys.* **93**, 2295 (2003).
- 34 V. Dierolf, C. Sandmann, V. Gopalan, S. Kim, and K. Polgar, *Radiat. Eff. Defects Solids* **158**, 247 (2003).
- 35 H. Sothe and J. M. Spaeth, *J. Phys.: Condens. Matter* **4**, 9901 (1992).
- 36 W. Keune, S. K. Date, I. Dezsi, and U. Gonser, *J. Appl. Phys.* **46**, 3914 (1975).
- 37 W. Keune, S. K. Date, U. Gonser, and H. Bunzel, *Ferroelectrics* **13**, 443 (1976).
- 38 L. Kovacs, L. Rebouta, J. C. Soares, M. F. Dasilva, M. Hageali, J. P. Stoquert, P. Siffert, C. Zaldo, Z. Szaller, and K. Polgar, *Mater. Sci. Eng., B* **9**, 505 (1991).

- 39 T. Gog, M. Griebenow, and G. Materlik, *Phys. Lett. A* **181**, 417 (1993).
- 40 T. Gog, T. Harasimowicz, B. N. Dev, and G. Materlik, *Europhys. Lett.* **25**, 253 (1994).
- 41 C. Prieto and C. Zaldo, *Solid State Commun.* **83**, 819 (1992).
- 42 L. Rebouta, M. F. Dasilva, J. C. Soares, M. Hageali, J. P. Stoquert, P. Siffert, J. A. Sanzgarcia, E. Dieguez, and F. Agullolopez, *Europhys. Lett.* **14**, 557 (1991).
- 43 I. Baumann, R. Brinkmann, M. Dinand, W. Sohler, L. Beckers, C. Buchal, M. Fleuster, H. Holzbrecher, H. Paulus, K. H. Muller, T. Gog, G. Materlik, O. Witte, H. Stolz, and W. vanderOsten, *Appl. Phys. A: Mater. Sci. Process.* **64**, 33 (1997).
- 44 T. Nolte, T. Pawlik, and J. M. Spaeth, *Solid State Commun.* **104**, 535 (1997).
- 45 D. M. Gill, J. C. Wright, and L. Mccaughan, *Appl. Phys. Lett.* **64**, 2483 (1994).
- 46 D. M. Gill, L. McCaughan, and J. C. Wright, *Phys. Rev. B* **53**, 2334 (1996).
- 47 O. Witte, H. Stolz, and W. vanderOsten, *J. Phys. D* **29**, 561 (1996).
- 48 V. V. Kharton, F. M. Figueiredo, L. Navarro, E. N. Naumovich, A. V. Kovalevsky, A. A. Yaremchenko, A. P. Viskup, A. Carneiro, F. M. B. Marques, and J. R. Frade, *J. Mater. Sci.* **36**, 1105 (2001).
- 49 M. Mogensen, N. M. Sammes, and G. A. Tompsett, *Solid State Ionics* **129**, 63 (2000).
- 50 V. V. Kharton, F. M. B. Marques, and A. Atkinson, *Solid State Ionics* **174**, 135 (2004).
- 51 T. H. Etsell and S. N. Flengas, *Chemical Reviews* **70**, 339 (1970).
- 52 V. V. Kharton, E. N. Naumovich, and A. A. Vecher, *Journal of Solid State Electrochemistry* **3**, 61 (1999).
- 53 S. P. S. Badwal, *Solid State Ionics* **52**, 23 (1992).
- 54 R. M. Dell and A. Hooper, *Solid Electrolytes* (Academic Press, New York, 1978).
- 55 H. Inaba, R. Sagawa, H. Hayashi, and K. Kawamura, *Solid State Ionics* **122**, 95 (1998).
- 56 T. Inoue, T. Setoguchi, K. Eguchi, and H. Arai, *Solid State Ionics* **35**, 285 (1989).
- 57 A. Trovarelli, *Catalysis Reviews-Science and Engineering* **38**, 439 (1996).
- 58 L. Minervini, M. O. Zacate, and R. W. Grimes, *Solid State Ionics* **116**, 339 (1999).
- 59 E. A. Kummerle and G. Heger, *Journal of Solid State Chemistry* **147**, 485 (1999).

- 60 B. C. H. Steele, *High Conductivity Solid Ionic Conductors* (World Scientific, Singapore, 1989).
- 61 S. A. Fabritsiev and A. S. Pokrovsky, *Fusion Eng. Des.* **65**, 545 (2003).
- 62 R. M. Martin, *Electronic Structure: Basic Theory and Practical Methods* (Cambridge University Press, New York, USA, 2004).
- 63 D. S. Sholl and J. A. Steckel, *Density Functional Theory: A Practical Introduction* (Wiley, Hoboken, New Jersey, 2009).
- 64 M. P. Allen and D. J. Tildesley, *Computer Simulation of Liquids* (Oxford University Press, Oxford, 1987).
- 65 C. Kittel, *Introduction to Solid State Physics* (John Wiley & Sons Inc., Hoboken, NY, 2005).
- 66 M. Born and R. Oppenheimer, *Annalen Der Physik* **84**, 0457 (1927).
- 67 P. Hohenberg and W. Kohn, *Phys. Rev.* **136**, B864 (1964).
- 68 W. Kohn and L. J. Sham, *Phys. Rev.* **140**, 1133 (1965).
- 69 J. P. Perdew and Y. Wang, *Phys. Rev. B* **45**, 13244 (1992).
- 70 J. P. Perdew, K. Burke, and M. Ernzerhof, *Chemical Applications of Density-Functional Theory* **629**, 453 (1996).
- 71 G. B. Bachelet, D. R. Hamann, and M. Schluter, *Phys. Rev. B* **26**, 4199 (1982).
- 72 M. Veithen and P. Ghosez, *Phys. Rev. B* **65** (2002).
- 73 K. Parlinski and Z. Q. Li, *Phys. Rev. B* **61**, 272 (2000).
- 74 Q. K. Li, B. Wang, C. H. Woo, H. Wang, and R. Wang, *J. Phys. Chem. Solids* **68**, 1336 (2007).
- 75 P. E. Blochl, *Phys. Rev. B* **50**, 17953 (1994).
- 76 G. Kresse and D. Joubert, *Phys. Rev. B* **59**, 1758 (1999).
- 77 N. A. W. Holzwarth, G. E. Matthews, R. B. Dunning, A. R. Tackett, and Y. Zeng, *Phys. Rev. B* **55**, 2005 (1997).
- 78 A. I. Liechtenstein, V. I. Anisimov, and J. Zaanen, *Phys. Rev. B* **52**, R5467 (1995).
- 79 S. L. Dudarev, G. A. Botton, S. Y. Savrasov, C. J. Humphreys, and A. P. Sutton, *Phys. Rev. B* **57**, 1505 (1998).

- 80 D. Wolf, P. Keblinski, S. R. Phillpot, and J. Eggebrecht, *J. Chem. Phys.* **110**, 8254 (1999).
- 81 S. M. Foiles, M. I. Baskes, and M. S. Daw, *Phys. Rev. B* **33**, 7983 (1986).
- 82 M. I. Baskes, *Phys. Rev. B* **46**, 2727 (1992).
- 83 R. G. Hennig, T. J. Lenosky, D. R. Trinkle, S. P. Rudin, and J. W. Wilkins, *Phys. Rev. B* **78** (2008).
- 84 T. J. Lenosky, B. Sadigh, E. Alonso, V. V. Bulatov, T. D. de la Rubia, J. Kim, A. F. Voter, and J. D. Kress, *Modelling and Simulation in Materials Science and Engineering* **8**, 825 (2000).
- 85 M. P. Allen and D. J. Tildesley, *Computer Simulation of Liquids* (Oxford Science, Oxford, 2004).
- 86 C. Gear, *Numerical Initial Value Problems in Ordinary Differential Equation* (Prentice-Hall, Englewood Cliffs, NJ, 1971).
- 87 Y. H. Hu and S. B. Sinnott, *J. Comput. Phys.* **200**, 251 (2004).
- 88 K. Huang, *Statistical Mechanics* (John Wiley & Sons Inc., New York, 1987).
- 89 H. J. C. Berendsen, J. P. M. Postma, W. F. Vangunsteren, A. Dinola, and J. R. Haak, *J. Chem. Phys.* **81**, 3684 (1984).
- 90 H. C. Andersen, *J. Chem. Phys.* **72**, 2384 (1980).
- 91 M. Parrinello and A. Rahman, *J. Appl. Phys.* **52**, 7182 (1981).
- 92 G. D. Boyd, K. Nassau, R. C. Miller, W. L. Bond, and A. Savage, *Appl. Phys. Lett.* **5**, 234 (1964).
- 93 L. Tian, V. Gopalan, and L. Galambos, *Appl. Phys. Lett.* **85**, 4445 (2004).
- 94 P. F. Bordui, R. G. Norwood, D. H. Jundt, and M. M. Fejer, *J. Appl. Phys.* **71**, 875 (1992).
- 95 C. Baumer, C. David, A. Tunyagi, K. Betzler, H. Hesse, E. Kratzig, and M. Wohlecke, *J. Appl. Phys.* **93**, 3102 (2003).
- 96 Y. H. Han and D. M. Smyth, *Am. Ceram. Soc. Bull.* **62**, 852 (1983).
- 97 H. Donnerberg, S. M. Tomlinson, C. R. A. Catlow, and O. F. Schirmer, *Phys. Rev. B* **44**, 4877 (1991).
- 98 N. Iyi, K. Kitamura, F. Izumi, J. K. Yamamoto, T. Hayashi, H. Asano, and S. Kimura, *J. Solid State Chem.* **101**, 340 (1992).

- 99 N. Zotov, H. Boysen, F. Frey, T. Metzger, and E. Born, *J. Phys. Chem. Solids* **55**, 145 (1994).
- 100 G. S. Zhdanov, S. A. Ivanov, E. V. Kolontsova, and A. E. Korneev, *Ferroelectrics* **21**, 463 (1978).
- 101 S. A. Ivanov, A. E. Korneev, E. V. Kolontsova, and Y. N. Venevtsev, *Kristallografiya* **23**, 1071 (1978).
- 102 E. M. Ivanova, N. A. Sergeev, and A. V. Yatsenko, *Crystallogr. Rep.* **43**, 303 (1998).
- 103 A. V. Yatsenko, E. N. Ivanova, and N. A. Sergeev, *Physica B* **240**, 254 (1997).
- 104 T. W. D. Farley, W. Hayes, S. Hull, R. Ward, M. T. Hutchings, and M. Alba, *Solid State Ionics* **28**, 189 (1988).
- 105 J. B. Goodenough and A. Hamnett, *Physics of Non-Tetrahedrally Bonded Binary Compounds III* (Springer-Verlag, Berlin, 1984).
- 106 I. P. Zibrov, V. P. Filonenko, P. E. Werner, B. O. Marinder, and M. Sundberg, *J. Solid State Chem.* **141**, 205 (1998).
- 107 F. Holtzberg, A. Reisman, M. Berry, and M. Berkenblit, *J. Am. Chem. Soc.* **78**, 1536 (1956).
- 108 G. Kresse and J. Furthmuller, *Comput. Mater. Sci.* **6**, 15 (1996).
- 109 G. Kresse and J. Furthmuller, *Phys. Rev. B* **54**, 11169 (1996).
- 110 P. Blaha, K. Schwarz, P. Sorantin, and S. B. Trickey, *Comput. Phys. Commun.* **59**, 399 (1990).
- 111 D. Vanderbilt, *Phys. Rev. B* **41**, 7892 (1990).
- 112 P. Pulay, *Chem. Phys. Lett.* **73**, 393 (1980).
- 113 H. Boysen and F. Altorfer, *Acta Crystallogr., Sect. B: Struct. Sci.* **50**, 405 (1994).
- 114 W. Y. Ching, Z. Q. Gu, and Y. N. Xu, *Phys. Rev. B* **50**, 1992 (1994).
- 115 D. Redfield and W. J. Burke, *J. Appl. Phys.* **45**, 4566 (1974).
- 116 A. Dhar and A. Mansingh, *J. Appl. Phys.* **68**, 5804 (1990).
- 117 H. J. Monkhorst and J. D. Pack, *Phys. Rev. B* **13**, 5188 (1976).
- 118 C. G. Van de Walle and J. Neugebauer, *J. Appl. Phys.* **95**, 3851 (2004).

- 119 C. G. Vandewalle, P. J. H. Denteneer, Y. Baryam, and S. T. Pantelides, *Phys. Rev. B* **39**, 10791 (1989).
- 120 S. G. Louie, M. Schluter, J. R. Chelikowsky, and M. L. Cohen, *Phys. Rev. B* **13**, 1654 (1976).
- 121 W. E. Pickett, K. M. Ho, and M. L. Cohen, *Phys. Rev. B* **19**, 1734 (1979).
- 122 A. F. Kohan, G. Ceder, D. Morgan, and C. G. Van de Walle, *Phys. Rev. B* **61**, 15019 (2000).
- 123 G. Makov and M. C. Payne, *Phys. Rev. B* **51**, 4014 (1995).
- 124 U. Gerstmann, E. Rauls, T. Frauenheim, and H. Overhof, *Phys. Rev. B* **67** (2003).
- 125 D. Segev and S. H. Wei, *Phys. Rev. Lett.* **91** (2003).
- 126 K. Reuter and M. Scheffler, *Phys. Rev. B* **65**, 035406 (2002).
- 127 P. Erhart and K. Albe, *J. Appl. Phys.* **102** (2007).
- 128 T. Tanaka, K. Matsunaga, Y. Ikuhara, and T. Yamamoto, *Phys. Rev. B* **68** (2003).
- 129 R. DeHoff, *Thermodynamics in Materials Science* (Taylor & Francis Group, Boca Taton, FL, 2006).
- 130 J. Malcolm W. Chase, *NIST-JANAF thermochemical tables* (American Chemical Society, Washington, D.C., 1998).
- 131 I. Barin, O. Knacke, and O. Kubaschewski, *Thermochemical properties of inorganic substances: supplement* (Springer-Verlag, New York, 1977).
- 132 O. Knacke, O. Kabaschewski, and K. Hesselmann, *Thermochemical properties of inorganic substances* (Spring, Berlin, 1991).
- 133 J. He, R. K. Behera, M. W. Finnis, X. Li, E. C. Dickey, S. R. Phillpot, and S. B. Sinnott, *Acta Mater.* **55**, 4325 (2007).
- 134 P. W. Anderson, *Phys. Rev. Lett.* **34**, 953 (1975).
- 135 S. Kim, V. Gopalan, K. Kitamura, and Y. Furukawa, *J. Appl. Phys.* **90**, 2949 (2001).
- 136 H. X. Xu, D. Lee, J. He, S. B. Sinnott, V. Gopalan, V. Dierolf, and S. R. Phillpot, *Phys. Rev. B* **78**, 174103 (2008).
- 137 J. H. Yao, J. J. Xu, G. Y. Zhang, X. J. Chen, B. Li, and G. G. Li, *Chin. Phys. Lett.* **17**, 513 (2000).
- 138 R. L. Byer, *J. Nonlinear Opt. Phys. Mater* **6**, 549 (1997).

- 139 A. Mehta, E. K. Chang, and D. M. Smyth, *J. Mater. Res.* **6**, 851 (1991).
- 140 T. K. Halstead, *J. Chem. Phys.* **53**, 3427 (1970).
- 141 N. Schmidt, K. Betzler, M. Grabs, S. Kapphan, and F. Klose, *J. Appl. Phys.* **65**, 1253 (1989).
- 142 D. P. Birnie, *J. Mater. Sci.* **28**, 302 (1993).
- 143 V. Dierolf and C. Sandmann, *J. Lumin.* **125**, 67 (2007).
- 144 J. Zou, S. M. Zhou, J. Xu, L. H. Zhang, Z. L. Xie, P. Han, and R. Zhang, *J. Appl. Phys.* **98** (2005).
- 145 H. Suche, R. Wessel, S. Westenhofer, W. Sohler, S. Bosso, C. Carmannini, and R. Corsini, *Opt. Lett.* **20**, 596 (1995).
- 146 J. G. Sole, L. Bausa, D. Jaque, E. Montoya, H. Murrieta, and F. Jaque, *Spectrochim. Acta, Part A* **54**, 1571 (1998).
- 147 V. Dierolf, C. Sandmann, A. B. Kutsenko, and T. Troster, *Radiat. Eff. Defects Solids* **155**, 253 (2001).
- 148 S. Balsamo, S. Maio, I. Montrosset, H. Suche, and W. Sohler, *Opt. Quantum Electron.* **31**, 29 (1999).
- 149 I. Baumann, S. Bosso, R. Brinkmann, R. Corsini, M. Dinand, A. Greiner, K. Schafer, J. Sochtig, W. Sohler, H. Suche, and R. Wessel, *IEEE J. Sel. Top. Quantum Electron.* **2**, 355 (1996).
- 150 J. Amin, J. A. Aust, D. L. Veasey, and N. A. Sanford, *Electron. Lett.* **34**, 456 (1998).
- 151 V. Voinot, R. Ferriere, and J. P. Goedgebuer, *Electron. Lett.* **34**, 549 (1998).
- 152 L. Rebouta, M. F. daSilva, J. C. Soares, D. Serrano, E. Dieguez, F. AgulloLopez, and J. Tornero, *Appl. Phys. Lett.* **70**, 1070 (1997).
- 153 R. M. Araujo, K. Lengyel, R. A. Jackson, L. Kovacs, and M. E. G. Valerio, *J. Phys.: Condens. Matter* **19**, 046211 (2007).
- 154 R. D. Shannon, *Acta Crystallographica Section A* **32**, 751 (1976).
- 155 R. M. Moon, W. C. Koehler, H. R. Child, and Raubenhe.Lj, *Phys. Rev.* **1**, 722 (1968).
- 156 M. Faucher, J. Pannetier, Y. Charreire, and P. Caro, *Acta Crystallogr., Sect. B: Struct. Sci.* **38**, 344 (1982).
- 157 J. S. Olsen, C. S. G. Cousins, L. Gerward, H. Jhans, and B. J. Sheldon, *Phys. Scr.* **43**, 327 (1991).

- 158 C. T. Prewitt, R. D. Shannon, D. B. Rogers, and A. W. Sleight, *Inorg. Chem.* **8**, 1985 (1969).
- 159 A. M. Boring and J. L. Smith, *Challenges in Plutonium Science I*, 91 (2000).
- 160 K. T. Moore and G. van der Laan, *Rev. Mod. Phys.* **81**, 235 (2009).
- 161 U. Vonbarth and C. D. Gelatt, *Physical Review B* **21**, 2222 (1980).
- 162 A. Kiejna, G. Kresse, J. Rogal, A. De Sarkar, K. Reuter, and M. Scheffler, *Phys. Rev. B* **73** (2006).
- 163 J. Hafner, *J. Comput. Chem.* **29**, 2044 (2008).
- 164 T. Oguchi, K. Terakura, and A. R. Williams, *Phys. Rev. B* **28**, 6443 (1983).
- 165 M. Cococcioni and S. de Gironcoli, *Phys. Rev. B* **71** (2005).
- 166 Y. Wang and D. J. Doren, *Solid State Commun.* **136**, 186 (2005).
- 167 L. Wang, T. Maxisch, and G. Ceder, *Phys. Rev. B* **73**, 195107 (2006).
- 168 R. Grau-Crespo, F. Cora, A. A. Sokol, N. H. de Leeuw, and C. R. A. Catlow, *Phys. Rev. B* **73** (2006).
- 169 A. Rohrbach, J. Hafner, and G. Kresse, *Phys. Rev. B* **70** (2004).
- 170 R. Zimmermann, P. Steiner, R. Claessen, F. Reinert, S. Hufner, P. Blaha, and P. Dufek, *J. Phys.: Condens. Matter* **11**, 1657 (1999).
- 171 C. A. Mccammon and L. G. Liu, *Physics and Chemistry of Minerals* **10**, 106 (1984).
- 172 J. Kubler and A. R. Williams, *J. Magn. Magn. Mater.* **54-7**, 603 (1986).
- 173 P. D. Battle and A. K. Cheetham, *Journal of Physics C: Solid State Physics* **12**, 337 (1979).
- 174 C. N. R. R. a. B. Raveau, *Transition Metal Oxides* (Wiley-VCH, New York, 1995).
- 175 E. N. Maslen, V. A. Streltsov, N. R. Streltsova, and N. Ishizawa, *Acta Crystallogr., Sect. B: Struct. Sci.* **50**, 435 (1994).
- 176 G. Rollmann, A. Rohrbach, P. Entel, and J. Hafner, *Phys. Rev. B* **69** (2004).
- 177 B. Hourahine, S. Sanna, B. Aradi, C. Kohler, and T. Frauenheim, *Physica B* **376**, 512 (2006).
- 178 A. Lazreg, Z. Dridi, F. Benkabou, and B. Bouhafs, *Physica B* **403**, 2702 (2008).

- 179 M. Losurdo, M. M. Giangregorio, P. Capezzuto, G. Bruno, R. G. Toro, G. Malandrino, I. L. Fragala, L. Armelao, D. Barreca, E. Tondello, A. A. Suvorova, D. Yang, and E. A. Irene, *Adv. Funct. Mater.* **17**, 3607 (2007).
- 180 J. P. McKelvey, *Solid State Physics For Engineering and Materials Science* (Krieger Publishing Company, Malabar, Florida, 1993).
- 181 M. Carrascosa and F. Agullolopez, *Journal of the Optical Society of America B-Optical Physics* **7**, 2317 (1990).
- 182 A. Harhira, L. Guilbert, P. Bourson, and H. Rinnert, *Applied Physics B-Lasers and Optics* **92**, 555 (2008).
- 183 F. Jermann and J. Otten, *Journal of the Optical Society of America B-Optical Physics* **10**, 2085 (1993).
- 184 I. W. Kim, S. S. Yi, V. F. Pichugin, V. Y. Yakovlev, and M. S. Dmitriev, *J. Cryst. Growth* **253**, 319 (2003).
- 185 J. E. Alfonso, M. J. Martin, and C. Zaldo, *Appl. Phys. Lett.* **71**, 2904 (1997).
- 186 L. S. Qiang, H. X. Zhang, and C. Q. Xu, *Mater. Chem. Phys.* **77**, 6 (2003).
- 187 D. L. Zhang, D. C. Wang, and E. Y. B. Pun, *J. Appl. Phys.* **97** (2005).
- 188 D. M. B. P. Milori, I. J. Moraes, A. C. Hernandez, R. R. Desouza, M. S. Li, M. C. Terrile, and G. E. Barberis, *Phys. Rev. B* **52**, 3802 (1995).
- 189 K. Polgar and A. P. Skvortsov, *Opt. Spektrosk.* **58**, 229 (1985).
- 190 J. Blumel, E. Born, and T. Metzger, *J. Phys. Chem. Solids* **55**, 589 (1994).
- 191 S. Y. Wu and W. C. Zheng, *Phys. Rev. B* **65** (2002).
- 192 C. Buchal and S. Mohr, *J. Mater. Res.* **6**, 134 (1991).
- 193 V. B. Ptashnik, T. Y. Dunaeva, and I. V. Myasnikov, *Inorg. Mater.* **21**, 1814 (1985).
- 194 V. I. Lapshin and A. P. Rumyantsev, *Inorg. Mater.* **12**, 1797 (1976).
- 195 G. I. Malovichko, V. G. Grachev, and O. F. Schirmer, *Solid State Commun.* **89**, 195 (1994).
- 196 H. Wang, X. Y. Kuang, D. Dong, Y. Xiong, and K. W. Zhou, *Physica B* **367**, 53 (2005).
- 197 T. Gog, P. Schotters, J. Falta, G. Materlik, and M. Grodzicki, *J. Phys.: Condens. Matter* **7**, 6971 (1995).
- 198 D. S. Yang, N. Sung, and T. H. Yeom, *J. Phys. Soc. Jpn.* **78**, 114605 (2009).

- 199 G. I. Malovichko, V. G. Grachev, O. F. Schirmer, and B. Faust, *J. Phys.: Condens. Matter* **5**, 3971 (1993).
- 200 G. E. Peterson, A. M. Glass, and T. J. Negran, *Appl. Phys. Lett.* **19**, 130 (1971).
- 201 S. Omar, in *Department of Materials Science and Engineering* (University of Florida, Gainesville, 2008), Vol. Ph.D.
- 202 N. E. Brese and M. Okeeffe, *Acta Crystallographica Section B-Structural Science* **47**, 192 (1991).
- 203 L. Pauling, *The Nature of the Chemical Bond* (Cornell University Press, New York, 1960).
- 204 I. Syozi, *Progress of Theoretical Physics* **6**, 306 (1951).
- 205 P. G. Watson, *Physica* **75**, 627 (1974).
- 206 M. Yashima, S. Kobayashi, and T. Yasui, *Solid State Ionics* **177**, 211 (2006).
- 207 I. U. o. Crystallography, *The International Tables of Crystallography* (Kluwer Academic Publishers, 1996).
- 208 H. Hayashi, R. Sagawa, H. Inaba, and K. Kawamura, *Solid State Ionics* **131**, 281 (2000).
- 209 A. Atkinson and A. Selcuk, *Solid State Ionics* **134**, 59 (2000).
- 210 J. D. Gale, *Journal of the Chemical Society-Faraday Transactions* **93**, 629 (1997).
- 211 J. D. Gale and A. L. Rohl, *Molecular Simulation* **29**, 291 (2003).
- 212 R. W. Grimes, G. Busker, M. A. McCoy, A. Chroneos, J. A. Kilner, and S. P. Chen, *Berichte Der Bunsen-Gesellschaft-Physical Chemistry Chemical Physics* **101**, 1204 (1997).
- 213 S. Vyas, R. W. Grimes, D. H. Gay, and A. L. Rohl, *Journal of the Chemical Society-Faraday Transactions* **94**, 427 (1998).
- 214 V. Butler, C. R. A. Catlow, B. E. F. Fender, and J. H. Harding, *Solid State Ionics* **8**, 109 (1983).
- 215 A. Gotte, K. Hermansson, and M. Baudin, *Surface Science* **552**, 273 (2004).
- 216 A. Gotte, D. Spangberg, K. Hermansson, and M. Baudin, *Solid State Ionics* **178**, 1421 (2007).
- 217 R. W. Grimes, G. Busker, M. A. McCoy, A. Chroneos, J. A. Kilner, and S. P. Chen, *Physical Chemistry Chemical Physics* **101**, 1204 (1997).
- 218 R. W. Grimes, D. J. Binks, and A. B. Lidiard, *Philosophical Magazine A* **72**, 651 (1995).

- 219 M. A. McCoy, R. W. Grimes, and W. E. Lee, *Philosophical Magazine A* **76**, 1187 (1997).
- 220 H. Inaba, R. Sagawa, H. Hayashi, and K. Kawamura, *Solid State Ionics* **122**, 95 (1999).
- 221 J. R. Sims and R. N. Blumenthal, *High Temperature Science*, 99 (1976).
- 222 H. W. Chiang, R. N. Blumenthal, and R. A. Fournelle, *Solid State Ionics* **66**, 85 (1993).
- 223 J. R. Sims and R. N. Blumenthal, *High Temperature Science* **8**, 99 (1976).
- 224 A. Nakajima, A. Yoshihara, and M. Ishigame, *Physical Review B* **50**, 13297 (1994).
- 225 L. Gerward, J. S. Olsen, L. Petit, G. Vaitheeswaran, V. Kanchana, and A. Svane, *Journal of Alloys and Compounds* **400**, 56 (2005).
- 226 Y. L. Wang, K. Duncan, E. D. Wachsman, and F. Ebrahimi, *Solid State Ionics* **178**, 53 (2007).
- 227 V. Kanchana, G. Vaitheeswaran, A. Svane, and A. Delin, *Journal of Physics-Condensed Matter* **18**, 9615 (2006).
- 228 S. J. Duclos, Y. K. Vohra, A. L. Ruoff, A. Jayaraman, and G. P. Espinosa, *Physical Review B* **38**, 7755 (1988).
- 229 D. J. Green, *An introduction to the mechanical properties of ceramics* (Cambridge University Press, 2004).
- 230 D. J. M. Bevan and J. Kordis, *Journal of Inorganic & Nuclear Chemistry* **26**, 1509 (1964).
- 231 R. J. Panlener, R. N. Blumenthal, and J. E. Garnier, *Journal of Physics and Chemistry of Solids* **36**, 1213 (1975).
- 232 S. Sameshima, H. Ono, K. Higashi, K. Sonoda, Y. Hirata, and Y. Ikuma, *Journal of the Ceramic Society of Japan* **108**, 1060 (2000).
- 233 N. Sammes, G. Tompsett, Y. J. Zhang, A. Cartner, and R. Torrens, *Denki Kagaku* **64**, 674 (1996).
- 234 M. W. Barsoum, *Fundamentals of Ceramics* (McGraw-Hill, 1997).
- 235 M. Katsuragawa, H. Kashihara, and M. Akebi, *J. Nucl. Mater.* **204**, 14 (1993).
- 236 R. N. Hill, D. C. Wade, J. R. Liaw, and E. K. Fujita, *Nucl. Sci. Eng.* **121**, 17 (1995).
- 237 T. Inoue, M. Sakata, H. Miyashiro, T. Matsumura, A. Sasahara, and N. Yoshiki, *Nucl. Technol.* **93**, 206 (1991).
- 238 B. Cox and Y. M. Wong, *J. Nucl. Mater.* **270**, 134 (1999).

- 239 S. I. Hong, K. W. Lee, and K. T. Kim, *J. Nucl. Mater.* **303**, 169 (2002).
- 240 E. Vitikainen and P. Nenonen, *J. Nucl. Mater.* **78**, 362 (1978).
- 241 R. E. Stoller, G. R. Odette, and B. D. Wirth, *J. Nucl. Mater.* **251**, 49 (1997).
- 242 J. Gan, G. S. Was, and R. E. Stoller, *J. Nucl. Mater.* **299**, 53 (2001).
- 243 R. E. Stoller, *J. Nucl. Mater.* **276**, 22 (2000).
- 244 R. E. Stoller and A. F. Calder, *J. Nucl. Mater.* **283**, 746 (2000).
- 245 S. J. Wooding, D. J. Bacon, and W. J. Phythian, *Philosophical Magazine a-Physics of Condensed Matter Structure Defects and Mechanical Properties* **72**, 1261 (1995).
- 246 Y. M. Kim, B. J. Lee, and M. I. Baskes, *Phys. Rev. B* **74** (2006).
- 247 J. F. Ziegler, J. P. Biersak, and U. Littmark, *The Stopping and Range of Ions in Matter*, Pergomon, New Youk, 1985).
- 248 D. R. Trinkle, (The Ohio State University, 2003), Vol. Ph.D.
- 249 M. I. Baskes, *Mater. Chem. Phys.* **50**, 152 (1997).
- 250 J. H. Rose, J. R. Smith, F. Guinea, and J. Ferrante, *Phys. Rev. B* **29**, 2963 (1984).
- 251 B. J. Lee and M. I. Baskes, *Phys. Rev. B* **62**, 8564 (2000).
- 252 B. J. Lee, M. I. Baskes, H. Kim, and Y. K. Cho, *Phys. Rev. B* **64**, 18 (2001).
- 253 B. J. Lee, J. H. Shim, and M. I. Baskes, *Phys. Rev. B* **68** (2003).
- 254 F. H. Stillinger and T. A. Weber, *Phys. Rev. B* **31**, 5262 (1985).
- 255 R. A. Johnson, *Philosophical Magazine a-Physics of Condensed Matter Structure Defects and Mechanical Properties* **63**, 865 (1991).
- 256 G. J. Ackland, *Philosophical Magazine a-Physics of Condensed Matter Structure Defects and Mechanical Properties* **66**, 917 (1992).
- 257 E. A. Brandes, *Smithells Metals Reference Book* (Butterworths, London, 1983).
- 258 C. S. Barrett and T. B. Massalski, *Structure of Metals* (McGraw-Hill, New York, 1966).
- 259 G. Simmons and H. Wang, *Single Crystal Elastic Constants and Calculated Aggregate Properties: A Handbook* (MIT Press, Cambridge, 1971).
- 260 A. T. Dinsdale, *Calphad-Computer Coupling of Phase Diagrams and Thermochemistry* **15**, 317 (1991).

- 261 F. R. de Boer, W. C. M. Mattens, A. R. Miedema, and A. K. Niessen, *Cohesion in Metals: Transition Metal Alloys* (Horth-Holland, Amsterdam, 1988).
- 262 R. Smith, *Atomic & Ion Collisions in Solids and at Surfaces* (Cambridge University Press, Cambridge, UK, 1997).
- 263 D. Faken and H. Jonsson, *Comput. Mater. Sci.* **2**, 279 (1994).
- 264 A. Meldrum, L. A. Boatner, and R. C. Ewing, *Nuclear Instruments & Methods in Physics Research Section B-Beam Interactions with Materials and Atoms* **207**, 28 (2003).

## BIOGRAPHICAL SKETCH

Haixuan Xu was born in Anshan, Liaoning Province, China. He received his Bachelor of Engineering degree in Metallic Materials Engineering from Dalian University of Technology, Dalian, in 2005. He was also a member of Institute of University Students Innovation of the university. Then he came to the United States of America for higher education. He joined Computational Materials Science Focus Group (CMSFG) in the Department of Materials and Engineering at University of Florida, with Prof. Simon R. Phillpot as his advisor. He received Master of Science from University of Florida at 2007. He was awarded the Doctoral Degree in Materials Science and Engineering in May 2010.